

**I. IR Photodissociation Spectroscopy of Large van der Waals Clusters**  
**II. UV Laser-induced Photochemistry of Fe(CO)<sub>5</sub> on Single Crystal Surfaces**

Thesis by  
*Francis Gabriel Celi*

In Partial Fulfillment of the Requirements  
for the Degree of  
Doctor of Philosophy

California Institute of Technology  
Pasadena, California  
1986  
(Submitted August 16, 1985)

© 1986

Francis Gabriel Celi

All Rights Reserved

## Acknowledgments

A number of people have helped make my stay at Caltech scientifically rewarding and personally enriching, and it is a sincere pleasure to acknowledge them.

First is my advisor, Ken Janda, whose guidance and patience have nurtured my growth as a researcher. I hope some of his abilities of defining important questions and generating ideas for novel experiments have rubbed off on me. My previous mentors, Doug Ridge, Denis Bogan and Bert Strieb, also deserve thanks for their roles in my formative years.

Two coworkers have contributed much to the following pages, and I owe them special thanks. Paul Whitmore shared the joys of building the UHV chamber with me and added to my vocabulary words such as wavevector and CMA-port. Michael Casassa got me started on the van der Waals molecule project, and introduced me to Bill's Chicken and fake garlic toast. Others that have contributed to the construction of the surface apparatus and to whom I am grateful are Paul Beeken, Steve Kong, Shouleh Nikzad, and especially Eric Sinn, for sprucing up the lab with his racing stripes and fuse sublimator. Dan Auerbach and Malina Hills have also lent time and expertise which I have appreciated.

My officemates for the last 6 years have provided a good mix of diversion and scientific interest. Barry Swartz, Dave Brinza, Fritz Thommen and Colin Western were always willing help program, eat raclette or windsurf. The same is true of the present gang, Dwight Evard, Joe Cline, Sally Hair, Mike O'Loughlin and Brian Reid, who also deserve a special tip-of-the-hat for help rendered during that special

time of thesis writing such as proofreading and refraining from playing football in the office.

The staff have been an invaluable resource, providing much knowledgeable and friendly assistance. I thank everyone, especially Tom Dunn, Bill Schuelke, Tony Stark, Guy Duremberg, Jim Olson, Sig Jenner and Valerie Purvis. Besides their prompt and excellent work, I appreciate their willingness to take the time to share the knowledge of their crafts with me.

My life outside the lab has been much fun and for that I have many people to thank. Miles Collins, Concetto Geremia, Mike Pettersen have been special friends, along with the the rest of the Caltech Men's Glee Club have provided plenty of entertaining times, to say the least. Charlie Koerting, Jerry Winniczek, Dave Moll and Don Berry trekked through the high country or sailed the seas with me. The Beauchamp group, Bop and Susie Cave, Tom and Margaret Dunn and Liz Thomas were also important people in helping me stay sane.

The support of my family through this time is implicit and was always appreciated. Special thanks go also to my thesis tag-team of Miles Collins and Lelia Hanratty, for their time and energy.

Financial support for this work which was provided by the Department of Energy, the Office of Naval Research and the Atlantic Richfield Corporation are all gratefully acknowledged.

Finally but most importantly, I thank my wife, Maureen, for her love and support.

## ABSTRACT

Chapter 2 is a summary of vibrational predissociation spectra of weakly bound clusters containing either  $\text{CF}_3\text{I}$  or  $\text{CF}_3\text{Br}$ . Spectra indicative of  $\text{ArCF}_3\text{I}$ ,  $\text{KrCF}_3\text{I}$ ,  $(\text{CF}_3\text{I})_2$ ,  $\text{ArCF}_3\text{Br}$  and  $(\text{CF}_3\text{Br})_2$  clusters are presented with comparison to the matrix-isolation spectra of  $\text{CF}_3\text{I}$  and  $\text{CF}_3\text{Br}$ .

The infrared photodissociation technique can be applied to the study of weakly bonded clusters which do not absorb in the infrared by attaching an IR chromophore; this work is presented in Chapter 3. Vibrational predissociation spectra of large clusters of Ar, Kr,  $\text{N}_2$  and  $\text{CH}_4$  containing a single  $\text{CH}_3\text{F}$  or  $\text{C}_2\text{H}_4$  chromophore are obtained as a function of cluster size. The IR spectra distinguish three regimes of cluster size in the  $\text{CH}_3\text{F}$  case. The dissociation profiles yield information on the chromophore environment and the lifetime of the excited vibration. The clusters are gas-phase analogies to the matrix-isolation technique, although differences between the two are consistent with the presumed icosahedral cluster geometry, and “matrix” and “surface” sites are distinguishable.

Chapter 4 presents the application of a simple two-level-with-decay model to the photodesorption of weakly bound adsorbates on crystal surfaces. Feasibility estimates are reported and establish that vibrational predissociation of the excited adsorbates can be induced in the infrared, where energy quenching mechanisms on surfaces can be quite fast. The effect of these quenching mechanisms on the lineshapes present the opportunity to probe the processes with the use of the photodesorption technique. Extraction of the phenomenological rate constants is described. Also reported are attempts to observe photodesorption induced by low-

power lasers.

The photodecomposition of  $\text{Fe}(\text{CO})_5$  on three single crystal surfaces, sapphire ( $\text{Al}_2\text{O}_3$ ),  $\text{Si}(100)$  and  $\text{Ag}(110)$ , using UV irradiation is described in Chapter 5. The quenching of excited electronic states of adsorbates is expected to be quite different on the surfaces, yet dissociation of the  $\text{Fe}(\text{CO})_5$  is observed in all cases. The results allow determination of the dissociation mechanism and also imply that the  $\text{Fe}(\text{CO})_5$  dissociation rate is ultra-fast ( $< 10^{-13}$ ). Extensions of this initial investigation are discussed.

**Table of Contents**

Dedication . . . . .	ii
Acknowledgments . . . . .	iii
Abstract . . . . .	v
List of Figures . . . . .	viii
List of Tables . . . . .	xi
Chapter 1 . . . . .	1
<b>Introduction</b>	
References . . . . .	7
Chapter 2 . . . . .	9
<b>IR Photodissociation Spectroscopy of van der Waals Clusters Containing     CF<sub>3</sub>I or CF<sub>3</sub>Br</b>	
References . . . . .	35
Chapter 3 . . . . .	39
<b>Infrared Spectroscopy of Large van der Waals Clusters: Matrix Isolation     Spectra of Gas-Phase Molecules</b>	
References . . . . .	119
Chapter 4 . . . . .	127
<b>Photodesorption Lineshapes of Weakly Bound Molecules</b>	
References . . . . .	174
Chapter 5 . . . . .	181
<b>UV Laser-Induced Dissociation of Fe(CO)<sub>5</sub> on Single Crystal Surfaces</b>	
References . . . . .	223
Appendix 1 . . . . .	237
<b>Vibrational Predissociation Spectrum of (CH<sub>3</sub>F)<sub>2</sub></b>	
Appendix 2 . . . . .	240
<b>Bakeout Controller System.</b>	

## List of Figures

<b>Chapter 2</b>	<b>Infrared Photodissociation Spectra of CF<sub>3</sub>I and CF<sub>3</sub>Br Clusters.</b>	
Figure 1.	CF <sub>3</sub> I, CF <sub>3</sub> Br absorption spectra in Ar matrices . . . . .	16
Figure 2.	Dissociation spectra of Ar <sub>n</sub> CF <sub>3</sub> Br clusters . . . . .	21
Figure 3.	(CF <sub>3</sub> Br) <sub>n</sub> dissociation profiles . . . . .	24
Figure 4.	Dissociation spectra of Ar <sub>n</sub> CF <sub>3</sub> I and Kr <sub>n</sub> CF <sub>3</sub> I clusters . . . . .	28
Figure 5.	Dissociation profiles of clusters containing (CF <sub>3</sub> I) <sub>2</sub> . . . . .	29
<b>Chapter 3</b>	<b>IR Photodissociation Spectra of Large van der Waals Clusters.</b>	
Figure 1.	Experimental schematic: molecular beam spectrometer . . . . .	49
Figure 2a.	Mass spectrum of a highly-clustered molecular beam . . . . .	53
Figure 2b.	Schematic of electron-impact cluster fragmentation . . . . .	54
Figure 3.	Small-cluster limit $\nu_3$ dissociation spectra of CH <sub>3</sub> F clusters . . . . .	61
Figure 4.	Pressure dependence of CH <sub>3</sub> F <sup>+</sup> dissociation profile in Ar . . . . .	66
Figure 5.	Dissociation profiles of Ar <sub>n</sub> CH <sub>3</sub> F <sup>+</sup> ion masses . . . . .	69
Figure 6.	Dissociation spectra of CH <sub>3</sub> F-containing Kr clusters . . . . .	72
Figure 7.	IR spectra of (N <sub>2</sub> ) <sub>n</sub> CH <sub>3</sub> F clusters . . . . .	77
Figure 8.	Dissociation profiles of Ar clusters containing C <sub>2</sub> H <sub>4</sub> . . . . .	81
Figure 9.	IR photodissociation spectra of (CH <sub>4</sub> ) <sub>n</sub> C <sub>2</sub> H <sub>4</sub> clusters . . . . .	83
Figure 10.	Dissociation spectra of N <sub>2</sub> clusters containing C <sub>2</sub> H <sub>4</sub> . . . . .	85
Figure 11.	“Characteristic cluster size,” (N/Z)*, vs. pressure . . . . .	93
Figure 12.	Mass spectral pressure dependences of Ar <sub>n</sub> <sup>+</sup> cluster ions . . . . .	95
Figure 13.	Schematic of A <sub>12</sub> X cluster models . . . . .	101
<b>Chapter 4</b>	<b>Photodesorption of Weakly Bound Molecules</b>	
Figure 1.	Schematic of two-level-plus-decay model . . . . .	137
Figure 2.	Lineshape expression applied to (C <sub>2</sub> H <sub>4</sub> ) <sub>3</sub> spectrum . . . . .	142
Figure 3.	Photodesorption probability (1-F <sub>m</sub> ) vs. ( $\omega_R$ ) . . . . .	154

**Chapter 4 (cont.)**

Figure 4.  $1-F_m$ , varying quenching rate ( $\gamma_q$ ) and irradiation time ( $t$ ) 156

Figure 5.  $1-F_m$ , varying desorption ( $\gamma_D$ ) and quenching ( $\gamma_q$ ) rates . 157

Figure 6.  $1-F_m$ ,  $\gamma_q$  and  $\gamma_D$  varied . . . . . 159

Figure 7. Logarithmic plot ( $\ln(1-F_m)$ ) and FWHM *vs.*  $\omega_R$  . . . . . 162

Figure 8.  $\ln(1-F_m)$  and FWHM, varying  $t$  and  $\gamma_q$  . . . . . 164

Figure 9.  $\ln(1-F_m)$  and FWHM,  $\gamma_D$  varied for a given  $\gamma_q$  . . . . . 166

Figure 10.  $\ln(1-F_m)$  and FWHM, with fast quenching rate . . . . . 168

**Chapter 5 UV Laser-induced Photochemistry of  $\text{Fe}(\text{CO})_5$  on Single Crystal Surfaces.**

Figure 1.  $\text{Fe}(\text{CO})_x$  energy levels with  $\text{Fe}(\text{CO})_5$  absorption spectrum . 184

Figure 2. Diagram of the ultra-high vacuum chamber . . . . . 188

Figure 3a. Diagram of the crystal manipulator . . . . . 191

Figure 3b. Detail of the refrigerator coupling to the crystal holder . . 192

Figure 4. Auger electron (AES) spectrum, Ag(110) . . . . . 196

Figure 5. LEED pattern, clean Ag(110) . . . . . 197

Figure 6. Observed cracking pattern of  $\text{Fe}(\text{CO})_5$  . . . . . 198

Figure 7. Schematic of the surface photochemistry experiment . . . . 200

Figure 8. Thermal desorption spectra,  $\text{Fe}(\text{CO})_5/\text{Al}_2\text{O}_3$  . . . . . 203

Figure 9. Schematic, observed photochemistry signals *vs.* time . . . 206

Figure 10. Annealing phenomenon,  $\text{Fe}(\text{CO})_5$  on Si(100) . . . . . 207

Figure 11. Photochemical, thermal desorption yields,  $\text{Fe}(\text{CO})_5/\text{Al}_2\text{O}_3$  . 210

Figure 12. Power dependence of dissociation yield,  $\text{Fe}(\text{CO})_5$  on  $\text{Al}_2\text{O}_3$  212

Figure 13. Schematic of  $\text{Fe}(\text{CO})_5$  dissociation mechanisms . . . . . 218

Figure 14. Model for energy transfer considerations . . . . . 223

**Appendix 1 Vibrational Predissociation of the Methyl Fluoride Dimer.**

Figure 1. Predissociation spectrum of  $(\text{CH}_3\text{F})_2$  . . . . . 240

**Appendix 2 Bakeout Controller**

Figure 1. Schematic of the bakeout controller system . . . . .	244
Figure 2. Diagram of the bakeout controller . . . . .	246
Figure 3. Diagram of the refrigerator pulser . . . . .	247
Figure 4. Diagram of the oven interlock . . . . .	248
Figure 5. Ion gauge trace during bakeout of UHV chamber . . . . .	250

**List of Tables**

**Chapter 2** Infrared Photodissociation Spectra of CF<sub>3</sub>I and CF<sub>3</sub>Br Clusters.

Table 1. Gas-phase absorption frequencies of CF <sub>3</sub> I and CF <sub>3</sub> Br . . . . .	14
Table 2a. CF <sub>3</sub> Br frequencies in matrices and dissociation spectra . . . . .	18
Table 2b. CF <sub>3</sub> I frequencies in matrices and dissociation spectra . . . . .	19

**Chapter 3** IR Photodissociation Spectra of Large van der Waals Clusters.

Table 1. CH <sub>3</sub> F small cluster (A <sub>x</sub> CH <sub>3</sub> F) spectral parameters . . . . .	63
Table 2. CH <sub>3</sub> F( $\nu_3$ ) frequencies in matrices and large clusters . . . . .	105
Table 3. C <sub>2</sub> H <sub>4</sub> ( $\nu_7$ ) frequencies in matrices and large clusters . . . . .	107

**Chapter 4** Photodesorption of Weakly Bound Molecules.

Table 1. IR Reflection-Absorption Spectra on Surfaces . . . . .	151
---	-----

**Chapter 5** UV Photochemistry of Fe(CO)<sub>5</sub> on Single Crystal Surfaces.

Table 1. Surface heating parameters and calculations . . . . .	216
Table 2. Calculated energy transfer rates . . . . .	225

*CHAPTER 1*

**INTRODUCTION**

The advent of the supersonic expansion technique<sup>1</sup> revolutionized many chemical fields of study. The spectroscopy of gas-phase species experienced a renaissance, moving from room-temperature gas bulbs to the beam environment in which the internal degrees of freedom of a molecule can often be cooled to within a few degrees of absolute zero.<sup>2</sup> The simplification of spectral interpretation resulting from this cooling effect is widely documented in small molecules (e.g., NO<sub>2</sub><sup>3</sup>) as well as large (e.g., pentacene<sup>4</sup> – C<sub>22</sub>H<sub>14</sub>). The study of chemical reaction dynamics has progressed from determination of thermally and spatially averaged rate constants to differential scattering cross sections, which can yield direct information on intermolecular potentials,<sup>5</sup> and state-to-state reaction cross sections at specific translational and internal energy.<sup>6</sup> The supersonic beam technique has affected in a most dramatic way the study of “esoteric” species, those which are normally stable only at low temperature. It is the potential of the beam environment as a synthetic tool, the ability to stabilize species bound only by the van der Waals interaction, that is exploited in the experiments reported in the first part of this thesis.

Dispersion forces between atoms and molecules are the basis of van der Waals bonding, and the characterization of these forces is nearly a century-old topic, beginning with consideration of transport phenomena in bulk liquids and gases.<sup>5</sup> Before the wide usage of supersonic expansions, a small number of van der Waals complexes were spectroscopically identified in high pressure gas mixtures.<sup>7</sup> With the use of expansion techniques in conjunction with electric resonance, microwave and laser-based (IR and visible/UV) detection techniques, rapid progress has been

made in the characterization of a wide variety of van der Waals molecules,<sup>8</sup> such as hydrogen bonded complexes.<sup>9</sup>

An intriguing use of the van der Waals bond has been in the formation of weakly bound molecules that are used as model compounds for the study of intramolecular energy transfer in isolated molecules. A wide range of “energy randomization rates” (determined mainly from linewidth studies) have been reported, even within series of complexes containing the same initially excited moiety.<sup>10,11</sup> It appears that the specifics of the van der Waals potential surface between a probed molecule and its inert partner may dominate the dynamics of the relaxation, as opposed to characteristics of the isolated probe molecule;<sup>11</sup> even so, the description of the dynamics of van der Waals molecules has become a challenging topic in its own right. We have employed the infrared photodissociation technique in the study of these weakly bound complexes. Chapter 2 is a report of the infrared spectra of van der Waals clusters containing  $\text{CF}_3\text{I}$  and  $\text{CF}_3\text{Br}$ . A brief report of the infrared photodissociation spectrum of the  $\text{CH}_3\text{F}$  dimer is included as appendix 1.

The study summarized in chapter 3 is a novel application of the IR photodissociation technique: the use of an IR chromophore to probe large clusters, or microcrystallites, of rare gases or inert molecules. Condensation of these agglomerates is made feasible by the high collision rate and low local temperature in the expansion region. There is currently a great deal of effort to generate and characterize these gas-phase versions of condensed matter, ranging from rare gases crystals<sup>12</sup> to “catalytic” metal<sup>13</sup> clusters. Interest in the energetics and structure of rare gas clusters grew out of consideration of homogeneous nucleation phenomena.<sup>14</sup>

Simple theories show the observed nucleation rate can be calculated using the cluster distribution which, in turn, is reflective of the free energy of the individual clusters. Hence, determination of the stability of various cluster geometries became an active theoretical field. Questions of this nature can now be addressed in the experimental arena: it is possible to observe in the cluster distribution relatively stable, or “magic number,” cluster sizes. Surprisingly, even small clusters show crystallographic structure similar to the bulk solid. Presented in Chapter 3 is a study of large rare gas clusters by the vibrational predissociation technique, employing two infrared chromophores ( $\text{CH}_3\text{F}$  and  $\text{C}_2\text{H}_4$ ) to couple laser excitation into the clusters. An extensive review is presented of cluster properties and the extent to which they can be expected to influence the dissociation lineshapes.

The second part of this thesis (Chapters 4 and 5) deals with experiments from a vastly different realm: laser-surface interactions. The conceptual relation between our efforts in the two diverse areas, molecular beam spectroscopy and laser-surface chemistry, is divulged in Chapter 4. A simple model used to describe predissociation spectra of van der Waals molecules can be applied to IR-induced desorption of weakly bound adsorbates. Phenomenological rate constants for desorption, surface quenching and dephasing mechanisms can be extracted from the desorption lineshapes. Very little experimental work demonstrating single-photon desorption presently exists,<sup>15</sup> and our own attempts to observe this effect were not successful. Feasibility estimates for the process are generated and example cases are evaluated in light of the sensitivity demonstrated in our experiments.

The gas-solid interface is an area of long-standing practical interest. The

understanding of empirically optimized catalysts for industrial chemical processes has been the stimulus of metal-gas surface chemistry. In an analogous manner, the rapidly expanding electronics industry is mandating semiconductor interfaces as the area of highest priority and is consequently redirecting efforts in the field of surface science efforts toward an understanding of these non-metallic systems.<sup>16</sup> The drive in this direction has had an obvious impact on the young field of laser interactions with surfaces. The resolution capabilities of lasers (especially in the UV) for producing circuit patterns of sub-micron size provides an obvious choice for device fabrication by “direct writing” – without the use of masks.<sup>17</sup> There is clearly an intense effort to explore practical aspects of laser-induced processes in the areas of etching, deposition and annealing of materials related to semiconductor processing.<sup>18</sup> The need for basic experiments under more controlled conditions is an obvious and necessary extension. The ultra-high vacuum (UHV) environment is ideal for the study of reaction mechanisms that occur on clean substrate surfaces without competing gas phase chemistry. While this analysis can not be utilized under processing conditions, the growing use of high pressure reactors interfaced to UHV analysis stations<sup>19</sup> will assuredly be important tools for the study of semiconductor processing chemistry.

Chapter 5 describes basic experiments that we have performed which are directed toward exploring surface photochemical reactions under UHV conditions. Dissociation mechanisms are restricted to those that occur at the gas-solid interface. Energy transfer from the excited surface species to the bulk solid, an area of basic research interest,<sup>20</sup> is in this case an important consideration for practical reasons:

if the rate of energy transfer to the solid is fast, the reaction will be quenched. Specifically, we have examined the ultra-fast UV-induced dissociation of  $\text{Fe}(\text{CO})_5$  on three surfaces: single-crystal  $\text{Al}_2\text{O}_3$ ,  $\text{Si}(100)$  and  $\text{Ag}(110)$ . The progression from insulator through semiconductor to metal was examined in anticipation of progressively faster rates of energy transfer from an excited adsorbate to the solid bulk; in fact, the reaction occurs so rapidly that there is no discernable difference in the dissociation yield between the different surfaces. Future work to complement these preliminary findings is also discussed.

## References

1. A. Kantrowitz and J. Grey, *Rev. Sci. Instrum.* **22** (1951) 328;  
J.B. Anderson and J.B. Fenn, *Phys. Fluids* **8** (1965) 780.
2. D.H. Levy, *Ann. Rev. Phys. Chem.* **31** (1980) 197;  
R.E. Smalley, L. Wharton and D.H. Levy, *Acc. Chem. Res.* **xx** (1977) 139.
3. R.E. Smalley, B.L. Ramakrishna, D.H. Levy and L. Wharton, *J. Chem. Phys.* **61** (1974) 4363.
4. A. Amirav, U. Even and J. Jortner, *Chem. Phys.* **51** (1980) 31.
5. G.C. Maitland, M. Rigby, E.B. Smith and W.A. Wakeham, *Intermolecular Forces*, (Clarendon, Oxford, 1981).
6. R.D. Levine and R.B. Bernstein, *Molecular Reaction Dynamics*, (Clarendon, Oxford, 1974).
7. G. Ewing, *Can. J. Phys.* **54** (1976) 487.
8. See, for example, *Faraday Disc. Chem. Soc.*, **1973** (1982).
9. B.J. Howard, T.R. Dyke and W. Klemperer, *J. Chem. Phys.* **81** (1984) 5417.  
A.S. Pine and W.J. Lafferty, *J. Chem. Phys.* **78** (1983) 2154;  
A.C. Legon, *J. Phys. Chem.* **87** (1983) 2084.
10. K.C. Janda, *Adv. Chem. Phys.* **60** (1985) 201;  
M.P. Casassa, C.M. Western and K.C. Janda, *Resonances in Electron-Molecule Scattering, van der Waals Molecules and Reactive Chemical Dynamics*, ed., D.G. Truhlar (American Chemical Society, Washington, D.C., 1984).
11. G.T. Fraser, D.D. Nelson, Jr., A. Charo and W. Klemperer, *J. Chem. Phys.* **82** (1985) 2535.

12. See the review in Chapter 3.
13. R.L. Whetten, D.M. Cox, D.J. Trevor and A. Kaldor, *J. Phys. Chem.* **89** (1985) 566;  
M.E. Geusic, M.D. Morse and R.E. Smalley, *J. Chem. Phys.* **82** (1985) 590.
14. D.L. Freeman and J.D. Doll, *J. Chem. Phys.* **82** (1985) 462;  
F.F. Abraham, *Homogeneous Nucleation Theory* Supplement I, Advances in Theoretical Chem. (Academic, New York, 1974).
15. T.J. Chuang and I. Hussla, *Phys. Rev. Lett.* **52** (1984) 2045.
16. J. Dieleman, *Thin Solid Films* **86** (1981) 147.
17. R.M. Osgood, Jr., *Ann. Rev. Phys. Chem.* **34** (1983) 77.  
I.P. Herman, in *Laser Processing and Diagnostics*, ed. D. Bäuerle (Springer-Verlag, Berlin, 1984).
18. *Laser Processing and Diagnostics*, ed. D. Bäuerle (Springer-Verlag, Berlin, 1984).
19. C.T. Campbell and M.T. Paffett, *Surf. Sci.* **143** (1984) 517.  
S.A. Joyce, B. Roop, J.C. Schultz, K. Suzuki, J. Thoman and J.I. Steinfeld, in *Laser Processing and Diagnostics*, ed. D. Bäuerle (Springer-Verlag, Berlin, 1984).
20. A.P. Alivisatos, D.H. Waldeck and C.B. Harris, *J. Chem. Phys.* **82** (1985) 541.  
Ph. Avouris and B.N.J. Persson, *J. Phys. Chem.* **88** (1984) 837.

*CHAPTER 2*

**IR PHOTODISSOCIATION SPECTROSCOPY OF  
VAN DER WAALS CLUSTERS CONTAINING  $\text{CF}_3\text{I}$  OR  $\text{CF}_3\text{Br}$**

## 1. Introduction

The growing list of infrared photodissociation spectra of polyatomic van der Waals complexes is responsible for the significant growth and progress exhibited by the field.<sup>1</sup> Of special interest have been a variety of complexes containing the C<sub>2</sub>H<sub>4</sub> molecule which exhibit a wide range of homogeneous linewidths suggesting that the dissociation rate is sensitive to both the molecular structure of the complex and angular momentum constraints in the decomposition.<sup>1,2</sup> It is desirable to extend these efforts to other molecular systems which could probe the variation of other parameters that may affect the dissociation rate, such as the presence of lower-lying vibrational states, or the excitation of levels nearly degenerate in energy but of different class or symmetry.<sup>3,4</sup> The recent use of rotational state-selection techniques in conjunction with infrared excitation<sup>5</sup> allows unequivocal identification of the species excited, but the experiment requires molecules which have permanent dipoles. In this chapter I report the extension of infrared dissociation techniques employed in the initial C<sub>2</sub>H<sub>4</sub>-complex study to clusters containing CF<sub>3</sub>I and CF<sub>3</sub>Br.

The large excitation cross sections exhibited by vibrations in fluorinated species combined with the availability of high-power IR sources (i.e., CO<sub>2</sub> lasers) that overlap the transitions have made these compounds natural choices for studies of IR multiphoton excitation and dissociation. Of the small molecules whose spectroscopy is relatively uncongested, the CF<sub>3</sub>X series (X = Cl, Br, I) is noteworthy, possessing a weak C-X bond which can be ruptured after sequential absorption of IR photons.<sup>6-13</sup> The dissociation was shown to be rapid in a collisionless environment ( $\tau < 1$  nsec<sup>11</sup>), and the IR-induced decomposition of these species has been studied

for potential application in iostope separation schemes.<sup>9,10</sup> Dissociation spectra of the ionic species  $\text{CF}_3\text{I}^+$  have also been reported.<sup>12,13</sup> The large transition moment dipole also makes this an attractive system for a vibrational predissociation study of the van der Waals complexes.

A preliminary survey of the IR predissociation spectra of van der Waals clusters containing  $\text{CF}_3\text{I}$  and  $\text{CF}_3\text{Br}$  is presented here. Specifically, the dissociation profiles as a function of wavelength are obtained for the complexes  $\text{Ar}\cdot\text{CF}_3\text{I}$ ,  $\text{Kr}\cdot\text{CF}_3\text{I}$ ,  $(\text{CF}_3\text{I})_2$ ,  $\text{Ar}\cdot\text{CF}_3\text{Br}$  and  $(\text{CF}_3\text{Br})_2$  throughout the frequency range of a line-tunable  $\text{CO}_2$  laser, although contributions from higher clusters interfere. The intense  $\nu_1$  vibration can be excited in both molecules, while the  $\nu_2+\nu_3$  combination band as well as the first overtone of the  $\nu_5$  mode (which is in Fermi resonance with the  $\nu_1$  mode) can also be excited in  $\text{CF}_3\text{I}$ . Broad bands are observed in the dissociation spectra, which are compared to known gas-phase and matrix-isolation spectra. The rich spectral features evident at the present level of study suggest that further refinement of the spectra may be warranted.

A report of the  $(\text{CF}_3\text{Br})_2$  spectrum has been published by Geraedts *et al.*<sup>15</sup> The spectra of  $(\text{CF}_3\text{Br})_n$  presented here are in agreement with the profile observed in that study but the interpretation of the spectral features is slightly different. Our interpretation, based upon the  $\text{CF}_3\text{I}$  cluster results and comparison to  $\text{CF}_3\text{Br}$  and  $\text{CF}_3\text{I}$  matrix studies, as well as previously reported spectra of large clusters containing  $\text{CH}_3\text{F}$ <sup>14</sup> is that the profiles contain significant contributions from clusters larger than the dimer. Also, a feature assigned as due to  $2\nu_5$  is most likely a higher cluster feature. We feel additional studies must be conducted in

order to isolate the spectra of these van der Waals molecules.

## 2. Experimental

The apparatus used in this study will be described in detail in the next chapter (see Chapter 3, or Ref. [2b]). A continuous supersonic expansion of gas into a high-pressure ( $10^{-3}$ - $10^{-2}$  Torr) source region and is skimmed to produce a molecular beam of gas mixtures containing  $\text{CF}_3\text{Br}$  (Matheson, >99.0%) or  $\text{CF}_3\text{I}$  (PCR Research Chemicals, Inc. 99.4%) in Ar/He or Kr/He mixtures. The mixtures are pressurized up to 150 psig and expanded through a room temperature, 25  $\mu\text{m}$  nozzle. These conditions easily produce clusters in the beam, including  $(\text{CF}_3\text{X})_2$  and  $\text{ArCF}_3\text{X}$ . The molecular beam is irradiated uniformly over a 60 cm flight path by an unfocused, low power ( $\sim 10$ - $15$  W/cm<sup>2</sup>) line-tunable cw  $\text{CO}_2$  laser which is directed anti-parallel to the molecular beam. The long flight path insures dissociation of a significant fraction of the clusters, even with the low power laser. The clusters are detected by an off-axis quadrupole mass spectrometer with electron-impact ionization source. Irradiation of the molecular beam with mechanically chopped laser light produces a modulated ion signal due to loss of dissociated clusters from the beam. The amplified and digitized ion signal is computer averaged with background subtraction and laser power measurement on each datum. Wavelength spectra are obtained by manually tuning the laser grating, and repeating the measurement. The power transmitted through the beam apertures to the *in vacuo* calorimeter is kept constant during a wavelength scan so that only minimal power scaling is necessary.

Spectra are obtained by monitoring an appropriate ion mass, and scanning the

laser wavelength. Many different clusters present in the beam can give ion intensity at a single ion mass as a result of fragmentation upon electron impact. Thus, dissociation spectra are convolutions of the individual cluster spectra weighted by the quantity present in the distribution and the fragmentation efficiency to the monitored ion mass. Expansion conditions can be varied to obtain a single dominant dimeric species, and the resultant IR spectrum is truly that of the van der Waals complex.<sup>2,14</sup> It cannot be stated that the spectra recorded were obtained under these stringent conditions, only that they are at the sensitivity limit for the present spectrometer and reported gas mixtures, and thus serve only as an initial foray into the study of  $\text{CF}_3\text{I}$  and  $\text{CF}_3\text{Br}$  complexes.

### 3. Results and discussion

The vibrational modes of the  $\text{CF}_3\text{I}$  and  $\text{CF}_3\text{Br}$  molecules are given in Table 1, along with the integrated absorption intensities for each mode.<sup>16</sup> The  $\nu_1$  and  $\nu_4$  vibrations are the symmetric and anti-symmetric C–F stretch modes, respectively, and are understandably quite intense. The  $\nu_3$  vibration is the C–X stretch, while  $\nu_2$ ,  $\nu_5$  and  $\nu_6$  are bends.<sup>17</sup> The primary mode accessible to the  $\text{CO}_2$  laser in both species is the strongly absorbing  $\nu_1$  C–F symmetric stretch. In addition, the  $\nu_5$  overtone lies close in energy to  $\nu_1$  ( $\sim 4 \text{ cm}^{-1}$  for  $\text{CF}_3\text{I}$ ,  $\sim 10 \text{ cm}^{-1}$  in  $\text{CF}_3\text{Br}$ ), and derives its absorption intensity through Fermi resonance. The  $\nu_2 + \nu_3$  combination band can also be excited in the  $\text{CF}_3\text{I}$  molecule, but lies outside of the laser tuning range in  $\text{CF}_3\text{Br}$ . Unlike the  $\text{C}_2\text{H}_4^2$  and  $\text{CH}_3\text{F}^{14}$  cluster systems in which the excited mode was the lowest energy vibrational mode in the monomer,  $\text{CF}_3\text{I}$  and  $\text{CF}_3\text{Br}$  exhibit low energy vibrations which could accept excess energy from a dissociation

**Table 1**  
*CF<sub>3</sub>I and CF<sub>3</sub>Br Normal Modes*<sup>†</sup>

Mode	CF <sub>3</sub> I		CF <sub>3</sub> Br	
	$\nu$ (cm <sup>-1</sup> )	A (km/mol)	$\nu$ (cm <sup>-1</sup> )	A (km/mol)
$\nu_1$	1075.2	573.3	1084.6	463.6
$\nu_2$	743.1	43.0	762.1	29.4
$\nu_3$	286.2	0.15	351.4	<0.2
$\nu_4$	1187.2	445.2	1208.8	464.8
$\nu_5$	539.0	2.1	574.8	23.9
$\nu_6$	261.0	0.04	302.7	<0.2

<sup>†</sup> from Person *et al.* [16]

event, thus providing a fast relaxation channel.

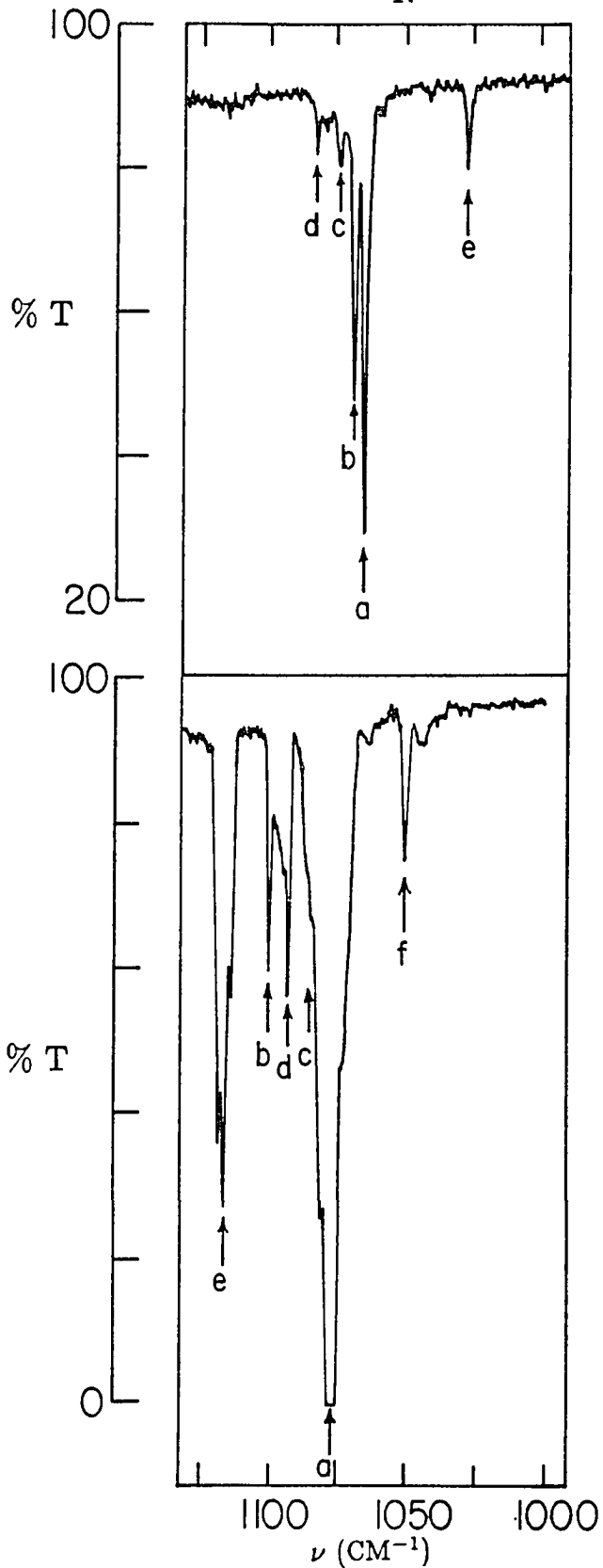
The absorption spectra of  $\text{CF}_3\text{I}$  and  $\text{CF}_3\text{Br}$  isolated in argon matrices are presented in Figure 1. The spectra, obtained from Dr. M.E. Jacox<sup>18</sup> of NBS, are of samples relatively rich in  $\text{CF}_3\text{I}$  or  $\text{CF}_3\text{Br}$  ( $\text{CF}_3\text{X} : \text{Ar}$  of 1 : 400), and allow for deposition of these molecules in adjacent sites to form dimeric (or higher) species. The absorption frequencies from these spectra, those of a similar study of  $\text{CF}_3\text{Br}$  in Ne matrices<sup>19</sup> and results of the dissociation study presented here are collected in Tables 2a and 2b. The  $\nu_1$  mode in both species (as well as the similarly intense  $\nu_4$  mode) is shifted to the red of the gas phase value by a large amount ( $\Delta\omega \sim 10 \text{ cm}^{-1}$ ) compared to other vibrations in the molecules such as  $\nu_5$  and  $\nu_2$  ( $\Delta\omega = 1 - 2 \text{ cm}^{-1}$ ). The frequency shift is caused by the dipole-induced dipole coupling of the vibrating dipole with the matrix environment. The large shift for  $\nu_1$  is consistent with its large transition moment. Also from the matrix spectra, one sees the  $2\nu_5$  absorption is nearly equal in intensity to the  $\nu_1$  absorption in the  $\text{CF}_3\text{I}$  case, but down in intensity by at least a factor of ten for  $\text{CF}_3\text{Br}$ . The polymeric species (i.e.,  $(\text{CF}_3\text{I})_n$  and  $(\text{CF}_3\text{Br})_n$ ) are observed to absorb at higher frequencies than the isolated monomer in the matrix. The unassigned peak (f) in the  $\text{CF}_3\text{Br}/\text{Ar}$  spectrum appears shifted by too great an amount to be considered a dimer absorption.

The wavelength dependences of dissociation for the  $\text{CF}_3\text{I}$  and  $\text{CF}_3\text{Br}$  van der Waals clusters are reported below. The observed beam attenuation is presented with curves that highlight qualitative features of the spectra. The deconvolution consists of exponentiated Lorentzian lineshapes, from the two-level-plus-decay model lineshape expression derived elsewhere (see Ref. [20] or the summary given

**Figure 1.** Absorption spectra of (a)  $\text{CF}_3\text{I}$  and (b)  $\text{CF}_3\text{Br}$  isolated in Ar matrices, from Jacox.<sup>18</sup> The gas conditions are rich in  $\text{CF}_3\text{I}$  and  $\text{CF}_3\text{Br}$  ( $\text{CF}_3\text{X}:\text{Ar} :: 1:400$ ), which allows production of large  $(\text{CF}_3\text{I})_n$  or  $(\text{CF}_3\text{Br})_n$  clusters. The absorption peaks are collected in Table 1 and assigned as follows:

Ar/ $\text{CF}_3\text{I}$ : (a)  $\nu_1$ ; (b)  $2\nu_5$ ; (c),(d)  $(\text{CF}_3\text{I})_2$ ; (e)  $\nu_2+\nu_3$ .

Ar/ $\text{CF}_3\text{Br}$ : (a)  $\nu_1$ ; (b),(c)  $(\text{CF}_3\text{Br})_2$ ; (d)  $2\nu_5$ ; (e)  $\nu_2+\nu_3$ ; (f) unassigned.



$\text{CF}_3\text{I} : \text{Ar}$   
1 : 400

$\text{CF}_3\text{Br} : \text{Ar}$   
1 : 400

Table 2a  
*CF<sub>3</sub>I* Absorption Frequencies<sup>†</sup>

Mode	Dissoc. <sup>a</sup>	gas-phase <sup>b</sup>	CF <sub>3</sub> I/Ar <sup>c</sup>
$\nu_5$	—	543.1	542.
$\nu_2$	—	743.1	742.5
$\nu_2+\nu_3$	1027.3	1028.0	1027.5
$\nu_1$	1074.6	1075.0	1065.0
$2\nu_5$	1080.5	1080.8	1069.2
dimer ( $\nu_1$ )	1076, 1081 <sup>d</sup> 1069, ? <sup>e</sup>	—	1074.
trimer ( $\nu_1$ )	—	—	1083.5
$\nu_4$	—	1187.2	1077.

<sup>†</sup> All values in cm<sup>-1</sup>.

<sup>a</sup> Vibrational predissociation spectrum (this work).

<sup>b</sup> from Fuss [20].

<sup>c</sup> M.E. Jacox, unpublished results [18].

<sup>d</sup> “Free” CF<sub>3</sub>I moiety.

<sup>e</sup> “Bound” CF<sub>3</sub>I moiety; second feature undetermined due to lack of CO<sub>2</sub> laser lines in this region.

Table 2b  
 $CF_3Br$  Absorption Frequencies<sup>†</sup>

Mode	Dissoc. <sup>a</sup>	Gas-phase <sup>b</sup>	$CF_3Br/Ar^c$	$CF_3Br/Ne^b$
$\nu_5$	—	547.8	545.8	546.4
$\nu_2$	—	761.9	761.8	759.9
$\nu_1$	1085.2	1084.6	1076.	1081.4
$2\nu_5$	>1092.5 <sup>d</sup>	1095.6	1092.5	1094.1
n-mer ( $\nu_1$ )	1078.6	—	1095.	—
n-mer ( $\nu_1$ )	1086.2	—	1099.	—
$\nu_2 + \nu_3$		1112.	1116.8	1119.1
$\nu_4$	—	1208.8	1200.	1203.5

<sup>†</sup> All values in  $cm^{-1}$ .

<sup>a</sup> Vibrational predissociation spectrum (this work).

<sup>b</sup> from Bürger *et al.* [19].

<sup>c</sup> M.E. Jacox, unpublished results [18].

<sup>d</sup> from J. Geraedts *et al.* [15].

in Chapter 5). Results of the derivation yield the expression:

$$F_p(\omega, t) = \frac{I}{I_0} = \exp \left[ -\omega_R^2 \gamma_D^{-1} t \cdot \frac{\gamma_D^2}{4(\omega - \omega_0)^2 + \gamma_D^2} \right], \quad (1)$$

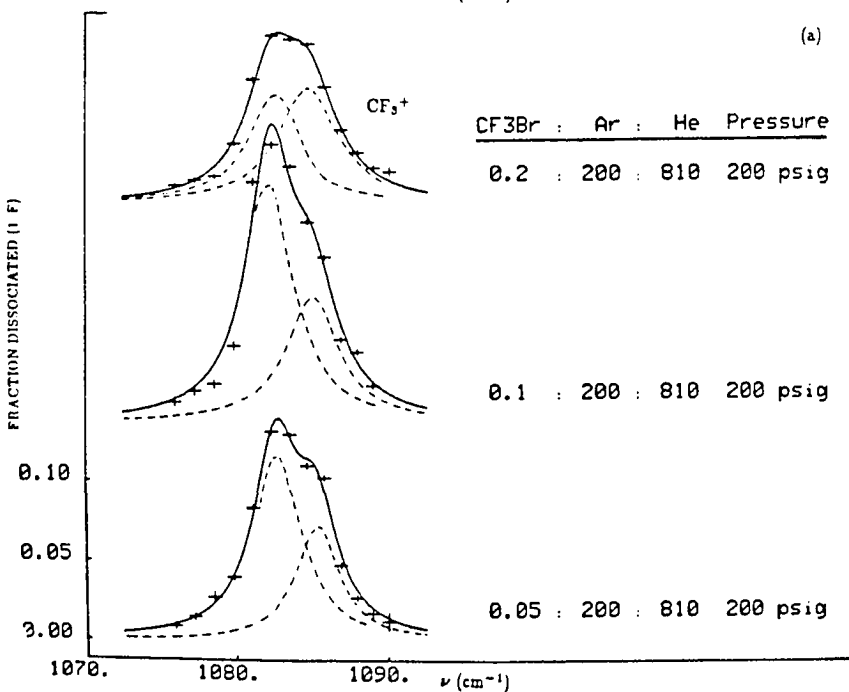
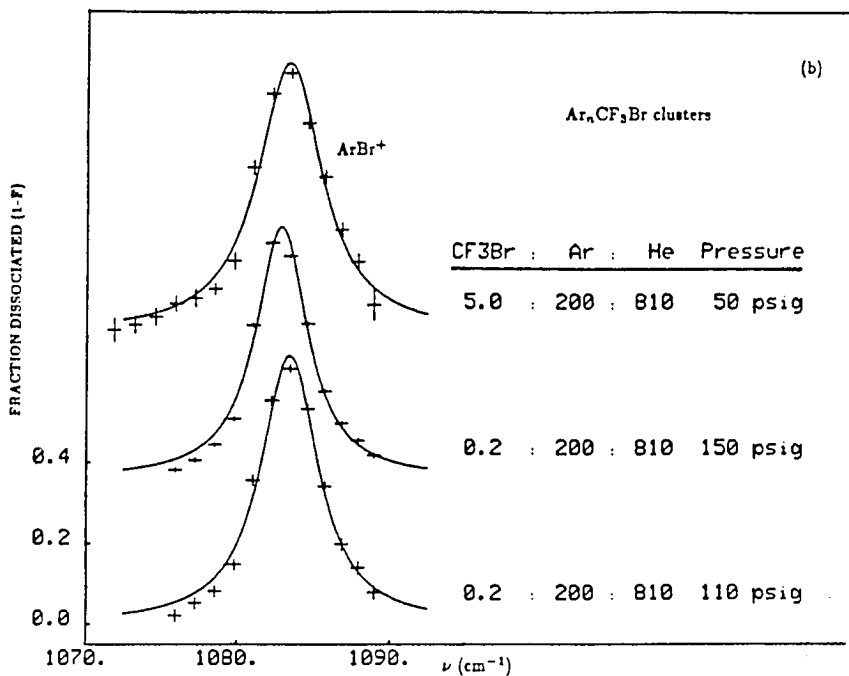
where  $F_p$  is the fraction of van der Waals species remaining after irradiation of duration  $t$ ,  $\omega_R$  is the Rabi frequency of the transition and  $\omega_0$  is the frequency of maximum dissociation intensity. The first-order (dissociation) rate constant,  $\gamma_D$ , derived from the linewidth is

$$\gamma_D = \tau^{-1} = 2\pi c \cdot FWHM, \quad (2)$$

where  $FWHM$  is the full width at half maximum of the Lorentzian factor in (1), or the width of the logarithm of the profile. In the case of a homogeneous spectrum of a specific cluster,  $\gamma_D$  represents the rate of decay out of the initially prepared state. This is often thought to be the rate of dissociation of the complex, but other mechanisms could be responsible for the observed linewidth. All clusters which contain the same single chromophore (e.g.,  $CF_3I$  or  $CF_3Br$ ) should exhibit the same integrated intensity:  $\langle \mu \rangle^2$ , which is proportional to the Rabi frequency ( $\omega_R$ ) which appears in the Lorentzian prefactor  $\omega_R^2 t \gamma_D^{-1}$ .

The simplest of the observed cluster wavelength profiles are those exhibited by the Ar/ $CF_3Br$  system, shown in Figure 2. The absolute percentage of the clusters dissociated by the  $CO_2$  laser is plotted as a function of laser wavelength. The lower set of spectra (Figure 2(a)) are obtained by monitoring  $m/e$  69 ( $CF_3^+$ ), while the upper set (Figure 2(b)) is accumulated by detection at  $m/e$  119 ( $ArBr^+$ ). Note the different intensity scales which are indicative, not of the cluster dissociation

**Figure 2.** Dissociation spectra of  $\text{Ar}_n\text{CF}_3\text{Br}$  clusters. The data points are fractional attenuation in the intensity of the monitored mass due to irradiation with a  $\text{CO}_2$  laser. (a) Detection of dissociation at  $\text{CF}_3^+$  ( $m/e$  69), which shows two absorption features due to  $\text{Ar}_n\text{CF}_3\text{Br}$  clusters with different values of  $n$ , under various expansion conditions. (b) Detection at the cluster mass  $\text{ArBr}^+$  ( $m/e$  119), which exhibits only a single resolvable feature. The solid and dashed curves are generated using Eq. 1. The mixtures were expanded through a  $25 \mu\text{m}$  room temperature pinhole at the backing pressure conditions indicated. The high frequency component of the  $\text{CF}_3^+$  profile is the best approximation to the spectrum of the  $\text{Ar}\cdot\text{CF}_3\text{Br}$  van der Waals molecule.

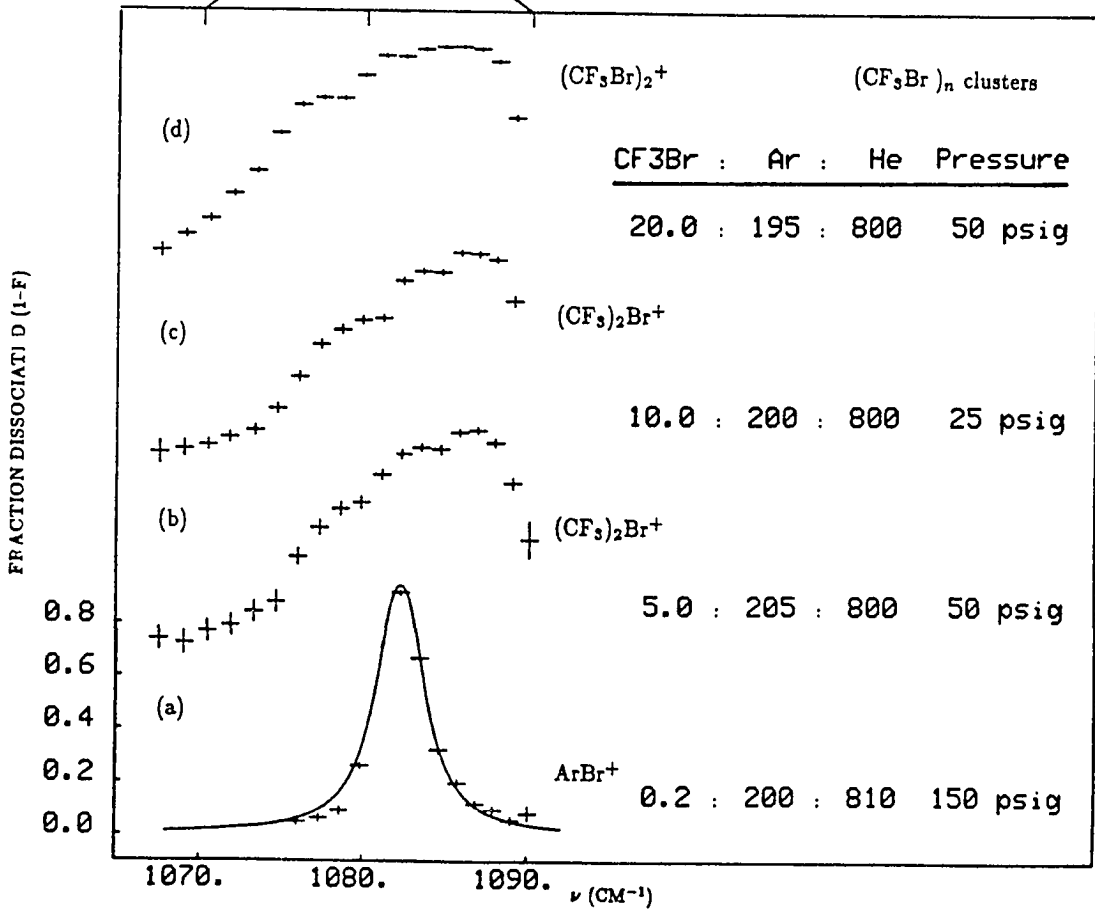
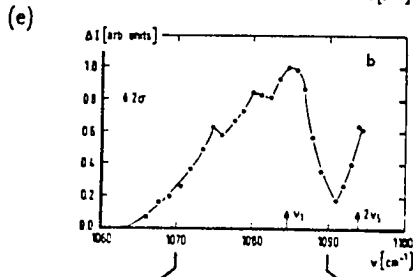
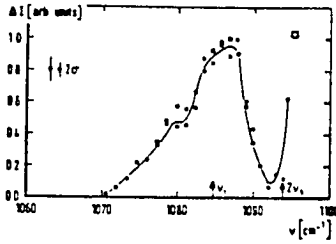


efficiency, but of the fact that both dissociating ( $\text{CF}_3\text{Br}$ -containing clusters) and non-dissociating ( $\text{CF}_3\text{Br}$ ) parent molecules fragment to give mass intensity at  $\text{CF}_3^+$ , while only van der Waals clusters ( $\text{Ar}_n(\text{CF}_3\text{Br})_m$ ) contribute to the  $m/e$  119 ion intensity. This type of behavior is also seen in the  $\text{CH}_3\text{F}$  cluster system, in which the profiles obtained at monomer fragment masses (e.g.,  $\text{CH}_3\text{F}^+$ ) displayed spectra which were indicative of smaller clusters than those obtained at nominal cluster ion masses under similar expansion conditions.

Spectra taken at the  $\text{CF}_3^+$  mass are composed of (at least) 2 components, one nearly coincident with the gas-phase absorption frequency ( $1085.2$ ,  $\Delta(\omega_0 - \omega_{gas}) = +0.2\text{cm}^{-1}$ ), and a red-shifted absorption ( $\sim 1082.5$   $\text{cm}^{-1}$ ,  $\Delta(\omega_0 - \omega_{gas}) = -2.5$   $\text{cm}^{-1}$ ), at approximately the same frequency as the profiles determined using the  $\text{ArBr}^+$  mass ( $1082.5$ - $1083.5$   $\text{cm}^{-1}$ ,  $\Delta(\omega_0 - \omega_{gas}) = -(2.5$ - $1.5)$   $\text{cm}^{-1}$ ). Similarly, it was found in the  $\text{Ar}_n\text{C}_2\text{H}_4$  system that the van der Waals complex  $\text{Ar}_1\text{C}_2\text{H}_4$  exhibited a slight *blue* shift,<sup>2b</sup> while large  $\text{Ar}_n\text{C}_2\text{H}_4$  clusters were *red-shifted* towards the matrix value.<sup>14</sup> The fact that the  $\text{CF}_3^+$  profiles show two distinct features indicates the frequency shift per additional Ar atom is on the order of  $2.5$   $\text{cm}^{-1}$ . We thus attribute the high frequency component as due to  $\text{Ar}_x\text{CF}_3\text{Br}$  ( $x \leq 2$ ) clusters, containing one less Ar atom than the clusters represented by the low frequency feature or the  $\text{ArBr}^+$  profiles. Accurate determination of  $x$ , the number of Ar atoms complexed with the  $\text{CF}_3\text{Br}$  chromophore, is not possible without further work using  $\text{CF}_3\text{Br}/\text{Ar}$  mixtures of higher dilution.

Figure 3 shows the dissociation spectra of clusters containing  $(\text{CF}_3\text{Br})_2$ , along with an inset of the spectra of Geraedts *et al.*<sup>15</sup> While the overall width of the

**Figure 3.**  $(\text{CF}_3\text{Br})_n$  dissociation profiles. (b), (c) The spectra obtained at  $(\text{CF}_3)_2\text{Br}^+$  (m/e 217) and (d)  $(\text{CF}_3\text{Br})_2^+$  (m/e 256) under the displayed conditions arise from clusters of the form  $(\text{CF}_3\text{Br})_n$ . (a) For comparison purposes, the  $\text{Ar}_n\text{CF}_3\text{Br}$  profile obtained at  $\text{ArBr}^+$  (Figure 3b), and (e) the published  $(\text{CF}_3\text{Br})_2$  spectra of Geraedts *et al.*<sup>15</sup> are included.



dissociation profile is much broader ( $> 10 \text{ cm}^{-1}$ ) than the  $\text{Ar}_n\text{CF}_3\text{Br}$  spectra of Figure 2, the structure of the profile indicates that inhomogeneous contributions account for much of the width: three maxima at  $\sim 1080$ ,  $1083$  and  $1086 \text{ cm}^{-1}$  are present throughout the various conditions represented in Figure 3(b)-(d). By comparison with the  $\text{Ar}_n\text{CF}_3\text{Br}$  profile (Figure 3(a)), and the  $(\text{CF}_3\text{Br})_2$  spectra of Gereadts *et al.*<sup>15</sup> (obtained with mixtures that do not contain He), we assign the  $1083 \text{ cm}^{-1}$  feature as due to  $(\text{CF}_3\text{Br})_n$  species which are additionally perturbed by an Ar atom, i.e.,  $\text{Ar}(\text{CF}_3\text{Br})_n$ . The two remaining features, assumed to arise from the dimer ( $n = 2$ ), appear due to  $\nu_1$  vibrations from inequivalent  $\text{CF}_3\text{Br}$  molecules, a “free” and “bound” type, analogous to the distinct hydrogen stretches observed in  $(\text{HF})_2$ .<sup>22</sup> This interpretation is more consistent with the observed  $\text{CF}_3\text{I}$ -containing cluster dissociation spectra and matrix-isolation absorption spectra (see below), rather than the dipole-induced splitting of equivalent  $\nu_1$  vibrations.<sup>15,23</sup> Also in the lower spectrum of the Figure 3 inset, the intensity of the blue peak is nearly twice that of the peak to the red, while the two features are of comparable intensity in Figures 3(b)-(d) indicating saturation effects may be present at these fluence levels ( $\sim 10 \text{ mJ}\cdot\text{cm}^{-2}$ ). The intense peaks evident to the blue of the inset spectrum have been assigned as the  $2\nu_5$  mode, but may be due to larger  $(\text{CF}_3\text{Br})_n$  clusters by comparison to the matrix-isolation spectrum which exhibits a number of features in this region.

Dissociation profiles of  $\text{CF}_3\text{I}$  clusters contain more structure than those of  $\text{CF}_3\text{Br}$ -containing clusters due to the presence of the strong  $2\nu_5$  absorption in close proximity to the  $\nu_1$  feature. Dissociation spectra of  $\text{Ar}_n\text{CF}_3\text{I}$  and  $\text{Kr}_n\text{CF}_3\text{I}$  clusters

are presented in Figure 4. Two resolved features in  $\text{Ar}_x\text{CF}_3\text{I}$  cluster spectra are apparent and assigned to the  $\nu_1$  ( $1074.6\text{ cm}^{-1}$ ) and  $2\nu_5$  ( $1080.5\text{ cm}^{-1}$ ) vibrations. An additional feature is observed to the red of the  $\nu_1$  absorption, at  $\sim 1070.5\text{ cm}^{-1}$ , which is attributed to larger  $\text{Ar}_n\text{CF}_3\text{I}$  clusters, since it increases in percent dissociation intensity with a higher order pressure dependence than the  $\nu_1$  and  $2\nu_5$  peaks. Also, dissociation intensity to the red of the  $2\nu_5$  peak (i.e., in the valley between the  $\nu_1$  and  $2\nu_5$  features) likewise increases under conditions of higher clustering, consistent with assignment as a companion peak to the  $2\nu_5$  feature. It seems incongruous with both the strong static and dynamic dipoles of  $\text{CF}_3\text{I}$  that small frequency shifts ( $\Delta\omega < 1\text{ cm}^{-1}$ ) from the gas-phase value should be observed. An explanation is that, analogous to spectra of  $\text{CF}_3\text{Br}$ -containing clusters, the spectrum of  $\text{Ar}_x\text{CF}_3\text{I}$  is *blue-shifted* with respect to the gas-phase absorption while larger  $\text{Ar}_n\text{CF}_3\text{I}$  clusters exhibit a spectral red-shift, toward the value observed in matrices.<sup>18</sup> Some of the  $\text{Ar}_n\text{CF}_3\text{Br}$  spectra were in fact obtained at higher dilution than the  $\text{CF}_3\text{I}$  mixtures, and are thus more indicative of the  $\text{Ar}\cdot\text{CF}_3\text{X}$  van der Waals complex. This explains why the blue shift was observed in the  $\text{CF}_3\text{Br}$  cluster spectra and not in the  $\text{CF}_3\text{I}$  system.

The dissociation spectra of  $(\text{CF}_3\text{I})_n$  clusters are collected in Figure 5. In addition to features in the  $1070\text{-}1080\text{ cm}^{-1}$  region similar to those observed for  $\text{Ar}_n\text{CF}_3\text{I}$  clusters (Figure 4 and Figure 5a), an intense dissociation feature is observed, to the red of the  $\nu_1$  and  $2\nu_5$  peaks which extends through the missing Q-branch region of the  $\text{CO}_2$  laser emission spectrum. In the dimer, it appears that the C–F stretches can be distinguished, one being very similar to that in small

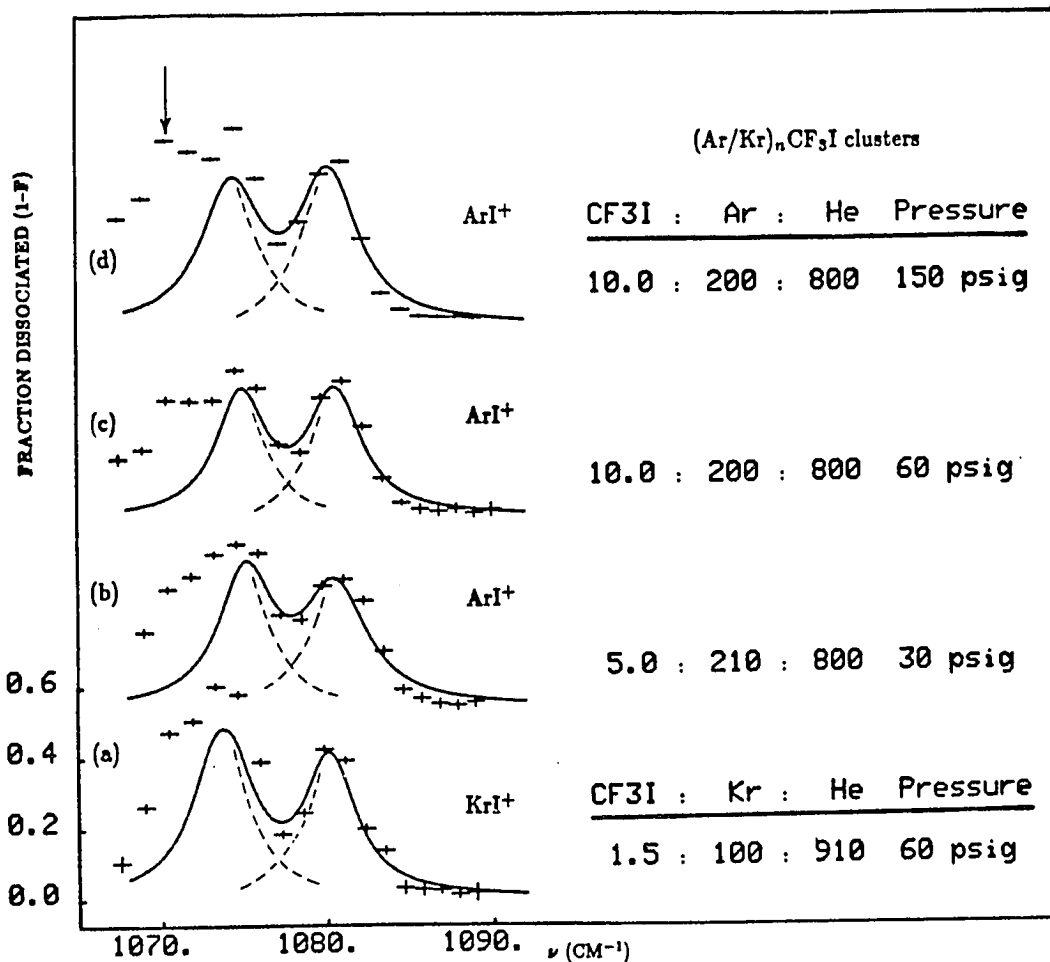


Figure 4. The dissociation spectra of  $Ar_n CF_3 I$  and  $Kr_n CF_3 I$  clusters. (b)-(d) Two features in the  $Ar_n CF_3 I$  cluster spectra, assigned to the  $\nu_1$  ( $1074.6 \text{ cm}^{-1}$ ) and  $2\nu_5$  ( $1080.5 \text{ cm}^{-1}$ ) vibrations of the  $CF_3 I$  monomer, are resolved. The additional feature to the red of the  $\nu_1$  band ( $\downarrow$ ) is attributed to larger  $Ar_n CF_3 I$  clusters. (a) The profile of  $Kr_n CF_3 I$  clusters is red-shifted  $0.5\text{-}1.0 \text{ cm}^{-1}$  from the  $Ar_n CF_3 I$  cluster profile.

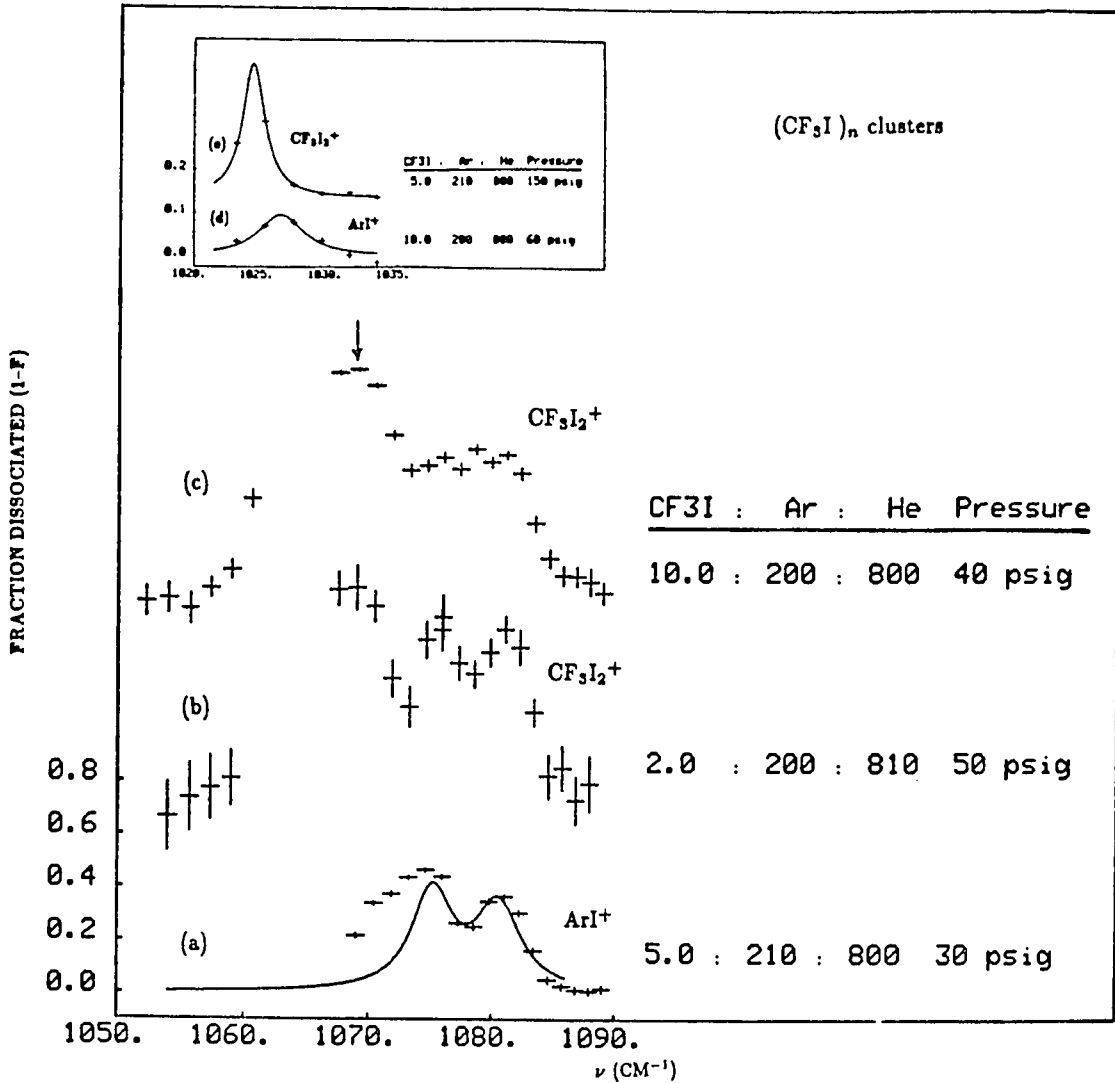


Figure 5. Dissociation profiles for clusters containing  $(CF_3I)_2$ . (b),(c) Spectral features of the  $(CF_3I)_n$  cluster spectra in the  $1070-1080\text{ cm}^{-1}$  region are similar to those obtained for (a)  $Ar_nCF_3I$  clusters (see also Figure 4), but an additional intense dissociation feature ( $\downarrow$ ) is observed to the red ( $\sim 1065\text{ cm}^{-1}$ ). Assignment based on a dimer containing inequivalent units ("free" and "bonded"  $CF_3I$  molecules) is proposed. The inset shows the  $\nu_2 + \nu_3$  region ( $\sim 1030\text{ cm}^{-1}$ ) for both (d)  $Ar_nCF_3I$  and (e)  $Ar_n(CF_3I)_m$ ,  $m \geq 2$  clusters.

$\text{Ar}_n\text{CF}_3\text{I}$  clusters (from a “free”  $\text{CF}_3$  group), and the second (due to the “bonded”  $\text{CF}_3$  group) significantly perturbed, at least  $6\text{ cm}^{-1}$  to the red of the  $\nu_1$  absorption. Unfortunately, the lack of laser lines in the  $1065\text{ cm}^{-1}$  region prevents determination of whether two peaks ( $\nu_1$  and  $2\nu_5$ ) exist in the dissociation spectrum which could tie down the assignment to the “bonded” dimer. The matrix-isolation spectrum (Figure 1a) shows 3 features to the red of the  $\nu_1$  absorption, but assignment of these peaks requires additional spectra at various  $\text{CF}_3\text{I}:\text{Ar}$  concentration ratios to determine monomer and dimer features from those of larger polymers. The inset of Figure 5 displays the  $\nu_2+\nu_3$  region for  $\text{CF}_3\text{I}$  complexes, with dissociation arising from (d)  $\text{Ar}_n\text{CF}_3\text{I}$  and (e)  $\text{Ar}_n(\text{CF}_3\text{I})_m$  clusters. Finally, note that the relative intensities of the  $\nu_1$  and  $2\nu_5$  peaks is similar to that observed in the gas and matrix spectra. No change of the peak intensities caused by perturbation of the Fermi resonance is observed, while a perturbation effect has been proposed by Geraedts *et al.*<sup>15</sup> to explain the apparently intense  $2\nu_5$  feature in the  $(\text{CF}_3\text{Br})_2$  spectrum.

Both static and dynamical information can theoretically be derived from the observed wavelength and laser power dependences of the dissociation intensity. As discussed previously,<sup>2,14</sup> the dissociation lineshapes are sensitive to the bonding environment (as measured by the frequency shift of the profile), the lifetime of the excited chromophore (linewidth), as well as the absorption intensity and dissociation efficiency (integrated intensity). The dissociation profiles observed under conditions employed in this study are probably convolutions of individual cluster spectra, but the trends exhibited by the profiles can be deduced. The information extracted

from each lineshape parameter is discussed in turn.

The frequency shifts exhibited by the complexes are particularly informative, especially when viewed in conjunction with the observed matrix-isolation spectra and gas-phase values. Spectra of  $C_2H_4$ -containing van der Waals dimers excited in the  $\nu_7$  (out-of-plane bend) region are blue-shifted, consistent with repulsive interaction between the  $C_2H_4$  partner and the vibrating H atoms,<sup>2</sup> while the red-shifted  $\nu_3$  (C–F stretch) absorptions of  $CH_3F$  complexes are consistent with a structure which locates the rare gas partner above the molecular figure axis.<sup>14</sup> The present work indicates the  $Ar_xCF_3X$  absorptions are first blue-shifted and then shift to lower frequency toward the matrix absorption value as  $x$  increases. The blue-shift indicates the rare gas atom interacts repulsively with the stretching C–F motion, suggesting the structure of the van der Waals complex may have the rare gas atom located close to a fluorine atom, perhaps along the figure axis. Additional complexation with rare gas atoms introduces a red-shift as the atoms condense around the  $CF_3I$  or  $CF_3Br$  molecule and stabilize the excited vibrational level by dipole-induced dipole interactions.

The frequency shift of the  $CF_3X$  dimer spectra, particularly that of  $(CF_3I)_2$ , are consistent with a tandem chain geometry, rather than an anti-parallel staggered geometry. A dimer with the former structure would possess both a  $CF_3$  group which is only slightly perturbed by the bonding interaction and absorbs near the gas-phase absorption frequency of free  $CF_3I$ , and another  $CF_3$  moiety which interacts strongly (but not repulsively) with the F atom of the first  $CF_3I$  monomer. A structure with the molecules aligned head-to-tail and with the two figure axes parallel is

conjectured. The  $(\text{CF}_3\text{Br})_2$  case would conceivably be similar, but is not well-resolved due to the broader bands observed in the  $\text{CF}_3\text{Br}$  clusters. An interesting feature of both systems is that the gas-phase  $(\text{CF}_3\text{I})_n$  and  $(\text{CF}_3\text{Br})_n$  cluster spectra are red-shifted while the matrix polymeric peaks are blue-shifted. This indicates significant repulsive interaction between the excited vibration and the matrix cage is present.

Dynamical information about the timescale for decay out of the prepared vibrationally excited van der Waals complex can be extracted from the homogeneous width of the dissociation profiles.<sup>2</sup> Inhomogeneous contributions to the width under beam conditions are mainly due to rotational congestion, spectral congestion (overlapping lines from individual cluster types, or different modes within a specific cluster), or dephasing of the vibration.  $\text{CF}_3\text{I}$  and  $\text{CF}_3\text{Br}$  cluster spectra, certainly exhibit both types of spectral congestion. However, rotational congestion (simulated using various reasonable dimer structures<sup>24</sup> and known constants of the monomers<sup>25,26</sup>) is expected to account for  $\leq 1 \text{ cm}^{-1}$  of the profile widths for the dimers, with slightly higher widths for the  $\text{Ar}\cdot\text{CF}_3\text{X}$  complexes with high (10 K) rotational temperatures. The similarity between the widths of the various complexes suggests a substantial degree of homogeneous broadening is likely present in the profiles, in which case the vibrational lifetime approaches the limit determined by the width of the profile. Without less congested spectra or a continuous profile (the discrete  $\text{CO}_2$  laser transitions are spaced every  $1 \text{ cm}^{-1}$ , so very narrow linewidths due to longer-lived vibrational states are not resolvable) we can at present only place bounds on the excited state vibrational lifetime. As an upper bound to the

dissociation lifetime, the complexes must decompose in less than  $\sim 0.5$  msec, the irradiation flight time of clusters from nozzle to detector. Assuming the entire width is homogeneously broadened yields a lower bound for the lifetime of the excited vibration: for the  $\text{CF}_3\text{I}$  and  $\text{CF}_3\text{Br}$  clusters, the observed widths on the order of  $2\text{-}5\text{ cm}^{-1}$  which indicates that the vibrational lifetime,  $\tau$ , must be longer than 1-3 psec.

The dissociation intensity of a specific van der Waals cluster should correlate, at low laser fluence, to the integrated absorption coefficient for the excited vibration of the monomer (neglecting contribution from polarization of the partner of the chromophore). While this was borne out in other studies,<sup>2,14</sup> it is not the case with the clusters studied here: the dissociation intensity is a factor of 2-4 times *smaller* than expected from consideration of the integrated absorption intensity of the  $\nu_1$  vibration of the  $\text{CF}_3\text{I}$  and  $\text{CF}_3\text{Br}$  monomers. Causes that may be responsible for this are: (1) a substantial fraction of the absorption intensity is not accounted for due to narrow absorption features which are not detected with the present grid of laser lines; (2) saturation effects or sample inhomogeneity reduce the fraction of molecules which may be dissociated at a given laser frequency,<sup>2d</sup> resulting in a lower apparent dissociation intensity.

#### 4. Conclusions

The dissociation spectra of van der Waals clusters containing  $\text{CF}_3\text{I}$  and  $\text{CF}_3\text{Br}$  are complex in nature due to inhomogeneous contributions to the lineshapes.  $\text{CF}_3\text{I}$ -containing clusters exhibit a strong Fermi resonance between  $\nu_1$  and  $2\nu_5$ , as observed in both the gas phase and matrix isolation absorption spectra of

the monomer.  $(\text{CF}_3\text{I})_n$  clusters exhibit a structured spectrum which has been interpreted in terms of distinct (“free” and “bound”)  $\nu_1$  vibrational modes in the dimer. The observed frequency shifts of the cluster vibrations indicate strong repulsive interaction between a rare gas atom and the  $\nu_1$  ( $\text{CF}_3\text{I}$  and  $\text{CF}_3\text{Br}$ ) and  $2\nu_5$  ( $\text{CF}_3\text{I}$ ) vibrations, and a stabilizing effect in the case of dimers of  $\text{CF}_3\text{I}$  or  $\text{CF}_3\text{Br}$ .

#### **Acknowledgements**

This work was supported by the Division of Chemical Sciences, Office of Basic Energy Science, U.S. Department of Energy. We thank Prof. J.L. Beauchamp for the loan of the  $\text{CO}_2$  laser.

## References

1. K.C. Janda, *Adv. Chem. Phys.* **66** (1985) 201.
2. (a) M.P. Casassa, D.S. Bomse and K.C. Janda, *J. Chem. Phys.* **74** (1981) 5044;  
(b) M.P. Casassa, C.M. Western, F.G. Celii, D.E. Brinza and K.C. Janda, *J. Chem. Phys.* **79** (1983) 3227;  
(c) C.M. Western, M.P. Casassa and K.C. Janda, *J. Chem. Phys.* **80** (1984) 4781;  
(d) M.P. Casassa, C.M. Western and K.C. Janda, *J. Chem. Phys.* **81** (1984) 4950.
3. G. Fischer, R.E. Miller, and R.O. Watts, *Chem. Phys.* **80** (1983) 147.
4. W.-L. Liu, K. Kolenbrander and J.M. Lisy, *Chem. Phys. Lett.* **112** (1984) 585.
5. G.T. Fraser, D.D. Nelson, Jr., A. Charo and W. Klemperer, *J. Chem. Phys.* **82** (1985) 2535.
6. M. Quack and G. Seyfang, *J. Chem. Phys.* **76** (1982) 955.
7. M.J. Rossi, J.R. Barker and D.M. Golden, *Chem. Phys. Lett.* **65** (1979) 523.  
M.J. Rossi, J.R. Barker and D.M. Golden, *J. Chem. Phys.* **76** (1982) 406.
8. D. Borsella, R. Fantoni, A. Ferretti, A. Giardini-Guidoni, M. Dilonardo and J. Reuss, *Chem. Phys.* **94** (1985) 309.  
E. Borsella, R. Fantoni, A. Giardini-Guidoni, D. Masci, A. Palucci and J. Reuss, *Chem. Phys. Lett.* **93** (1982) 523.
9. M. Drouin, M. Gauthier, R. Pilon, P.A. Hackett and C. Willis, *Chem. Phys. Lett.* **60** (1978) 16.  
M. Gauthier, P.A. Hackett and C. Willis, *Chem. Phys.* **45** (1980) 39.
10. M. Nève de Mévergnies and P. del Marmol, *J. Chem. Phys.* **73** (1980) 3011.

11. Aa.S. Sudbø, P.A. Schulz, E.R. Grant, Y.R. Shen and Y.T. Lee, *J. Chem. Phys.* **70** (1979) 912.
12. (a) L.R. Thorne and J.L. Beauchamp, *J. Chem. Phys.* **74** (1981) 5100.  
(b) M.F. Jarrold, A.J. Illies, N.J. Kirchner, W. Wagner-Redeker, M.J. Bowers, M.L. Mandich, and J.L. Beauchamp, *J. Phys. Chem.* **87** (1983) 2213.
13. M.J. Coggiola, P.C. Cosby and J.R. Peterson, *J. Chem. Phys.* **72** (1980) 6507.
14. F.G. Celi and K.C. Janda, to be published.
15. J. Geraedts, M.N.N. Snels, S. Stolte and J. Reuss, *Chem. Phys. Lett.* **106** (1984) 377.
16. W.B. Person, S.K. Rudys and J.H. Newton, *J. Phys. Chem.* **79** (1975) 2525.  
W.B. Person and S.R. Polo, *Spectrochim. Acta* **17** (1961) 101.
17. G. Herzberg, in *Molecular Spectra and Molecular Structure, vol. 2*, (van Nostrand Reinhold, New York, 1945), pp. 312-314 (for CH<sub>3</sub>Cl).
18. M.E. Jacox, private communication.
19. H. Bürger, K. Burczyk, D. Bielefeldt, H. Willner, A. Ruoff and K. Molt, *Spectrochim. Acta* **35A** (1979) 875.
20. W. Fuss, *Spectrochim. Acta* **38A** (1982) 829.
21. M.P. Casassa, F.G. Celi and K.C. Janda, *J. Chem. Phys.* **76** (1982) 5295.
22. A.S. Pine and W.J. Lafferty, *J. Chem. Phys.* **78** (1983) 2154.
23. J. Geraedts, S. Stolte and J. Reuss, *Z. Phys. A* **304** (1982) 167;  
J. Geraedts, M. Waayer, S. Stolte and J. Reuss, *Faraday Disc. Chem. Soc.* **73** (1982) 375;

- J. Geraedts, S. Setiadi, S. Stolte and J. Reuss, *Chem. Phys. Lett.* **78** (1981) 277.
24. R.L. DeLeon and J.S. Muentner, *J. Chem. Phys.* **75** (1981) 1113.
25. J. Sheridan and W. Gordy, *J. Chem. Phys.* **20** (1952) 591.
26. K. Burczyk, H. Bürger, A. Ruoff and P. Pinson, *J. Mol. Spectrosc.* **77** (1979) 109.



*CHAPTER 3*

**INFRARED PHOTODISSOCIATION SPECTRA**

**OF**

**LARGE VAN DER WAALS CLUSTERS**

**INFRARED PHOTODISSOCIATION SPECTRA OF LARGE VAN DER WAALS  
CLUSTERS: THE MATRIX ISOLATION SPECTROSCOPY OF GAS-PHASE  
MOLECULES\***

Francis G. Celi,† and Kenneth C. Janda‡

*Arthur Amos Noyes Laboratory of Chemical Physics,  
California Institute of Technology, Pasadena, California 91125, USA*

**ABSTRACT**

We report the infrared photodissociation spectra of clusters of Ar, Kr, N<sub>2</sub> and CH<sub>4</sub> containing a single CH<sub>3</sub>F or C<sub>2</sub>H<sub>4</sub> chromophore. The clusters are vibrationally excited by a line-tunable CO<sub>2</sub> laser in the  $\nu_3$  (CH<sub>3</sub>F) or  $\nu_7$  (C<sub>2</sub>H<sub>4</sub>) region and dissociate as the energy delocalizes within the cluster. The dissociation is detected as intensity loss of mass peaks monitored by an off-axis electron-impact ionization quadrupole mass spectrometer. From the infrared dissociation spectra, there are three regimes of cluster size distinguished for CH<sub>3</sub>F-containing clusters. The center absorption frequencies of small A<sub>n</sub>CH<sub>3</sub>F clusters (A = Ar, Kr, N<sub>2</sub>, n < 12) shift to lower frequency and toward the matrix value with increasing cluster size and the widths are fairly constant. The dissociation profiles exhibit a high degree of inhomogeneity in the moderate cluster regime corresponding to clusters with a partially filled second solvation shell. The linewidths of the transitions narrow in this cluster regime, quite dramatically for the Ar/CH<sub>3</sub>F system. Dissociation is attenuated in all large clusters A<sub>n</sub>CH<sub>3</sub>F and A<sub>n</sub>C<sub>2</sub>H<sub>4</sub>, n > 50. The A<sub>n</sub>C<sub>2</sub>H<sub>4</sub> clusters

---

\* Contribution No. 7235

† Atlantic Richfield Foundation Fellow

‡ Camille and Henry Dreyfus Foundation Fellow

(A = Ar, N<sub>2</sub>, CH<sub>4</sub>) shift only a slight degree and show no signs of inhomogeneity in these profiles.

Two chromophore sites, the “matrix” and “surface” sites, are observed in the cluster dissociation spectra. The shift of the center absorption frequency for A<sub>n</sub>CH<sub>3</sub>F clusters is further red-shifted from the gas phase CH<sub>3</sub>F value than that of matrix-isolated CH<sub>3</sub>F, consistent with a reduced lattice spacing of the presumed icosahedral geometry. No spectral inhomogeneity indicative of a matrix cluster absorption site is observed for various C<sub>2</sub>H<sub>4</sub>-containing clusters despite the reduced spacing between laser lines in this wavelength region as compared to the CH<sub>3</sub>F ν<sub>3</sub>-absorption region. We interpret these results in terms of a strong dipole-induced dipole force in the case of CH<sub>3</sub>F-containing clusters which favors formation of solvated (“matrix”) absorption sites. Finally, the dissociation spectra of ion clusters of similar mass can be radically different: e.g., the profile obtained by monitoring Ar<sub>9</sub>CH<sub>3</sub>F<sup>+</sup> exhibits ~50% dissociation on the P(30) laser line, while this feature is totally absent in the Ar<sub>13</sub>CH<sub>3</sub>F<sup>+</sup> spectrum under identical conditions. The large variation in spectral profiles may indicate selective ionization fragmentation even in cluster beams with a broad neutral cluster distribution. Additional experiments which would complement the present data are discussed.

## 1. Introduction

Intramolecular vibrational energy transfer and randomization in isolated molecules is the focus of much chemical physics research today. Two techniques that have been employed in the study of this area are the photodissociation of van der Waals molecules<sup>1–10</sup> and matrix isolation spectroscopy.<sup>11–17</sup> In the first technique, a supersonic expansion both internally cools the molecule of interest, **X** (e.g., **X** = C<sub>2</sub>H<sub>4</sub>,<sup>1,2a,3a,4,5</sup> CO<sub>2</sub>,<sup>2b</sup> SF<sub>6</sub>,<sup>3b</sup> I<sub>2</sub>,<sup>7</sup> or Cl<sub>2</sub><sup>8</sup>), and provides the environment necessary for formation of a weak bond to an inert partner **A** (e.g., **A** = Ar, Ne, N<sub>2</sub> or X). Vibrational energy in either the ground or excited electronic manifold, may cause dissociation of the A-X complex by coupling to the low energy van der Waals bond. To the degree that **A** is a minor perturbation on the electronic properties of **X**, one can consider the X-subunit isolated; in this case, the rate of the dissociation indicates the time scale of energy delocalization into the van der Waals modes. When inhomogeneity, pure dephasing and instrumental broadening are not significant<sup>18</sup> or can be taken into account,<sup>1d</sup> the dissociation rate can be extracted from the width of the profile.

In the second technique, matrix isolation spectroscopy, a cold structure of rare gas atoms is used to trap, isolate and internally cool the species **X**. The interaction between the molecule of interest and the surrounding cage atoms determines the degree to which the energy transfer properties observed for **X** are unperturbed. While vibrational lifetimes of matrix isolated molecules have been observed to be in the range of microseconds or longer,<sup>11–13</sup> lifetimes of vibrationally excited van der Waals molecules inferred from linewidths have in general been much shorter,

ranging from sub-picosecond<sup>1–4</sup> to tens of psecs<sup>19</sup> in dissociation studies to <10 nsec from absorption spectra.<sup>20</sup>

In this paper, we report attempts to bridge the gap between these two techniques and their distinct range of lifetimes by obtaining the infrared dissociation profiles of CH<sub>3</sub>F and C<sub>2</sub>H<sub>4</sub> molecules imbedded in in large van der Waals clusters, or gas-phase “matrices”. The specific information we obtain is derived from the dissociation lineshapes: the fractional attenuation, vibrational linewidth and frequency shift as a function of expansion backing pressure are obtained for the excited  $\nu_3$  vibration in CH<sub>3</sub>F and the  $\nu_7$  vibration of C<sub>2</sub>H<sub>4</sub> in various inert clusters. The appearance of narrow spectral features in some clustering regimes serves to indicate that the lifetime of the excited vibration has increased, but the quantitative lifetime information is limited due to the discrete nature of the probing CO<sub>2</sub> laser. The dissociation intensity gives a measure of the homogeneity of the profiles. the frequency shift of the cluster absorption is a sensitive measure of the environment around the chromophore and is compared to the extensive matrix data which is available. We correlate these results with the cluster size and properties that we expect at the given expansion pressure. By correlating mass-specific spectra with estimates of cluster distributions, we observe that fairly small clusters ( $\leq 1$  complete shell) shift the CH<sub>3</sub>F  $\nu_3$  absorption to near the values observed in matrices. A structural ordering of rare gas atoms around a central CH<sub>3</sub>F molecule is indicated from comparison with spectra of C<sub>2</sub>H<sub>4</sub>-containing clusters.

## 2. Background

Of the many studies of relaxation processes in matrix isolated species,<sup>11</sup> a small

number involve polyatomic molecules vibrationally excited in their ground electronic state, most of which have involved an isotopic form of methyl fluoride.<sup>12-17</sup> Only recently, however, has even this system approached being well understood. The decay of IR fluorescence from  $2\nu_3$  was observed by Apkarian and Weitz<sup>12</sup> and attributed to the ladder-climbing relaxation  $2\cdot\text{CH}_3\text{F}(\nu_3) \rightarrow \text{CH}_3\text{F}(2\nu_3) + \text{CH}_3\text{F}(0)$ , but this relaxation pathway will not occur in the gas-phase clusters which contain a single  $\text{CH}_3\text{F}$  molecule. An IR pump-probe technique was used by Abouaf-Marguin *et al.*<sup>13</sup> to monitor the population loss induced by by rare gas and  $\text{N}_2$  matrices from the  $\nu_3 = 1$  level of  $^{12}\text{CH}_3\text{F}$  and the  $\nu_6 = 1$  level of  $^{12}\text{CD}_3\text{F}$  and  $^{13}\text{CH}_3\text{F}$ . The  $\nu_3$ -excited  $\text{CD}_3\text{F}$  is observed to relax ( $\tau < 1 \mu\text{sec}$ ) much faster than  $\nu_3$ -excited  $\text{CH}_3\text{F}$  ( $\tau \sim 10 \mu\text{sec}$ ) presumably because the  $\nu_6$  level lies below  $\nu_3$  in the deuterated species and provides a fast intramolecular V→V energy transfer pathway, independent of the matrix. Young and Moore<sup>14</sup> obtained IR emission lifetimes for both  $\nu_3$  and  $2\nu_3$  levels of  $\text{CH}_3\text{F}$  which were populated by fast intramolecular relaxation of levels excited at  $3.0 \mu\text{m}$ . The non-radiative rates determined by the two lifetime measurement techniques are in good agreement:  $k(\nu_3) = 3.2 \times 10^5$  and  $3.8 \times 10^4 \text{ s}^{-1}$  in Ar and Kr matrices, respectively.<sup>14</sup> The matrix environment induces non-radiative relaxation at rates over 500 times faster than the isolated molecule radiative rate of  $15 \text{ s}^{-1}$ .

A physical picture for the  $\text{CH}_3\text{F}$  isolated in matrices which provides insight into the relaxation mechanism can be obtained from IR absorption studies,<sup>14-17</sup> but there has been some disagreement in interpretation. Weak blue-shifted satellite peaks of  $\nu_3$  observed in concentrated  $\text{CH}_3\text{F}/\text{Kr}$  matrices<sup>15</sup> were interpreted to

be indicative of  $\text{CH}_3\text{F}$  librations which would substantiate a  $\text{V} \rightarrow \text{R}$  relaxation mechanism for  $\text{CH}_3\text{F}(\nu_3)$  in matrices with  $\text{CH}_3\text{F}$  rotation as the energy accepting mode.<sup>13</sup> It is now believed<sup>16</sup> that these peaks are due to  $\text{CH}_3\text{F}$  aggregates in the concentrated matrices, although the failure to see phonon wings or a librational satellite in the studies using more dilute matrices<sup>16</sup> may be consistent with estimates of their low intensity due to a broadened profile.<sup>17</sup> Apkarian and Weitz<sup>17</sup> have modelled  $\text{CH}_3\text{F}$  in Kr as a free spinner about the figure axis while the tumbling motion perpendicular to the figure axis is hindered. The end-over-end motion would produce rotational lines spaced  $\sim 1.7 \text{ cm}^{-1}$  from the main  $\nu_3$  (Q-branch) absorption, but these are not observed.<sup>14</sup> If relaxation occurred through the free spinner rotation with phonons as the acceptor of the energy mismatch, the rate would exhibit a strong temperature dependence which is not observed. Collisional relaxation between  $\text{CH}_3\text{F}$  and the matrix cage has been suggested as the dominant mechanism of de-excitation. Lastly, vibrational dephasing of the vibration may contribute inhomogeneous width to the linewidths,<sup>16</sup> since the  $\text{CH}_3\text{F} \nu_3$  absorption line is narrower in Ar than in Kr, which is the reverse of the behavior expected from the direct lifetime measurements.<sup>12,13</sup>

At present, there is a great deal of effort to characterize the solvation of gas-phase molecules by sequentially adding weak binding partners (**A**) to a prototypical molecule (**X**), usually one that can be probed by fluorescence<sup>21–24</sup> or MPI.<sup>25</sup> The electronic origins of individual  $\text{X}_n\text{-A}$  species are often well separated, for  $n \leq 6$ , so structural information about individual neutral clusters can be obtained from the incremental shift of the 0-0 transition with additional solvent species. In addition,

the fluorescence lifetimes of the transitions yield the rate of non-radiative decay, and this can be obtained as a function of cluster size for small clusters. Saturation of the frequency shift, however, eliminates the possibility of studying *specific* large clusters. Studies of complexes between large aromatics (e.g., X = anthracene) and rare gases (e.g., A = Ar), which include time and energy resolved fluorescence excitation and emission spectra, have been reported. In the large cluster regime (i.e., for pressures at which individual  $A_nX$  features cannot be distinguished) the fluorescence excitation spectra exhibit additional red-shifting as the pressure, and thus complexation, is increased. The fluorescence lifetime, however, saturates with respect to change in pressure. The lifetime of large  $A_nX$  clusters is only 2-3 times smaller than the bare X molecule (7-9 vs. 24 nsec for uncomplexed anthracene). The lifetime of gas-phase anthracene isolated in large Ar clusters is the same as its lifetime in a methylnmethacrylate glass,<sup>23</sup> but is much longer than its lifetime in an Ar matrix (10 psec<sup>26</sup>).

Vibrational spectroscopy of molecules embedded in clusters<sup>27-29</sup> is hampered by the reduced frequency shift per atom compared to that observed in electronic excitation spectra, which makes even the assignment of infrared spectra of small clusters difficult. Gough *et al.*<sup>29</sup> have obtained the 10  $\mu\text{m}$  dissociation spectrum of  $Ar_nCH_3F$  and  $Ar_nSF_6$  clusters using a bolometer for detection of dissociation, finding correspondence between the reported matrix absorption peaks and limiting frequency shifts in the cluster dissociation profiles. The saturation of the frequency shift at that of the matrix value was found to occur after the filling of the "first shell" of Ar atoms around  $SF_6$ . Also by comparison to the matrix absorption

spectra in which spectral features arising from *normal* and *dislocation/surface* sites are observed, the  $\text{Ar}_n\text{CH}_3\text{F}$  spectra were interpreted as consisting of contributions from clusters in either “matrix” or “surface” sites. The surface peak dominates in the cluster spectra, whereas one would expect the polar  $\text{CH}_3\text{F}$  to be located at the center of an Ar cluster (the “matrix” site) with greater probability than in the case of the  $\text{SF}_6$  clusters. A recently reported technique<sup>29b</sup> has provided identification of an absorption feature attributed to  $\text{SF}_6$  on an Ar cluster surface site in the dissociation spectra of  $\text{Ar}_n\text{SF}_6$  clusters. Application of this technique to  $\text{CH}_3\text{F}$  clusters may similarly provide positive identification of surface site and matrix absorption features.

While the bolometer has proven to be a rather sensitive tool for monitoring dissociation of van der Waals molecules, it is not mass selective. The detected signal (heat loss at the bolometer) results from all species which are dissociated by the laser and scattered out of the molecular beam. One advantage of this technique for a study of highly clustered beams is that contributions from the entire cluster distribution can be detected at once. The spectra reported in this work are likewise sums of spectra of various cluster sizes, due to electron-impact fragmentation, but the summation includes only clusters whose mass is *greater than or equal to* the mass being monitored. This mass filtering, not available in the bolometer study,<sup>29</sup> enables us to uncover interesting features in the cluster dissociation spectra. For instance, under some conditions in the  $\text{Ar}/\text{CH}_3\text{F}$  cluster system, very dissimilar dissociation spectra can be obtained by monitoring ions of similar mass. We can also probe the entire cluster distribution in a way analogous to the bolometer detection

technique<sup>29</sup> by monitoring the attenuation of the  $\text{CH}_3\text{F}^+$  or  $\text{C}_2\text{H}_4^+$  parent ion peaks which convolute contributions from all clusters (although still depending on fragmentation efficiencies). In addition, our apparatus allows determination of the fractional dissociation at a given cluster mass so the absolute dissociation intensity of the clusters is obtained.

### 3. Experimental

The apparatus used in this study has been described previously,<sup>1</sup> and is shown schematically in Figure 1. Van der Waals clusters containing  $\text{CH}_3\text{F}$  are formed by supersonic expansion of pre-mixed gases through Ni pinholes (12-25 $\mu\text{m}$ ) and into a high-pressure ( $10^{-3}$ - $10^{-2}$  Torr) source region. Experiments with  $\text{C}_2\text{H}_4$ -containing clusters were performed using a modified source chamber pumped by a 10'' diffusion pump. The jet is skimmed well after condensation to form clusters is complete and travels 60 cm through two regions of differential pumping, then through the electron-impact ionization region of an off-axis quadrupole mass spectrometer. Irradiation occurs over the entire flight path and thus allows significant fractions of clusters to be dissociated with an unfocused, low power ( $\sim 10$ - $15$  W/cm<sup>2</sup>) line-tunable cw  $\text{CO}_2$  laser. After being modulated with a mechanical chopper, the laser light is directed colinearly along the molecular beam – through a ZnSe entrance window, the ionization region of the mass spectrometer and the collimators that define the position of the molecular beam. Uniform irradiance is ensured as all apertures are smaller than the laser beam waist ( $\sim 6$  mm). Alignment is facilitated by replacing the nozzle assembly with a  $\text{BaF}_2$  window so that the laser power can be transmitted and maximized over the path length through the entire apparatus ( $>1$  m).

**Figure 1.** Schematic diagram of the molecular beam apparatus including the electron-impact ionization quadrupole mass spectrometer, data collection electronics with computer and CO<sub>2</sub> laser used in these experiments.



The data collection system consists of single-ion counting of current pulses from an amplifier/discriminator following a channeltron electron multiplier. The count total is relayed to a minicomputer (ISC 8001) via a homebuilt interface. The computer starts the photon counter on both on and off phases of the chopped laser light, takes the difference of the two count totals and repeats the cycle to generate a datum. Background subtraction is performed automatically on each point. Data averaging times of a few minutes (1000-3000 cycles) usually provide adequate S/N in the dissociation intensity.

An important component of the spectrometer is a calibrated Scientech calorimeter located inside the vacuum chamber. By translating a small mirror, the laser power propagating down the molecular beam axis is *directly* measured before and after each datum. This allows accurate determination of power irradiating the clusters, independent of laser mode quality outside the chamber. In addition, dissociation spectra at constant power can be obtained directly, with a minimum of power scaling for fluctuations between data points.

Gas mixtures consisted of CH<sub>3</sub>F (Matheson, >99.0%) and C<sub>2</sub>H<sub>4</sub> (Scientific Gas Products, >99.95%), used without further purification, seeded either in pure Ar or N<sub>2</sub>, or ternary mixtures with the Ar, Kr, Ne, N<sub>2</sub> or CH<sub>4</sub> diluted in He. CH<sub>3</sub>F and C<sub>2</sub>H<sub>4</sub> were typically  $\leq 0.1\%$  of the mixture, while the rare gas concentration in He was varied from 10-100%. Each prepared mixture was equilibrated for at least 6 hours prior to experiments.

## 4. Results

### 4.1 Mass spectrometry

A portion of the mass spectrum typical of those obtained in this study is reproduced in Figure 2(a). The molecular beam characterized by this mass spectrum was produced by expansion of a 0.5 : 1010 mixture of  $\text{CH}_3\text{F} : \text{Ar}$  at 400 psig backing pressure through a room temperature 25  $\mu\text{m}$  pinhole. The series of  $\text{Ar}_n^+$  ions is dominant with less intense series of  $\text{Ar}_n\text{CH}_3\text{F}^+$ ,  $\text{Ar}_n\text{CH}_2\text{F}^+$ ,  $\text{Ar}_n\text{CH}_3^+$  and  $\text{Ar}_n\text{F}^+$  cluster ions also observed. The assignment of the  $\text{Ar}_n\text{F}^+$  cluster series is based upon the fact that the IR dissociation spectra obtained at  $m/e$  59 ( $\text{ArF}^+$ ) are identical to  $\text{Ar}_n\text{CH}_3\text{F}$  spectra which are obtained from other masses (e.g.,  $\text{Ar}_n\text{CH}_3\text{F}^+$  or  $\text{CH}_3\text{F}^+$ ). Using mixtures of  $\text{CH}_3\text{F}$  seeded in pure Ar and stagnation pressures up to 700 psig,  $\text{CH}_3\text{F}$ -containing Ar clusters as large as  $\text{Ar}_{19}\text{CH}_3\text{F}^+$  ( $m/e$  794) could be detected although larger Ar clusters can be safely assumed to be present (*vide infra*). Dilute mixtures (<.05%  $\text{CH}_3\text{F}$ , <20% Ar in He) and low backing pressures were used to obtain spectra of small clusters, such as  $\text{CH}_3\text{F}$  solvated with 1 or 2 Ar atoms, designated as  $\text{Ar}_x\text{CH}_3\text{F}$ .

Formation of  $(\text{CH}_3\text{F})_n$  or rare gas clusters containing  $(\text{CH}_3\text{F})_n$ ,  $n \geq 2$ , while certainly facile, was not of direct interest in this work, and thus was inhibited by maintaining the  $\text{CH}_3\text{F}$  concentration below 0.1%. This concentration seems high compared to those usually necessary for well-isolated matrix spectra ( $\leq 0.01\%$ ), but is suitable here because of the mass selection capability. Clusters of the form  $(\text{CH}_3\text{F})_n^+$  and  $(\text{CH}_3\text{F})_n\text{H}^+$ ,  $n \geq 2$ , are both observed.  $(\text{CH}_3\text{F})_2$  is expected to undergo an internal ion-molecule reaction after ionization to give predominantly

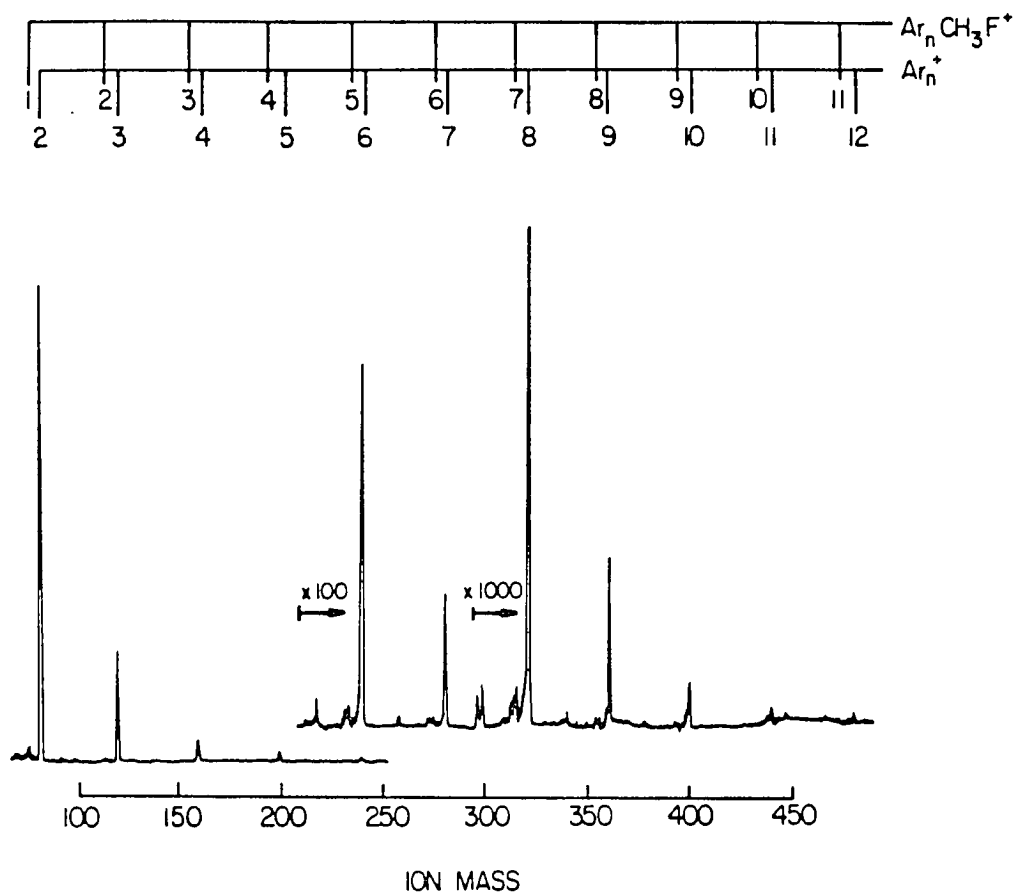


**Figure 2a.** Mass spectrum of a richly-clustered molecular beam. A mixture consisting of 0.5:1014  $CH_3F:Ar$  was expanded at 400 psig through a 25  $\mu m$  room temperature pinhole.  $Ar_n^+$  and  $Ar_n CH_3 F^+$  cluster series are indicated. The observed mass spectral intensities decrease rapidly with increasing cluster size under these conditions, although a neutral cluster distribution peaked at  $Ar_{100}$  is calculated (see the discussion of Figure 11). The ionization electron energy was 65 eV.

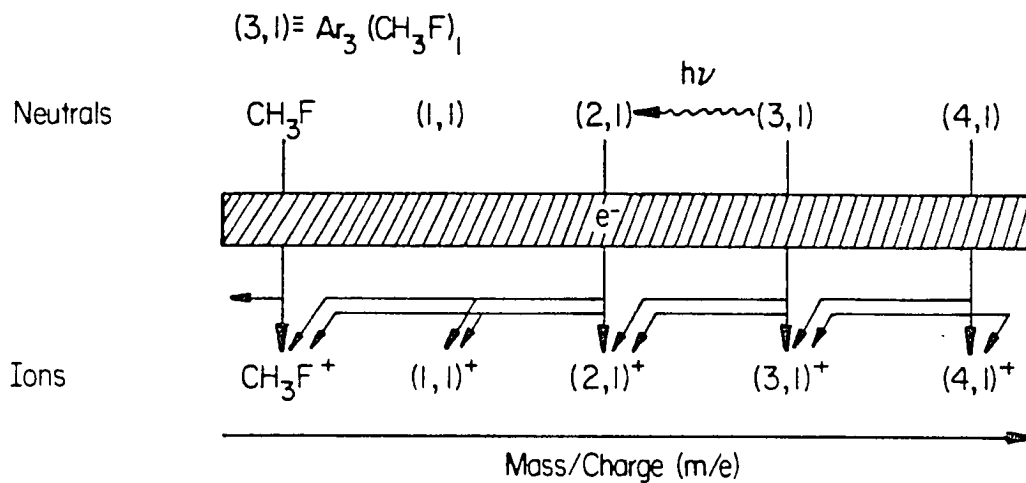


**Figure 2b.** Schematic drawing depicting fragmentation of clusters upon electron-impact ionization, and the partial mass filtering that results. Clusters of size larger than and equal to a specific mass contribute ion intensity to the detected mass peak. Neutral cluster dissociation upon absorption of infrared radiation is monitored by decrease in the intensity of an ion mass, so contribution from higher mass fragments must be taken into account.

$(\text{CH}_3\text{F})\text{H}^+$ .<sup>30</sup> The IR dissociation spectrum attributed to  $(\text{CH}_3\text{F})_2$  was obtained at this mass (see Appendix 1). The observation of  $(\text{CH}_3\text{F})_n\text{H}^+$  clusters suggests the  $(\text{CH}_3\text{F})\text{H}^+$  traps the positive charge on the cluster,<sup>31</sup> leaving a cluster which can be described as  $(\text{CH}_3\text{F})_{n-2}\cdot(\text{CH}_3\text{F})\text{H}^+$ . A full characterization of this behavior was not pursued.

The fragmentation of the  $\text{Ar}_n\text{CH}_3\text{F}^+$  cluster series deserves special note. The  $\text{Ar}_n\text{CH}_3\text{F}^+$  and  $\text{Ar}_n\text{CH}_2\text{F}^+$  ions are of comparable intensity, while the  $\text{Ar}_n\text{CH}_3^+$  clusters are  $\sim 7$  times less intense than either of these two. The 70 eV electron-impact mass spectrum<sup>32</sup> shows nearly identical intensities for  $\text{CH}_3\text{F}^+$ ,  $\text{CH}_2\text{F}^+$  and  $\text{CH}_3^+$ , and similar intensities are likewise observed in our apparatus for these masses ( $m/e$  15, 33 and 34). Production of  $\text{CH}_3^+$  results from ionization into the first excited ( $\tilde{A}$ ) state of  $\text{CH}_3\text{F}^+$  and is accompanied by significant release of kinetic energy in the fragments (up to 2 eV in  $\text{CH}_3^+$ ).<sup>32,33</sup> Recent fragmentation studies of Ar clusters containing an organic molecule are interpreted in terms of initial ionization of the Ar followed by charge transfer to the lower IP guest species.<sup>34</sup> In the case of  $\text{CH}_3\text{F}$ , the appearance potential of the  $\tilde{A}$  electronic state (15.8-16.0 eV<sup>32</sup>) is at or just above the IP of Ar (15.76 eV) and well above the IP of  $\text{Ar}_n$  (14.25 eV<sup>35</sup>). Charge transfer from  $\text{Ar}^+$  to  $\text{Ar}_2^+$  would compete with transfer to  $\text{CH}_3\text{F}^+$  ( $\tilde{A}$ ), and initial formation of  $\text{Ar}_2^+$  from  $\text{Ar}^+$  would preclude this possibility entirely. We do not expect a high probability for charge transfer excitation to the ( $\tilde{A}$ )  $\text{CH}_3\text{F}^+$  state. Furthermore, population of the  $\tilde{A}$  state would result in the immediate release of 2 eV of kinetic energy into the cluster, which would result in significant evaporation of the cluster (see Section 5.1.1). This may produce different

fragmentation compared to the case where the energy is retained initially in the  $\text{CH}_3\text{F}^+$  ion.<sup>34a</sup> Finally, we also observe the unexpected series  $\text{Ar}_n\text{F}^+$  in the mass spectrum. As noted previously, the IR dissociation of  $m/e$  59 ( $\text{ArF}^+$ ) indicates these ions are fragments of Ar clusters containing  $\text{CH}_3\text{F}$ . Formation of an  $\text{Ar-F}^+$  dimer species (isoelectronic with  $\text{Cl-F}$ ) may be responsible for these clusters. Prior to this observation, ion fragments which are not formed in ionization of a molecule (e.g.,  $\text{F}^+$  from  $\text{CH}_3\text{F}$ ) had not been observed in clusters (e.g.,  $\text{Ar}_n\text{F}^+$  from  $\text{Ar}_n\text{CH}_3\text{F}$ ).

The effect of electron-impact ionization and fragmentation of the clusters on the infrared dissociation spectra must be considered.<sup>36</sup> Fragmentation patterns of a few specific clusters have only recently been determined,<sup>37</sup> and expansions can contain a complex variety of clusters. As illustrated schematically in Figure 2(b), the mass spectral intensity at a given mass and pressure contains contributions from larger clusters. For example, the infrared dissociation spectrum obtained by monitoring  $m/e$  154 (nominally  $\text{Ar}_3\text{CH}_3\text{F}^+$ , or  $(3,1)^+$ ), would contain the spectra of all species that contribute intensity at that mass, weighted by their abundance and their efficiency to fragment to  $m/e$  154. For neutral species of the type  $\text{Ar}_3(\text{CH}_3\text{F})_n$ ,  $n \geq 2$ , fragmentation to  $m/e$  154 can be distinguished in the IR spectrum due to the larger frequency shift associated with clusters containing more than a single  $\text{CH}_3\text{F}$  molecule, so these absorptions can be subtracted out of a spectrum. The shifts due to the clustering rare gas atoms (as well as complexes containing  $(\text{C}_2\text{H}_4)_n$ ,  $n \geq 2$ , in the  $\text{C}_2\text{H}_4$ -containing cluster system) are generally small compared to the width of the profiles, so fragmentation contributions from  $\text{Ar}_n\text{CH}_3\text{F}$ ,  $n > 3$ , to  $m/e$  154 are not easily separable by cluster size.

There is growing evidence that ions produced from electron-impact ionization of weakly bound clusters are *much smaller* than the neutrals from which they derive.<sup>37</sup> While fragmentation makes the identification of corresponding neutral clusters quite difficult, it has proven useful for providing a probe of the *entire cluster distribution*: such a large percentage of the seed molecule becomes complexed in the high-pressure expansions that virtually all mass intensity detected at the CH<sub>3</sub>F or C<sub>2</sub>H<sub>4</sub> parent ion peak results from fragmentation of clusters containing the seed molecule. Thus monitoring the dissociation profile of CH<sub>3</sub>F<sup>+</sup> or C<sub>2</sub>H<sub>4</sub><sup>+</sup> samples the individual spectra of the many cluster sizes present in the beam, in a way similar to optothermal detection (also see the discussion of Figure 4). This is in contrast to the small cluster limit<sup>1,38</sup> in which infrared spectra obtained at the parent ion or fragment mass of the van der Waals molecule correspond directly to the spectra of single neutral clusters.

We postpone for the moment a full discussion of the cluster size distributions of the molecular beams. As a guide, we note here that the pressure dependence of the infrared spectra suggest demarcation of three cluster regimes which we designate as “small,” “moderate” and “large.” From evidence to be presented later, we associate the “small” cluster regime with cluster sizes with less than one rare gas or molecular shell; e.g., Ar<sub>n</sub>CH<sub>3</sub>F, with  $n < 12$ . The “moderate” cluster regime denotes clusters with a partially filled second solvation shell,  $12 < n < 54$ , while “large” clusters are indicative of microcrystallites ( $n > 50$ ). The three cluster regimes are delineated to various degrees in each of the CH<sub>3</sub>F systems we have studied. The cluster range serve only to correlate regimes of IR spectral behavior with a physical model, and

there is no means at present with which to determine the exact ranges of  $n$  within this model. Given our limited mass range ( $< 1000$  amu), we have adopted the results of other studies to gauge clustering conditions. The results of these estimates (see Section 5.1.3 for details) are included along with the dissociation spectra in the figures below, to be used as rough guides of the maximum of the neutral cluster distribution.

#### 4.2 Lineshape Analysis

Both simple<sup>18</sup> and more extensive<sup>1d</sup> models have been presented to extract information from the dissociation profiles of van der Waals molecules. Because of electron-impact fragmentation, the profiles observed in the experiments reported here are convolutions of individual cluster spectra. The use of the simple two-level-with-decay model lineshape<sup>18</sup> to fit the observed dissociation profiles can still, however, provide insight into the trends of cluster properties with increasing size, such as solvation shifts and vibrational lifetimes. In effect, we are considering how well a range of cluster sizes or types can be represented by a single dissociation profile.

The observed dissociation wavelength dependences are presented with fits to the pure case two-level-with-decay model lineshape formula:<sup>18</sup>

$$F_p(\omega, t) = \frac{I}{I_0} = \exp \left[ -\omega_R^2 \gamma_D^{-1} t \cdot \frac{\gamma_D^2}{4(\omega - \omega_0)^2 + \gamma_D^2} \right], \quad (1)$$

where  $F_p$  is the fraction of van der Waals species remaining after irradiation of duration  $t$ ,  $\omega_R$  is the Rabi frequency of the transition and  $\omega_0$  is the frequency

of maximum dissociation intensity. The lineshape is the exponential of a scaled Lorentzian. The first-order dissociation rate constant,  $\gamma_D$ , is derived from the linewidth:

$$\gamma_D = \tau^{-1} = 2\pi c \cdot FWHM, \quad (2)$$

where FWHM is the full width at half maximum of *the Lorentzian factor* in (1), or the width of the *logarithm* of the profile. In the case of a homogeneous spectrum of a specific cluster,  $\gamma_D$  represents the rate of dissociation of the complex.

The intensity of the dissociation profile is determined by the Lorentzian prefactor,  $\omega_R^2 \gamma_D^{-1} t$ . The Rabi frequency,  $\omega_R$ , is defined as:

$$\omega_R = (\vec{\mu} \cdot \vec{E}) / \hbar, \quad (3)$$

where  $\vec{\mu}$  is the dipole moment of the absorption (proportional to the integrated absorption intensity) and  $\vec{E}$  is the electric field vector (proportional to the laser power). All clusters containing one particular chromophore (e.g., CH<sub>3</sub>F) have the same absorption strength. Integrating Eq. 1, we have:

$$\int_{-\infty}^{+\infty} F_p(t, \omega) d\omega = (\pi/4) \cdot \omega_R^2 t, \quad (4)$$

or, in the absence of additional quenching factors (treated in eq. 5), the integrated dissociation intensity is independent of the dissociation rate and thus the same for any cluster containing only a single CH<sub>3</sub>F molecule (neglecting contributions from polarizable partners<sup>1b</sup>). The summation of the spectra of various clusters by electron-impact fragmentation yields a dissociation profile at a given cluster

ion mass whose integrated profile should reproduce the transition dipole moment for absorption by the free chromophore. This is a valuable constraint on the intensity of the profiles. Additional consideration must be given to profiles obtained at the parent ion mass of  $\text{CH}_3\text{F}^+$  ( $m/e$  34) or  $\text{C}_2\text{H}_4^+$  ( $m/e$  28): with mild expansion conditions (producing small clusters), the ion signal is due primarily to the uncomplexed seed molecule, so the total fraction dissociated will be quite small. Under conditions where practically the entire quantity of seed molecule is clustered, the integrated dissociation intensity at  $\text{CH}_3\text{F}^+$  or  $\text{C}_2\text{H}_4^+$  will approach that of the absorption strength of the free molecule.

#### *4.3 Small cluster limit spectra*

The simplest point from which to embark on a study of the dissociation spectra of  $\text{A}_x\text{CH}_3\text{F}$  clusters is the small-cluster ( $x = 1$ ) limit: the van der Waals complexes between single rare gas atoms or  $\text{N}_2$  molecule and  $\text{CH}_3\text{F}$ . Unfortunately, the isolation of these complexes without the presence of larger clusters is a nontrivial task – the strong dipole moment of  $\text{CH}_3\text{F}$  (1.86 D<sup>39</sup>) makes it an efficient clusterer – and was not the focus of the present study. The spectra we report, collected in Figure 3 and summarized in Table 1, are the low-clustering limit of  $\text{CH}_3\text{F}$ -containing clusters and are best described as  $\text{A}_x\text{CH}_3\text{F}$ , with  $x \leq 2$  (see below). The dissociation spectra which exhibit the smallest frequency shifts away from the gas-phase value are considered the low-clustering limit listed in Table 1. All of the main absorptions are red-shifted, indicating that long-range attractive (dispersion) forces dominate over short-range repulsive interactions.<sup>1b</sup> The magnitude of the shift of the  $\text{CH}_3\text{F}$   $\nu_3$  vibration correlates with the polarizability of the partner, except for

**Figure 3.** Small-cluster limit dissociation spectrum in the  $\text{CH}_3\text{F } \nu_3$  region. The spectra represent the absorption spectra of  $\text{A}_x\text{CH}_3\text{F}$  neutral clusters, where A = (a) Ne; (b) Ar; (c) Kr; (d)  $\text{N}_2$ , and  $x \leq 2$ . The gas-phase  $\nu_3$  absorption of free  $\text{CH}_3\text{F}$  occurs at  $1048.6 \text{ cm}^{-1}$  while the absorption of  $\text{CH}_3\text{F}$  in these clusters is red-shifted. Note the scale changes between spectra which are indicative of the percentage of cluster fragmentation to the monitored ion mass. The solid line is a least-squares best fit to at most 2 exponentiated Lorentzians. Fit parameters are included in Table I. The indicated gas mixtures were expanded through a  $25 \mu\text{m}$  room temperature nozzle.

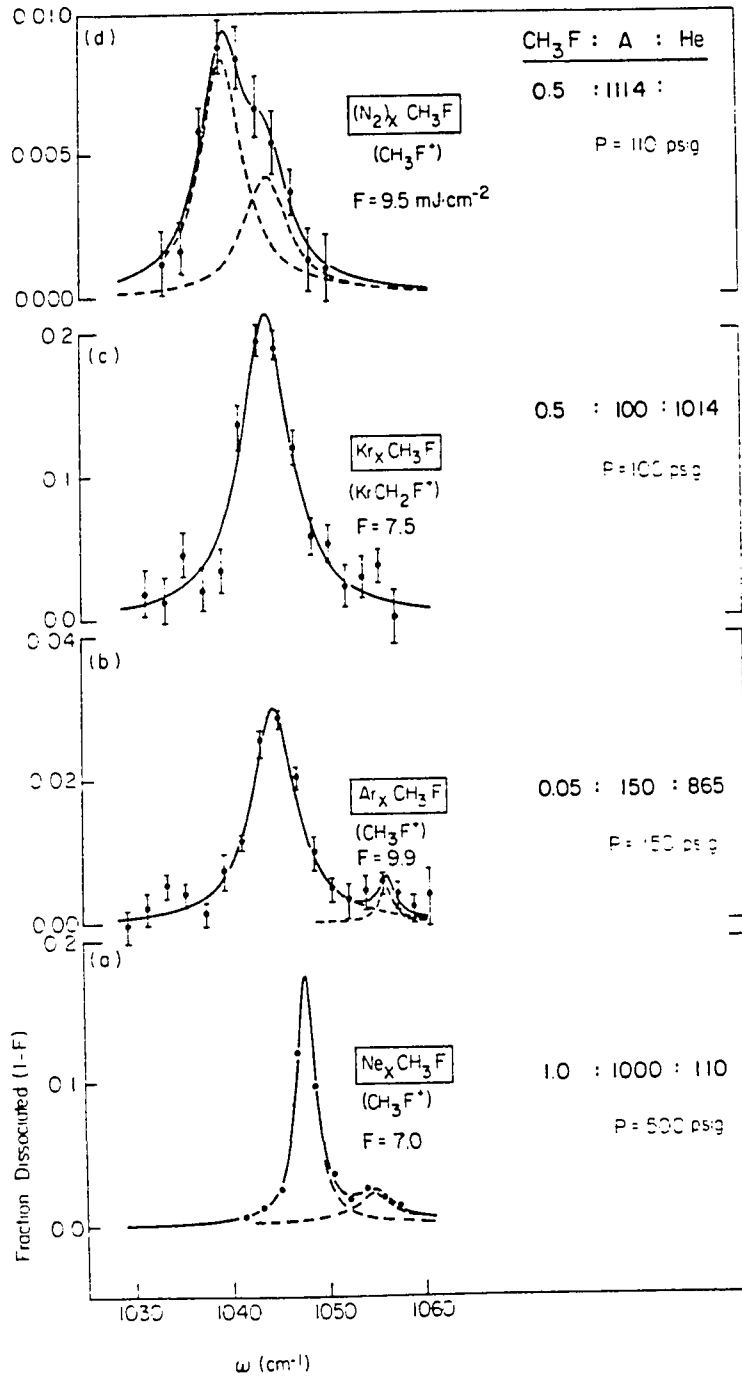


**Table 1**  
*CH<sub>3</sub>F* Small-cluster (*A<sub>z</sub>CH<sub>3</sub>F*) Spectral Parameters<sup>a</sup>

	<b>A =</b>	<b>Ne</b>	<b>Ar</b>	<b>Kr</b>	<b>N<sub>2</sub></b>
$\omega_0$ ( $\nu_3$ )		1047.6	1044.7	1044.1	1044.3
$\omega_g^* - \omega_0$		1.0	2.9	3.5	3.3
$\gamma$ (FWHM')		2.0	5.7	5.7	5.5
$\omega_i$ ( $\nu_3 + \nu_i$ )		1054.6	1056.3		
$\omega_0 - \omega_i$		7.0	11.6		
$\gamma$ (FWHM')		4.7	2.3		
$\alpha^\dagger$		0.395	1.64	2.48	1.76 <sup>‡</sup>

<sup>a</sup> All numbers (except  $\alpha$ ) in  $\text{cm}^{-1}$

\* Gas-phase value,  $\omega_g = 1048.6 \text{ cm}^{-1}$ , from Refs. [40,41]

† Polarizability  $\alpha$  in  $\text{cm}^3$ , from Refs. [42,43].

‡  $\alpha_{perp} = 1.45 \text{ cm}^3$ ;  $\alpha_{parl} = 2.38 \text{ cm}^3$

that of  $\text{Kr}_n\text{CH}_3\text{F}$  (in which clusters larger than  $\text{Kr}_2\text{CH}_3\text{F}$  likely contribute to the observed spectrum at the expansion conditions given, and thus distort the simple shift/polarizability comparison). Parameters used to generate the fitted curves in Figure 3 are also collected in Table 1. Spectra of van der Waals molecules containing  $\text{C}_2\text{H}_4$  is the subject of other work<sup>1–6,44</sup> so we report only spectra of large clusters containing  $\text{C}_2\text{H}_4$ .

The less intense features evident to the blue of the main dissociation peaks (as well as to the blue of the gas-phase absorption) in Figures 3(a) and (b) are reminiscent of early spectra<sup>1a</sup> of rare gas· $\text{C}_2\text{H}_4$  complexes (see also Figure 8) which were later refined to yield structure indicative of a hindered internal rotor.<sup>1c</sup> This is the reason we do not specify our observed small-cluster limiting spectra as corresponding to those of the van der Waals dimers. We believe the refined spectra of van der Waals complexes between  $\text{CH}_3\text{F}$  and rare gas atoms and  $\text{N}_2$  will likely contain additional structure which would permit the assignment of a combination band or hindered rotor transitions. At the present level, we observe features shifted 7.0 and 11.6  $\text{cm}^{-1}$  from the major  $\text{Ne}_x\text{CH}_3\text{F}$  and  $\text{Ar}_x\text{CH}_3\text{F}$  absorptions, respectively. Further refinement of these spectra will be fruitful once continuously tunable sources are developed in this spectral region. In spite of the dilute mixtures used here, the difficulty involved in establishing conditions which isolate the spectrum of these van der Waals dimers indicates that other IR studies, especially those involving a polar constituent, should be treated with caution.

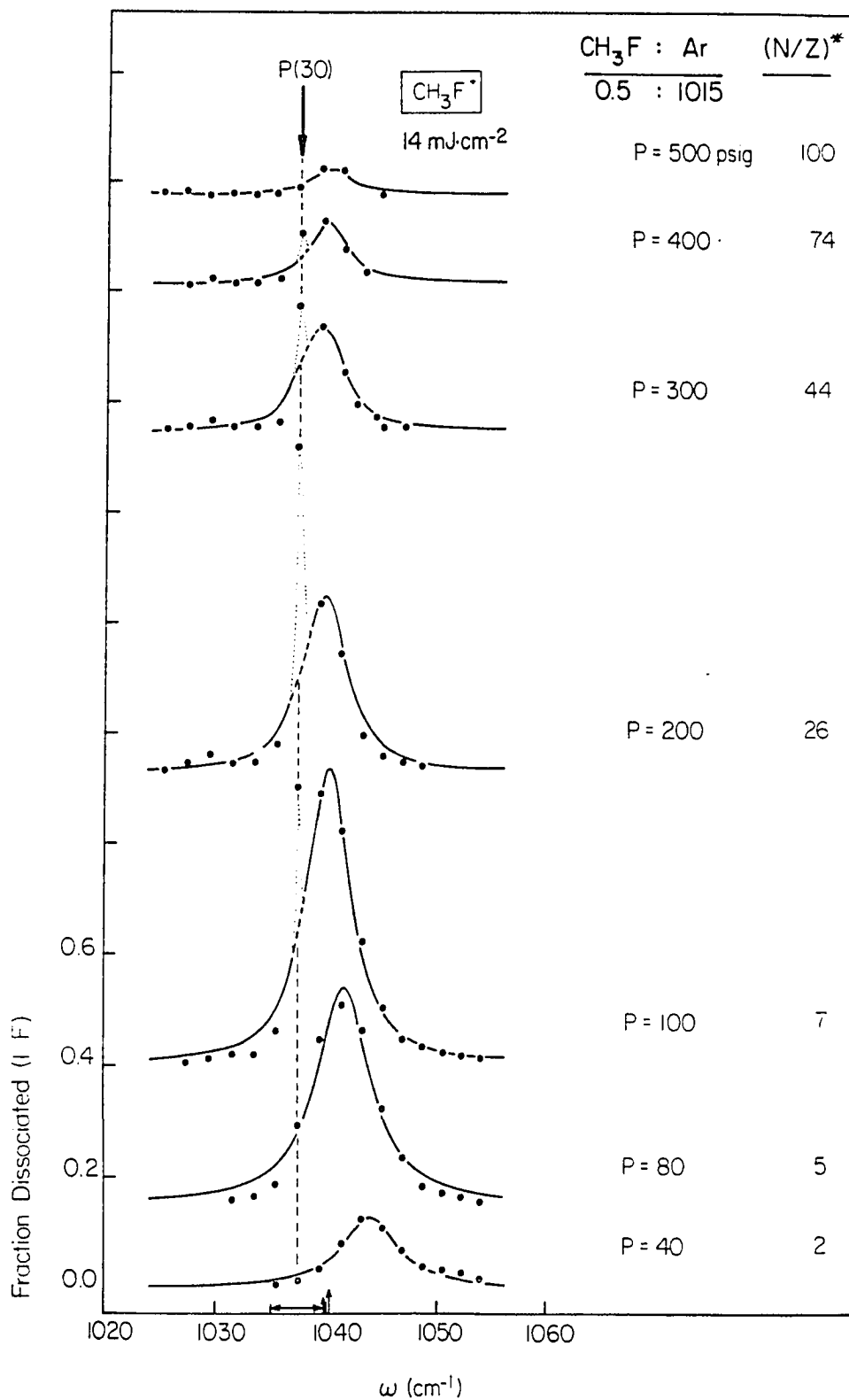
#### 4.4 *Large clusters containing $\text{CH}_3\text{F}$*

There are three regimes of clustering that we can distinguish in the infrared

dissociation spectra of the  $\text{CH}_3\text{F}$ -containing clusters studied which are best illustrated in the  $\text{Ar}/\text{CH}_3\text{F}$  cluster system. The salient features associated with the cluster spectra as the transition is made from small through moderate to large cluster sizes are reflected in the dissociation profiles shown in Figure 4, obtained by monitoring the  $\text{CH}_3\text{F}^+$  mass ( $m/e$  34). In the “small” cluster regime, the spectra are seen to shift further to the red of the low-cluster  $\text{Ar}_x\text{CH}_3\text{F}$  absorption as the average cluster size increases (Figure 4,  $P=40$  and  $80$  psig). The width of the profile remains essentially constant ( $4\text{-}6\text{ cm}^{-1}$ ) until the appearance of an extremely narrow component of the spectra occurring at the P(30) emission line ( $1037.43\text{ cm}^{-1}$ ) in the  $(00^0_1)-(02^0_1)$   $\text{CO}_2$  laser band. This feature dominates the dissociation profile in the “moderate” cluster size regime, becoming more intense at higher backing pressures ( $P=100, 200$  psig). Note the low fractional dissociation on the low frequency side of the enhanced P(30) feature, when compared to the Lorentzian fit. This indicates very narrow dissociation profiles ( $\text{FWHM} \leq 0.5\text{ cm}^{-1}$ ) are dominant in the  $1037\text{-}1038\text{ cm}^{-1}$  region. At still higher pressures ( $P=300$  to  $500$  psig), when “large” clusters begin to dominate the neutral cluster distribution, the fractional attenuation at P(30) decreases dramatically, leaving the broad ( $3.7\text{ cm}^{-1}$ ) absorption centered at  $\sim 1040\text{ cm}^{-1}$ . The curves drawn with the data, qualitative fits to Eq. (1), serve both to: (a) highlight the dramatic increase, then decrease, in dissociation intensity at P(30), and; (b) emphasize the dissociation intensity needed in the  $1032\text{-}1037\text{ cm}^{-1}$  region to fit the data points with a single Lorentzian.

The profile obtained at  $P=200$  psig (Figure 4) is similar to that reported by Gough *et al.* (Figure 3 of Ref. [29]), but here with negligible contribution from

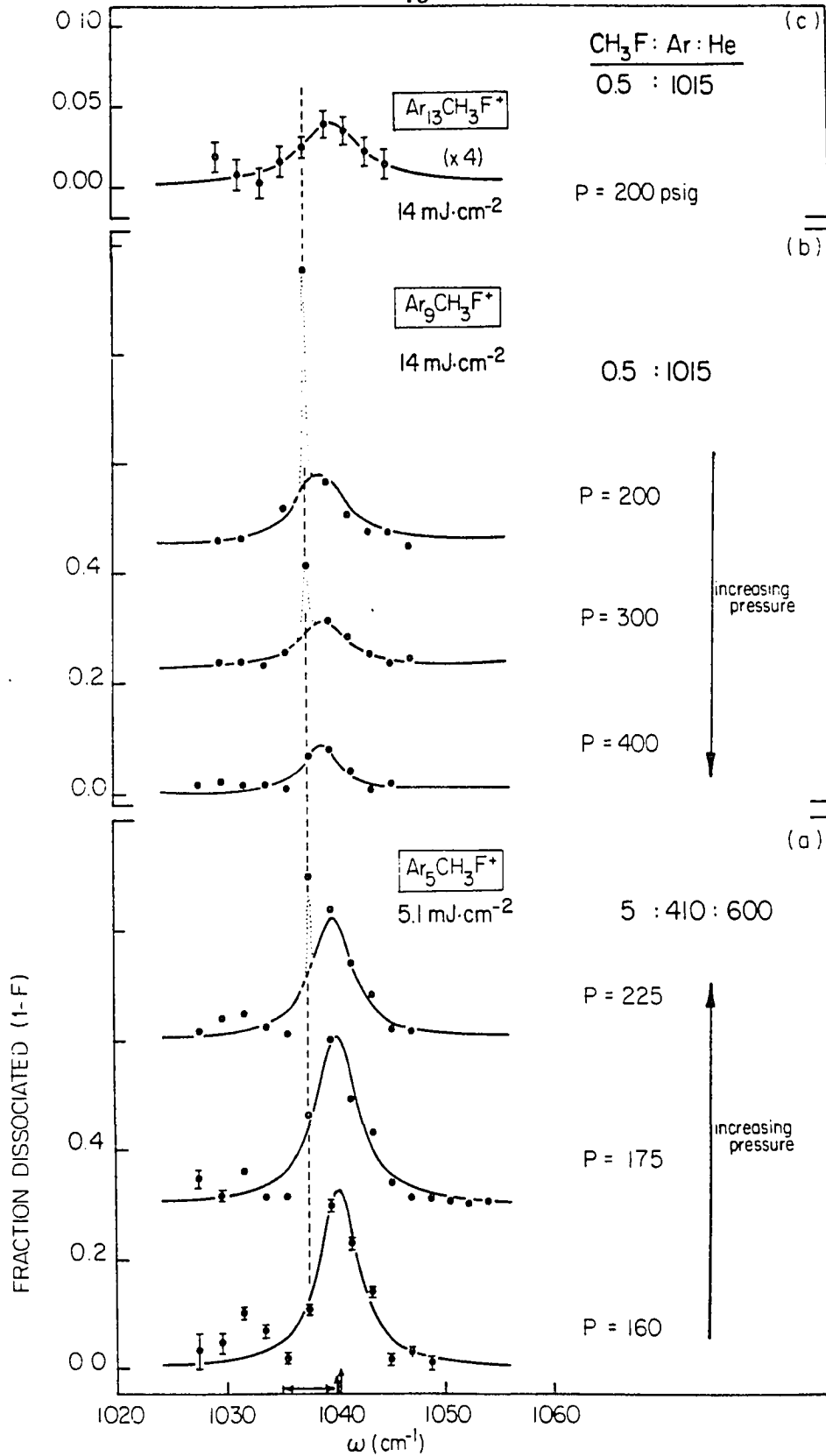
**Figure 4.** Pressure dependence of the dissociation profile of  $\text{Ar}_n\text{CH}_3\text{F}$  clusters detected at  $m/e$  34 ( $\text{CH}_3\text{F}^+$ ). The curves are offset arbitrarily in the vertical coordinate for clarity, and  $1\sigma$  error in the dissociation is indicated when larger than the height of the circles. At low backing pressures the profiles are broad and fairly symmetric. Between 100 and 300 psig, the fraction dissociated with the P(30) laser line ( $1037.4\text{ cm}^{-1}$ ) increases dramatically. At higher pressures this feature disappears, leaving a broad feature with low fractional dissociation intensity. Matrix isolation absorption peaks are indicated ( $\uparrow$ ) along the abscissa. The “characteristic cluster size,”<sup>46</sup>  $(N/Z)^*$ , is the mean of the neutral Ar cluster distribution calculated from Figure 11 under the given conditions.



$\text{Ar}_n(\text{CH}_3\text{F})_2$  clusters. The pressure dependence we obtain highlights the dramatic rise and fall of the dissociation feature near the P(30) laser line. The  $\nu_3$  absorption spectrum for  $\text{CH}_3\text{F}$  in an Ar matrix exhibits two discernible features (indicated along the abscissa of Figure 4):<sup>14–16</sup> a strong, narrow ( $< 0.2 \text{ cm}^{-1}$ ) absorption at  $1040 \text{ cm}^{-1}$  attributed to the normal matrix site and a less intense, broad ( $\sim 1 \text{ cm}^{-1}$ ) feature centered at  $\sim 1039 \text{ cm}^{-1}$  associated with surface of dislocation sites in the matrix. Note the intense P(30) feature is shifted  $\sim 2.5 \text{ cm}^{-1}$  beyond where one would expect  $\text{CH}_3\text{F}$  in a matrix site to absorb. As indicated by the (N/Z)\* values listed in Figure 4 (*vide infra*), the narrow P(30) feature appears to correspond to the cluster range in which a second solvation shell of Ar atoms is being filled.

Dissociation spectra obtained at various cluster ion masses for the Ar/ $\text{CH}_3\text{F}$  system are gathered in Figure 5. In general, the spectra show features similar to the  $\text{CH}_3\text{F}^+$  dissociation profiles: a frequency shift to the red with increasing cluster size, the narrow dissociation feature at P(30), and a broad component that persists in the highest cluster range. Note, however, that while the beam attenuation at P(30) is the *dominant* feature in the  $\text{Ar}_9\text{CH}_3\text{F}^+$ , or  $(9,1)^+$ , spectrum (Figure 5(b), P=200), it is *absent* in the  $(13,1)^+$  profile (Figure 5(c)) at the same expansion conditions. Also, the spectrum of the neutral clusters which at relatively low backing pressure contribute to the mass  $(5,1)^+$  (Figure 5(a), 160 psig) shows no indication of enhanced absorption on the P(30) line. With these spectra we can set specific bounds on the range of cluster size whose spectrum is best represented by the narrow component at  $1037.4 \text{ cm}^{-1}$ . The  $(5,1)^+$  profile sets a strict lower

**Figure 5.** Infrared dissociation detected at specific cluster ion masses. (a) The dissociation spectrum of the  $\text{Ar}_5\text{CH}_3\text{F}^+$  cluster ion ( $m/e$  234) detected with 160 psig backing pressure appears with a symmetric profile, whereas at higher pressures enhanced dissociation on the P(30) line is observed. (b) At 200 psig in an Ar expansion, 50% of all neutral clusters contributing to  $\text{Ar}_9\text{CH}_3\text{F}^+$  cluster ion ( $m/e$  394) dissociate at P(30), while *with identical expansion conditions* there is no evidence for this feature in (c), the  $\text{Ar}_{13}\text{CH}_3\text{F}^+$  ( $m/e$  554) profile. It is possible to place limits on the cluster sizes responsible for this enhanced absorption feature. Also in (b), the P(30) feature disappears at higher backing pressures while the broad profile to the blue likewise decreases in percent dissociated.

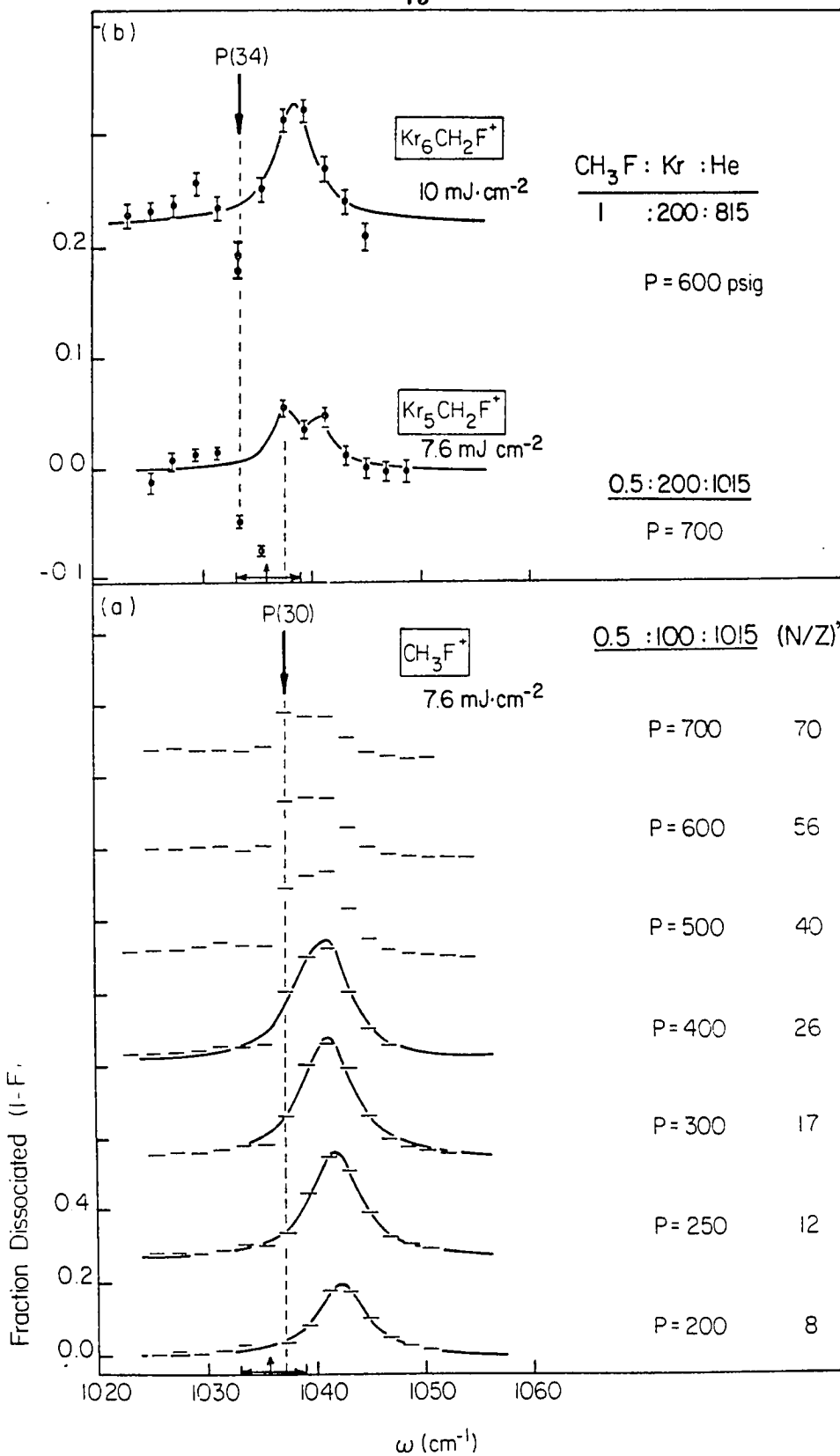


bound as the  $\text{Ar}_5\text{CH}_3\text{F}$  cluster. For the upper bound (and a better lower bound), we must estimate the neutral clusters that contribute to the observed spectra due to fragmentation. For example, if we assume the ion masses correspond directly to neutrals for backing pressure at the sensitivity limit of detection for the particular ion, then clusters of the form  $\text{Ar}_n\text{CH}_3\text{F}$ ,  $5 < n < 13$ , produce the observed narrow component in the infrared dissociation profile at  $1037.4 \text{ cm}^{-1}$ . However, this is probably not a realistic estimate because fragmentation of the large weakly bound clusters is extensive. Recent determination of  $\text{Ar}_n$  fragmentation ratios<sup>37c</sup> would suggest both upper and lower limits are likely significantly higher, while the presence of a dipole such as  $\text{CH}_3\text{F}$  would tend to reduce fragmentation.<sup>45</sup>

Whatever the range of neutral clusters that contribute to the observed ion masses, we believe it is important to take note of the great difference in spectra of two ion masses, those of  $(9,1)^+$  and  $(13,1)^+$ , *separated by only 4 Ar atoms*. This indicates either that the dissociation spectra recorded at individual cluster ion masses are sensitive to only a small range of cluster sizes, or (more likely) that specific ion clusters are formed preferentially from a range of ionized neutral clusters. These points are discussed further in section 5.2.

Figure 6 is a presentation of spectra obtained for  $\text{Kr}_n$  clusters containing  $\text{CH}_3\text{F}$ . The red shift progression with increasing backing pressure of the  $\text{CH}_3\text{F}^+$  profile (Figure 6(a)) is observed but is seen to develop more slowly than in the Ar cluster case (Figure 4), as the Kr mixture is more dilute (10% Kr in He compared with 100% Ar). The profile likewise converges on the P(30) line as a limit for the frequency shift, at which point attenuation of the dissociation intensity commences. The

**Figure 6.** (a) Dissociation spectra of CH<sub>3</sub>F-containing Kr clusters, detected at CH<sub>3</sub>F<sup>+</sup>. Although inhomogeneity is present, the profiles do not show the dramatic dissociation intensity on a single CO<sub>2</sub> laser line as in the Ar/CH<sub>3</sub>F system. (b) *Negative* dissociation features give evidence for larger Kr clusters absorbing further to the red, close to the matrix absorption peaks near 1037 cm<sup>-1</sup>, indicated (↑) along the abscissa.



presence of narrow components in the lineshape is apparent, both in the profiles shown in Figure 6(a) and in individual mass dissociation spectra of  $\text{Kr}_n\text{CH}_3\text{F}^+$ ,  $n \leq 6$ , which are not pictured. The maximum in the fraction dissociated profile occurs at P(30) while there is a sharp dropoff in dissociation intensity on the adjacent P(32) line. In none of the profiles, over a range of backing pressure, is there observed the intense single-line dissociation peak seen in the Ar cluster case. With mass spectral intensity spread over the Kr isotopes, we could obtain dissociation spectra only up to  $m/e$  621 ( $\text{Kr}_7\text{CH}_2\text{F}^+$ ), using a 20% Kr in He mixture expanded at 400 psig. We judge that the spectra sample the moderate cluster regime, where we might expect to observe the enhanced absorption feature similar to that seen for  $\text{Ar}_n\text{CH}_3\text{F}$ , because of the loss of fractional dissociation intensity at the  $\text{Kr}_7\text{CH}_2\text{F}^+$  ion mass compared to that observed for smaller clusters and lower backing pressures. There is some indication of a narrow absorption present in the  $\text{Kr}_n\text{CH}_3\text{F}$  spectrum near  $1037.4 \text{ cm}^{-1}$  which may be shifted into the gap between  $\text{CO}_2$  laser lines.

An interesting feature in the Kr/ $\text{CH}_3\text{F}$  system occurs at higher pressure where a *negative* fractional dissociation is observed; that is, the mass spectral intensity at a given mass peak *increases* in intensity upon laser irradiation. Figure 6(b) shows individual mass dissociation spectra taken at two different expansion conditions. Negative dissociation is observed at P(34) ( $1033.49 \text{ cm}^{-1}$ ) in both cases, and also at P(32) ( $1035.47 \text{ cm}^{-1}$ ) under conditions favoring slightly smaller clusters. The main feature of the  $\nu_3$  absorption of  $\text{CH}_3\text{F}$  in a Kr matrix,<sup>15,17</sup> marked with an arrow along the abscissa of Figure 6, occurs at  $1035.8 \text{ cm}^{-1}$ ,  $2 \text{ cm}^{-1}$  to the blue of the P(34) negative dissociation features and similar to the shift between the matrix

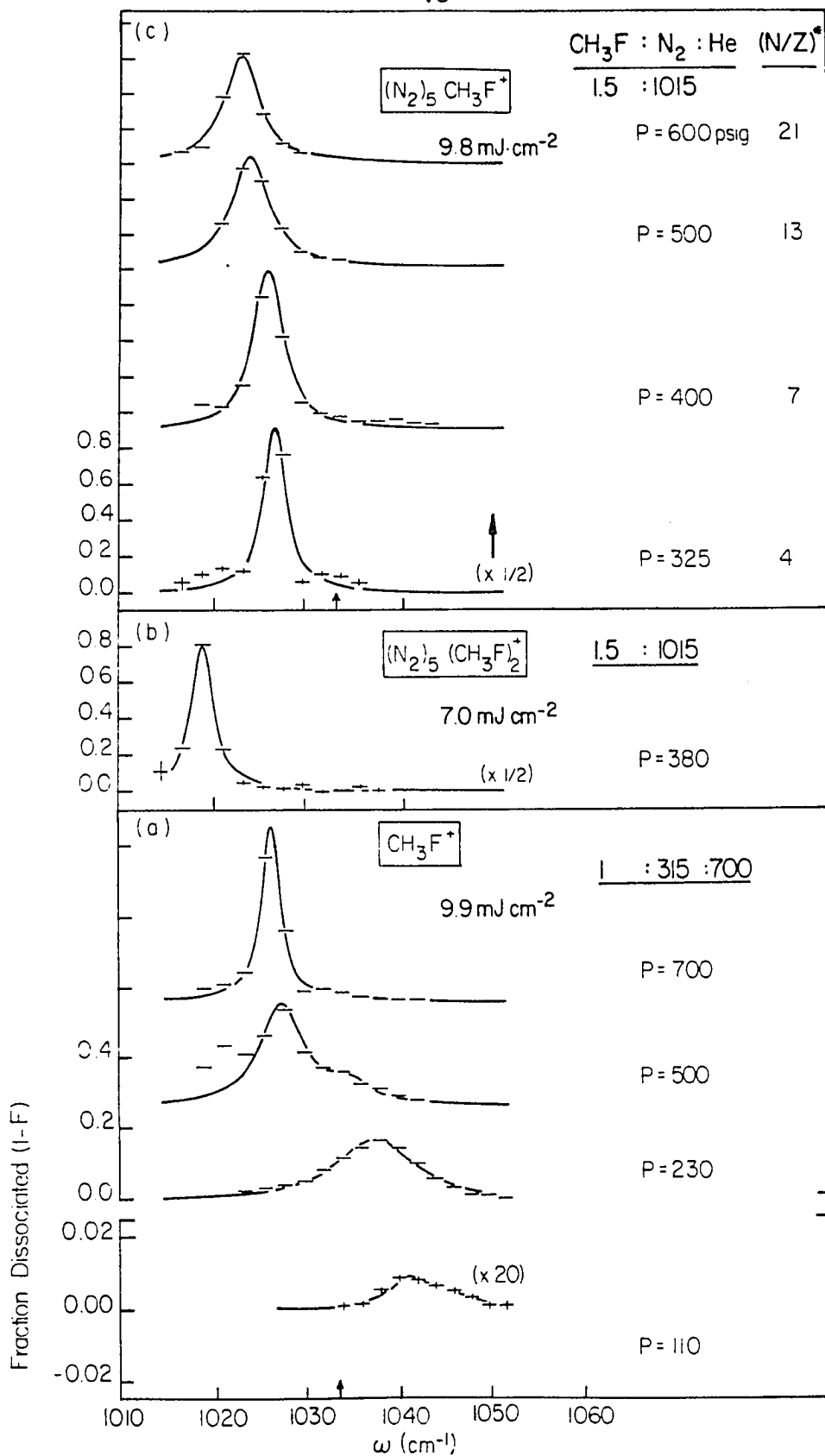
value and enhanced P(30) feature in the  $\text{Ar}_n\text{CH}_3\text{F}$  cluster spectra. There is thus evidence for matrix-like  $\text{Kr}_n\text{CH}_3\text{F}$  clusters analogous to the case of  $\text{CH}_3\text{F}$  in large Ar clusters. Negative dissociation features may be present in other cluster spectra from beams with a similar degree of clustering, and in fact may be the reason for the sharp drop in dissociation intensity in the  $1037\text{-}1038\text{ cm}^{-1}$  region, to the red of the enhanced P(30) peak in the Ar/ $\text{CH}_3\text{F}$  system, (see, for example, Figure 5(a), P = 160-225).

We discuss two explanations for the negative dissociation feature. First, the fragmentation of large clusters ( $\text{Kr}_n\text{CH}_3\text{F}$ ,  $n > 7$ ) could increase with the addition of vibrational energy and result in an increase of mass spectral intensity at the detected ion mass. Second, clusters may “dissociate,” but without leaving the molecular beam. For the second case, consider a set of large Kr clusters ( $\text{A}_M\text{CH}_3\text{F}$ ) which do not contribute intensity to the detected ion mass  $\text{A}_n\text{CH}_3\text{F}^+$  (from  $\text{A}_N\text{CH}_3\text{F}$  neutral clusters), and which can boil off the  $1000\text{ cm}^{-1}$  of energy deposited by the laser with little gain in transverse momentum, thus remaining in the molecular beam; the resultant cluster of reduced size ( $\text{A}_m\text{CH}_3\text{F}$ ) is then ionized, fragments and yields intensity at the detected ion mass. An increase would be observed in the situation where there is a greater population of the large  $\text{A}_M\text{CH}_3\text{F}$  clusters which dissociate to contribute to the detected ion mass than there are  $\text{A}_N\text{CH}_3\text{F}$  clusters which contribute before laser irradiation but are lost upon dissociation. Such an effect is plausible given the fact that in the mass-selected  $\text{Ar}_n\text{CH}_3\text{F}$  spectra, we observe significantly different dissociation spectra for similar ion masses. Further discussion of this effect can be found in Section 5.1.1.

Dissociation spectra of the  $\text{N}_2/\text{CH}_3\text{F}$  cluster system are shown in Figure 7. The progressive red shift in the small cluster regime is much larger than with Kr or Ar. For small  $(\text{N}_2)_x\text{CH}_3\text{F}$  clusters, the shift of the  $\text{CH}_3\text{F}^+$  profile per additional  $\text{N}_2$  is on the order of the linewidths and distinct shoulders are apparent. Deconvolution of these spectra suggest the following shifts from the uncomplexed value for each additional  $\text{N}_2$  molecule:  $\Delta\omega_x = 4.3, 4.3, 2.0, 4.0$  and  $4.6$ , starting from the small-cluster limiting spectrum ( $x = 1$  or  $2$ ) which peaks at  $1044.3 \text{ cm}^{-1}$ . At moderate clustering conditions (Figure 7(a),  $P=500, 700 \text{ psig}$ ), an intense dissociation feature grows into prominence on lines P(40) and P(42). Although reminiscent of the profiles obtained for  $\text{Ar}_n\text{CH}_3\text{F}$ , there are now *two* adjacent laser lines on which intense dissociation is observed. Furthermore, at the harder expansion conditions in Figure 7(c), the transition to the large cluster regime can be seen as the absorption peak continues to broaden and smoothly shift with pressure to lower frequency in contrast to the simple disappearance of the single-line P(30) feature in the  $\text{Ar}_n\text{CH}_3\text{F}$  large-cluster case. A slight shift of the narrow peak in the  $\text{Ar}/\text{CH}_3\text{F}$  case is thus proposed to account for the loss of dissociation intensity.

The  $\nu_3$  absorption of  $\text{CH}_3\text{F}$  in a  $\text{N}_2$  matrix<sup>15</sup> at 7 K, indicated in Figure 7, occurs at  $1033.1 \text{ cm}^{-1}$ , whereas  $\text{CH}_3\text{F}$  in large  $\text{N}_2$  clusters are shifted past this value, exhibiting a maximum peak shift to  $1023.0 \text{ cm}^{-1}$  in our spectra. The spectrum of  $\text{N}_2$ -solvated  $\text{CH}_3\text{F}$  dimer, in Figure 7(b), exhibits an additional  $4.4 \text{ cm}^{-1}$  shift ( $\omega_0 = 1018.6 \text{ cm}^{-1}$ ) from the large cluster  $(\text{N}_2)_n\text{CH}_3\text{F}$  spectrum. Analogous to the monomer case, the dimer isolated in the gas-phase cluster absorbs at lower

**Figure 7.** (a)  $\text{N}_2$  molecules shift the  $\text{CH}_3\text{F}$   $\nu_3$  absorption frequency enough that separate shoulders for different size clusters are observed under small cluster conditions. In the moderate cluster regime, the infrared spectra exhibit *two* points having enhanced dissociation. (c) In the large cluster regime, the absorption peak broadens and shifts to higher frequency, analogous to the temperature-dependent behavior of the  $\nu_3$  absorption line of  $\text{CH}_3\text{F}$  in a  $\text{N}_2$  matrix. The profiles are shifted *beyond* the matrix absorption (indicated,  $\uparrow$ ). (b) The dissociation spectrum of  $(\text{N}_2)_5\text{CH}_3\text{F}^+$  is included to illustrate the additional  $4.4 \text{ cm}^{-1}$  shift due to the presence of  $(\text{CH}_3\text{F})_2$ .



frequency than  $(\text{CH}_3\text{F})_2$  in a  $\text{N}_2$  matrix:<sup>15</sup>  $\omega_0 = 1023.7 \text{ cm}^{-1}$  at 7 K, with only a small red-shift at increasing matrix temperature.

The dissociation intensities of  $(\text{N}_2)_n\text{CH}_3\text{F}$  clusters, obtained by fitting a Lorentzian to the observed dissociation spectrum, appear anomalously high (by roughly a factor of 2) compared to the absorption intensity of uncomplexed  $\text{CH}_3\text{F}$  as well as the dissociation intensity of the other cluster systems. A simple explanation is that the clusters contain more than one  $\text{CH}_3\text{F}$  molecule in the clusters, but we do not believe this to be the case at these dilutions. The intense features could be indicative of very narrow absorption features, as invoked in explanation of features in the  $\text{Ar}/\text{CH}_3\text{F}$  and  $\text{Kr}/\text{CH}_3\text{F}$  cluster systems, but the peak is observed to smoothly shift to the red as the backing pressure is increased indicating the lines have width on the order of the line spacing. Also, the large fraction of clusters dissociated with the low laser fluence indicates a substantial degree of homogeneity is present in the profiles. Another possibility for the enhanced absorption strength in the  $\text{N}_2/\text{CH}_3\text{F}$  cluster spectra is enhancement of the  $\text{CH}_3\text{F}$  dipole moment by the polarization of the  $\text{N}_2$  environment.<sup>1b</sup> Such a large effect may be consistent given the large frequency shift that is observed for the  $(\text{N}_2)_n\text{CH}_3\text{F}$  clusters. As a final note, the spectra of cluster ions up to  $(\text{N}_2)_9\text{CH}_3\text{F}^+$  (obtained at  $P=600$  psig) exhibit similar profiles to the displayed  $(\text{N}_2)_5\text{CH}_3\text{F}^+$  spectra.

We attempted to observe the spectra of large  $\text{Ne}_n\text{CH}_3\text{F}$  clusters but did not observe parent ions above  $\text{Ne}_1\text{CH}_3\text{F}^+$  using a room temperature nozzle. Dissociation profiles detected at  $m/e$  34 ( $\text{CH}_3\text{F}^+$ ) were similar to that reported in Figure 3, with the peak of the (asymmetrical) dissociation feature shifting to the

P(20) CO<sub>2</sub> laser line (1047.46 cm<sup>-1</sup>) at the highest clustering conditions. The peak of the cluster absorption is only 1.8 cm<sup>-1</sup> red-shifted from the gas phase absorption and 0.8 cm<sup>-1</sup> shifted from the low-cluster limit spectrum. The  $\nu_3$  absorption of CH<sub>3</sub>F in a Ne matrix is observed 5-7 cm<sup>-1</sup> to the red of the gas-phase value, observed at 1041.5 and 1043.5 cm<sup>-1</sup> depending on the crystal structure of the Ne matrix (fcc and hcp, respectively).<sup>15</sup>

#### 4.5 Clusters containing C<sub>2</sub>H<sub>4</sub>

The 2 cm<sup>-1</sup> gap between CO<sub>2</sub> laser lines in the CH<sub>3</sub>F  $\nu_3$  absorption region prevents resolution of the narrow absorption features observed in the moderate cluster regime of CH<sub>3</sub>F-containing clusters. The availability of additional N<sub>2</sub>O laser lines (spacing  $\sim$ 0.8 cm<sup>-1</sup>) in the spectral region of the C<sub>2</sub>H<sub>4</sub>  $\nu_7$  vibration ( $\sim$ 950 cm<sup>-1</sup>) makes it attractive to attempt an analogous study of large clusters containing C<sub>2</sub>H<sub>4</sub>. In this section we present dissociation spectra of C<sub>2</sub>H<sub>4</sub> isolated in clusters of Ar, CH<sub>4</sub> and N<sub>2</sub>. Even with the higher laser resolution, no evidence for narrow dissociation profiles on the order of the laser spacing is observed in these systems.

Dissociation profiles for C<sub>2</sub>H<sub>4</sub>-containing Ar clusters are shown in Figure 8. The small-cluster spectra (Figure 8(a), ArC<sub>2</sub>H<sub>4</sub><sup>+</sup>) exhibit the rotationally-structured profile attributed to hindered internal rotation of the Ar·C<sub>2</sub>H<sub>4</sub> van der Waals complex<sup>1c</sup> (see also Section 3.3). With increasing pressure, the spectra become dominated by a broad absorption centered at 949.5-951.5 cm<sup>-1</sup> as the Ar<sub>n</sub>C<sub>2</sub>H<sub>4</sub> clusters grow in size (Figure 8(a)). Initially the maxima are blue-shifted with respect to the gas phase value (949 cm<sup>-1</sup>),<sup>1b</sup> but are *red-shifted* at

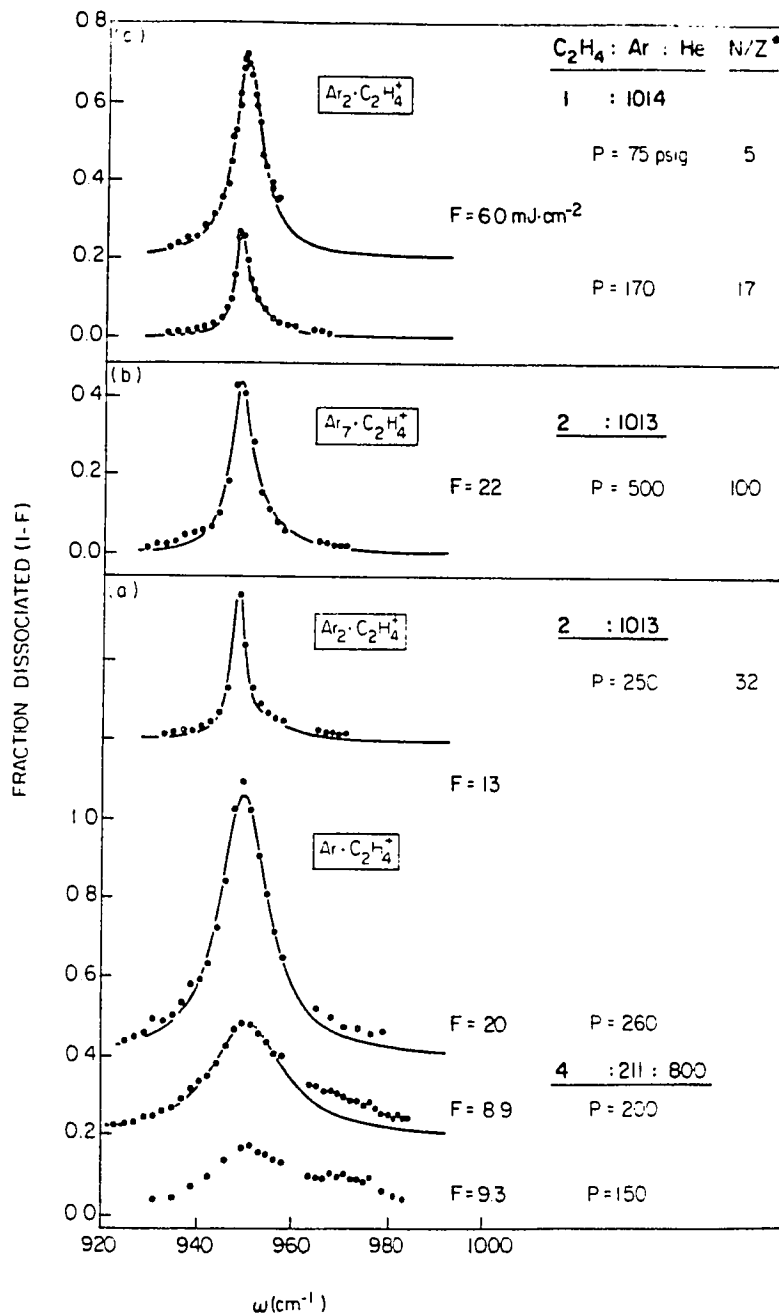


**Figure 8.** Dissociation profiles for large Ar clusters containing  $C_2H_4$ . The same Ar clustering regime characterized by the profiles in Figures 4 and 5 were explored with  $C_2H_4$  as the chromophore. Smaller frequency shifts and no evidence for cluster-dependant inhomogeneity in the profiles are observed in (a) small and (b) large cluster ions. (c) Even though additional  $N_2O$  laser lines in this spectral region give increased resolution near the absorption peak, no enhanced dissociation features are observed.

the larger cluster conditions. The spectrum obtained at the ion mass corresponding to  $\text{Ar}_2\text{C}_2\text{H}_4^+$  is shifted  $0.8\text{ cm}^{-1}$  to the red of the gas-phase value, and  $3.2\text{ cm}^{-1}$  to the red of the small cluster spectra. The profile is also considerably narrower compared to the small clusters,  $3.1$  vs.  $9.5\text{ cm}^{-1}$  for the (small cluster)  $\text{Ar}_x\text{C}_2\text{H}_4$  cluster absorption. At higher backing pressures, in the regime where the dissociation profiles are attenuated from their maximum values, the spectrum taken at ion mass  $\text{Ar}_7\text{C}_2\text{H}_4^+$  (Figure 8(b)) is slightly broader ( $\sim 4\text{ cm}^{-1}$ ), but shows no enhanced dissociation feature akin to that seen in the spectra of  $\text{Ar}_n\text{CH}_3\text{F}$  complexes. A closer look at the peak region using  $\text{N}_2\text{O}$  laser lines (Figure 8(c)) shows only a smoothly varying lineshape in beams of both low and moderate cluster sizes. Dissociation profiles of larger cluster ions at high pressure, for example,  $(10,1)^+$  and  $(14,1)^+$  (not shown), likewise exhibit smooth profiles fit well by a single Lorentzian.

Spectra of  $(\text{CH}_4)_n\text{C}_2\text{H}_4$  clusters (Figure 9) show only slight shifts in frequency: the maximum separation between spectra of clusters prepared over a wide range of clustering conditions is  $0.8\text{ cm}^{-1}$ , from  $950.3$  to  $951.1\text{ cm}^{-1}$  in going from small to large cluster conditions. Both the presence of large cluster ions in the mass spectrum and the depletion in the intensity of the IR dissociation spectra (Figure 9(a) and 9(b)) indicate expansion conditions are indeed accessing the moderate and large cluster regimes similar to those explored in the  $\text{Ar}_n\text{CH}_3\text{F}$  system. There is, however, no profile narrowing or indication of sub-structure, even with the increased resolution provided by the additional  $\text{N}_2\text{O}$  laser lines (Figure 9(c)). All dissociation profiles exhibit widths (FWHM') of  $8\text{-}9\text{ cm}^{-1}$ .

Photodissociation profiles of  $\text{N}_2$  clusters containing  $\text{C}_2\text{H}_4$  are compiled

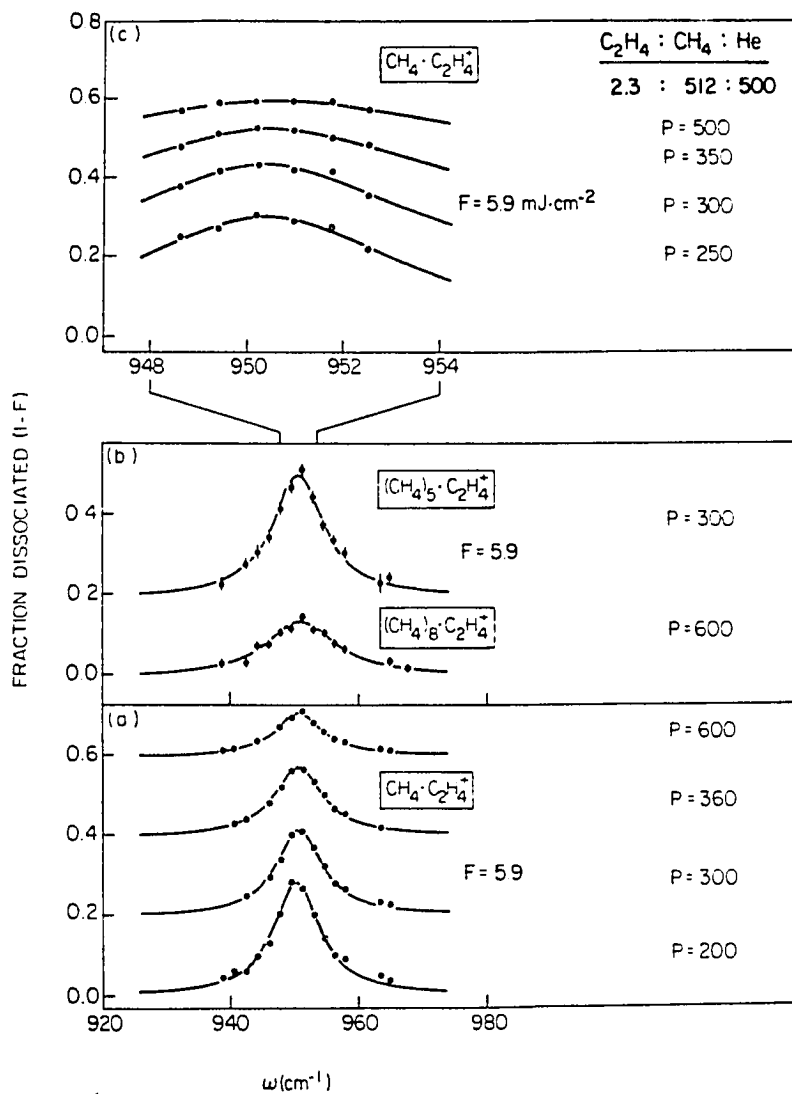


**Figure 9.** IR photodissociation spectra of (a) small and (b) large  $CH_4$  clusters containing  $C_2H_4$ . (c) At higher wavelength resolution (i.e., with additional laser lines) in the peak region, no inhomogeneity is detected.

in Figure 10. Because of the mass degeneracy between  $N_2$  and  $C_2H_4$ , care was taken to insure that the spectra are representative of clusters containing a single  $C_2H_4$  group. The concentrations of  $C_2H_4$  used were lower than in mixtures containing  $CH_3F$ . The infrared dissociation spectra are themselves distinct enough to provide differentiation, by both frequency shift and linewidth. Clusters with more than one  $C_2H_4$  unit would also be expected to show enhanced dissociation intensity; however,  $(N_2)_n \cdot C_2H_4$  clusters are mass-degenerate with  $(N_2)_n$  clusters as well, so there are non-dissociating fractions which reduce the apparent intensity of the cluster ion dissociation profiles. To avoid this problem, some spectra were obtained at the  $C_2H_4$  fragment ion mass  $C_2H_3^+$  ( $m/e$  27) where  $N_2$  does not contribute mass intensity.

The  $N_2$  molecule blue-shifts the  $C_2H_4$   $\nu_7$  absorption further than either Ar or  $CH_4$  (consistent with the  $CH_3F$  results), and also further than additional  $C_2H_4$  units. The dashed line in Figure 10 at  $952.4 \text{ cm}^{-1}$  references the center of the observed  $(C_2H_4)_{10}^+$  profile, which is practically the same for the van der Waals dimer,<sup>1a</sup>  $(C_2H_4)_2$ , as for  $(C_2H_4)_n$ , with  $n$  very large (Figure 10(c)). The center frequency of the small-cluster  $N_2C_2H_4^+$  absorption (Figure 10(a)) is similar to that of  $(C_2H_4)_n$  but at moderate cluster size ( $(N_2)_7 \cdot C_2H_4^+$ , Figure 10(b)), the profile is blue-shifted at least  $5.5 \text{ cm}^{-1}$  from the  $(C_2H_4)_n$  and  $\sim 8 \text{ cm}^{-1}$  from the gas-phase value. Further tracking of the shift is not possible due to the lack of transitions in the missing Q-branch region of the  $CO_2$  laser spectrum. The widths of the dissociation profiles in the small cluster regime (Figure 10(a), monitored on the  $C_2H_3^+$  ion) are also distinctively narrower than the  $(C_2H_4)_n$  spectra,

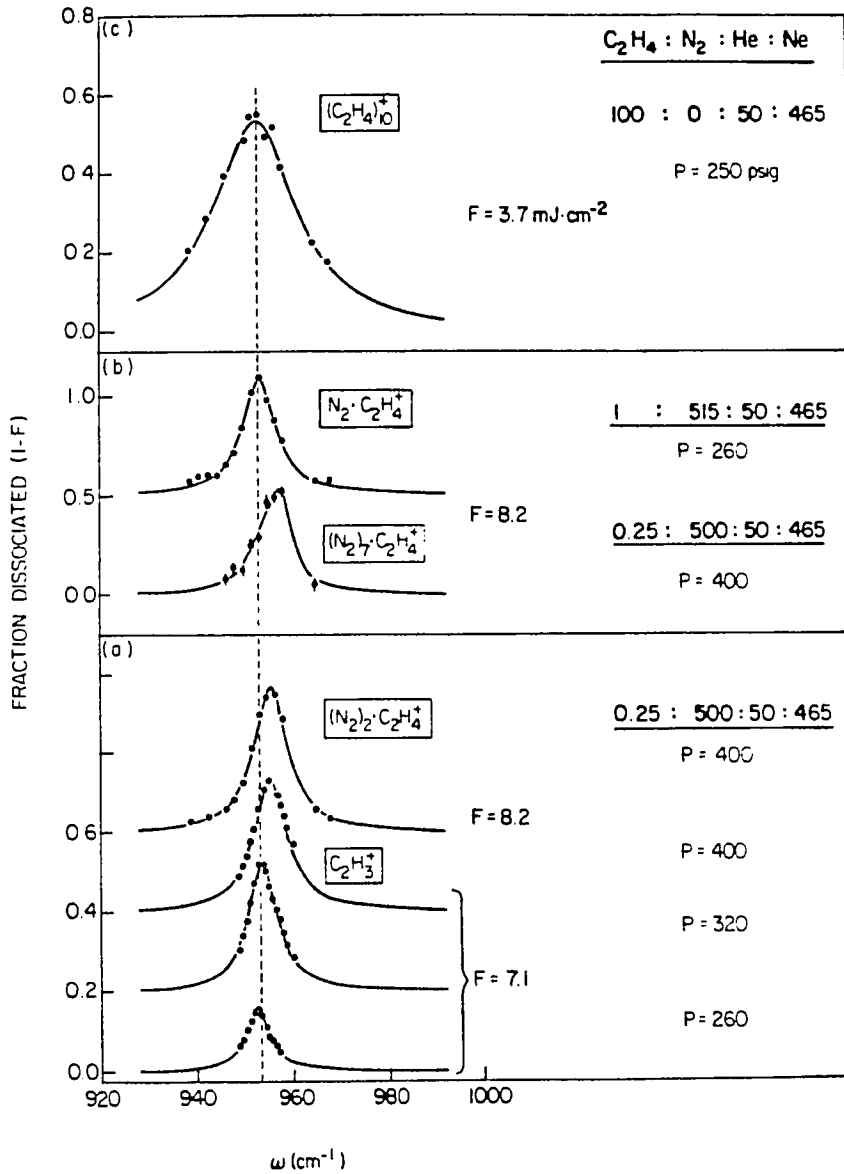


**Figure 10.**  $N_2$  clusters containing  $C_2H_4$ , analogous to the  $(N_2)_nCH_3F$  clusters exhibit large frequency shifts, seen in both (a) small and (b) large cluster ions. No evident structure was observed in any case. (c) The IR dissociation spectrum of large  $(C_2H_4)_n$  clusters distinguishes these type of clusters from the mass-degenerate  $N_2$ -containing clusters by both linewidth and absorption frequency. For reference, the peak of the large  $C_2H_4$  cluster profile is drawn through the panels.

6-8  $\text{cm}^{-1}$  vs. 17.6  $\text{cm}^{-1}$ , respectively, aiding in the assignment of these spectra as representative of  $(\text{N}_2)_n\text{C}_2\text{H}_4$  clusters. In no case, including spectra obtained at higher pressures than those shown, is a narrowed or enhanced absorption feature detected.

## 5. Discussion

The vibrational predissociation profiles of neutral rare gas and  $\text{N}_2$  clusters containing  $\text{CH}_3\text{F}$  or  $\text{C}_2\text{H}_4$  have been obtained as a function of backing pressure of the supersonic expansion. The lineshapes of the transition will be sensitive to changes in the solvation environment (frequency shift of the profile) and lifetime of the excited chromophore (linewidth), as well as the dissociation efficiency (intensity). The cluster distribution changes drastically over the range of expansion conditions employed in this study, containing monomers and dimers at the lower pressures, with clusters of over 200 atoms at the higher pressure conditions. Other characteristics of the clusters are expected to change as well and may be reflected in the dissociation spectra. For instance, temperature effects may be observed since small clusters are efficiently cooled, while large clusters are expected to be very near their boiling points. The structure of the cluster will be dependent on the temperature and may affect the lifetime or frequency shift of the excited chromophore.

In order to consider these points, the discussion section is somewhat lengthy. In the first two sub-sections, 5.1 & 5.2, we summarize relevant literature regarding cluster distributions in supersonic expansions, then the structure and properties of these clusters, respectively. Models are formulated which are consistent with both

the prior work and the IR dissociation spectra reported here. We then explore the variation of each lineshape parameter (5.3 to 5.5) and the information each yields about the cluster systems studied.

### *5.1 Cluster size and distribution*

A central issue in the analysis of the reported results is the nature of the neutral cluster distribution probed by the observed dissociation profiles: in particular, what are the neutral species that contribute to the dissociation at a given ion mass? While significant advances are presently being made in this field of research, the current level of understanding of cluster beams and electron-impact induced fragmentation does not allow unequivocal assignment of the major neutral species that correspond to a specific mass peak. There is a sufficient body of literature, though, from which one can make reasonable estimates of the range of cluster sizes that are important in these experiments.

#### *5.1.1 Cluster characterization*

The extensive study<sup>46–50</sup> of rare gas dimers and kinetics of their formation has provided characterization of the initial stages of cluster formation. Preparation of a useful concentration of dimers, such as  $\text{Ar}_2$ ,<sup>46–50</sup>  $\text{Ar}\cdot\text{C}_2\text{H}_4$ <sup>1d</sup> or  $(\text{CH}_3\text{F})_2$ ,<sup>38</sup> is both feasible and practical; larger clusters of specific size are another matter. Although it is not known whether the mechanism for initial formation of dimers is a one-step termolecular or two-step process involving stabilization of a bimolecular collision complex, it is generally agreed that larger cluster formation is a two-body process (see, however, ref. 22). Once the simple world of dimer kinetics is left behind, the evolution of specific cluster sizes is not easily followed. Only those detection schemes

capable of resolving differences between successive neutral clusters can be used to follow their growth, and most properties, such as ionization potential,<sup>35</sup> change very little. Laser-induced fluorescence is capable of resolving spectral features of chromophores in specific size clusters, but even then only for clusters of less than about 6-10 rare gas atoms.<sup>21-25</sup> Due to the generally broad linewidths observed, the infrared photodissociation spectroscopy employed here is hindered in resolving spectral features of individual clusters, except in the case of clusters containing molecules with large static dipoles<sup>1b,38</sup> (and hence large frequency shifts). IR photodissociation spectra<sup>1b</sup> as well as other techniques<sup>35,44</sup> give evidence that the onset for formation of larger clusters occurs within a narrow range of backing pressure (for a given nozzle diameter and temperature), and usually at lower pressures than cluster ion mass peak pressure dependences would indicate. With a population of dimers established,<sup>51</sup> bimolecular substitution reactions facilitate rapid higher cluster formation. It is thus not feasible to obtain a single predominant cluster size in this manner. A beam containing  $\text{Ar}_5\text{CH}_3\text{F}$ , for example, must also contain similar quantities of  $\text{Ar}_6\text{CH}_3\text{F}$  and larger clusters, unless a particularly stable molecular cluster is formed. New techniques for producing ion clusters<sup>52</sup> may soon be adapted to allow study of neutral clusters of a specific size.

Mass spectrometry is a natural choice for cluster beam analysis but the problems associated with analyzing the composition of a molecular beam containing van der Waals clusters using electron-impact ionization are well-known.<sup>36</sup> Fragmentation of larger clusters contributes to the intensity of lower mass peaks, as well as decreasing the apparent intensity of larger clusters. A graphic illustration

of problems associated with analyzing a neutral cluster beam with electron-impact ionization is given by the observation that the peak in the apparent distribution of  $(\text{N}_2\text{O})_n$  clusters decreases from  $n = 1000$  to 400 when the electron ionization energy is increased from 35 to 300 eV, respectively.<sup>53</sup>

The problem of cluster fragmentation is receiving theoretical attention as a result of controversy over the observation of “magic numbers” in rare gas cluster distributions (see Section 5.2). Ionization of homogeneous neutral clusters (e.g.,  $\text{Ar}_n$ ) is proposed to proceed by formation of a vibrationally-excited dimer ion ( $\text{Ar}_{n-2}\cdot\text{Ar}_2^{+*}$ ) which relaxes by evaporation.<sup>54</sup> Photodestruction of  $\text{CO}_2^+$  can be understood in terms of absorption by a dimer ion within the cluster; i.e., the cluster can be described as  $(\text{CO}_2)_{n-2}\cdot(\text{CO}_2)_2^+$ . Also, as discussed in Section 3.1,  $(\text{CH}_3\text{F})_n$  clusters which form  $(\text{CH}_3\text{F})_{n-2}\cdot(\text{CH}_3\text{F})\text{H}^+$  upon ionization are consistent with this model. Molecular dynamics simulations find that within 200 psec of ionization, an  $\text{Ar}_{13}$  cluster will evaporate to form  $\text{Ar}_5^+$ , and an  $\text{Ar}_7$  cluster reduces to  $\text{Ar}_2^+$ .<sup>37c</sup> It thus seems surprising that we have observed a significant difference between the dissociation spectra from nearly equal cluster ion masses (Figure 5). The explanation for this effect may have to do with the stabilization of the cluster by the  $\text{CH}_3\text{F}$  dipole (*vide infra*).

Consideration of cluster evaporation and the dimer ion formation model may account for the observation of “negative” dissociation peaks only in the  $\text{Kr}/\text{CH}_3\text{F}$  system (fig 6). The  $\text{Ar}_2^+$  ion is 1.5 eV more stable than a single ionized  $\text{Ar}^+$  ion, so formation of the dimer within the cluster after initial Ar atom ionization can release enough energy to boil off  $\sim 22$  atoms. The heat of vaporization ( $\Delta H_v$ ) for

Kr is higher ( $\Delta H_v = 2.16$  (Kr) *vs.* 1.55 kcal/mole (Ar)<sup>55</sup>) and the difference in IP between Kr and Kr<sub>2</sub> is smaller (1.13 eV<sup>35</sup>) so only half as many atoms (~11) need to be lost from the cluster upon ionization, so ionization is “gentler” in the case of the Kr clusters. More importantly,  $\Delta H_v$  is just less than the photon energy, meaning that at most two Kr atoms must be lost from the large Kr<sub>n</sub>CH<sub>3</sub>F clusters so the Kr clusters will have a higher probability to remain in the molecular beam following vibrational excitation.

There has only recently been work to quantify the branching ratios of cluster ions produced from electron bombardment of large neutral clusters.<sup>37,45</sup> Using a crossed molecular beam scattering apparatus and 100 eV ionization electron energy, Buck and Meyer<sup>37</sup> found that 70% of Ar<sub>2</sub> fragmented to Ar<sup>+</sup>, while Ar<sub>3</sub> fragmented 38% to Ar<sub>2</sub><sup>+</sup> and 62% to Ar<sup>+</sup>. No Ar<sub>3</sub><sup>+</sup> was produced directly from ionization of Ar<sub>3</sub>. Contributions to the observed Ar<sub>3</sub><sup>+</sup> signal are from clusters Ar<sub>5</sub> and higher, with the maximum near Ar<sub>10</sub>.<sup>37c</sup> These results are at least qualitatively modelled by the ionization dynamics model discussed above.<sup>37</sup> In addition, there was little change in fragmentation branching over the 30 - 100 eV electron energy range. Using the same beam scattering techniques, Worsnop *et al.*<sup>45</sup> likewise explored the fragmentation properties of large rare gas clusters, finding that fragmentation of heterogeneous species was less severe than for the homogeneous Ar<sub>n</sub> cluster. For example, the intensity of Ar<sub>n-1</sub>HI<sup>+</sup> or Ar<sub>n-1</sub>Xe<sup>+</sup> clusters is 10<sup>2</sup> times smaller than that of ArXe<sup>+</sup> or ArHI<sup>+</sup>, respectively, while the Ar<sub>7</sub><sup>+</sup> intensity is 10<sup>5</sup> times smaller than Ar<sub>2</sub><sup>+</sup>, for the same expansion conditions. The Ar clusters containing a more polarizable moiety fragment to a lesser extent than pure Ar clusters. In

our cluster beams, we observe intensity ratios between  $\text{Ar}_n^+$  and  $\text{Ar}_{n-1}\text{CH}_3\text{F}^+$  cluster masses of  $\sim 10 : 1$ , while the  $\text{Ar} : \text{CH}_3\text{F}$  concentration in the mixture is  $1000 : 1$ . Assuming similar ionization cross sections, this observation is consistent with Ar clusters containing  $\text{CH}_3\text{F}$  undergoing substantially less fragmentation than  $\text{Ar}_n$  clusters. We presume this effect will similarly be operative in the other cluster systems studied.

### 5.1.2 Mean Cluster Size and Distribution

Insight into cluster size distributions present in this study is provided by the extensive work of Hagen *et al.*,<sup>56,57</sup> who mapped out equivalent clustering conditions for various nozzle types and expansion conditions, as well as demonstrating the principle of corresponding jets for beams of different gases. Using expansions which generate clusters whose mean size is in the range  $10^2$  to  $10^4$  atoms, the source pressure and temperature, nozzle shape and diameter, seed gas and concentration were all systematically varied and a set of scaling laws relating the parameters was determined. Analysis of the pulsed beams was carried out by means of electron-impact ionization and a retarding-field analyzer. The relationship between the beams was gauged by a single parameter, the “characteristic cluster size,”  $(N/Z)^*$ , the mean of the ionized cluster beam distribution.<sup>56,57</sup> Limited but useful information regarding the relationship between  $(N/Z)^*$  and  $\bar{N}$ , the mean of the *neutral* cluster distribution was obtained by monitoring the change of  $(N/Z)^*$  with ionization electron energy.<sup>56</sup>

The shape of the distribution for neither the neutral nor the ion cluster beams was elucidated in the Hagen study;<sup>56,57</sup> however, Soler *et al.*<sup>58</sup> recently obtained

the distribution of a highly-clustered  $\text{CO}_2$  expansion at 35 eV ionization energy. With increasing stagnation pressure, the distribution exhibited the transition from the low-pressure region of successive monomer addition, which exhibits an exponentially decreasing cluster distribution, to that of coagulation of large clusters, which shows a log-normal distribution (i.e., the intensity *vs.* the logarithm of the cluster size is Gaussian). The mean of the cluster distribution agrees qualitatively with the  $(N/Z)^*$  value measured previously,<sup>57</sup> which suggests that for suitably large values of  $(N/Z)^*$  ( $(N/Z)^* > 10$ ), the cluster distribution is log-normal peaked roughly at  $(N/Z)^*$ . The difference between  $(N/Z)^*$  and  $\bar{N}$  depends upon fragmentation and ionization efficiency of the cluster sizes. Both works<sup>56,58</sup> observed very little shift of the cluster distribution for electron energies below 40 eV. Mindful of the distribution results and using Hagena’s parametrization of molecular beam clustering, we can scale our expansion conditions to obtain a measure of the neutral clustering present in the beams employed in our IR photodissociation experiments.

### 5.1.3 *Extrapolation of mean cluster size data, $(N/Z)^*$*

In Figure 11, we present the data from Figure 2, Ref. [57a], for room temperature expansions of pure Ar and pure  $\text{N}_2$  scaled to the nozzle conditions used in our experiments and extrapolated to the pressure range in which infrared spectra were taken. In addition, estimates for clustering of the Ne and Kr mixtures used in this study are plotted (see the Appendix for details of the scaling and estimates). The electron ionization energy was 65 eV in our work, compared to  $\sim 125$  eV for the data from Ref. [57].<sup>59</sup> Our expansion conditions result in beams

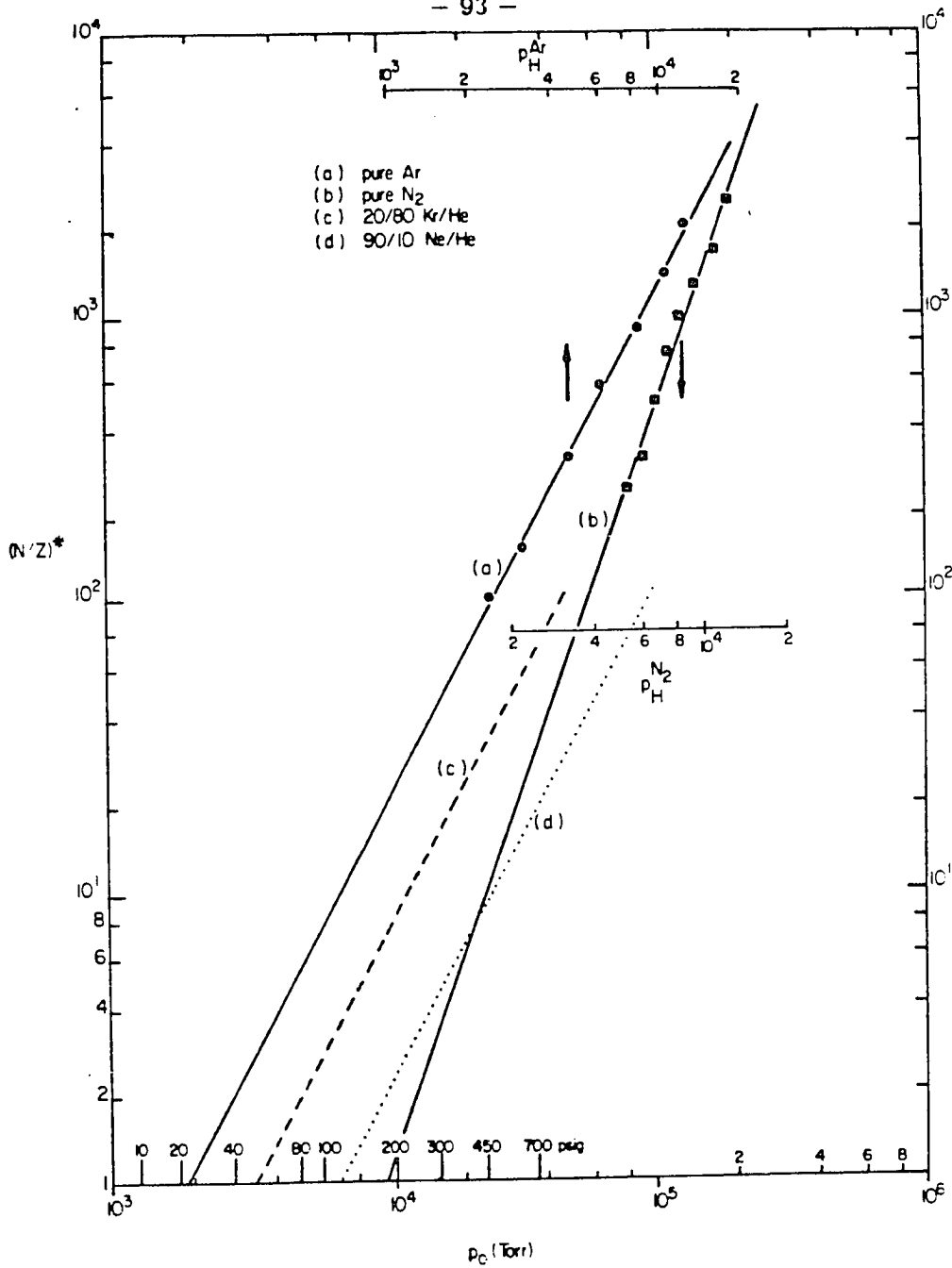
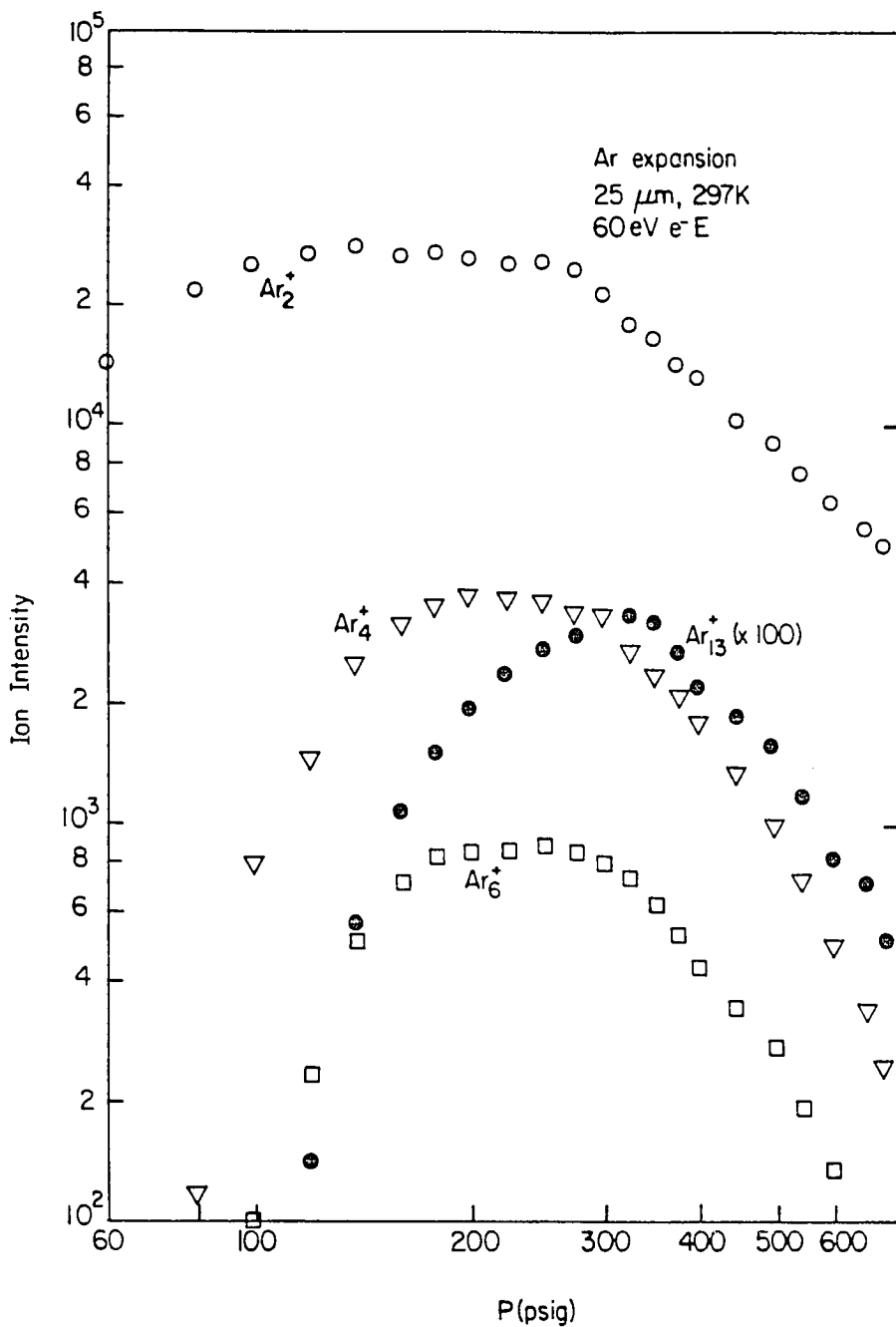


Figure 11. Extrapolation of the "characteristic cluster size" data of Hagena<sup>57</sup> to expansion conditions used in this study (along the abscissa).  $(N/Z)^*$  is roughly the mean of the cluster ion distribution found under the expansion conditions given in the figure ( $p_H^i$ ) and in Ref. [57] for: (a) pure Ar and ; (b) pure N<sub>2</sub> beams.  $(N/Z)^*$  estimates for the (c) Kr and (d) Ne mixtures used in this work are also given. (The appendix contains details of the scaling.) The electron energy is  $\sim 125-150$  eV.

with clusters substantially smaller than in Hagena's work<sup>57</sup> – the expansions that produce the largest clusters in our work ( $(N/Z)^* \sim 200$ ) overlap the most gentle conditions in Refs. [56,57]. The extrapolation will become invalid at small values of  $(N/Z)^*$ . Due to the dilution in our expansions ( $\chi_{\text{solute}} \sim .005$ ), we have ignored any perturbation of the  $\text{CH}_3\text{F}$  or  $\text{C}_2\text{H}_4$  on the clustering, but dimer depletion effects have been observed for seed gas concentrations on the order of a few percent.<sup>60</sup>

The cluster distributions we observe appear quite different from those predicted by the extrapolation in Figure 11. In Figure 3, for example, the intensity of mass peaks falls sharply with increasing mass whereas a distribution peaked at  $\text{Ar}_{70}^+$  is predicted. Figure 12 shows the observed pressure dependence for a pure Ar beam expanded through a 25  $\mu\text{m}$  room temperature nozzle. The intensity of small cluster ion masses ( $\text{Ar}_2^+$ ,  $\text{Ar}_4^+$  and  $\text{Ar}_6^+$  in Figure 12) “turns over,” or begins to *decrease* with increasing backing pressure, indicating a substantial fraction of the total mass is being directed into moderate size clusters. This observation is in agreement with the  $(N/Z)^*$  extrapolation which predicts mean cluster sizes of 8-15 over the 100-140 psig pressure range. (Note that this is the same pressure range in which the enhanced IR dissociation feature observed for Ar clusters containing  $\text{CH}_3\text{F}$  is first observed.) Moderate size cluster ions (e.g.,  $\text{Ar}_{13}^+$ , Figure 12) are seen to increase in intensity in this pressure region before they, too, show the intensity turnover at slightly higher backing pressure. The relative intensities still show, however, a rapid decrease from dimer to higher clusters –  $\text{Ar}_{13}^+$ , for instance, is always an order of magnitude less intense than  $\text{Ar}_2^+$  over the observed pressure range. This discrepancy can be understood partly by simple mass considerations (i.e., 6



**Figure 12.** Pressure dependence of mass spectral intensities of cluster ions from a pure Ar expansion. Small cluster ions decrease in intensity as mass is shifted to larger clusters, such as  $\text{Ar}_{13}^+$ . Mass weighting and discrimination against large clusters must be invoked to account for the apparently low intensity of these larger cluster ion peaks when compared with the predicted distributions. See the text for further discussion.

Ar<sub>2</sub> dimers are consumed to make a single Ar<sub>12</sub> cluster), and by the fact that the quadrupole mass filter and the particle detector both discriminate against higher masses. The result is that for a broad distribution which is basically flat over the small mass range accessible with the quadrupole filter, the intensity will appear to exponentially decrease. We conclude that, at least for the Ar case, the (N/Z)\* extrapolation is in qualitative agreement with the cluster ion intensities observed in this study.

#### 5.1.4 Cluster size estimates and IR dissociation spectra

The (N/Z)\* values from the extrapolations in Figure 11 are included in Figures 4, 6 and 7 to indicate the predicted neutral cluster distributions probed by the infrared photodissociation spectra of CH<sub>3</sub>F<sup>+</sup>. For the Ar cluster spectra, the enhanced feature at P(30) is present over the pressure range expected to produce neutral cluster distributions peaked at 7 to 44 atoms (Figure 4, P=100–300 psig), which roughly corresponds to the addition of a second shell of Ar atoms. While the same domain of clustering is also accessed by the Kr, Ne and N<sub>2</sub> expansions according to the data of Figure 11, only the Kr and N<sub>2</sub> cluster spectra exhibit obvious inhomogeneity analogous to that seen in the Ar cluster spectra, and, even then, over different extrapolated ranges of (N/Z)\* than in the Ar case. Narrow features in Kr cluster spectra (Figure 6) occur for (N/Z)\* > 40, but the similarity of conditions for the  $\nu_3$  frequency progression for CH<sub>3</sub>F in Ar and Kr clusters indicates that the (N/Z)\* estimates for Kr<sub>n</sub> clusters are too high. The particularly narrow CH<sub>3</sub>F<sup>+</sup> profiles observed in N<sub>2</sub> cluster expansions occur at pressures where (N/Z)\* is relatively low ((N/Z)\* ~ 5). Again, the extrapolation may be in error in

this cluster regime due to the severity of the logarithmic  $(N/Z)^*$  plot: if the two low-cluster data points<sup>56a</sup> are omitted, a line similar to Figure 11(c) can fit the data and raise the estimate to  $(N/Z)^* \sim 20$ , more in agreement with the cluster distribution estimate which corresponds to the narrow spectral feature in the Ar cluster case. For Ne cluster beams, the transition through the second shell regime is estimated to occur between 200 and 500 psig, yet the spectra show little change from the low-cluster spectrum shown in Figure 3(a), and the absorption frequency is far removed from the matrix limit. For the Ar, Kr and  $N_2/CH_3F$  systems, we observe correlation between the cluster size regime at which the second solvation shell is filling and the narrow features observed in the dissociation spectra.

If the dissociation spectra probe mainly details of the rare gas or  $N_2$  clusters, then spectra obtained with  $C_2H_4$  as the infrared-absorbing chromophore should exhibit features similar to the  $CH_3F$ -containing cluster spectra. For Ar,  $CH_4$  and  $N_2$  clusters containing  $C_2H_4$ , no enhanced dissociation or narrow features are observed (Figures 8-10), even though similar  $(N/Z)^*$  regimes are accessed. Assuming the solute concentrations used in this study do not drastically alter the neutral cluster distributions,<sup>60</sup> these results suggest that the cluster dissociation spectra are sensitive to properties or dynamics, other than cluster size, which are quite different in the  $CH_3F$ - and  $C_2H_4$ -containing clusters.

## 5.2 Cluster Properties: Structure and Temperature

At the higher end of the cluster-size spectrum lies the study of homogeneous nucleation phenomenon<sup>61</sup> where coagulation, condensation and evaporation are more descriptively correct in summarizing growth kinetics. Between this higher

cluster limit and dimer formation lie interesting questions concerning the structure, temperature and subsequent growth of these microcrystallites. The stable packing configuration of small clusters does not transform into the bulk crystal structure, so the transition between these two regimes may be observed. The temperature of the clusters will naturally play a vital role in this transition, and the nature of the growth will, to a large degree, determine the temperature of the clusters. The properties of large clusters is certainly a wide-ranging topic with many active experimental and theoretical areas of study.

Experimentally observed maxima in cluster distributions of rare gases<sup>45,53,62,63</sup> as well as SF<sub>6</sub> and C<sub>2</sub>F<sub>4</sub>Cl<sub>2</sub> clusters<sup>62b</sup> have been interpreted as verification of “magic numbers” of crystal packing – the closed Mackay icosahedral shells.<sup>64</sup> In the Mackay single-icosahedral packing scheme, the  $n^{th}$  shell contains  $(10n^2+2)$  spherical atoms or molecules (e.g., Ar or CH<sub>4</sub>). The first three shells contain, respectively, 12, 42 and 92 spheres around a central sphere, totaling 13, 55 and 147 spheres. These structures are theoretically expected to be the low-energy configurations for the moderate size clusters,<sup>65,66</sup> but transition to a crystallographic structure must take place as bulk properties are approached. Recent experimental<sup>67,68</sup> and theoretical<sup>54</sup> studies show that the maxima in the observed cluster distributions are indicative of the stability of particular *ion* clusters, due to evaporation of the excited ionized cluster, and not neutral clusters as was originally believed.<sup>62,63</sup> The secondary evaporation causes the neutral distribution to evolve into one exhibiting “magic number” peaks indicative of stable ion clusters, as is demonstrated by a recent study of (H<sub>2</sub>O)<sub>n</sub><sup>+</sup> cluster distributions.<sup>67</sup> There is, however, evidence that structure exists

even in the small *neutral* clusters. Electron diffraction studies of neutral Ar cluster beams<sup>69a</sup> show the presence of crystalline structure in large clusters ( $\overline{N} > 800$ ), as would be expected, but also in *smaller clusters*, diffraction rings are observed which are consistent with polyicosahedral ( $\overline{N} < 20$ ) and multilayer icosahedral ( $20 < \overline{N} < 800$ ) models. While the matter of magic numbers in *neutral* rare gas cluster distributions is lacking proof, there is good evidence for structural stability induced by attractive sites (neutral<sup>45</sup> or ionic<sup>60</sup>) within the cluster.

Evidence for solid structure in large clusters is seen in the  $(\text{N}_2\text{O})_n$  cluster dissociation work of Miller *et al.*<sup>70</sup> Using bolometer detection of the molecular beam, dissociation occurs after absorption of IR light near the  $(\nu_1 + \nu_3)$  combination band of  $\text{N}_2\text{O}$ . The frequency shift of the dissociation spectra for the cluster distribution approaches that of the solid crystal. Semiclassical calculations reproduce features of the spectra, including the observation that moderate-size clusters (55 molecules in the calculation) exhibit solid-like absorptions.

Supersonic expansions provide a unique way to reduce the relative translational and internal temperatures of molecules to  $< 10$  K as well as to provide an isolated environment which can support formation of weak van der Waals bonds. Cooling occurs by relaxation of internal and transverse translational modes by collisions with the carrier gas. Massive clustering will provide large amounts of energy to the clusters from the heat of condensation. Collisions occur more frequently between clusters in this expansion regime, and there are few collisions between clusters and monomers to carry off excess energy and provide cooling. After passage through the Mach disk, evaporation of atoms is the only mechanism for clusters to release

energy and stabilize.<sup>71</sup> Thus, while van der Waals molecules and small clusters are characterized by low internal temperatures, the temperature of larger clusters should rise to near the sublimation or boiling point of the cluster. Consistent with these expectations, large Ar clusters are found to have a constant internal temperature ( $38 \pm 4$  K)<sup>69</sup>, virtually identical to calculated melting transition temperatures.<sup>71b,72,73</sup> The translational temperature of small  $(\text{H}_2\text{O})_n$  clusters increases throughout the range  $5 \leq n \leq 25$ , while large clusters ( $n > 25$ ) are isothermal.<sup>71a,73</sup> Other fragmentation reactions have also been interpreted as indicative of differences in cluster temperature.<sup>34a,74</sup>

### 5.3 Cluster model

The presence of inhomogeneity in the dissociation profiles of clusters in the second-shell regime suggests a model for structure and ionization dynamics. First, the presence of substantial inhomogeneity in the profiles of  $\text{CH}_3\text{F}$ -containing species is absent in spectra of  $\text{C}_2\text{H}_4$ -containing clusters; second, the profiles of specific ion mass clusters in the Ar/ $\text{CH}_3\text{F}$  system are in some cases substantially different. From the first point, consider the two cluster structures in Figure 13 which can be distinguished for  $\text{A}_n\text{X}$  ( $\text{X} = \text{CH}_3\text{F}$  or  $\text{C}_2\text{H}_4$ ) with  $n \geq 12$ . The first structure has the probe molecule X central in the cluster (Figure 13(a)) while the probe occupies a surface site in the second (Figure 13(b)). For otherwise indistinguishable atoms, the surface-site cluster (b) is favored by probability when the cluster is small (less than  $\sim 300$  atoms). Since  $\text{CH}_3\text{F}$ -containing clusters exhibit distinct dissociation features which seem indicative of clusters specifically in the second-shell regime while clusters of similar size with  $\text{C}_2\text{H}_4$  as the probe molecule do not, this suggests that  $\text{CH}_3\text{F}$ ,

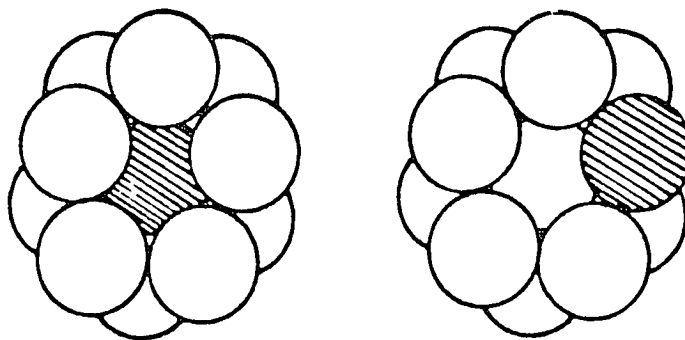


**Figure 13.** Schematic drawings of structural isomers of  $A_nX$  clusters, with  $n \geq 12$ . These depict: (a) the cluster with solvated probe molecule, X (hatched circle), and (b) the surface-site probe cluster.

which has a strong permanent dipole while  $C_2H_4$  does not, tends to form a much higher percentage of solvated probe clusters. It may be correct to think of  $CH_3F$  as a nucleation site since the concentrations employed in this study should not perturb the clustering.<sup>60</sup> The two cluster isomers should thus be distinguishable in both the IR frequency shift and dissociation linewidth (see Sections 5.4 and 5.6). The data are consistent with, although not conclusive of, the proposed model.

While the  $Ar/CH_3F$  profiles in Figure 4 together with the  $(N/Z)^*$  extrapolation from Figure 11 indicate a separate, narrow absorption is associated with the second shell region of cluster formation, the mass-specific spectra presented in Figure 5 suggest that a much smaller range of cluster size may be responsible for the narrow feature. There is a substantial difference in the dissociation profiles taken at the  $Ar_9CH_3F^+$  and  $Ar_{13}CH_3F^+$  ion masses: the enhanced P(30) feature is present in the smaller cluster ion spectrum, but absent in the spectrum for the larger one. The neutral cluster distribution is expected to be fairly broad in this regime. The ionization considerations discussed in Section 5.1.1 suggest the neutral clusters that fragment to these ions may be  $\leq 20$  atoms larger than the observed ion mass. The rare gas atom shells close to the solvated dipole would be more strongly bound, and rare gas clusters containing a polarizable moiety exhibit less of a tendency to fragment upon ionization.<sup>45</sup> Cluster ions smaller than the closed shell  $Ar_{12}CH_3F^+$  cluster may thus be the termination point for the cascade of evaporative relaxation from a large number of ionized second-shell clusters, and thus exhibit the strong P(30) absorption feature (e.g., as does  $Ar_9CH_3F^+$ ) while larger clusters (e.g., those that fragment to yield  $Ar_{13}CH_3F^+$  – perhaps in the third shell regime) do not. It is

still quite intriguing that the fragmentation should be so specific that the enhanced P(30) feature should be totally absent from the  $\text{Ar}_{13}\text{CH}_3\text{F}^+$  spectrum.

The  $\text{Ar}_n\text{CH}_3\text{F}^+$ ,  $n \geq 12$ , profiles appear indicative of a class of larger clusters which only show the broad surface-type IR dissociation profile. The loss of P(30) intensity could be due to frequency shifts or because of additional narrowing to where it does not efficiently interact with the laser (see section 5.3 and 5.5 for further discussion of this point). The specific cluster ion effect suggests another possibility: the matrix-site cluster fragments to a lesser degree to masses than can be detected within our range, leaving only contribution from the clusters with surface-site probe. Since we observe a fractional attenuation, an increase in intensity of the surface-site should be observed in this scenario unless a “quenching” effect, such as accommodation of the vibrational energy by a bulk crystal or liquid.

#### 5.4 Frequency shifts

The non-degenerate  $\nu_3$  vibration of  $\text{CH}_3\text{F}$ , the lowest energy normal mode of the molecule, is primarily a C–F stretch occurring at  $1048.6\text{ cm}^{-1}$  in the gas phase.<sup>16,40</sup> Complexation with rare gas atoms or  $\text{N}_2$  molecules results in a red-shift of the center absorption frequency,  $\omega_0$ . In the small cluster limit, this is consistent with a structure for the  $\text{CH}_3\text{F}$ -containing van der Waals molecules analogous to that of the determined structure of the  $\text{Ar}\cdot\text{CH}_3\text{Cl}$  molecule, in which case the Ar atom is located  $3.8\text{ \AA}$  above the C–Cl bond axis.<sup>75</sup> The frequency shift of  $\nu_3$  for  $\text{A}\cdot\text{CH}_3\text{F}$  ( $\text{A} = \text{Ne}, \text{Ar}, \text{Kr}, \text{N}_2$ ) complexes with A located above the C–F axis would be expected to exhibit a red-shift due to the dispersive interaction between the  $\text{CH}_3\text{F}$  and the polarizable A moiety. This is in contrast to the blue shift of the  $\nu_7$  vibration

in C<sub>2</sub>H<sub>4</sub>-containing complexes which is due to repulsive interaction between the C<sub>2</sub>H<sub>4</sub> partner (e.g., A = Ar, HF, HCl), located above the C<sub>2</sub>H<sub>4</sub> plane, and the out-of-plane  $\nu_7$  motion of the H atoms.<sup>1b</sup> The magnitude of the CH<sub>3</sub>F  $\nu_3$  frequency shift due to nearby N<sub>2</sub> molecules seems quite large considering the polarizability, and may be an interesting area for further experimental and theoretical studies.

The absorption maxima of matrix isolated CH<sub>3</sub>F and large clusters containing CH<sub>3</sub>F are presented in Table 2. The  $\nu_3$  red-shift for CH<sub>3</sub>F-containing clusters (A<sub>n</sub>CH<sub>3</sub>F) increases as the number of inert partners increases, reaching the matrix limit and even *exceeding* it in the case of N<sub>2</sub> complexes. The Ar/CH<sub>3</sub>F system shows the best correspondence to the matrix isolation spectra. At 9 K, the  $\nu_3$  absorption spectra of CH<sub>3</sub>F in an Ar matrix shows two features: the primary absorption is an intense and narrow ( $\sim 0.2$  cm<sup>-1</sup>) peak at 1040.0 cm<sup>-1</sup> and a secondary broad ( $\sim 1.0$  cm<sup>-1</sup>) feature at  $\sim 1038.5$  is assigned to CH<sub>3</sub>F trapped at a surface or defect site.<sup>14-16</sup> In the gas phase, the dissociative  $\nu_3$ -absorption of Ar<sub>n</sub>CH<sub>3</sub>F clusters approaches 1039.9 cm<sup>-1</sup> as a limit, even after presumably only a single shell of Ar atoms surrounds the CH<sub>3</sub>F molecule. With larger clusters (second shell regime) the intense absorption at 1037.4 cm<sup>-1</sup> best represents CH<sub>3</sub>F totally encapsulated by Ar atoms while the broader absorption to the blue must be indicative of clusters containing CH<sub>3</sub>F at a surface site. The solvated cluster absorption frequency, being further red-shifted than in the matrix, indicates the Ar atoms have not assumed a solid lattice structure (see below). In larger clusters, the intense dissociation peak disappears, which we believe is due to either further frequency shifting or formation of large clusters that are stable to IR dissociation.

**Table 2**

(a)  $\text{CH}_3\text{F}$   $\nu_3$  Absorption Frequency in Matrices<sup>a,b,c</sup>

	Ne	Ar	Kr	N <sub>2</sub>
matrix abs.	1041.5 <sup>†</sup> 1043.5 <sup>‡</sup>	1040.1 1039.9*	1035.8 1035.6*	1033.2
surface abs.		1035-1039	1033-1036	

(b)  $\text{CH}_3\text{F}$   $\nu_3$  Dissociation Frequency in Large Clusters<sup>d</sup>

solvated $\text{CH}_3\text{F}$	(1047)	1037.4	1033.5-1035.5	1025-1027
surface $\text{CH}_3\text{F}$	—	1039.5-1040.3	1037-1041	1023-1025

<sup>a</sup> All frequencies in  $\text{cm}^{-1}$ .

<sup>b</sup> Gas-phase value  $\omega_g = 1048.6 \text{ cm}^{-1}$ , from Refs. [40,41].

<sup>c</sup> Data from Refs. [14-17].

<sup>d</sup> This work.

<sup>†</sup> fcc lattice.

<sup>‡</sup> hcp lattice.

\* unstable monomer site.

For the Kr/CH<sub>3</sub>F system, the cluster dissociation profiles observed at the CH<sub>3</sub>F<sup>+</sup> ion mass shift only to approximately the same limit as in the Ar/CH<sub>3</sub>F system (1040 cm<sup>-1</sup>). The “negative” dissociation features, however, are additionally shifted and close to the Kr matrix-isolated  $\nu_3$  absorption. (N<sub>2</sub>)<sub>n</sub>CH<sub>3</sub>F clusters, similar to the Ar cluster case, exhibit intense and narrow dissociation features but the frequency of the N<sub>2</sub>-solvated CH<sub>3</sub>F absorption is shifted *well beyond* the matrix value, 10 cm<sup>-1</sup>, at the largest cluster size. This behavior parallels the trend of the matrix-isolated absorption peak with increasing temperature – the peak reversibly decreases in intensity and shifts to lower frequency – but the magnitude of the gas phase shift is much larger, 10 cm<sup>-1</sup> as compared to 1.5 cm<sup>-1</sup> in the matrix.<sup>15</sup>

Absorption maxima for matrix isolated C<sub>2</sub>H<sub>4</sub> and large C<sub>2</sub>H<sub>4</sub>-containing clusters is presented in Table 2. The C<sub>2</sub>H<sub>4</sub>-containing clusters studied are interesting in that the  $\nu_7$  vibration in the van der Waals complexes is blue-shifted from the gas phase absorption, while C<sub>2</sub>H<sub>4</sub> isolated in a matrix is red-shifted. Although an extensive high-resolution study akin to those performed on CH<sub>3</sub>F<sup>12–17</sup> has not been done with C<sub>2</sub>H<sub>4</sub>, the data available show a red shift of 1.6 cm<sup>-1</sup> in Ar and 2.2 cm<sup>-1</sup> in N<sub>2</sub>.<sup>76</sup> The Ar<sub>n</sub>C<sub>2</sub>H<sub>4</sub> clusters are blue-shifted  $\sim 1.5$  cm<sup>-1</sup> at low  $n$ , then red-shift toward the matrix value as the cluster size increases, achieving only half of the full matrix red-shift ( $-1.6$  cm<sup>-1</sup>) in the spectra of the largest clusters. On the other hand, (N<sub>2</sub>)<sub>n</sub>C<sub>2</sub>H<sub>4</sub> clusters exhibit a blue-shift which increases as the cluster size is increased. The largest N<sub>2</sub> clusters have shifted the C<sub>2</sub>H<sub>4</sub>  $\nu_7$  vibration at least  $+8$  cm<sup>-1</sup> for the gas-phase and  $+10$  cm<sup>-1</sup> from the matrix value. CH<sub>4</sub> clusters similarly induce an increasing blue-shift over the observed range of

**Table 3**

*C<sub>2</sub>H<sub>4</sub>  $\nu_7$  Absorption Frequency in Matrices and Large Clusters<sup>a,b,c</sup>*

	Ar	N <sub>2</sub>	CH <sub>4</sub>
matrix abs.	947.4	946.8	—
cluster abs.	948.2	~957	951.1

<sup>a</sup> All frequencies in cm<sup>-1</sup>.

<sup>b</sup> Matrix data from Ref. [76]; cluster data from this work.

<sup>c</sup> Gas-phase value  $\omega_g = 949$  cm<sup>-1</sup>, from Ref. [1].

cluster size (from  $1.3 \text{ cm}^{-1}$ , for small  $n$ , to  $2.1 \text{ cm}^{-1}$  for large  $n$ ).

The frequency shift observed for the  $\text{CH}_3\text{F}$  and  $\text{C}_2\text{H}_4$  chromophores between the van der Waals cluster and the gas phase values increases as the cluster size increases, for all cases studied except  $\text{Ar}/\text{C}_2\text{H}_4$ . This indicates the interaction between the excited vibration and the inert partner (rare gas,  $\text{N}_2$  or  $\text{CH}_4$ ) which dominates at the small cluster limit continues to dominate through the large cluster regime. This point is obviated by the absorption maximum shift in the  $(\text{N}_2)_n\text{C}_2\text{H}_4$  case, in which the direction of the shift (blue) is contrary to that in the matrix (red); by comparison, the shift of the  $(\text{N}_2)_n\text{CH}_3\text{F}$  clusters past the matrix limit can be understood to be a consequence of the matrix and van der Waals shift being in the same direction. Reversal of the frequency shift with large clusters is required for both  $\text{C}_2\text{H}_4$  and  $\text{CH}_3\text{F}$  in larger  $\text{N}_2$  clusters, and suggests that a plausible theory for the disappearance of the narrow P(30) absorption in the  $\text{Ar}/\text{CH}_3\text{F}$  system is a frequency shift back toward the matrix value, and between adjacent laser lines. Also, the frequency shifts for the  $\text{CH}_3\text{F}$  systems show a much closer correspondence to the matrix values, corroborating our view of  $\text{CH}_3\text{F}$  as a nucleation site in these clusters. The large magnitude of the frequency shifts in the case of  $\text{N}_2$  is paralleled in the matrix,<sup>76,77</sup> and is thought to be due to interactions of higher order than dipole-induced dipole which are active in a distorted matrix. The large shifts in the  $\text{N}_2$  cluster cases may then be an indication that a solid lattice has not been achieved in these clusters, while the similarity in shifts between the matrix values and  $\text{C}_2\text{H}_4$ - and  $\text{CH}_3\text{F}$ -containing Ar clusters suggests an ordered solid may be formed in these cases.

### 5.5 Dissociation Intensities

As seen from the two-level-with-decay lineshape equation, Eq. (1), the integrated dissociation intensity is determined by the prefactor  $\omega_R^2 t \tau$ . The absorption strength of the complex,  $\langle \mu \rangle^2$ , due basically to the  $\text{CH}_3\text{F}$  or  $\text{C}_2\text{H}_4$  moiety, is proportional to the Rabi frequency,  $\omega_R$ . From Eq. (3),

$$\omega_R^2 t = \frac{(\vec{\mu} \cdot \vec{E})^2 t}{\hbar^2} = \frac{8\pi \langle \mu \rangle^2 (S \cdot t)}{3\hbar^2 c}, \quad (5)$$

where  $(S \cdot t)$  is the laser fluence. As was shown in Eq. (4), the dissociation intensity for all complexes of the form  $\text{A}_n\text{CH}_3\text{F}$ , at constant irradiation time, will be the same (or, likewise, all  $\text{A}_n\text{C}_2\text{H}_4$  clusters), since they contain only a single chromophore. This will be true for dissociation profiles taken at  $\text{Ar}_n\text{CH}_3\text{F}^+$  parent peaks (at all pressures) as well as for  $\text{CH}_3\text{F}^+$  profiles at high pressure conditions under which all observed ion signal results from cluster fragmentation. When large fractions of the observed  $\text{CH}_3\text{F}^+$  or  $\text{C}_2\text{H}_4^+$  intensity are attenuated by the  $\text{CO}_2$  laser at high backing pressure, virtually all the mass spectral intensity at that mass must be a result of fragmented clusters. At mild expansion conditions, the absorption intensity information from the  $\text{CH}_3\text{F}^+$  or  $\text{C}_2\text{H}_4^+$  peaks is lost, as the dissociation intensity is also a function of the clustering and fragmentation percentages. The presence of unresolved inhomogeneity at higher backing pressures prevents quantitative analysis of the lineshape progression using the dissociation intensity.

In the  $\text{Ar}/\text{CH}_3\text{F}$  system, dissociation intensity of van der Waals molecules in the small cluster regime is consistent with the absorption strength of free  $\text{CH}_3\text{F}$ .<sup>41</sup>

The appearance of the strong P(30) absorption at higher pressures, when clusters filling the second solvation shell are produced, does not initially appear to carry significant absorption intensity: due to the increased percentage of clustered m/e 34, both the P(30) feature *and* the broad surface-cluster absorption increase in intensity (Figure 4, P=100 psig). At still higher pressure (P=200 psig), the P(30) feature appears to grow at the expense of the broad feature, before both eventually diminish in intensity (P=300 psig). That both the CH<sub>3</sub>F<sup>+</sup> profile and those of specific ion cluster masses decrease in apparent integrated intensity indicates a change in fragmentation efficiency is *not* responsible for the observed loss in the m/e 34 dissociation profile. Mechanisms that would result in such an intensity loss are now examined, but because it is possible to “hide” all the dissociation intensity in a narrow absorption between laser lines, it is not possible to unequivocally distinguish between these possibilities from the intensity information alone.

At very large cluster size, the  $\nu_3$  vibrational excitation might remain localized in the CH<sub>3</sub>F moiety, being decoupled from the matrix environment; this lifetime lengthening is manifested as a narrower absorption line which might then fall between the CO<sub>2</sub> laser line grid, resulting in an apparent loss of dissociation intensity. A significant fraction or all of the absorption intensity may be shifted into the inaccessible frequency gap between CO<sub>2</sub> laser lines, becoming “lost” as far as the observed profile is concerned. This possibility is consistent with the frequency shift behavior discussed in section 5.4. A narrow absorption line could account for all integrated absorption intensity without being fluence broadened<sup>1b</sup> to where the profile would be wider than adjacent CO<sub>2</sub> laser lines.

An alternate and intuitive situation is the onset of a quenching mechanism, such as loss of vibrational energy to create vibrations (phonons) in the cluster (solid) which would decrease the dissociation probability. This can be seen from the mixed case two-level-plus-decay lineshape formula,<sup>18</sup>

$$F_m(\omega, t) = \exp \left[ -\omega_R^2 \gamma_T^{-1} t \cdot \frac{\gamma_T^2}{4(\omega - \omega_0)^2 + \gamma_T^2} \cdot \frac{\gamma_D}{\gamma_Q + \gamma_D} \right], \quad (6)$$

which is derived from a two-level-with-decay model that also includes phenomenological quenching and dephasing mechanisms which have rates  $\gamma_Q$  and  $\gamma_{PD}$ , respectively. The intensity of the dissociation is attenuated by the factor  $\gamma_D/(\gamma_Q + \gamma_D)$ , and the sum of all rate constants,  $\gamma_T = \gamma_D + \gamma_Q + 2\gamma_{PD}$ , determines the width. An intensity decrease in the Ar/CH<sub>3</sub>F cluster system profiles following the appearance of the second-shell peak may indicate that two complete shells of Ar atoms approximates a matrix in so far as inhibiting dissociation of the large clusters by providing a bath for the vibrational energy of the excited CH<sub>3</sub>F. Note, however, that Eq. 6 also dictates additional line broadening would result from a quenching mechanism which becomes competitive with a fixed dissociation rate. Since the lines in general are observed to *narrow*, and from the frequency shift information already discussed, we believe the P(30) absorption feature lies between the available laser lines. Certainly as the cluster becomes large enough to accommodate 1000 cm<sup>-1</sup> of energy by increasing its internal temperature without boiling off atoms, the dissociation would be quenched. The fluorescence lifetime of anthracene in Ar clusters decreases as the cluster size increases, indicative of a non-radiative pathway

( $k_{nr} \sim 10^8 \text{ s}^{-1}$ ) which quenches the fluorescence.<sup>22,23</sup> A scenario which provides an increase in the quenching rate requires a concomitant decrease in the predissociative rate to account for the lineshape narrowing observed in the  $\text{CH}_3\text{F}$  and  $\text{C}_2\text{H}_4$  cluster spectra. A study using a continuously tunable source in this spectral region would verify this hypothesis.

In the  $\text{Kr}/\text{CH}_3\text{F}$  system, loss of intensity in the main absorption band is accompanied by appearance of the “negative” dissociation features further to the red. This is an *instrumental* loss of dissociation intensity, as the spectrometer can not detect dissociation from fragments which scatter with small kinetic energy such that they remain within the solid angle of the molecular beam. This highlights the fact that the experiments reported here are dissociation spectra, and that other absorptions may be present that do not lead to observable dissociation. That attenuation of dissociation intensity is common to all cluster systems studied, but no additional broadening indicative of a quenching mechanism is observed, may indicate this instrumental effect may be responsible.

### 5.6 Linewidths and vibrational lifetimes

Dynamical information on the decay process out of the vibrationally excited van der Waals molecules can be extracted from the *homogeneous* width of the dissociation profiles.<sup>1c,18</sup> For instance, the lineshape of ethylene dimer is virtually homogeneous with a width that corresponds to a vibrational predissociation lifetime of 0.33 psec.<sup>1a</sup> In the case of  $\text{C}_2\text{H}_4$ -complexes with HF and HCl, the linewidth contained significant inhomogeneous broadening due to rotational structure.<sup>1c</sup>

In the ethylene experiments, as well as the small cluster limit spectra reported

here, the large fraction of clusters dissociated and the correlation of dissociation intensity with integrated absorption coefficients for the vibration is consistent with the lineshapes being predominantly homogeneously broadened. Inhomogeneous contributions to the width under these conditions are mainly due to rotational congestion, spectral congestion (different lineshapes for individual cluster sizes or isomers), and dephasing of the vibration. When inhomogeneously broadened, the linewidth yields a lower bound for the lifetime of the excited vibration. Given the discrete nature of the CO<sub>2</sub> laser transitions, very narrow linewidths will not be resolvable. A strict upper bound of 0.5 msec is set by the cluster flight time from nozzle to detector.

The initial purpose of this set of experiments was to observe the transition from generally short vibrational lifetimes, psec to nsec, for small van der Waals dimers, to longer-lived excitations,  $\mu$ sec to msec, for matrix-isolated species. One then expects a trend of decreasing homogeneous linewidth as a function of cluster size, and to the degree the CO<sub>2</sub> laser line spacing allows, this trend is indeed observed.

For small Ar<sub>n</sub>CH<sub>3</sub>F clusters, the linewidths are fairly constant with increasing cluster size, 4-6 cm<sup>-1</sup>, which nominally correspond to vibrational lifetimes,  $\tau$ , of 0.7-1.0 psec. Although strictly only a lower limit, the rotational contribution for small Ar<sub>n</sub>CH<sub>3</sub>F ( $n < 8-10$ ) clusters will be quite small since the moments of inertia rapidly increase as the cluster size increases. While the profile for the van der Waals dimer is likely to be rotationally structured (see the discussion of Figure 3), the fact that the spectra of the small clusters all exhibit a similar width also suggests that lifetime broadening is a major contributor to the linewidth. Large clusters, on

the other hand, may attain internal temperatures near their boiling points, so even though the rotational spacing is small, the rotational profiles can still be appreciable ( $\sim 1 \text{ cm}^{-1}$ ) due to the population of many initial states.

For the  $\text{Ar}_n\text{CH}_3\text{F}$  solvated-probe feature, the enhanced absorption at laser line P(30), the lower limit on the lifetime of the excited  $\nu_3$  vibration is  $\tau_{lower} = 3 \text{ psec}$  (from the spacing between the two adjacent laser lines,  $3.9 \text{ cm}^{-1}$ ), a factor of three longer than in the smaller clusters or for  $\text{CH}_3\text{F}$  in a surface-site. For the largest  $\text{Ar}_n\text{CH}_3\text{F}$  clusters in which the narrow absorption is thought to be between laser lines, the limit increases to  $\tau_{lower} > 6 \text{ psec}$ . A reasonable upper limit is derived from the assumption that because of the large fraction of clusters dissociated, the absorption linewidth must be at least on the order of the laser bandwidth, 150 MHz, which determines  $\tau_{upper}$  is  $\sim 1 \text{ nsec}$ . The calculated rovibrational spectrum of hindered  $\text{CH}_3\text{F}$  in an octahedral environment exhibits a relatively broad linewidth ( $\leq 0.25 \text{ cm}^{-1}$ ).<sup>17</sup> Arguments similar to those made for the Ar case can be applied to the Kr and  $\text{N}_2/\text{CH}_3\text{F}$  systems, where small  $\text{A}_n\text{CH}_3\text{F}$  clusters show widths similar to the Ar/ $\text{CH}_3\text{F}$  analog. Vibrational lifetimes increase in the moderate cluster regime since both systems exhibit inhomogeneous structure made up of narrower spectra components. Dephasing might be expected to become important as the temperature of the cluster increases, but only in one case (the  $\text{N}_2/\text{CH}_3\text{F}$  system) is a slight broadening with increasing cluster size observed.

The spectra of  $\text{C}_2\text{H}_4$ -containing clusters exhibit profile narrowing only in the Ar case. As noted previously,  $\text{C}_2\text{H}_4$  may not function as a nucleation center so, at the cluster size distributions studied,  $\text{C}_2\text{H}_4$  occupies shorter-lived surface or

partially-solvated sites by probability.  $C_2H_4$ -containing clusters with  $> 300$  atoms would be expected to exhibit narrowing and inhomogeneity similar to that observed in the  $CH_3F$ -probed systems as internal sites become more favored.

## 6. Conclusions

The dissociation spectra of large clusters of rare gas,  $N_2$  and  $CH_4$  clusters containing either  $CH_3F$  or  $C_2H_4$  have been reported. The spectra are sensitive to cluster size and the environment of the chromophore. Some aspects of the rare gas clusters (i.e., the frequency shift of the  $CH_3F$  vibration) appear matrix-like after only a single shell of atoms surrounds the  $CH_3F$  but further shifting of the profile as the clusters grow in size suggest a liquid-like environment may be more appropriate to describe the state of the clusters. The relaxation rate of  $\nu_3$   $CH_3F$  is within a factor of two of the value in a matrix.<sup>78</sup> The intense, narrow absorption feature is identified as due to  $CH_3F$  solvated in an Ar cluster with size in the second-shell regime,  $12 \leq n \leq 50$  and evidence for similar features in the Kr and  $N_2/CH_3F$  systems are observed. Vibrational excitation of the  $CH_3F$  upon ionization may result in the observed qualitative difference between spectra taken at slightly different cluster ion masses. The  $C_2H_4$  moiety does not exhibit the same propensity for attaining the solvated configuration, as judged by the lack of inhomogeneous structure in the dissociation profiles. The cluster-induced shifts of the  $C_2H_4$   $\nu_7$  vibration indicate small cluster-type interactions continue to be of importance in the clusters of moderate size (1-2 solvation shells).

Extension of these experiments to other spectral regions where continuously-tunable laser sources are available (e.g., 3.0-4.5  $\mu m$ ) would verify the models

proposed in this paper and enable direct measurement of a wider range of vibrational lifetimes. The use of optothermal detection (i.e., bolometers<sup>2,29,70</sup>) would allow the identification of absorption features which do not lead to dissociation and which may account for the decrease in spectral intensities observed in our studies. Also, the recent technique of Gough *et al.*<sup>29b</sup> for preparing clusters with surface-site chromophores may further clarify the matter of surface *vs.* matrix sites, if indeed polar molecules such as CH<sub>3</sub>F will not cause substantial rearrangement of the cluster. Information regarding specific cluster sizes may be possible with the development of neutralization of selected ion clusters.<sup>52</sup> The infrared technique applied here shows promise as a useful probe to characterize these clusters.

#### **Acknowledgements**

The authors would like to thank M.P. Casassa and C.M. Western for assistance with initial experiments, and Prof J.L. Beauchamp for helpful discussion and use of the CO<sub>2</sub> laser. This work was supported by the Division of Chemical Sciences, Office of Basic Energy Science, U.S. Department of Energy.

## Appendix

The details of the scaling used to generate the plots of Figure 11 are the following:

### (a) Pure vapor

(i) **Ar:** Considering our nozzle to be of the sonic type, the 490  $\mu\text{m}$  nozzle used to obtain the data in Figure 2d [46a] was scaled to 25  $\mu\text{m}$  using  $pd^q = \text{constant}$ ,  $q = 0.8$  for Ar [46a,b], resulting in  $p_o = 10.8 \cdot p_H^{\text{Ar}}$ .

(ii) **N<sub>2</sub>:** The 140  $\mu\text{m}$  conical nozzle used in obtaining the data in Figure 2b [46a] was calculated to be equivalent to a 1.39 mm sonic nozzle with the use of eq. (15) [46c] with  $\alpha = 5^\circ$  and  $K_{15} = 0.866$ . Scaling to the 25  $\mu\text{m}$  nozzle used in our experiments was accomplished using  $pd^q = \text{constant}$ ,  $q = 0.68$ ;  $q$  is determined using eq. (8) [46b] and  $r = 2.99$  determined from  $p_o \propto T_o^r$  and the data of Figure 3 [46a]. The resultant expression is  $p_o = 15.4 \cdot p_H^{\text{N}_2}$ .

### (b) Mixtures

Both Ne and Kr mixtures were scaled using the law of corresponding jets [46a], taking the isentrope, eq. (5) [46a], with reduced variables, eq. (15) [46a] to give:

$$\left( \frac{P_{Ar}}{P_i} \right) \cdot \left[ \frac{(\epsilon/\sigma^3)_i}{(\epsilon/\sigma^3)_{Ar}} \right] = \left( \frac{T_{Ar}}{T_i} \right)^{2.5} \left( \frac{\epsilon_i}{\epsilon_{Ar}} \right)^{2.5} \quad (A1)$$

For all expansions at room temperature,  $T_{Ar} = T_i$  and  $\epsilon$  and  $\sigma$  are taken from [72]. Finally, scaling by  $p_i = P_i(\sigma_i/\sigma_{Ar})^{0.8}$  gives  $p_{Ne} = 8.51 \cdot p_{Ar}$  and  $p_{Kr} = 0.54 \cdot p_{Ar}$ . Further scaling of the mixtures involves considering the reduced mole fraction (0.9 for Ne/He and 0.2 for Kr/He) and the effective diameter,  $d^* = d/\sigma_{eff}$ , of the

mixture:

- (iii) **90/10 Ne/He:** The estimation of the 90/10 Ne/He curve took into account only the mole fraction of Ne in the mixture, resulting in  $p_{Ne} = 9.5 \cdot p_{Ar}$ .
- (iv) **20/80 Kr/He:** Note from Figure 5 [46c] that seeding a vapor in a gas reduces the mole fraction necessary to achieve the same degree of clustering as in the pure vapor. We thus (arbitrarily) choose a factor of 2 in the Kr case so that our estimate for a 10/90 Kr/He mixture is simply that calculated by assuming the mole fraction of a 20/80 Kr/He mixture. The final expression is:  $p_{Kr} = 2.7 \cdot p_{Ar}$ .

## References

1. (a) M.P. Casassa, D.S. Bomse and K.C. Janda, *J. Chem. Phys.* **74** (1981) 5044;  
(b) M.P. Casassa, C.M. Western, F.G. Celii, D.E. Brinza and K.C. Janda, *J. Chem. Phys.* **79** (1983) 3227;  
(c) C.M. Western, M.P. Casassa and K.C. Janda, *J. Chem. Phys.* **80** (1984) 4781;  
(d) M.P. Casassa, C.M. Western and K.C. Janda, *J. Chem. Phys.* **81** (1984) 4950.
2. (a) G. Fischer, R.E. Miller, and R.O. Watts, *Chem. Phys.* **80** (1983) 147;  
(b) T.E. Gough, R.E. Miller and G. Scoles, *J. Phys. Chem.* **85** (1981) 4041;  
(c) T.E. Gough, R.E. Miller and G. Scoles, *J. Chem. Phys.* **69** (1978) 1588.
3. (a) M. Snels, J. Geraedts, S. Stolte and J. Reuss, *Chem. Phys.* **94** (1985) 1;  
(b) J. Geraedts, S. Setiadi, S. Stolte and J. Reuss, *Chem. Phys. Lett.* **78** (1981) 277;  
(c) J. Geraedts, M. Waayer, S. Stolte and J. Reuss, *Faraday Disc. Chem. Soc.* **73** (1982) 375.
4. (a) M.A. Hoffbauer, K. Liu, C.F. Giese and W.R. Gentry, *J. Chem. Phys.* **78** (1983) 5567, and references therein;  
(b) M.A. Hoffbauer, C.F. Giese and W.R. Gentry, *J. Chem. Phys.* **79** (1983) 192.
5. W.-L. Liu, K. Kolenbrander and J.M. Lisy, *Chem. Phys. Lett.* **112** (1984) 585.
6. D.S. Bomse, J.B. Cross and J.J. Valentini, *J. Chem. Phys.* **78** (1983) 7175.
7. D.H. Levy, *Ann. Rev. Phys. Chem.* **31** (1980) 197, and references therein.
8. D.E. Brinza, B.A. Swartz, C.M. Western and K.C. Janda, *J. Chem. Phys.* **79** (1983) 1541.

9. M.F. Vernon, D.J. Krajnovich, H.S. Kwok, J.M. Lisy, Y.R. Shen and Y.T. Lee, *J. Chem. Phys.* **77** (1982) 47;  
M.F. Vernon, J.M. Lisy, H.S. Kwok, D.J. Krajnovich, A. Tramer, Y.R. Shen and Y.T. Lee, *J. Phys. Chem.* **85** (1981) 3327;  
J.M. Lisy, A. Tramer, M.F. Vernon and Y.T. Lee, *J. Chem. Phys.* **75** (1981) 4733.
10. N. Halberstadt and B. Soep, *Chem. Phys. Lett.* **87** (1982) 109;  
C. Jouvét and B. Soep, *J. Chem. Phys.* **75** (1981) 1661.
11. For reviews, see: H. Dubost, *Ber. Bunsenges. Phys. Chem.* **82** (1978) 112;  
J. T. Yardley, in *Introduction to Molecular Energy Transfer*, (Academic Press, New York, 1980).  
V.E. Bondybey and L.E. Brus, *Adv. Chem. Phys.* **41** (1980) 269.
12. V.A. Apkarian and E. Weitz, *Chem. Phys. Lett.* **76** (1980) 68;  
W. Franisch, V.A. Apkarian and E. Weitz, *Chem. Phys. Lett.* **85** (1982) 505.
13. (a) L. Abouaf-Marguin and B. Gauthier-Roy, *Chem. Phys.* **51** (1980) 213;  
(b) B. Gauthier-Roy, L. Abouaf-Marguin and F. Legay, *Chem. Phys.* **46** (1980) 31;  
(c) L. Abouaf-Marguin, B. Gauthier-Roy and F. Legay, *Chem. Phys.* **23** (1977) 443.
14. L. Young and C.B. Moore, *J. Chem. Phys.* **76** (1982) 5869.
15. B. Gauthier-Roy, C. Almichel, A. Lecuyer and L. Abouaf-Marguin, *J. Mol. Spectrosc.* **88** (1981) 72.
16. L.H. Jones and B.I. Swanson, *J. Chem. Phys.* **76** (1982) 1634.
17. V.A. Apkarian and E. Weitz, *J. Chem. Phys.* **76** (1982) 5796.

18. M.P. Casassa, F.G. Celii and K.C. Janda, *J. Chem. Phys.* **76** (1982) 5295.
19. G.T. Fraser, D.D. Nelson, Jr., A. Charo and W. Klemperer, *J. Chem. Phys.* **82** (1985) 2535.
20. A.S. Pine and W.J. Lafferty, *J. Chem. Phys.* **78** (1983) 2154.  
G.D. Hayman, J. Hodge, B.J. Howard, J.S. Muentner and T.R. Dyke, *Chem. Phys. Lett.* submitted for publication.
21. S. Leutwyler, *J. Chem. Phys.* **81** (1984) 5480.
22. (a) A. Amirav, U. Even and J. Jortner, *J. Phys. Chem.* **86** (1982) 3345;  
(b) A. Amirav, U. Even and J. Jortner, *J. Chem. Phys.* **75** (1981) 2489;  
(c) A. Amirav, U. Even and J. Jortner, *Chem. Phys. Lett.* **72** (1980) 16;  
(d) A. Amirav and J. Jortner, *Chem. Phys.* **85** (1984) 19.
23. T.R. Hayes, W.E. Henke, H.L. Selzle and E.W. Schlag, *Chem. Phys. Lett.* **77** (1981) 19;  
W.E. Henke, W. Yu, H.L. Selzle E.W. Schlag, D. Wutz and S.H. Lin, *Chem. Phys.* **92** (1985) 187.
24. P.M. Felker and A.H. Zewail, *Chem. Phys. Lett.* **94** (1983) 454.
25. P.D. Dao, S. Morgan and A.W. Castleman, Jr., *Chem. Phys. Lett.* **111** (1984) 38;  
P.D. Dao, S. Morgan and A.W. Castleman, Jr., *Chem. Phys. Lett.* **113** (1985) 219.
26. K. Rebane and P. Saari, *J. Lumin.* **12/13** (1976) 23.
27. F. König, P. Oesterlin and R.L. Byer, *Chem. Phys. Lett.* **88** (1982) 477.
28. J.O. Geraedts, Ph.D. Thesis, University of Nijmegen, 1983;

- P. Melinon, J.-M. Zellweger, J.-M. Philippoz, R. Monot and H. van der Bergh in *9<sup>th</sup> Symposium on Molecular Beams*, Freiburg (June, 1983), p.8.
29. T.E. Gough, D.G. Knight and G. Scoles, *Chem. Phys. Lett.* **97** (1983) 155;  
(b) T.E. Gough, M. Mengel, P.A. Rowntree, G. Scoles, preprint.
  30. R.J. Blint, T.B. McMahon and J.L. Beauchamp, *J. Am. Chem. Soc.* **96** (1974) 1269.
  31. A.J. Stace, *Chem. Phys. Lett.* **113** (1985) 355.
  32. J.H.D. Eland, R. Frey, A. Kuestler, H. Schulte and R. Brehm, *Int. J. Mass Spectr. Ion Phys.* **22** (1976) 155.
  33. C.R. Brundle, M.R. Robin and H. Basch, *J. Chem. Phys.* **53** (1970) 2196.
  34. (a) A.J. Stace, *Chem. Phys. Lett.* **99** (1983) 470;  
(b) A.J. Stace, *J. Phys. Chem.* **87** (1983) 2286;  
(c) A.J. Stace, *J. Am. Chem. Soc.* **107** (1985) 755;  
(d) A.J. Stace, preprint.
  35. P.M. Dehmer and S.T. Pratt, *J. Chem. Phys.* **76** (1982) 843.
  36. (a) T.E. Gough and R.E. Miller, *Chem. Phys. Lett.* **87** (1982) 280;  
(b) W.R. Gentry, *Rev. Sci. Instrum.* **53** (1982) 1492;  
(c) H.L. Tien, S.B. Ryali, P.J. Gak and J.B. Fenn, *Chem. Phys. Lett.* **93** (1982) 213;  
(d) N. Lee and J.B. Fenn, *Rev. Sci. Instrum.* **49** (1978) 1269.
  37. (a) U. Buck and H. Meyer, in *9<sup>th</sup> Symposium on Molecular Beams*, Freiburg (June, 1983), p.113;  
(b) U. Buck and H. Meyer, *Phys. Rev. Lett.* **52** (1984) 109.  
(c) U. Buck, personal communication.

38. F.G. Celi and K.C. Janda, to be published.
39. M.D. Marshall and J.S. Muentner, *J. Mol. Spectrosc.* **83** (1980) 279.
40. G. Herzberg, in *Infrared and Raman Spectroscopy*, (Van Nostrand Reinhold Co., New York, 1945);  
W.L. Smith and I.M. Mills, *J. Mol. Spectrosc.* **11** (1963) 11.
41. S. Kondo and S. Saeki, *J. Chem. Phys.* **76** (1982) 809.
42. J.O. Hirschfelder, C.F. Curtiss and R.B. Bird, in *Molecular Theory of Gases and Liquids*, (Wiley, New York, 1954).
43. A. Dalgarno and A.E. Kingston, *Proc. Phys. Soc. London* **78** (1961) 607.
44. S.J. Hair and K.C. Janda, unpublished results.
45. D.R. Worsnop, S.J. Buelow and D.R. Herschbach, *J. Phys. Chem.* **88** (1984) 4506.
46. T.A. Milne and F.T. Greene, *J. Chem. Phys.* **47** (1967) 4095;  
T.A. Milne A.E. Vandergrift and F.T. Greene, *J. Chem. Phys.* **52** (1970) 1552.
47. D. Golomb, R.E. Good and R.F. Brown, *J. Chem. Phys.* **52** (1970) 1545;  
D. Golomb, R.E. Good, A.B. Bailey, M.R. Busby and R. Dawborn, *J. Chem. Phys.* **57** (1972) 3845.
48. A. van Deursen, A. van Lumig and J. Reuss, *Int. J. Mass Spectr. Ion Phys.* **18** (1975) 129;  
A. van Deursen and J. Reuss, *Int. J. Mass Spectr. Ion Phys.* **23** (1977) 109;  
A. van Deursen and J. Reuss, *Int. J. Mass Spectr. Ion Phys.* **24** (1977) 199.
49. E.L. Knuth, *J. Chem. Phys.* **66** (1977) 843.
50. H.F. Godfried and I.F. Silvera, *Phys. Rev.* **B27** (1983) 3008, 3019.

51. J.J. Breen, K. Kilgore, K. Stephan, R. Hoffmann-Sievert, B.D. Kay, R.G. Keesee, T.D. Märk and A.W. Castleman, Jr., *Chem. Phys.* **91** (1984) 305.
52. M.A. Johnson, M.L. Alexander and W.C. Lineburger, *Chem. Phys. Lett.* **112** (1984) 285.
53. K. Sattler, in *9<sup>th</sup> Symposium on Molecular Beams*, Freiburg (June, 1983), p.21.
54. J.M. Soler, J.J. Sáenz, N. García and O. Echt, *Chem. Phys. Lett.* **109** (1984) 71;  
J.J. Sáenz, J.M. Soler and N. García, *Chem. Phys. Lett.* **114** (1985) 15.
56. H. Falter, O.F. Hagen, W. Henkes and H.V. Wedel, *Int. J. Mass Spectr. Ion Phys.* **4** (1975) 145.
57. (a) O.F. Hagen and W. Obert, *J. Chem. Phys.* **56** (1972) 1793;  
(b) O.F. Hagen, *Phys. Fluids* **17** (1974) 894;  
(c) O.F. Hagen, *Surf. Sci.* **101** (1981) 106.
58. J.M. Soler, N. García, O. Echt, K. Sattler and E. Recknagel, *Phys. Rev. Lett.* **49** (1982) 1857.
59. Estimated from the  $(N/Z)^*$  plot, fig. 2 of ref. 46(a), and the electron energy dependance in fig. 7 of ref. 45.
60. M. Yamashita, T. Sano, S. Kotake and J.B. Fenn, *J. Chem. Phys.* **75** (1981) 5355.
61. F.F. Abraham, in *Homogeneous Nucleation Theory*, Supplement I, Advances in Theoretical Chem. (Academic, New York, 1974).
62. (a) O. Echt, K. Sattler and E. Recknagel, *Phys. Rev. Lett.* **47** (1981) 1121;  
(b) O. Echt, A. Reyes Flotte, M. Knapp, K. Sattler and E. Recknagel, *Ber. Bunsenges. Phys. Chem.* **86** (1982) 860;

63. A. Ding and J. Hesslich, *Chem. Phys. Lett.* **94** (1983) 54.
64. A.L. Mackay, *Acta Cryst.* **15** (1962) 916.
65. E. Polymeropoulos and J. Brickman, *Chem. Phys. Lett.* **96** (1983) 273;  
I. Oksuz, *Surf. Sci.* **122** (1982) L585;  
T. Halicioglu and P.J. White, *Surf. Sci.* **106** (1983) 45.
66. M.R. Hoare, P. Pal and P.P. Wegener, *J. Colloid Interface Sci.* **75** (1980) 126;  
M.R. Hoare, *Adv. Chem. Phys.* **40** (1979) 49;  
G.L. Griffin and R.P. Andres, *J. Chem. Phys.* **71** (1979) 2552.
67. I.A. Harris, R.S. Kidwell and J.A. Northly, *Phys. Rev. Lett.* **53** (1984) 2390.
68. O. Echt, D. Kreisle, M. Knapp and E. Recknagel, *Chem. Phys. Lett.* **108** (1984) 401.
69. J. Farges, M.F. De Feraudy, B. Raoult and G. Torchet, *Surf. Sci.* **106** (1981) 95.
70. R.E. Miller, R.O. Watts and A. Ding, *Chem. Phys.* **83** (1984) 155.
71. (a) J.M. Soler and N. García, *Phys. Rev.A* **27** (1983) 3300;  
(b) J.M. Soler and N. García, *Phys. Rev.A* **27** (1983) 3307.
72. C.L. Briant and J.J. Burton, *J. Chem. Phys.* **60** (1975) 2045;  
J. Ross and R.P. Andres, *Surf. Sci.* **106** (1981) 11.
73. D. Dreyfuss and H.Y. Wachman, *J. Chem. Phys.* **76** (1982) 2031.
74. K. Stephan and T.D. Märk, *Chem. Phys. Lett.* **90** (1982) 51.
75. R.L. DeLeon and J.S. Muentzer, *J. Chem. Phys.* **75** (1981) 1113.
76. L. Andrews, G.L. Johnson and B.J. Kendall, *J. Chem. Phys.* **76** (1982) 5767.

77. S. Schlick and O. Schnepp, *J. Chem. Phys.* **41** (1964) 463.
78. S.R.J. Brueck, T.F. Deutsch and R.M. Osgood, Jr., *Chem. Phys. Lett.* **51** (1977) 339.

*CHAPTER 4*

**PHOTODESORPTION LINESHAPES**

**OF**

**WEAKLY BOUND MOLECULES**

## PHOTODESORPTION OF WEAKLY BOUND MOLECULES\*

Francis G. Celii, Michael P. Casassa† and Kenneth C. Janda‡

*Arthur Amos Noyes Laboratory of Chemical Physics,  
California Institute of Technology, Pasadena, California 91125, USA*

Received 21 March 1983; accepted for publication 12 December 1983

Published: *Surf. Sci.*, **141** (1984) 169-190.

### ABSTRACT

A recently reported lineshape function which specifically applies to the problem of one-photon photodesorption is used to perform model calculations. The expected efficiency and timescale for such a process is obtained. Molecules physisorbed on solid surfaces may desorb when vibrational energy from laser excitation leaks into the surface-adsorbate bond. Using phenomenological rate constants for desorption, quenching and dephasing mechanisms, a simple expression for surface coverage as a function of laser and molecular parameters is obtained. Analogy is drawn to the vibrational predissociation of van der Waals molecules, to which this model has been previously applied. Sample experimental systems are examined and calculations are made to explore the feasibility and range of the photodesorption technique. Observable effects are calculated, even for low-power laser parameters and fast quenching rates. Conversely, the lineshape formula provides a method for extracting desorption and quenching rates from experimental data. Calculations are also presented for mass spectrometric desorbate detection. The dynamic range

---

\* Contribution No. 6814

† National Science Foundation Predoctoral Fellow.

‡ Alfred P. Sloan Foundation Fellow

of the mass spectrometer allows for a larger variation in molecular parameters which generate observable signal. The results of experimental attempts to observe one-photon photodesorption are summarized. Extension of the model to other systems is discussed.

## 1. Introduction

The investigation of photon-induced processes at solid surfaces has been conducted for many years. The development of laser technology has sparked new interest in utilizing this type of interaction in practical schemes such as chemical etching,<sup>1,2</sup> deposition of conducting films,<sup>3,4</sup> and stimulation of catalytic reactions.<sup>5,6</sup> Indeed, there are many demonstrations of reaction processes that have been initiated<sup>5,7–14,69</sup> or altered<sup>6,15,16</sup> using laser irradiation upon or near solid surfaces.

Another light-stimulated surface process which is the specific topic of this paper is photodesorption. We present a phenomenological model to describe the process of desorption induced by laser irradiation of adsorbate vibrations. The lineshape formula which solves the model problem that is presented contains parameters which are systematically varied to investigate the feasibility of photodesorption. Our conclusion is that photodesorption should be observable under fairly mild conditions (i.e., with low-power cw lasers), when the adsorbate bondstrength is less than the energy of the absorbed photon. Although little detail about the specific mechanisms are directly obtained, the wavelength dependence of the desorption carries information about the rate of dynamic processes occurring at the surface. The rates can be extracted by applying the phenomenological model.

## 2. Overview

The term photodesorption has appeared in the literature for over 20 years but it has been used to describe a variety of phenomena. We are interested in the specific case of a weakly bound (physisorbed) adsorbate which is vibrationally

excited by a photon source, and which then desorbs as a result of the excitation energy coupling to break the bond to the surface. (To eliminate confusion, this will be our definition of photodesorption throughout the paper.) Other processes, which have also been termed photodesorption but occur by mechanisms of a different nature are: laser desorption by thermal heating of the substrate<sup>17–22</sup>; desorption stimulated by electron-hole pairs produced as a result of bandgap irradiation of semiconductor surfaces or metal oxide layers<sup>23–26</sup>; or photon-stimulated desorption (PSD)<sup>27–29</sup> of ions from metal surfaces caused by an Auger process initiated by incident high energy irradiation. An extensive survey of laser-surface interactions has recently been published by Chuang.<sup>30</sup>

Since the direct photodesorption process involves adsorbate vibrations, isotope effects may be observed and this technique has thus been discussed in terms of isotope separation schemes.<sup>31,32</sup> Karlov *et al.*<sup>33</sup> observed selective evaporation of <sup>11</sup>BCl<sub>3</sub> from a solid isotope mixture using a single CO<sub>2</sub> laser wavelength operated at low power (1 W/cm<sup>2</sup>). Suslick<sup>34</sup> has reported isotopic enrichment of deuterium by irradiation of the H<sub>2</sub> vibration in condensed H<sub>2</sub>/HD/D<sub>2</sub> mixtures, but an attempt to reproduce the results was unsuccessful – McConnell<sup>35</sup> indeed observed desorption of H<sub>2</sub> and HD upon infrared irradiation, but found no evidence for isotopic selectivity. That desorption was also observed *off* resonance with the HD vibration indicates a heating effect may be responsible for some of the results.

Recently, Heidberg *et al.*<sup>36</sup> demonstrated resonant laser-induced desorption from surfaces for the first time. Using a high-power CO<sub>2</sub> laser ( $\leq 1$  MW/cm<sup>2</sup> peak power), the desorption flux of CH<sub>3</sub>F from NaCl surfaces was measured as a function

of laser frequency and intensity. The wavelength dependence indicates a desorption process which is resonant with the  $\text{CH}_3\text{F}$  adsorbate vibration at low laser fluence ( $\sim 0.02 \text{ J/cm}^2$ ). The desorption yield increases non-linearly with laser intensity above an onset value, indicating a multiphoton process ( $n \geq 2$ ). The wavelength dependence is a function of coverage and temperature, probably indicating the presence of different adsorbed phases, while the desorption yield also decreases at lower coverage. Similar observations were made by Chuang<sup>30</sup> for  $\text{C}_5\text{H}_5\text{N}$  on various ( $\text{KCl}$ ,<sup>37a,b,c</sup>  $\text{Ni}$ ,<sup>37b</sup>  $\text{Ag}$ <sup>37c</sup>) substrates. A single broad ( $5\text{-}8 \text{ cm}^{-1}$ ) feature resonant with the  $\nu_8$  vibration of  $\text{C}_5\text{H}_5\text{N}$  was observed at low laser fluence, while non-resonant laser heating was demonstrated at higher fluence ( $> 0.1 \text{ J/cm}^2$ ). In addition, no desorption could be detected from surfaces with pyridine coverage of less than 2 layers. Coadsorption experiments were then performed in which a non-absorbing molecule was deposited along with the laser absorbing species ( $\text{C}_2\text{H}_6$  with  $\text{CH}_3\text{F}$ <sup>38</sup> and  $\text{C}_5\text{D}_5\text{N}$  with  $\text{C}_5\text{H}_5\text{N}$ <sup>39</sup>). No desorption of  $\text{C}_2\text{H}_6$  was observed concurrently with desorbed  $\text{CH}_3\text{F}$ , which was interpreted as indicating highly localized desorption dynamics; however, both isotopic pyridine species desorbed when either species was initially irradiated.<sup>39</sup> Thermal desorption studies would help to resolve the apparent discrepancy between the two systems.

While the Heidberg<sup>36,38</sup> and Chuang<sup>37,39</sup> experiments deal with systems which require multiphoton vibrational excitation, Chuang and Hussla<sup>70</sup> recently reported both single and multiple photon desorption of  $\text{NH}_3$  over  $\text{Cu}(100)$ . At low coverages, the non-linear laser intensity dependence signals a multiphoton process which is consistent with the bond strength estimates of  $\text{NH}_3$  adsorbed on the  $\text{Cu}(100)$

surface. At higher coverages, multilayer  $\text{NH}_3$  can be desorbed with the energy from one photon, as both the intensity dependence and enhanced yield indicate. Thermal effects appear negligible as no desorption is observed with the laser off resonance. This case is the first well-characterized demonstration of single-photon photodesorption.

In other experiments, resonant photodesorption was observed for  $3 \mu\text{m}$  excitation of cyclopropane ( $\text{C}_3\text{H}_6$ ) on Ag,<sup>40</sup> but a low power cw CO laser ( $5 \mu\text{m}$  excitation) could effect only thermal desorption of CO on Pd,<sup>41</sup> presumably because the adsorbate-substrate bond strength is greater than the photon energy. Our experimental efforts in this area are described in Section 6.

Theoretical treatments have examined the range of mechanisms available for coupling light to the adsorbate-substrate systems. Wautelet<sup>42</sup> suggested that electronic excitations in the solid due to irradiation would enhance the desorption process. Modelling of desorption driven by multiphoton excitation of the *adsorbate-surface vibration* has yielded very high ( $\sim 10^7 \text{ W/cm}^2$ ) estimates for necessary laser intensity,<sup>43,44</sup> while much lower laser power ( $50 \text{ mW/cm}^2$ ) is necessary for calculated *direct* bound-continuum transitions in the adsorbate-surface well.<sup>71</sup>

A number of groups have modelled the photodesorption process we consider here. George *et al.*<sup>45</sup> used a quantum-stochastic method to determine the vibrational population distributions of excited adsorbates. Multiphoton absorption, and hence stimulated desorption, was calculated for light with an average laser intensity of  $10 \text{ W/cm}^2$  (more aptly described as 100 nsec pulses of  $100 \text{ MW/cm}^2$  intensity). Kruezer and Lowy<sup>46</sup> calculated the rate of desorption for vibrationally

excited CO molecules adsorbed on Cu and W with phonon-mediated coupling to desorbed states. They found the laser-induced rate could be faster than the thermal rate of desorption, assuming the laser has populated the vibrational level ( $n \geq 2$ ) of the adsorbate isoenergetic with continuum states above the surface-adsorbate potential well. Gortel *et al.*<sup>47</sup> have recently developed methods to calculate all transition rates (laser-induced vibrational, and phonon-mediated bound-bound and bound-continuum) quantum statistically, and have applied this treatment to the reported CH<sub>3</sub>F/NaCl experiments. While qualitative aspects were reproduced by the treatment, more experimental input is needed to bring the theory and experiment into quantitative agreement. A similar approach by Fain and Lin<sup>72</sup> has reproduced the desorption coverage dependence observed by Chuang.<sup>37</sup> The specific case of one-photon photodesorption has also been addressed by Lucas and Ewing,<sup>48</sup> who calculated the tunneling rate for transferring population from the vibrationally-excited bound adsorbate potential energy surface to the vibrationally relaxed desorbate surface. The overlap of the wavefunctions on the two potential surfaces governs the rate, and the momentum gap, which parametrizes the overlap, depends on the final state of the desorbed species: the desorption rate increases as the molecule retains more internal energy. The wide range of resultant desorption rates highlighted the qualitative impact of parameter variation.

The phenomenological model presented here takes the same philosophical approach as Lucas and Ewing – we apply to this problem a treatment which has been successfully employed to extract dynamics from gas-phase vibrational predissociation of van der Waals molecules.<sup>49</sup> Moreover, energy transfer dynamics

between the adsorbate and substrate will be probed by photodesorption studies, in a manner analogous to the gas phase experiments. We digress here and describe the gas-phase van der Waals molecule photodissociation experiments, as they will be used to illustrate application of the lineshape formula.

A weakly-bound complex which contains at least one species that absorbs infrared radiation is synthesized, cooled and isolated in a molecular beam.<sup>50,51</sup> The complex is irradiated by a suitable laser and dissociates after absorption of a single photon. The van der Waals complex is weakly bound - generally 0.5 to 10 kcal/mole ( $200\text{-}2000\text{ cm}^{-1}$ ) - and it has proven feasible to view the excitation as being localized in the absorbing substituent alone. Within this description, decomposition occurs when energy from the vibrationally excited component "leaks" into the van der Waals bond. If homogeneous, the dissociation spectrum of the complex (i.e., the loss of mass spectral intensity of the van der Waals molecule as a function of wavelength) and, in particular, the width of the profile indicate the timescale of the process which relaxes the vibrationally excited state. The rates have been extracted using a two-level-with-decay model.<sup>52</sup>

By analogy to the gas-phase experiments, a solid surface plays the role of non-absorbing and weakly-binding partner in the photodesorption process. The vibrationally excited adsorbate may break the weak bond to the surface and desorb, being detected directly (e.g., by a mass spectrometer) or as loss of surface coverage. Being somewhat more complex in nature than a rare gas atom, the solid surface has additional mechanisms which may quench the excited vibration. These "dark" energy transfer channels would compete with the desorption channel, and hence be

indirectly probed by the photodesorption.

In the following section we present the photodissociation/photo-desorption model and outline the derivation of lineshape formulae for both pure and mixed cases. The qualitative features of the results are discussed. In section 4 we discuss the range of parameter values used in the photodesorption calculations of section 5. After discussion of these results, we present our experimental observations in an effort to detect photodesorption (section 6), then summarize in section 7.

### 3. Model and Formulation

The model is based on an ensemble of two-level systems shown schematically in Figure 1. We use a perturbation Hamiltonian approach in which the two levels, representing the ground ( $v = 0$ ) and first ( $v = 1$ ) vibrational levels of the laser-excited species (either the infrared-absorbing partner in a van der Waals complex, or the adsorbate of a surface-adsorbate system), are solutions of the unperturbed molecular Hamiltonian. The dissociation or desorption channel is modelled by an exponential depletion of upper state population with rate constant  $\gamma_D$ . We differentiate between the **pure** case, in which the two levels are coupled solely by the laser radiation field, and the **mixed** case, in which an additional decay channel is considered which is non-dissociative and serves only to relax excited state population to the ground state.<sup>52</sup> The pure case is appropriate for the photodissociation of simple van der Waals clusters, while the mixed case will be used to treat the photodesorption process. Note that the characteristic rate of the exponential quenching decay,  $\gamma_Q$ , represents the *total* contribution of all relaxation mechanisms, such as phonon and electron-hole pair excitation in solids.

MODEL

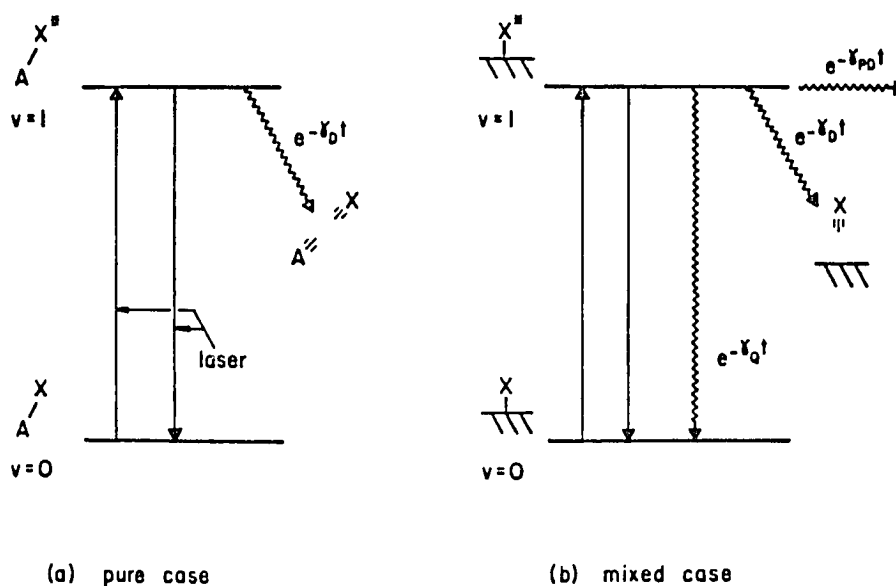


**Figure 1.** Schematic of two-level-plus-decay model: (a) **pure case** - the ground and first vibrational level are coupled by the radiation field of the laser while species in the excited state dissociate to products with an exponential rate; (b) **mixed case** - an incoherent quenching mechanism, which relaxes excited state species back to the ground state, plus a dephasing mechanism are added to the pure case model. The pure case is appropriate for the analysis of van der Waals molecule photodissociation spectra, while the mixed case is used to model photodesorption dynamics.

The model in its present form treats the two vibrational states in resonance with the laser as the only explicit population reservoirs. Transitions to and from other excited (vibrational or vibronic) states would involve additional feeding and depletion mechanisms.<sup>53</sup> Rotational levels are not treated directly. The energy of the first vibrational level is assumed to be greater than the energy needed to break the weak bond to either the van der Waals partner (pure case) or the surface (mixed case). Dependence of the photodesorption probability on the excess energy,  $\Delta E$  (where  $\Delta E = E_{h\nu} - E_{bond}$ ) is hidden in the desorption rate,  $\gamma_D$ , which is treated phenomenologically. The only quenching mechanisms considered here ultimately repopulate the ground state with relaxed upper state population. In addition, the local heating effect resulting from quenching by the phonon bath is treated only insofar as the desorption rate (which is not directly calculated) would change. The qualitative ideas that result from such a simple model, however, are valuable and help to indicate which approximations might be important in other systems.

Derivation of the lineshape expression for both cases was the subject of a previous paper,<sup>52</sup> and for completeness we outline the procedure and summarize the resultant expressions here. For both the pure and mixed case, the wavefunction for the ensemble is written as the linear combination of stationary-state wavefunctions with time-dependent coefficients:

$$|\Psi(\mathbf{r}, t)\rangle = c_0(t)|0\rangle + c_1(t)|1\rangle, \quad (1)$$

where  $|0\rangle \equiv |\phi_0(\mathbf{r})\rangle$  and  $|1\rangle \equiv |\phi_1(\mathbf{r})\rangle$  are the lower and upper state wavefunctions, respectively, for the unperturbed molecular Hamiltonian. The experimentally observed lineshape is the change in total (upper plus lower state) population after

a fixed irradiation time. The approach toward deriving a suitable expression of the lineshape is then to solve the differential equations of motion for  $c_0$  and  $c_1$  which are coupled by the laser-molecule interaction:

$$V = -\frac{1}{2}\vec{\mu} \cdot \vec{E}_0 e^{-i\omega t}, \quad (2)$$

where  $\omega$  is the angular frequency and  $\vec{E}_0$  the magnitude of the electric field of the incident radiation, and  $\vec{\mu}$  is the transition dipole moment of the absorption. In the mixed case, there is additional incoherent population exchange that suggests use of the density matrix formalism, which deals directly with population instead of wavefunction coefficients. The use of interaction picture probability amplitudes,  $C_i$ , is suitable for the pure case, where

$$c_i(t) = C_i(t)e^{-i\omega t}, \quad (3)$$

and  $\omega_i = E_i/h$ . The initial condition for species in a supersonic expansion or on a cold surface is that the entire population is in the ground vibrational level. Given this starting point, exact (and intractable) lineshape formulae can be derived.<sup>52</sup> Simplification results from considering the situation  $\omega_R < \gamma_D$  (pure case) or  $\omega_R < \gamma_T$  (mixed case); that is to say, the decay rates are faster than the laser-induced cycling rate ( $\omega_R$ ). The resultant expressions for  $I/I_0$ , or the fraction of molecules remaining undissociated ( $F_p(\omega, t)$ ), are then:

$$F_p(\omega, t) = \exp \left[ -\omega_R^2 \gamma_D^{-1} t \times \frac{\gamma_D^2}{4(\omega - \omega_0)^2 + \gamma_D^2} \right], \quad (4a)$$

$$F_m(\omega, t) = \exp \left[ -\omega_R^2 \gamma_T^{-1} t \times \frac{\gamma_D}{\gamma_D + \gamma_T} \times \frac{\gamma_T^2}{4(\omega - \omega_0)^2 + \gamma_T^2} \right], \quad (4b)$$

The Rabi frequency,  $\omega_R$ , is defined as  $\omega_R = (\mu \cdot \mathbf{E})/h$  and the rates of decay processes are:  $\gamma_D$  for desorption (mixed case) or dissociation (pure case),  $\gamma_Q$  for quenching and  $\gamma_{PD}$  for pure dephasing, with  $\gamma_T$  defined as  $\gamma_Q + \gamma_D + 2\gamma_{PD}$ . Since  $F_m$  or  $F_p$  is the fraction of species *remaining* after the irradiation time,  $F$  varies from 1 (no desorption) to 0 (entire population desorbed).

For both the pure and mixed cases, the lineshape is the exponential of a Lorentzian scaled by a prefactor. The prefactor determines the intensity of the spectrum (i.e., the extent or completeness of the dissociation). In the pure case, the prefactor  $\omega_R^2 \gamma_D^{-1} t$  is composed of excitation parameters (the laser power and the molecular transition dipole moment are contained within  $\omega_R$ , as well as the irradiation time,  $t$ ) and the rate of dissociation. For the mixed case, the sum of rate processes defined by  $\gamma_T$  appears in the prefactor in place of  $\gamma_D$ . In addition, the Lorentzian is attenuated by a second factor  $\epsilon$ , where  $\epsilon = \gamma_D / (\gamma_D + \gamma_Q)$ . The factor  $\epsilon$  makes the extent of dissociation sensitive to the relative sizes of  $\gamma_D$  and  $\gamma_Q$ ; increasing  $\gamma_Q$  for a fixed  $\gamma_D$  forces the exponential term to zero,  $F_m \rightarrow 1$ , and the desorption is quenched.

The width of the Lorentzian in the lineshape expression contains the rate information. For the pure case, the full width at half maximum (FWHM) of the Lorentzian term yields directly the dissociation rate:

$$\gamma_D = 2\pi c \cdot FWHM. \quad (5)$$

For the mixed case lineshape (eq.(4b)), eq. (5) provides  $\gamma_T$ , the sum of all rate processes. Thus, in situations where the mixed case expression is appropriate, it becomes important to obtain (for example) the fractional desorption so that one

can unravel the contributions of the decay rates to the total width, as well as to obtain the true total rate,  $\gamma_T$ . The desorption profile in arbitrary units yields only the (exponentiated) Lorentzian term without the prefactor. The width of the profile is the full width at half *minimum* (FWHM') of eq. (4b), which is:

$$FWHM' = \gamma_T \times \left[ \frac{\omega_R^2 \gamma_T^{-1} t \cdot \epsilon}{\ln 2 - \ln[1 + \exp(-\omega_R^2 \gamma_T^{-1} t \cdot \epsilon)]} \right]^{\frac{1}{2}}, \quad (6)$$

In the event that the prefactor,  $\omega_R^2 \gamma_T^{-1} t \cdot \epsilon$ , is small (i.e., the desorption is not near saturation, or fluence broadened<sup>52</sup>), the bracketed term of eq. (6) goes to 1, and  $\gamma_T$  can be recovered in the same manner as from eq. (5). The expression for FWHM' in the pure case can be obtained from eq. (6) by letting  $\gamma_T \rightarrow \gamma_D$  and  $\epsilon \rightarrow 1$  (since  $\gamma_D \gg \gamma_q$ ), as expected.

Before calculating specific examples of the photodesorption lineshape, we assert the validity of the model by examining results of van der Waals molecule photodissociation experiments to which the two level model has been applied.<sup>52</sup> Figure 2 displays the infrared photodissociation spectrum of the van der Waals complex ethylene trimer,  $(C_2H_4)_3$ . The decay rate,  $\gamma_D$ , could be determined using the pure-case version of eq. (6) but, since the absolute fraction of complexes dissociated is measured, a simpler way is to obtain the width of a Lorentzian fit to the logarithm of the fraction dissociated ( $\ln F$ ). The rate calculated in this manner ( $\gamma_D = 2.0 \times 10^{12} \text{ s}^{-1}$ ) is smaller than that obtained by a direct Lorentzian fit to the spectrum  $(1-F)$ ,  $\gamma_D = 2.5 \times 10^{12} \text{ s}^{-1}$ . Consider, however, a case where saturation is attainable; that is, when close to 100% of the molecules of interest can be dissociated over some range of frequency. This could be accomplished by using higher laser

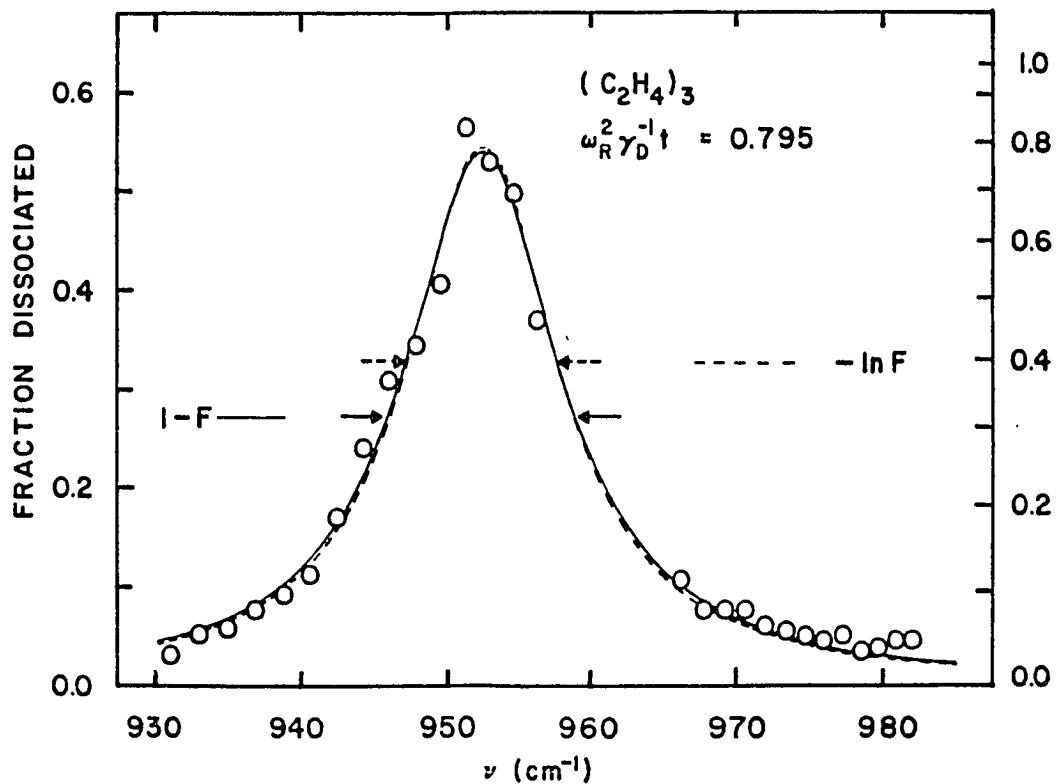


Figure 2. Application of the model lineshape expression to the IR photodissociation spectrum of the van der Waals molecule (C<sub>2</sub>H<sub>4</sub>)<sub>3</sub>. The experimental profile (circles) is fit by a Lorentzian (solid line) and eq. (4a) (broken line). The full widths at half maximum for each on their respective scales are indicated.

fluence (in a pulsed system, for example), a longer irradiation time, or a molecular system with stronger absorption such that the pure case prefactor,  $\omega_R^2 \gamma_D^{-1} t$ , becomes large, comparable to 1 (see the discussion of eq. (6)). A Lorentzian could not be fit to the plateau in the spectrum, whereas the model lineshape expression,  $F_p$ , could be employed to fit the spectrum and extract a meaningful dissociation rate from the fluence-broadened profile (early dissociation spectra of  $(C_2H_4)_2$  exhibited this behavior<sup>52</sup>). We note that this is an appropriate and valuable limit of the lineshape expressions, as the usual perturbation approximation, that the initial state population ( $|c_a(t)|^2$ ) remains unchanged, was not imposed.

In gas phase van der Waals molecule photodissociation experiments, the total number of complexes is monitored as a function of irradiation time, laser frequency and power. In a photodesorption experiment, utilization of a surface-sensitive technique (e.g., UPS or XPS) to monitor the adsorbate coverage as a function of irradiation time would yield information exactly equivalent to the gas-phase example; in particular, the fractional desorption. Eq. (4b) would give the fraction of initial coverage remaining after desorption:  $F_m = 1 - \theta^*/\theta_0$ , where  $\theta^*$  and  $\theta_0$  are the desorbed and initial coverages, respectively. By measuring  $\theta^*$  and  $\theta_0$ , or  $F_m$  directly, as a function of laser frequency ( $\omega$ ), power density ( $S$ ) and irradiation time ( $t$ ), one can determine the total decay rate,  $\gamma_T$ , and the absorption cross section. Additional information can be obtained due to the orientational nature or  $\omega_R^2$ . Determination of the photodesorption intensity as a function of the angle between the light field polarization and the surface normal might allow determination of adsorbate orientation, as well as the adsorbate vibrational absorption intensity.

In experiments performed to date<sup>36-39,70</sup> (see also Section 6) mass spectrometry was used to detect the flux of desorbed species. This detection method provides greater sensitivity than UPS when the fractional loss of coverage ( $\theta^*/\theta_0$ ) is small. Although the prefactor was not directly determined, the width of a Lorentzian fit to the observed  $\text{NH}_3$  photodesorption profile<sup>70</sup> allows an upper limit on the total decay rate,  $\gamma_T$ , to be set at  $1-2 \times 10^{13} \text{ s}^{-1}$ .

#### 4. Details of Calculations

Since there are few cases of desorption induced by resonant absorption, and with only one documented case involving a single photon process, a valuable application of the mixed case model lineshape equation is to determine the range of feasibility of vibrational desorption processes on surfaces. Within estimates of molecular rate parameters ( $\gamma_D$ ,  $\gamma_Q$  and  $\gamma_{PD}$ ), experimental conditions necessary for the observation of photodesorption of an adsorbed species can be calculated. In general, we expect estimates for desorption probability to be most realistic for molecules physisorbed on cold ( $< 100 \text{ K}$ ) surfaces. The surface-adsorbate bond energy for weak-binding surfaces may then be less than the photon energy (3-12 kcal/mole), and the population of molecular vibrations will be concentrated in the ground state. Thermal desorption will also be attenuated at lower temperatures making it easier to distinguish the laser-assisted desorption. For the photodesorption technique to specifically probe surface dynamics, adsorbate-adsorbate interactions should be negligible (low-coverage regime). With these stipulations, the analogy to the gas-phase experiments is also valid.

To study the effect of various parameters in the lineshape expression on the

probability for desorption, it is simplest to examine the intensity of the spectrum at the wavelength of maximum desorption. Information regarding the width of the profile can be set aside temporarily, as this is an important feature in terms of photodesorption feasibility only when the rate of desorption is very fast (see the discussion following Figure 5). The width is, however, crucial to the determination of rate constants, and is included with Figures 7-10.

Eq. (4b) with  $\omega = \omega_0$  reduces to

$$F_m(\omega_0, t) = \exp(-\omega_R^2 \gamma_T^{-1} t). \quad (7)$$

The peak intensity of the photodesorption spectrum is a function of  $\omega_R$ ,  $t$  and  $\gamma_T$ . The irradiation time,  $t$ , and the Rabi frequency,  $\omega_R$  (which depends on the laser power and polarization), can be controlled and measured experimentally. The decay rates,  $\gamma_D$ ,  $\gamma_Q$  and  $\gamma_{PD}$ , are properties of each surface-adsorbate system, and may take on a wide range of values. We perform two types of calculations. First, the quenching rate constant  $\gamma_Q$  is fixed to a rather high value and  $\omega_R$  is varied to see how the peak desorption intensity depends on accessible experimental variables. Then, with a conservative value of  $\omega_R$  and  $t$ , the decay rates are varied. These calculations illustrate the range of system variables which yield feasible estimates of photodesorption, and thus the magnitude of rates which can be probed by this technique. The calculations are performed with both surface-sensitive (Figures 3-6) and desorbate-sensitive (Figures 7-10) detection techniques in mind. Before the calculations are presented, we discuss the possible variance of each parameter.

#### *4.1 Excitation parameters*

##### *4.1.1 Laser power density*

The first experimental system we consider uses a cw CO<sub>2</sub> laser (for discussion of pulsed systems, see section 4.1.3) which is discretely tunable over the region 900-1100 cm<sup>-1</sup> and outputs typically 1-20 W over a 6 mm beam waist. The high power is advantageous for maximizing  $\omega_R$  (hence, making desorption more facile), but may be problematic due to background desorption caused by heating of the substrate. Molecular absorption strengths of vibrations in the 10  $\mu\text{m}$  spectral region tend to be high (another advantage), but the energy of the photon is low (1000 cm<sup>-1</sup> = 2.9 kcal/mol), restricting the choice of adsorbate-substrate system to cases where the physisorption bond energy is less than 3 kcal/mole. Direct surface photodesorption in the 10  $\mu\text{m}$  region should be possible with non-polar molecules condensed on inert semiconductor and insulator surfaces.

The second experimental case examined would be one in which photons of higher energy are used. Specifically, we consider a cw F-center laser which is continuously tunable between 3050 and 4500 cm<sup>-1</sup> with lower output powers compared to the CO<sub>2</sub> laser (1-30 mW range, 2 mm beam diameter). The photon energy is 3-4 times that of the CO<sub>2</sub> laser which would allow the study of, e.g., weakly bound adsorbates on noble metals, but the power density can be 1-3 orders of magnitude lower. Also, absorption intensities of the fundamental vibrations in this region (mostly hydrogen stretches) can be quite low, while overtones and combination bands are even weaker absorbers.

A factor which affects the power density at the surface is the angle of incidence

of the radiation. To optimally interact with a dipole oriented perpendicular to a metal surface, infrared radiation must strike the surface at a glancing incidence<sup>54,55</sup> ( $\theta = 88^\circ$ , measured from the surface normal); for a semiconductor surface such as GaAs,  $\theta \sim 75^\circ$ . Choosing the more severe geometrical configuration ( $\theta = 88^\circ$ ) and typical laser powers we find that the 10 W CO<sub>2</sub> laser beam would produce a power density,  $S$ , of 2.4 W/cm<sup>2</sup> at the surface, while the 10 mW F-center beam generates  $S = 2.2 \times 10^{-2}$  W/cm<sup>2</sup>.

#### 4.1.2 Absorption strength

Integrated absorption intensities,  $A_\omega$ , can be used to approximate the transition dipole moment,  $\mu$ :

$$\mu = \left( \frac{A_\omega}{2.504 \omega g_i} \right)^{1/2}, \quad (8)$$

where  $A_\omega$  is expressed in km mol<sup>-1</sup>, the absorption center,  $\omega$ , is in cm<sup>-1</sup> and  $g_i$  is the degeneracy of the initial state. The values of  $A_\omega$  vary between 10<sup>-2</sup> and 10<sup>2</sup> km mol<sup>-1</sup> for vibrational transitions in the gas phase which translate to transition dipole moments on the order of 10<sup>-3</sup> to 10<sup>-1</sup> D. We adopt the gas-phase values as rough estimates of adsorbate transition moments, given that the values for CO on Pt<sup>57</sup> and Cu<sup>58</sup> ( $\mu = 0.1$  D) are close to the gas-phase value, and that calculations<sup>59</sup> suggest an *enhancement* of intensity may occur when the overall transition moment is parallel to the surface normal.<sup>54-56</sup>

With values for the laser power density and adsorbate absorption strength,  $\omega_R$  can be determined. The Rabi frequency is written as:

$$\omega_R = \frac{\mu}{\hbar} \left( \frac{8\pi S}{c} \right)^{1/2} f(\theta), \quad (9a)$$

which reduces to:

$$\omega_R = 8.659 \times 10^7 \mu S^{\frac{1}{2}} f(\theta), \quad (9b)$$

and gives  $\omega_R$  in  $s^{-1}$  with the transition moment,  $\mu$ , in Debye (D) and the laser intensity,  $S$ , in  $W/cm^2$ . The orientational parameter  $f(\theta) = \langle \cos\theta \rangle$ , is 1 for molecules aligned with the laser polarization and  $1/\sqrt{3}$  for molecules with random orientation.<sup>50b</sup> For the above estimates of  $S$  and  $\mu$ ,  $\omega_R$  will vary between  $10^4$  and  $10^6 s^{-1}$  for a typical F-center laser experiment, and would be an order of magnitude higher in an experiment using a cw CO<sub>2</sub> laser. For the calculations with constant  $\omega_R$  we fix  $\omega_R = 1.5 \times 10^5 s^{-1}$  which corresponds to a 10 mW beam at glancing incidence interacting with an adsorbate whose transition dipole moment is 0.01 D. (Note that for decay rates  $\gamma_q, \gamma_D$  and  $\gamma_{PD} > 10^7 s^{-1}$ , the simplifying approximation  $\omega_R < \gamma_T$ , used to arrive at eq. (4), is valid over the estimated range of  $\omega_R$ , from  $10^4$  to  $10^7 s^{-1}$ .)

#### 4.1.3 Irradiation time, $t$

A distinct advantage in cw-laser photodesorption experiments over the analogous gas-phase photodissociation experiments is that irradiation can occur for much longer periods of time - minutes rather than milliseconds - so that desorption probability can be high even with low irradiation powers. For pulsed laser experiments,  $t$  is only the pulse length, but continual irradiation of a fixed coverage may result in an appreciable overlayer depletion. The upper limit of  $t$  ( $t_{max}$ ) is determined by the vacuum conditions as well as effects of laser heating of the substrate. For UHV systems,  $t_{max}$  greater than  $10^3 s$  (20 min) but less than  $10^4 s$  (2-3/4 h) is a reasonable estimate. For experiments utilizing desorbate

detection,  $t_{max}$  is just the sampling time of the detector. With mass spectrometry,  $t_{max}$  is the inverse of the pumping time constant,  $\sim 1$  msec. This can be increased using integrating techniques (see Chapter 5) to  $\sim 10$  msec. The high sensitivity of the mass spectrometer is compromised in photodesorption experiments by the shorter irradiation times possible. There is, however, the added advantage of signal-averaging capabilities not often possible with surface-sensitive techniques.

A prominent problem in photodesorption experiments is the thermal heating effects due to the incident radiation. This effect will be magnified with physisorbed systems. What temperature rise is expected for the irradiance used in the  $\omega_R$  estimates? The solution for the temperature rise induced by irradiation of an infinite solid has been presented.<sup>65</sup> For the case of a 10 W CO<sub>2</sub> laser at glancing incidence on a 77 K Cu substrate, the temperature rise calculated is 0.014 K after 1 s, with a  $t^{1/2}$  dependence. For the same laser power density but at normal incidence,  $\Delta T$  is 0.2 K after 1 s. Thus the temperature rise for the glancing incidence case is negligible, while heating would become significant for a normal incidence laser with  $t$  greater than 100 s. The irradiance in the second (F-center laser) example case is decreased by a factor of 100, so no significant thermal heating is expected. For transparent substrates, the temperature rise with the example irradiances will be negligible.

It is appropriate here to discuss pulsed systems. From eqs. (4) and (9), it can be seen that the Lorentzian prefactor  $\omega_R^2 \gamma_T^{-1} t$  scales with  $S \cdot t$ , or the total energy delivered over the irradiation time. In the experiments of Heidberg and co-workers<sup>36-38</sup> and Chuang and co-workers,<sup>37-39</sup> the average power density,  $S$ ,

was 10 mW/cm<sup>2</sup> to 1W/cm<sup>2</sup> (the same range considered in these calculations) but the high peak power, 10 mJ/cm<sup>2</sup> to 1.0 J/cm<sup>2</sup> in  $\sim$ 100 ns pulses, was necessary to stimulate the multiphoton desorption process. Only  $\sim$ 1 mJ/cm<sup>2</sup> is necessary for the onset of single-photon multilayer NH<sub>3</sub> desorption.<sup>70</sup> A transient thermal pulse can also be induced at the surface with high power laser pulses before equilibrium with the substrate is achieved. For single photon photodesorption, the same average power, and thus desorption probability, can be delivered by cw lasers without the complication of non-resonant thermal desorption.

#### 4.2 Decay ( $\gamma_q$ , $\gamma_D$ and $\gamma_{PD}$ ) and thermal desorption rates

##### 4.2.1 $\gamma_q$

The main source of experimental data on the quenching rate of adsorbate vibrations is infrared reflection-absorption spectra (see table 1). Spectral linewidths cannot be accounted for, in many cases, by the instrumental resolution or inhomogeneous broadening. Vibrational lifetimes to be inferred from these widths are lower limits and are in the 0.1 to 1.0 psec range. The mechanism for the quenching is thought to be charge oscillations<sup>58,61,62</sup> in the metal-adsorbate system (electron-hole pair excitation), as opposed to energy loss to the phonon bath.<sup>63</sup> An excellent summary of considerations for vibrational lineshapes of adsorbates has recently appeared.<sup>73</sup> For calculations with  $\gamma_q$  held constant, we use 10<sup>13</sup> s<sup>-1</sup> to represent fast quenching by a metal substrate. This choice most likely overestimates the rate for semiconductors and insulators, unless an energy match exists between the adsorbate vibration and a specific surface mode.<sup>64</sup>

Table 1  
IR Reflection-Absorption Spectra on Single Crystal Surfaces

Adsorbate	Substrate	Resolution ( $\text{cm}^{-1}$ )	FWHM ( $\text{cm}^{-1}$ )	$\tau^a)$ (ps)	Ref.
CO	Cu(100)	4	10	0.53	[60a]
	Cu(100)	2	4-6 <sup>b)</sup>	1.3-0.88	[60b]
	Cu(110)	2	8	0.66	[60c]
	Cu(111)	4	12	0.44	[60d,e]
	Cu(211)	4	8	0.66	[60e]
	Cu(311)	4	8	0.66	
	Cu(755)	4	11	0.48	
	Pt(100)	5	12	0.44	[60f]
	Pt(111) <sup>e)</sup>	5	7-10	0.76-0.53	[60f,g]
	Pt(111)	5	13	0.41	[60h]
	Pt(111)	5	50 <sup>d)</sup>	0.11	
	Pd(100)	2	>10	<0.53	[60i]
	Pd(111)	5	27	0.20	[60j]
	Pd(210)	5	17	0.31	
	Ru(001)	3.5	8-15 <sup>b)</sup>	0.66-0.35	[60k]
N <sub>2</sub>	Pt(111) <sup>e)</sup>		7-10 <sup>b)</sup>	0.76-0.59	[60l]
H <sub>2</sub> O	Ru(001)	10	250 <sup>e)</sup>	-	[60m]
CH <sub>3</sub> O	Cu(100)	4	14 <sup>f)</sup>	0.38	[60n]
			18 <sup>g)</sup>	0.29	
CD <sub>3</sub> O	Cu(100)	4	8 <sup>f)</sup>	0.66	[60o]
			10 <sup>g)</sup>	0.53	

<sup>a)</sup> From eq. (5).

<sup>b)</sup> Coverage dependent.

<sup>c)</sup> Recrystallized ribbon.

<sup>d)</sup> Low-frequency ( $\sim 1870 \text{ cm}^{-1}$ ) mode; all other spectra refer to the CO band in the  $2100 \text{ cm}^{-1}$  region.

<sup>e)</sup> Broad due to hydrogen bonding.

<sup>f)</sup> CH/CD symmetric stretch.

<sup>g)</sup> CH/CD asymmetric stretch.

#### 4.2.2 $\gamma_D$ and thermal desorption

The calculation of a realistic estimate of  $\gamma_D$ , the rate of desorption of the vibrationally excited adsorbate, was the subject of the work of Lucas and Ewing<sup>48</sup> and Kreuzer *et al.*<sup>46,47</sup> Using sample cases, Lucas and Ewing exemplified the wide range  $\gamma_D$  could achieve ( $10^{11}$  to  $10^{-5}$  s<sup>-1</sup>) as a result of the variety of pathways for the excess vibrational energy to be partitioned. The dissociation rate for vibrationally excited van der Waals molecules, as inferred from linewidth measurements, also span a wide range: sub-psec<sup>50</sup> to nsec<sup>72</sup> to <100  $\mu$ sec<sup>65</sup>. In fact, NeCl<sub>2</sub> with Cl<sub>2</sub> in the 1<sup>st</sup> excited vibrational state is detected<sup>66</sup>  $10^{-5}$  s after formation. We use  $10^{12}$  s<sup>-1</sup> for calculations with fixed  $\gamma_D$ , on the faster side of the observed photodissociation rates.

For weakly bound systems, thermal desorption will be competitive with laser desorption unless the surface temperature is low. Frenkel's estimate for the thermal desorption rate,

$$\nu_D = \nu_o e^{-E_D/kT} \quad (10)$$

using a pre-exponential factor,  $\nu_o$ , of  $10^{14}$  s<sup>-1</sup> ( $10^{12}$  s<sup>-1</sup>) yields a desorption rate of  $2.4 \times 10^{10}$  s<sup>-1</sup> ( $2.4 \times 10^8$  s<sup>-1</sup>) for a 1 kcal/mol bond to the surface at 60 K, but only  $5.8 \times 10^6$  s<sup>-1</sup> ( $5.8 \times 10^4$  s<sup>-1</sup>) at 30 K. For twice this bond strength (still below the energy of a CO<sub>2</sub> laser photon) the same rate will be observed at double the temperature. Thus, with a 60 K surface, the photodesorption of weakly bound (< 2 kcal/mol) adsorbates will dominate thermal desorption if the laser-assisted rate is  $\gamma_D > 10^9$  s<sup>-1</sup>; the restriction on  $\gamma_D$  is further lowered for a colder surface or a stronger bond energy. Our empirical estimate of the photodesorption rate

( $10^{10}$ - $10^{12}$ s $^{-1}$ ) meets this criterion.

For the purposes of this paper we consider  $\gamma_{PD}$  small compared to  $\gamma_D$  and  $\gamma_Q$ . Dephasing caused by interaction with the lattice should be small since the substrate is assumed to be at low temperature, and fluctuations are damped.<sup>67</sup> For photodesorption to probe dynamics of energy transfer between an excited adsorbate and the surface, one desires experimental conditions (i.e., low coverage) such that interadsorbate interactions, which would provide a dephasing channel, are negligible. Furthermore, inclusion of appreciable  $\gamma_{PD}$  rates leads to results similar to situations with fast  $\gamma_D$  rates: the lineshape is broadened with concomitant loss of peak desorption intensity. Comments below about broadening due to large values of  $\gamma_D$  apply equally well to the dephasing rate  $\gamma_{PD}$ . This fact implies that determination of  $\gamma_{PD}$  from experiments of this nature alone may be quite difficult. Further lineshape considerations<sup>73</sup> (shape, temperature dependence) may be necessary to sort out the values as well as the microscopic source of the rates.

## 5. Results and Discussion

The effect of the experimental variables  $\omega_R$ , the Rabi frequency, and  $t$ , the irradiation time, can be seen in Figures 3 and 4, respectively. Increasing either the irradiation time or  $\omega_R$  (e.g., by raising the laser power density or rotating the light polarization toward  $\mu$ ) increases the limiting value of the quenching rate,  $\gamma_Q$ , at which observable attenuation of the overlayer can occur. In Figure 3,  $\omega_R$  is varied, the desorption rate is set at  $10^{12}$  s $^{-1}$  and the irradiation time is 1000 s. The two values of  $\omega_R$  calculated in section 4.1.1 are indicated. Assuming a conservative estimate of 10% desorbed as a detection limit ( $F < 0.9$ ), photodesorption is seen to

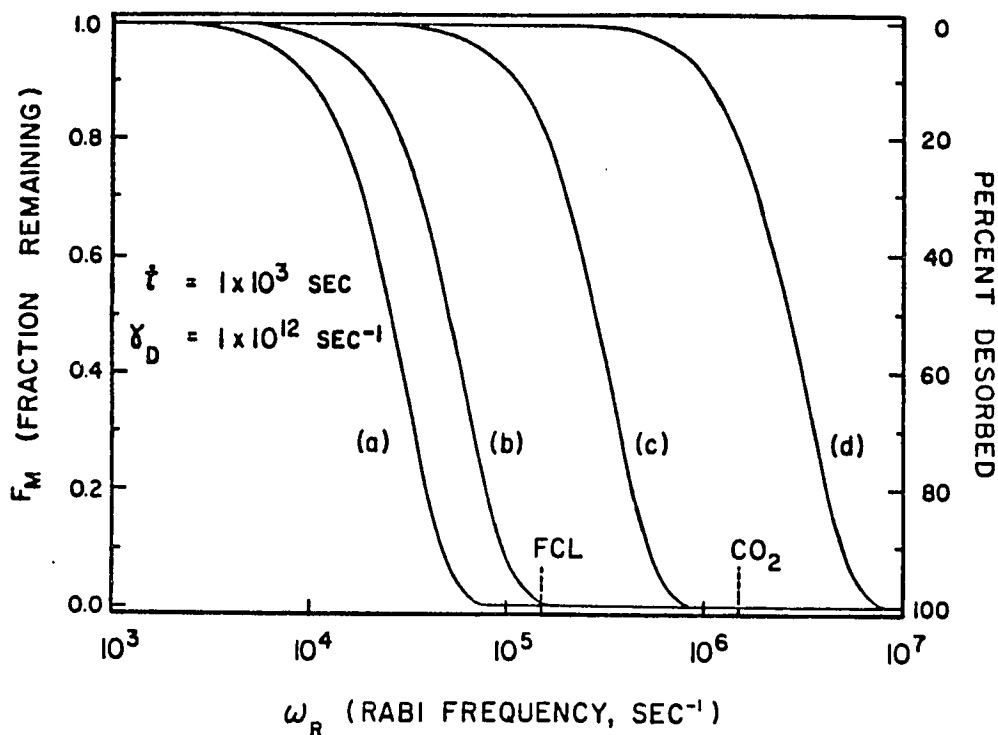


**Figure 3.** Calculation of photodesorption probability versus the Rabi frequency ( $\omega_R$ ). The fraction of adspecies remaining on the surface after irradiation is plotted against  $\omega_R$ , a measure of the laser-adsorbate interaction strength. The values of  $\omega_R$  for two example cases in the text are indicated: a 10 W CO<sub>2</sub> laser (CO<sub>2</sub>) and a 10 mW F-center laser (FCL). The quenching rates ( $\gamma_Q$ ) are: (a)  $10^{10}$ , (b)  $10^{12}$ , (c)  $10^{13}$  and (d)  $10^{14}$  s<sup>-1</sup>.

be feasible for quenching rates less than  $10^{13} \text{ s}^{-1}$  ( $\omega_R = 1.5 \times 10^5 \text{ s}^{-1}$ ). For higher laser powers and/or molecular absorption strengths ( $\omega_R = 10^6 \text{ s}^{-1}$ ) the upper limit on  $\gamma_Q$  for observable photodesorption is in the  $10^{14} \text{ s}^{-1}$  range. This limit is, of course, different for other values of  $\gamma_D$ .

Figure 4 illustrates the effect of irradiation time on the desorption probability, as a function of the quenching rate. As qualitatively expected, longer irradiation times yield a higher desorption probability for a given quenching rate. Quantitatively, the combination of long irradiation times ( $t$  on the order of seconds) and a single photon process ( $\omega_R \propto S$ ) results in the feasibility of a low-power laser successfully competing with moderately fast ( $10^{12} \text{ s}^{-1}$ ) quenching rates to induce resonant desorption. The rate of photodesorption is again chosen as  $10^{12} \text{ s}^{-1}$  while  $\omega_R$  calculated for the second experimental case (FCL) is used.

In Figure 5 we examine the interplay between the relative size of the system rates,  $\gamma_Q$  and  $\gamma_D$ , and the excitation term  $\omega_R^2 t$  (which also has the unit of a rate,  $\text{s}^{-1}$ ). A given quenching rate specifies a range of  $\gamma_D$  for which photodesorption is observable. For example, curve (a) is calculated using a quenching rate of  $10^{10} \text{ s}^{-1}$  and shows complete desorption of an irradiated coverage if the rate of photodesorption is anywhere between  $10^7 \text{ s}^{-1}$  and  $10^{13} \text{ s}^{-1}$ . As the rate of quenching increases (curves (b) to (d)), the range of feasible photodesorption rates becomes more restricted. The shapes of the curves are a result of two effects. The minima occur at  $\gamma_Q = \gamma_D$  and fall along the line defined by:

$$F_m^{min}(\omega_0, t) = \exp(-\omega_R^2 t / 4\gamma_D). \quad (11)$$

To the left of the dotted line the solid curves show increased desorption probability

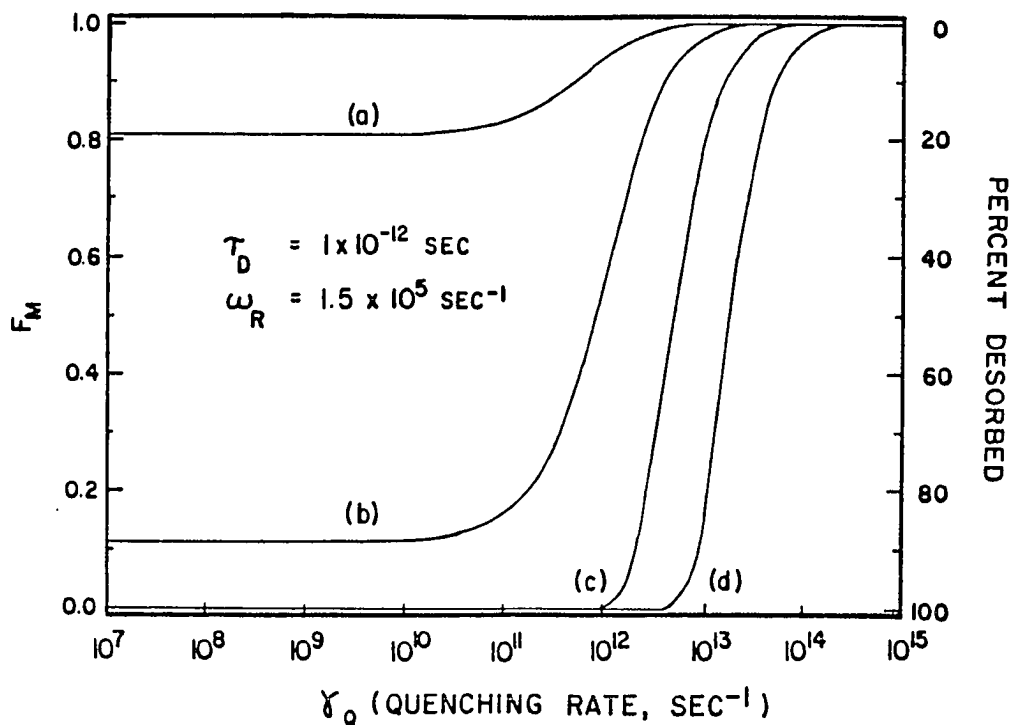
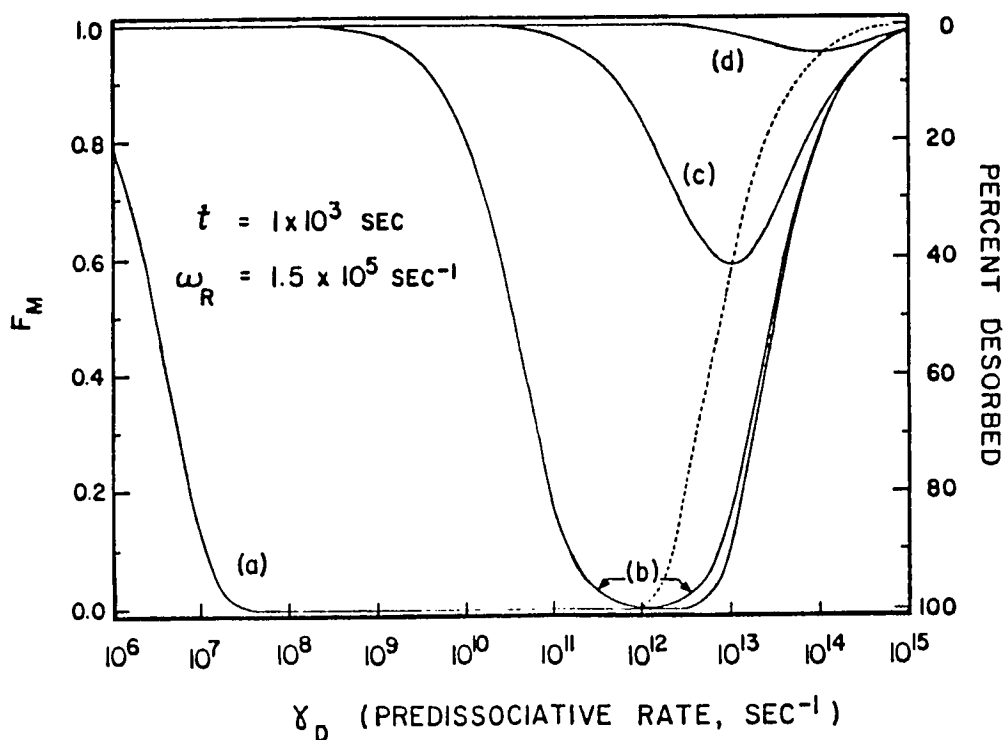


Figure 4. Fraction of adspecies remaining for a range of quenching rates. The effect of varying irradiation time is illustrated, with  $t$  equal to: (a) 10, (b)  $10^2$ , (c)  $10^3$  and (d)  $10^4$  s.



**Figure 5.** Photodesorption probability for various vibrationally excited desorption rates. Both  $\omega_R$  and  $t$  are fixed at the indicated values. The quenching rates ( $\gamma_Q$ ) are: (a)  $10^{10}$ , (b)  $10^{12}$ , (c)  $10^{13}$  and (d)  $10^{14}$  s<sup>-1</sup>.

(smaller  $F_m$ ) for increasing  $\gamma_D$  as the photodesorption rate becomes commensurate with the quenching rate in the attenuation factor,  $\epsilon = \gamma_D / (\gamma_D + \gamma_Q)$ . The overall rate,  $\gamma_T$ , also increases in the  $\omega_R^2 \gamma_T^{-1} t$  Lorentzian prefactor, acting to increase the percent desorbed. To the right of the dotted line, desorption probability decreases with increasing photodesorption rate due to a lifetime broadening effect: the peak intensity decreases as the profile broadens with larger values of  $\gamma_D$ . The same effect would occur if the dephasing rate were appreciable. Since  $\gamma_{PD}$  appears only in the width term,  $\gamma_T$ , and not in  $\epsilon$ , a dephasing mechanism would serve to distribute the total intensity in the photodesorption spectrum over a broader profile.

It is apparent that increasing either of the experimental variables  $\omega_R$  or  $t$  increases the fraction of adsorbates desorbed for given values of  $\gamma_D$  and  $\gamma_Q$ . In terms of the variables in Figure 5, the curves (c) and (d) would deepen, while curves (a) and (b) would broaden further; this behavior is shown in Figure 6. Using the conservative estimate for  $\omega_R$  and a fast quenching rate, the desorption percentage is plotted versus the photodesorption rate for different irradiation times. For  $t = 1000$  s (curve (b)), the photodesorption rate must fall within the range  $10^{12} \text{ s}^{-1}$  to  $10^{14} \text{ s}^{-1}$  for a 10% desorption to occur at a wavelength of maximum absorption. Longer irradiation time (or, similarly, a larger value of  $\omega_R$ ) increases this range (curve(c)).

In figures 7-10 we present calculations of photodesorption probability with parameters appropriate to mass spectrometric detection. The logarithm of the photodesorption probability is plotted because of the greater dynamic range of detection of desorbed molecules compared to the determination of fractional surface coverage. The sensitivity in our system is  $\sim 10^{-7}$  monolayer (see Section 6). The

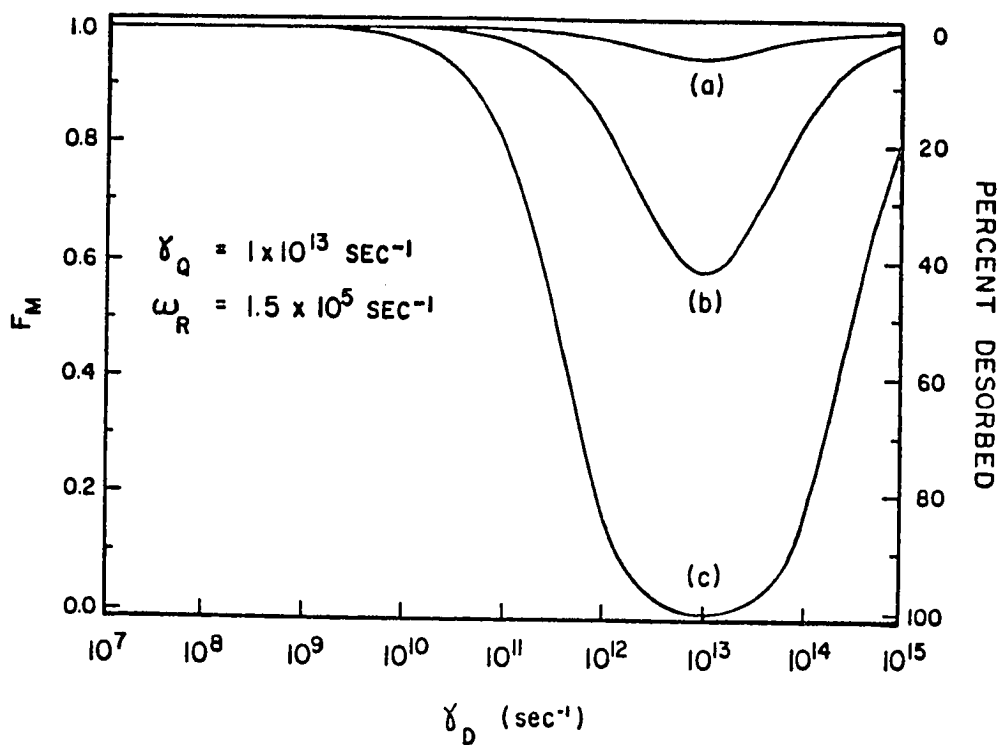


**Figure 6.** Fraction of adspecies remaining over a range of photodesorption rates with a fast ( $10^{13} \text{ s}^{-1}$ ) quenching rate to the surface. The experimental parameter  $\omega_R$  has the same value as in the previous figure. The irradiation times are: (a)  $10^2$ , (b)  $10^3$  and (c)  $10^4$  s.

parameters used to generate Figures 7-10 match those of Figures 3-6, respectively, except for the irradiation time:  $t_{max}$  can be no greater than the pumping time constant in the region of the mass spectrometer ( $\sim 1-10$  msec). With such short irradiation times compared to those used in the previous calculations, the percentage of molecules that are desorbed is much lower (i.e., the curves are shifted up, to lower photodesorption yield), but the particle detection limit with the mass spectrometer is much lower than the assumed detection limit (10% of a monolayer) in the plots of Figures 3-6. Also shown are the linewidths (FWHM') of the profiles. The widths are complex functions of the various rate parameters, and the plots in Figures 7-10 highlight the fact that a variety of rates and experimental conditions give rise to the *same* FWHM. As should be expected, to characterize both the laser-induced desorption rate and the quenching rate, both the linewidth and fractional desorption must be determined.

In terms of feasibility, the desorption probability plots as shown in Figures 7-10 exhibit a wider range of parameters for which photodesorption can be observed than in the case of long irradiations and coverage-sensitive detection. Perhaps a more interesting feature that is indicated is the possibility of deconvoluting the width and desorption intensity information to extract the rate constants. Regions of the curves in Figures 3-6 that are flat (i.e., various parameter values give rise to the same percentage of molecules remaining on the surface) can now be resolved into different fractional desorption signal intensities. The width plots graphically point out the variety of rate conditions which result in similar profile widths. It is important to obtain the absolute desorption percentage to extract the contribution

of quenching and desorption rates.

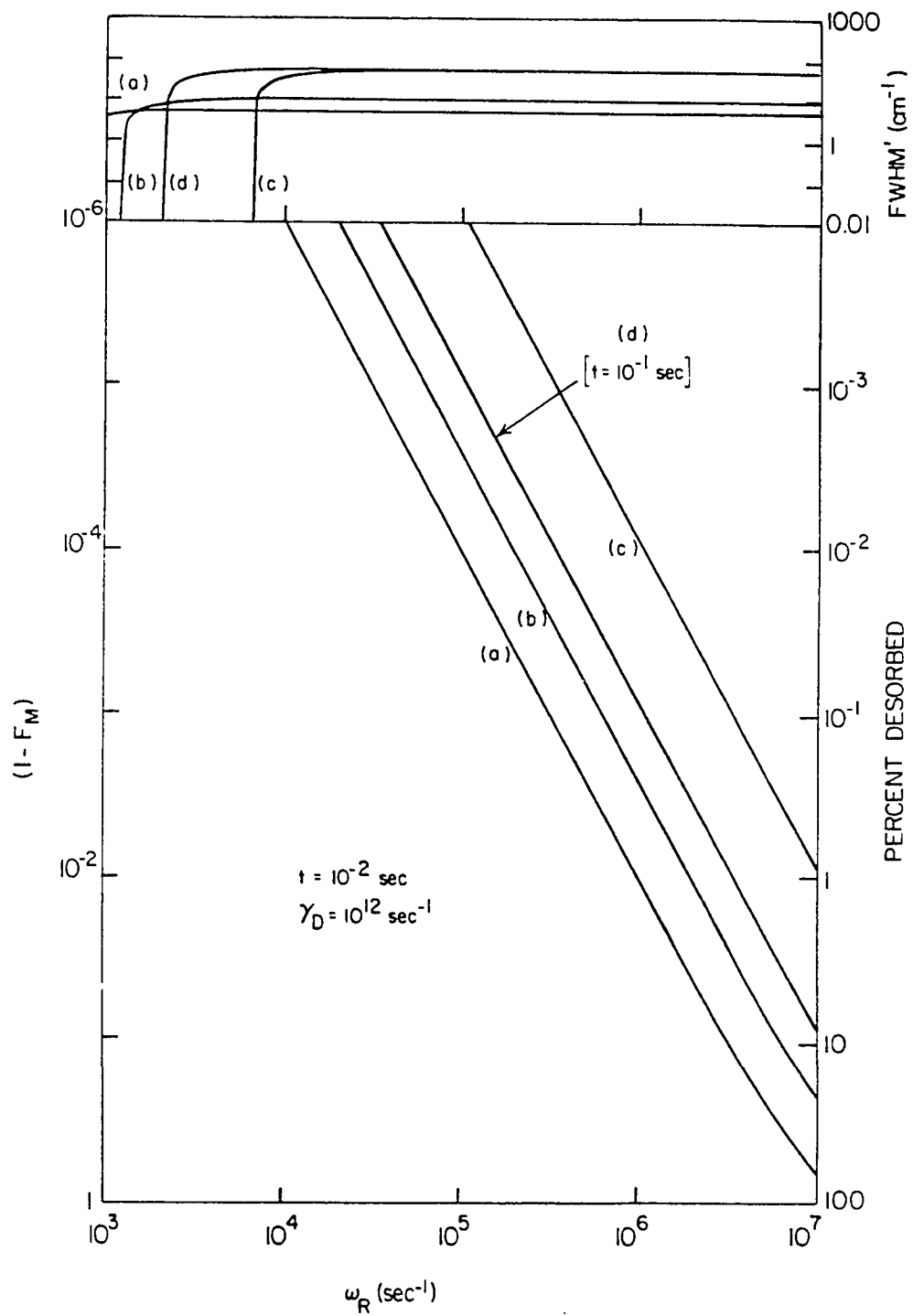
Shown in Figure 7 is the photodesorption probability calculated as a function of the Rabi frequency ( $\omega_R$ ), analogous to Figure 3. With shorter irradiation time, the detected fractional desorption is smaller than in Figure 3, but the lower detection limit of the mass spectrometer enables photodesorption to be detected over a comparable range of the rate constants. For  $\omega_R > 10^4$ , the widths attain the limiting value of  $\gamma_T = \gamma_Q + \gamma_D$ .

Figure 8 is a plot of percent desorbed for different irradiation times *vs.* versus the surface quenching rate,  $\gamma_Q$ , as in Figure 4. With the sensitivity of the mass spectrometer detector, photodesorption will be observable with the short irradiation time. The predissociative rate ( $\gamma_D$ ) dominates the width at small values of  $\gamma_Q$ . The quenching rate dominates the width at higher  $\gamma_Q$ , until the desorption is completely quenched.

Figure 9 is a plot analogous to Figure 5 with irradiation times representative of a mass spectrometer with an integrating cone which is sampling desorption induced in a laser-molecule system characterized by  $\omega_R = 1.5 \times 10^5 \text{ s}^{-1}$ . If the sampling time could be further increased to  $t \sim 0.1 \text{ s}$ , the curves would shift down to regions of higher percent desorbed (curve (e)), indicative of higher sensitivity.

In Figure 10, as in Figure 7, the quenching rate constant ( $\gamma_Q$ ) is fixed to a high value,  $10^{13} \text{ s}^{-1}$ , characteristic of an energy transfer rate to a metal surface. The percent desorbed is calculated as a function of the desorption rate ( $\gamma_D$ ). Curve (e) contrasts the enhanced range of desorption rates for which photodesorption

**Figure 7.** The calculated percent desorbed is plotted on a logarithmic scale *vs.* the Rabi frequency ( $\omega_R$ ), similar to Figure 3. The irradiation time is  $10^{-2}$  s with a laser-induced desorption rate ( $\gamma_D$ ) of  $10^{12}$  s $^{-1}$  and a quenching rate ( $\gamma_Q$ ) of: (a)  $10^{10}$ , (b)  $10^{12}$  and (c)  $10^{13}$  s $^{-1}$ . Curve (d) is for  $\gamma_Q$  of  $10^{13}$  s $^{-1}$  and  $10^{-1}$  s irradiation time. The widths of the wavelength profiles (FWHM') approach limiting values determined by  $\gamma_T$ .



**Figure 8.** Variation of photodesorption feasibility and width with the irradiation time ( $t$ ) and quenching rate ( $\gamma_Q$ ), as in Figure 4. The range of irradiation time is much shorter than in Figure 4: (a) 1, (b)  $10^{-1}$ , (c)  $10^{-2}$  and (d)  $10^{-3}$  s, for  $\gamma_D$  set at  $10^{12}$   $s^{-1}$ , and (e)  $t = 10^{-2}$  s for  $\gamma_D = 10^{10}$   $s^{-1}$ .

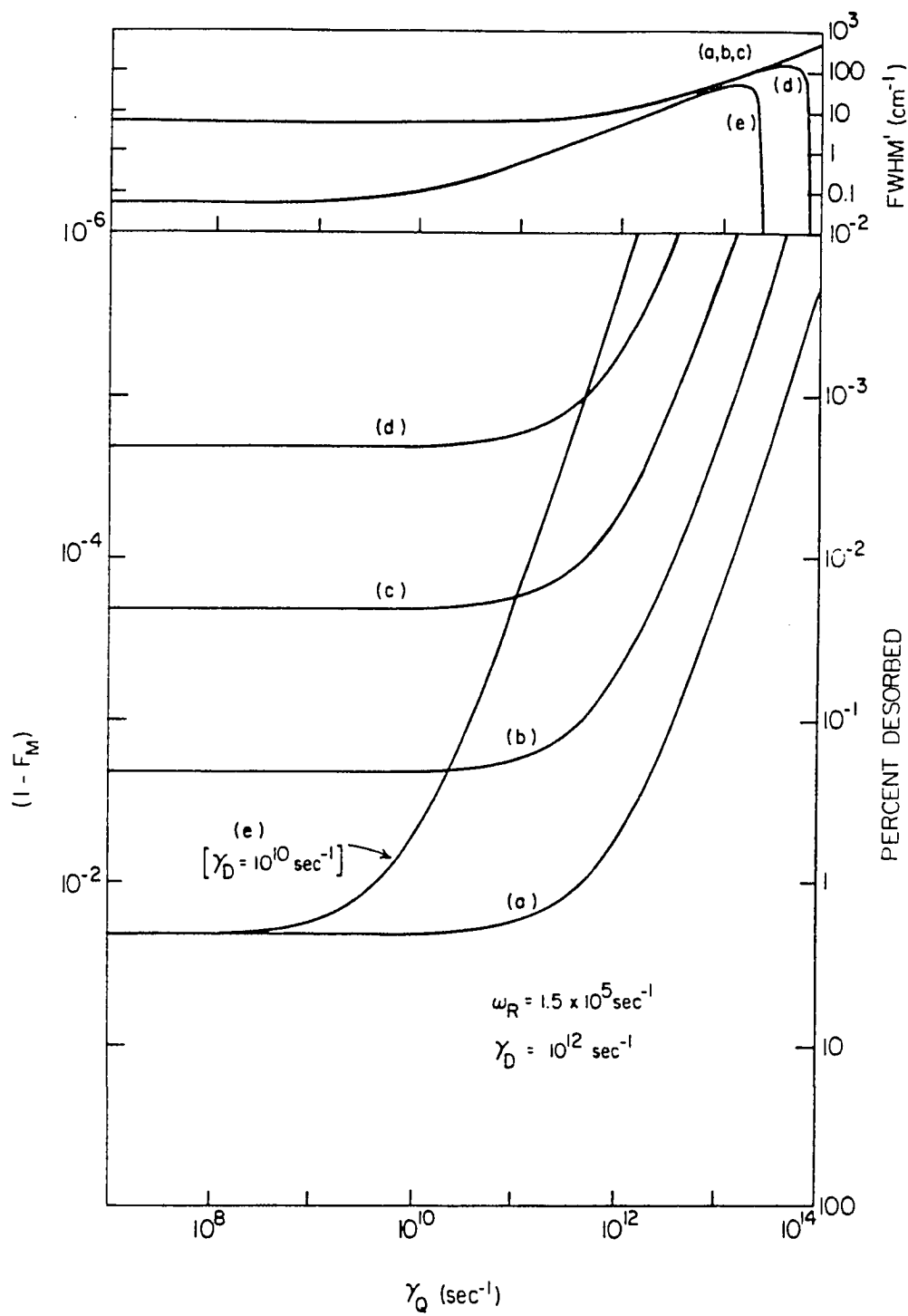


**Figure 9.** Range of detectable photodesorption rates ( $\gamma_D$ ) with irradiation time of  $10^{-2}$  s for a given quenching rate ( $\gamma_Q$ ): (a)  $10^{10}$ , (b)  $10^{12}$  and (c)  $10^{13}$ . Curve (d) is calculated for  $t = 10^{-1}$  s and  $\gamma_Q = 10^{13}$  s $^{-1}$ .

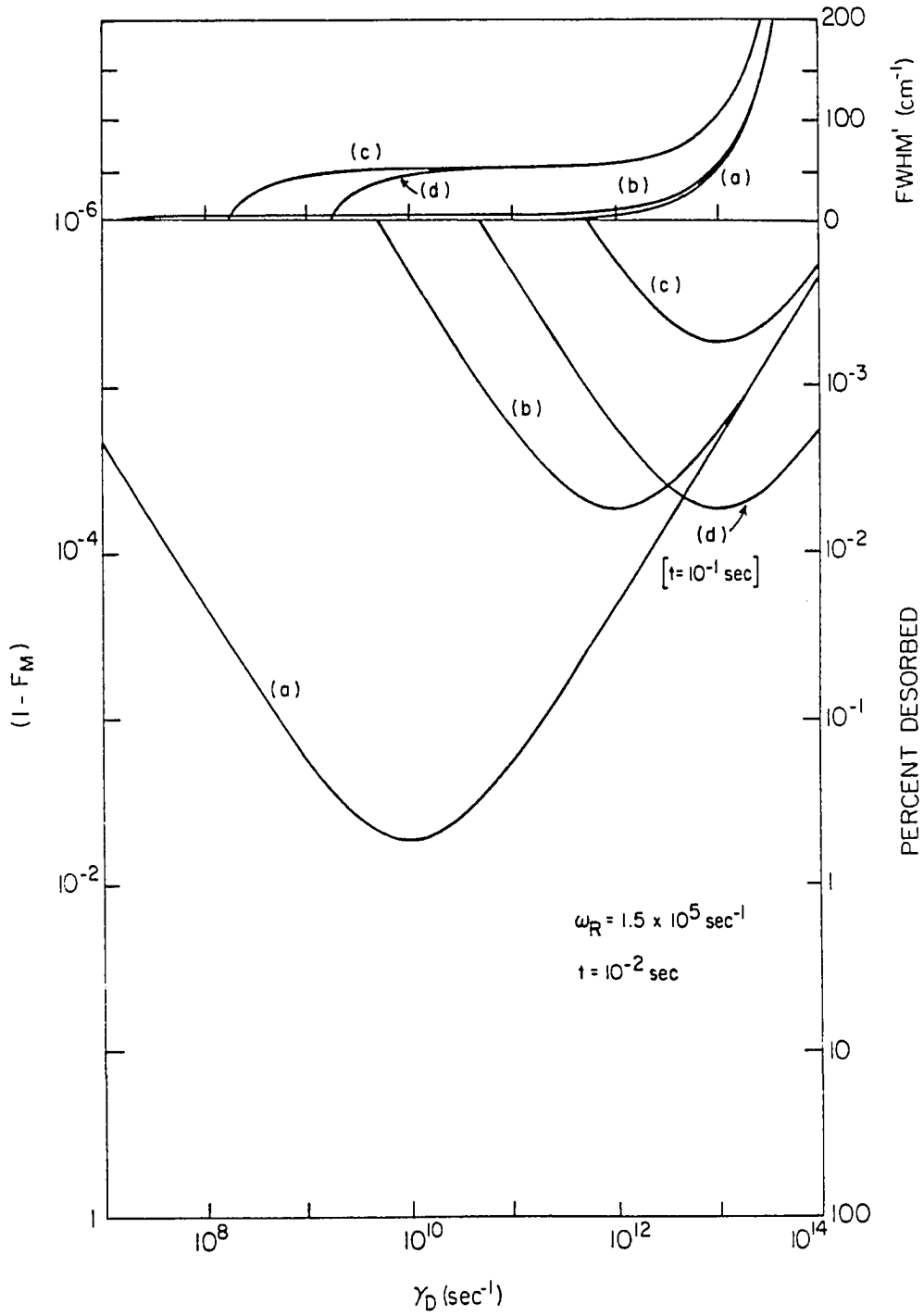
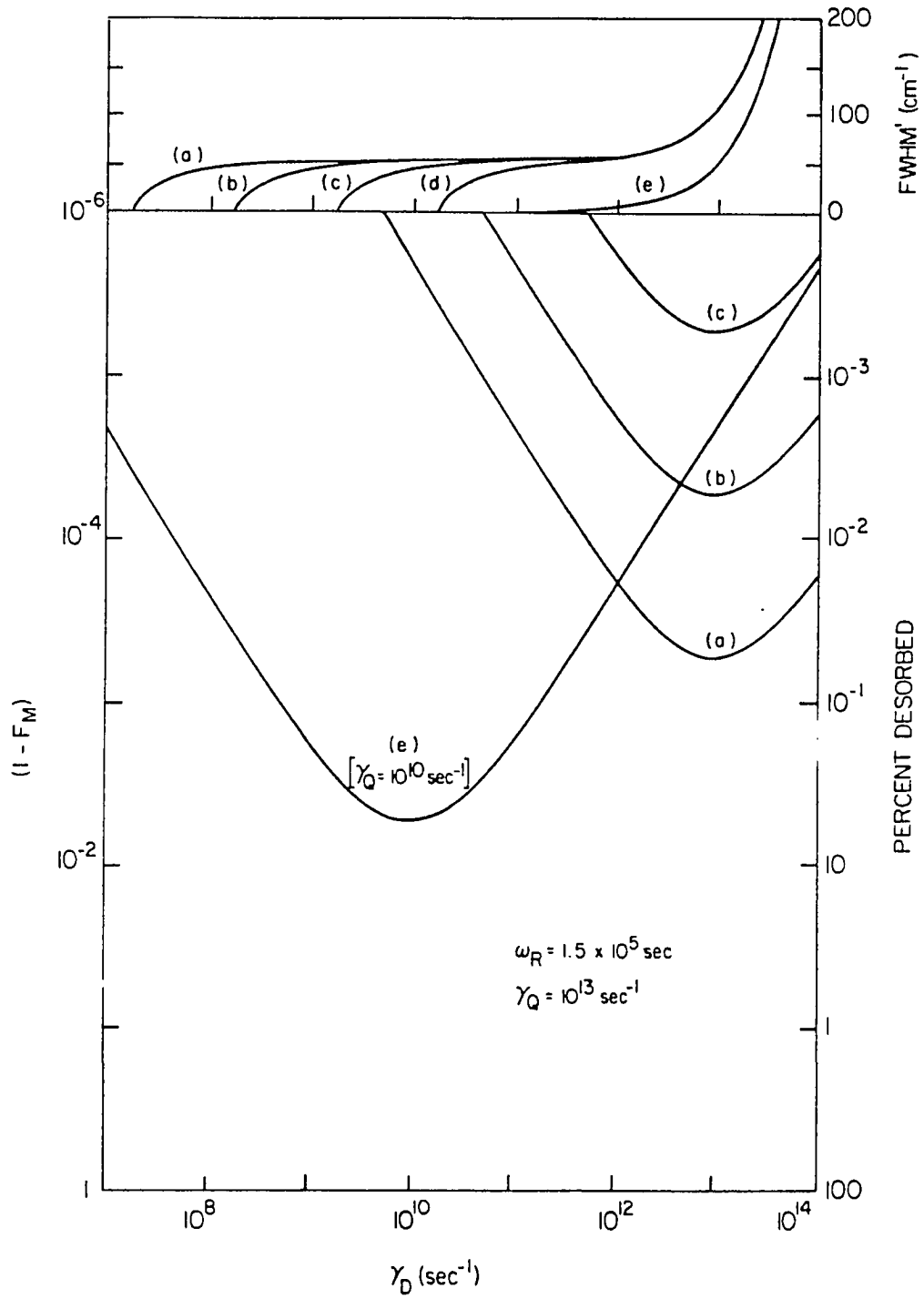


**Figure 10.** The percent desorption and linewidth calculated *vs.* the desorption rate ( $\gamma_D$ ) for a fast quenching rate ( $\gamma_Q = 10^{13} \text{ s}^{-1}$ ). The irradiation times are: (a) 1, (b)  $10^{-1}$ , (c)  $10^{-2}$  and (d)  $10^{-3}$  s. Also shown is the curve (e) for a much slower quenching rate,  $\gamma_Q = 10^{10}$ , with  $t = 10^{-2}$  s.



is feasible for a slower rate of quenching characteristic of a typical semiconductor. The plot of the linewidths shows that with  $\gamma_D$  small compared to  $\gamma_Q$ , the quenching process limits the lifetime of the excited vibrational state and determines the width. The onset behavior at lower values of  $\gamma_D$  is due to small photodesorption probability in that region.

We summarize our findings in a more qualitative fashion by outlining what experimental parameters would be necessary to stimulate photodesorption when one confronts an adsorbate-substrate system which has fixed values of the rate parameters  $\gamma_D$  and  $\gamma_Q$ .

(a)  $\gamma_D \ll \gamma_Q$ : Photodesorption is unlikely because the fast quenching mechanism relaxes vibrationally excited species before desorption can occur. Desorption may be induced by using very high laser power densities, very long irradiation times, or both, but there are practical limits due to desorption induced by laser heating and the finite time constant for adsorption of background gases. At this point, choosing (carefully) a different adsorbate may be an attractive option for two reasons: (1) a molecule with higher oscillator strength, or absorption intensity, would increase the photodesorption probability in the same manner as increased laser power density or irradiation time, and (2) if the quenching mechanism is fast due to a close resonance with the molecular vibration, an adsorbate with different vibrational frequency would create a mismatch, slow the quenching rate and possibly open the desorption channel.

(b)  $\gamma_D \gg \gamma_Q$ : Photodesorption dominates the quenching rate, but consideration must be given to the size of  $\gamma_D$  as compared to the adsorbate

absorption strength and the laser tuning range and linewidth, since the width of the desorption profile is directly proportional to  $\gamma_D$ . For the cw CO<sub>2</sub> laser which has lines spaced every 1 cm<sup>-1</sup>, the photodesorption rate must be greater than 10<sup>11</sup> s<sup>-1</sup> for the lineshape to be resolved. The F-center laser is continuously tunable with a 1-10 MHz linewidth, so photodesorption rates as slow as 10<sup>7</sup> s<sup>-1</sup> could be observed if the thermal desorption rate is not competitive. The width of the desorption spectrum gives the sum of photodesorption and dephasing rates.

(c)  $\gamma_D \sim \gamma_q$ : Photodesorption is probable, assuming the value of  $\gamma_D$  results in a profile which overlaps the range of the excitation laser (see above), but the linewidth contains contributions from all rates. The ratio between  $\gamma_D$  and  $\gamma_q$  in the attenuation factor can be obtained from the absolute photodesorbed fraction if the adsorbate absorption strength can be independently determined, from a similar photodesorption spectrum in which the quenching rate is negligible or from reflection-absorption data.

## 6. Photodesorption Experiments

We have attempted to observe the single-photon photodesorption which we have shown to be theoretically feasible and undertook experiments to measure the rate of molecular desorption induced by infrared radiation. The apparatus constructed for this purpose is described in Chapter 5, and consists of a UHV chamber for the attainment of clean surfaces, sample cooling to condense weakly bound adsorbates on the surfaces, and a mass spectrometer for detection of the desorbed molecules. The experiments which were performed were the IR irradiation of various small molecules which have absorptions in the range of the CO<sub>2</sub> (CH<sub>3</sub>F,

C<sub>2</sub>H<sub>4</sub>, C<sub>3</sub>H<sub>6</sub>) and F-center (C<sub>2</sub>H<sub>2</sub>, CO<sub>2</sub>, CH<sub>3</sub>OH) lasers which were employed, condensed on GaAs(110). In no case was resonant single-photon photodesorption observed. Desorption signals were observed upon irradiation but these did not exhibit reproducible wavelength dependence and are thought to be due to heating of the substrate, which also exhibited weak absorption in this wavelength region. The failure to observe photodesorption is thought to be due to either the surface-adsorbate bonds being stronger than the photon energy, in the case of the CO<sub>2</sub> laser experiments, or low laser intensity coupled with ill-determined absorption frequencies and possibly broad lineshapes of adsorbates in the F-center laser case. The sensitivity of the detection is  $\sim 1 \times 10^{-7}$  monolayers desorbed in a 15 msec chopping cycle; this estimate derives from a signal-to-noise ratio of unity for a steady state flux of  $7 \times 10^7$  molecules/sec and an experimental geometry with 20% collection efficiency of  $10^{14}$  molecules/cm<sup>2</sup> which are desorbed in a cosine distribution.

## 7. Conclusions

We have presented a simple model which has been successfully employed to treat the vibrational predissociation of van der Waals molecules and applied it to the analogous case of vibrational photodesorption of weakly bound adsorbates. Numerical calculations using estimates of relevant parameters show that single-photon experiments of this nature are quite feasible over a wide range of rate conditions, including fast ( $> 10^{13}$  s<sup>-1</sup> quenching rates). In fact, due to the potentially long irradiation times, fluence broadening of lineshapes could very possibly obscure rate information. The photodesorption technique should be a

valuable method to probe quenching and dephasing mechanisms, as well as the photodesorption rate itself, at the solid surface.

While explicitly dealing with desorption as the dissociative decay channel, other processes may be observable and competitive. Stimulation of chemisorptive bonding from a physisorbed precursor or initiation of dissociative reactions are possibilities which may also be treated within the model presented here. Pumping of high overtone states to desorb adsorbates using larger amounts of vibrational energy should also be possible if the small absorption cross-sections can be surmounted. The qualitative trends outlined in this paper will be valid in these cases.

Experiments performed in our lab were not successful in demonstrating resonant single-photon photodesorption. We believe this to be due either to the surface-adsorbate bonds being stronger than the photon energy in the case of CO<sub>2</sub> laser experiments or to broad multilayer absorption linewidths in the case of F-center laser experiments. The use of substrates with lower binding energy (e.g., rare gas crystals) at lower temperatures would alleviate the former problem. Using high-intensity pulsed sources (e.g., as in the experiments of Chuang and Hussla<sup>70</sup>) to roughly determine the absorption region would enable the use of low-intensity high-resolution sources such as an F-center laser over a narrow search range.

#### **Acknowledgements**

The authors would like to thank Dr. Paul Whitmore and Professor H. J. Kreuzer for stimulating discussions, and the referees of this paper for their constructive comments. This work was supported by the Office of Naval Research under Contract Number N00014-82-K-0506.

## References

1. D.J. Ehrlich, R.M. Osgood, Jr. and T.F. Deutsch, *IEEE J. Quantum Electron.* **QE-16** (1980) 1233, and references therein.
2. F.A. Houle and T.J. Chuang, *J. Vac. Sci. Tech.* **20** (1982) 790;  
F.A. Houle, *Chem. Phys. Lett.* **95** (1983) 5.
3. R.D. Coombe and F.J. Wodarczyk, *Appl. Phys. Lett.* **37** (1980) 846.
4. D.J. Ehrlich, R.M. Osgood, Jr. and T.F. Deutsch, *Appl. Phys. Lett.* **39** (1981) 957;  
D.J. Ehrlich, R.M. Osgood, Jr. and T.F. Deutsch, *J. Vac. Sci. Tech.* **20** (1982) 738.
5. J.C. Hemminger, R. Carr and G.A. Somorjai, *Chem. Phys. Lett.* **57** (1978) 100.
6. M.E. Umstead and M.C. Lin, *J. Phys. Chem.* **82** (1978) 2047.
7. M.R. Baklanov, I.M. Beterov, S.M. Repinskii, A.V. Rzhanov, V.P. Chebotaev and N.I. Yurshina, *Dokl. Akad. Nauk SSSR* **216** (1974) 524 [*Soviet Phys.-Dokl.* **19** (1974) 312.]
8. M.S. Djidjoev, R.V. Khokhlov, A.V. Kiselev, V.I. Lygin, V.A. Namiot, A.I. Osipov, V.I. Panchencko and B.I. Provotorov in *Tunable Lasers and Applications*, Ed. H.A. Mooradian (Springer, Berlin 1976).
9. Z. Karny and R.N. Zare, *Chem. Phys.* **23** (1977) 321.
10. A.V. Khmelev, V.V. Apollonov, V.C. Borman, B.I. Nikolaev, A.A. Sazykin, V.I. Troyan, K.N. Firsov and B.A. Frolov, *Kvantovaya Elektron. (Moscow)* **4** (1977) 2271 [*Soviet J. Quantum Electron.* **7** (1977) 1302].

11. C.T. Lin and T.D.Z. Atvars, *J. Chem. Phys.* **68** (1978) 4233.
12. D.R. Betteridge and J.T. Yardley, *Chem. Phys. Lett.* **62** (1979) 570.
13. T. Kawai and T. Sakata, *Chem. Phys. Lett.* **69** (1980) 33.
14. T.J. Chuang, *J. Chem. Phys.* **74** (1981) 1453;  
T.J. Chuang, *J. Vac. Sci. Tech.* **18** (1981) 638.
15. M.E. Umstead, L.D. Talley, D.E. Tevault and M.C. Lin, *Opt. Eng.* **19** (1980) 94.
16. T.J. Chuang, *J. Chem. Phys.* **74** (1981) 1461.
17. J.P. Cowin, D.J. Auerbach, C. Becker and L. Wharton, *Surf. Sci.* **78** (1978) 545;  
G. Wedler and H. Ruhmann, *ibid.* **121** (1982) 464.
18. G.L. Kellogg, *J. Chem. Phys.* **74** (1981) 1479.
19. D. Zakett, A.E. Schoen, R.G. Cooks and P.H. Hemberger, *J. Am. Chem. Soc.* **103** (1981) 1295;  
K.L. Busch, S.E. Unger, A. Vincze, R.G. Cooks and T. Keough, *ibid.* **104** (1982) 1507.
20. R. Viswanathan, D.R. Burgess, Jr., P.C. Stair and E. Weitz, *J. Vac. Sci. Tech.* **20** (1982) 605.
21. S.D. Allen, J.O. Porteus and W.N. Faith, *Appl. Phys. Lett.* **41** (1982) 416.
22. J.W. McAllister and J. M. White, *J. Chem. Phys.* **58** (1973) 1496.
23. For an excellent review, see: D. Lichtman and Y. Shapira, *CRC Critical Rev. Solid State Mater. Sci.* **8** (1978) 93.
24. W.J. Lange and H. Reimersma, *Trans. AVS Vacuum Symp.* **8** (1961) 167.

- W.J. Lange, *J. Vac. Sci. Tech.* **2** (1965) 74.
25. R. Gauthier, M. Babout and C. Guittard, *Phys. Status Solidi (a)* **48** (1978) 459.
26. G.W. Fabel, S.M. Cox and D. Lichtman, *Surf. Sci.* **40** (1973) 571;  
Y. Shapira, S.M. Cox and D. Lichtman, *Surf. Sci.* **50** (1975) 503;  
N. Van Hieu and D. Lichtman, *Surf. Sci.* **103** (1981) 535.
27. T.E. Madey, R. Stockbauer, J.F. van der Veen and D.E. Eastman, *Phys. Rev. Lett.* **45** (1980) 187;  
D.P. Woodruff, M.M. Traum, H.H. Farrell, N.V. Smith, P.D. Johnson, D.A. King, R.L. Benbow and Z. Hurych, *Phys. Rev.* **B21** (1980) 6531;  
B.E. Koel, G.M. Loubriel, M.L. Knotek, R.H. Stulen, R.A. Rosenberg and C.C. Parks, *Phys. Rev.* **B25** (1982) 5551.
28. P.J. Feibelman and M.L. Knotek, *Phys. Rev.* **B18** (1978) 6531;  
P.R. Antoniewicz, *Phys. Rev.* **B21** (1980) 3811.
29. D. Menzel, *J. Vac. Sci. Tech.* **20** (1982) 538.
30. T.J. Chuang, *Surf. Sci. Rep.* **3** (1983) 1.
31. K.S. Kockelashvili, N.V. Karlov, A.N. Orlov, R.P. Petrov, Yu. N. Petrov and A.M. Prokhorov, *Pis'ma Zh. Eksperim. Teor. Fiz.* **21** (1975) 640. [*JETP Letters* **21** (1975) 302].
32. T.Gangwer and M.K. Goldstein, *SPIE* **86** (1976) 154;  
T.E. Gangwer, *Opt. Laser Technol.* **10** (1978) 81.
33. N.V. Karlov, R.P. Petrov, Yu.N. Petrov and A.M. Prokhorov, *Pis'ma Zh. Eksperim. Teor. Fiz.* **24** (1976) 289. [*JETP Letters* **24** (1976) 258].
34. K.S. Suslick, U.S. Patent 4,010,100 (1977).

35. D.B. McConnell, Ontario Hydro Research Div. Report, No. 76-516-K (1976).
36. J. Heidberg, H. Stein, E. Riehl and A. Nestmann, *Z. Physik. Chem. (NF)* **121** (1980) 145;  
J. Heidberg, H. Stein and E. Riehl in *Vibrations at Surfaces*, Ed. R. Caudano, J.-M. Gilles and A.A. Lucas (Plenum, New York, 1980);  
J. Heidberg, H. Stein and E. Riehl, *Phys. Rev. Lett.* **49** (1982) 666;  
J. Heidberg, H. Stein and E. Riehl, *Surf. Sci.* **126** (1983) 183.
37. (a) T.J. Chuang, *J. Chem. Phys.* **76** (1982) 3828;  
(b) T.J. Chuang and F.A. Houle, *J. Vac. Sci. Tech.* **20** (1982) 603;  
(c) T.J. Chuang and H. Seki, *Phys. Rev. Lett.* **49** (1982) 382;  
(d) H. Seki and T.J. Chuang, *Sol. State Comm.* **44** (1982) 473.
38. J. Heidberg and I. Hussla, *J. Electron Spectrosc. Related Phenomena* **29** (1983) 105.
39. T.J. Chuang, *J. Electron Spectrosc. Related Phenomena* **29** (1982) 125.
40. R.B. Hall, personal communication.
41. Reference [22] and p. 76 of ref. [30].
42. M. Wautelet, *Surf. Sci.* **95** (1980) 299.
43. M.S. Slutsky and T.F. George, *J. Chem. Phys.* **70** (1979) 1231;  
W.C. Murphy and T.F. George, *Surf. Sci.* **102** (1981) L46;  
J.-T. Lin and T.F. George, *Surf. Sci.* **107** (1981) 417.
44. C. Jedrzejek, K.F. Freed, S. Efrima and H. Metiu, *Surf. Sci.* **109** (1981) 191;  
G. Korzeniewski, E. Hood and H. Metiu, *J. Vac. Sci. Tech.* **2** (1982) 594.
45. J.-T. Lin and T.F. George, *J. Chem. Phys.* **72** (1980) 2554;

- T.F. George, J.-T. Lin, K.-S. Lam and C.-H. Chang, *Opt. Eng.* **19** (1980) 100.
46. H.J. Kreuzer and D.N. Lowy *Chem. Phys. Lett.* **78** (1981) 50.
47. (a) Z.W. Gortel, H.J. Kreuzer, P. Piercy and R. Teshima, *Phys. Rev.* **B27** (1983) 5066;  
(b) Z.W. Gortel, H.J. Kreuzer, P. Piercy and R. Teshima, *Phys. Rev.* **B28** (1983) 2119.
48. D. Lucas and G.E. Ewing, *Chem. Phys.* **58** (1981) 385.
49. K.C. Janda, *Advan. Chem. Phys.* **00** (1984) 000.  
K.E. Johnson, W. Sharfin and D.H. Levy, *J. Chem. Phys.* **74** (1981) 163, and references therein.
50. (a) M.P. Casassa, D.S. Bomse and K.C. Janda, *J. Chem. Phys.* **74** (1981) 5044;  
(b) M.P. Casassa, C.M. Western, F.G. Celii, D.E. Brinza and K.C. Janda, *J. Chem. Phys.* **79** (1983) 3227.
51. Visible and UV excitation may also be used to prepare van der Waals complexes in vibrationally excited states. These are also reviewed in ref. [49]. The experiments reported in ref. [50] concern only ground electronic state vibrational excitation.
52. M.P. Casassa, F.G. Celii and K.C. Janda, *J. Chem. Phys.* **76** (1982) 5295.
53. W.G. Breiland, M.D. Fayer and C.B. Harris, *Phys. Rev.* **A13** (1976) 383.
54. R.G. Greenler, *J. Chem. Phys.* **44** (1966) 310.
55. J.F. Blanke, S.E. Vincent and J. Overend, *Spectrochim. Acta* **32A** (1976) 163.

56. H.A. Pearce and N. Sheppard, *Surf. Sci.* **59** (1976) 205.
57. H. Ibach, *Surf. Sci.* **66** (1977) 56.
58. B.N.J. Persson and M. Persson, *Sol. State Comm.* **36** (1980) 175.
59. S. Efrima, *Surf. Sci.* **110** (1981) 56.
60. (a) K. Horn and J. Pritchard, *Surf. Sci.* **55** (1976) 701.  
(b) R. Ryberg, *Surf. Sci.* **114** (1982) 627.  
(c) D.P. Woodruff, B.E. Hayden, K. Prince and A.M. Bradshaw, *Surf. Sci.* **123** (1982) 397.  
(d) P. Hollins and J. Pritchard, *Surf. Sci.* **89** (1970) 486.  
(e) J. Pritchard, T. Catterick and R.K. Gupta, *Surf. Sci.* **53** (1975) 1.  
(f) A. Crossley and D.A. King, *Surf. Sci.* **95** (1980) 131.  
(g) R.A. Shigeishi and D.A. King, *Surf. Sci.* **58** (1976) 379.  
(h) H.-J. Krebs and H. Lüth, *Appl. Phys.* **14** (1977) 337.  
(i) A. Ortega, F. M. Hoffmann and A.M. Bradshaw, *Surf. Sci.* **119** (1982) 79.  
(j) A.M. Bradshaw and F.M. Hoffmann, *Surf. Sci.* **72** (1978) 513.  
(k) H. Pfnür, D. Menzel, F.M. Hoffmann, A. Ortega and A.M. Bradshaw, *Surf. Sci.* **93** (1980) 431.  
(l) R.A. Shigeishi and D.A. King, *Surf. Sci.* **62** (1977) 379.  
(m) K. Kretschmar, J.K. Sass, A.M. Bradshaw and S. Holloway, *Surf. Sci.* **115** (1982) 183.  
(n) R. Ryberg, *Chem. Phys. Lett.* **83** (1981) 423.  
(o) B.N.J. Persson and R. Ryberg, *Phys. Rev. Lett.* **48** (1982) 549.
61. B.N.J. Persson and M. Persson, *Surf. Sci.* **97** (1980) 609.
62. J.W. Gadzuk, *Phys. Rev.* **B24** (1981) 1651.
63. H. Metiu and W.E. Palke, *J. Chem. Phys.* **69** (1978) 2574.

64. L.E. Brus, *J. Chem. Phys.* **74** (1981) 737.
65. A.S. Pine and W.J. Lafferty, *J. Chem. Phys.* **78** (1983) 1541.
66. D.E. Brinza, B.A. Swartz, C.M. Western and K.C. Janda, *J. Chem. Phys.* **79** (1983) 1541.
67. J.H. Bechtel, *J. Appl. Phys.* **46** (1975) 1585;  
H.S. Carslaw and J.C. Jaeger, in *Conduction of Heat in Solids*, 2<sup>nd</sup> ed. (Oxford Univ. Press, London, 1959).
68. R.J. Abbott and D.W. Oxtoby, *J. Chem. Phys.* **70** (1979) 4703.
69. J.Y. Tsao and D.J. Ehrlich, *J. Chem. Phys.* **81** (1984) 4620;  
C.J. Chen and R.M. Osgood, *Appl. Phys. A* **31** (1983) 171;  
C. Fiori, *Phys. Rev. Lett.* **52** (1984) 2077.
70. T.J. Chuang and I. Hussla, *Phys. Rev. Lett.* **52** (1984) 2045.
71. K.A. Peralstine and G.M. McClelland, *Surf. Sci.* **134** (1983) 389.
72. B. Fain and S.H. Lin, *Chem. Phys. Lett.* **114** (1985) 497.
73. J.W. Gadzuk and A.C. Luntz, *Surf. Sci.* **144** (1984) 429;  
D.C. Langreth, *Phys. Rev. Lett.* **54** (1985) 126.

*CHAPTER 5*

**UV LASER-INDUCED PHOTOCHEMISTRY OF  
 $\text{Fe}(\text{CO})_5$  ON SINGLE CRYSTAL SURFACES**

## 1. Introduction

The photochemical modification of solid surfaces is a topic of much current and practical interest.<sup>1-6</sup> The use of lasers in this application brings the inherent sub-micron resolution to bear on the challenge of producing even smaller semiconducting devices. One particular area which has met with much success is the light-induced deposition of conducting metallic structures using volatile organometallic precursors.<sup>3-5</sup> There is a growing need, however, to examine these reactions under conditions that allow one to sort out contributions from various mechanisms such as photolysis, pyrolysis, electron-induced processes and ablation.

The metal carbonyls are of tremendous practical importance for deposition, being volatile sources of metal species which readily undergo photochemistry. The deposition of metallic films from the corresponding carbonyl has been reported.<sup>5,6</sup> The photochemistry of metal carbonyls is an extensive topic which spans both spectroscopic and dynamical characterization of the excited states and the synthetic generation of novel compounds.<sup>7-9</sup> Highly-reactive metal clusters have been generated in the gas phase by irradiation of the corresponding carbonyl aggregates.<sup>10,11</sup> Photocatalytic activity to isomerization has been demonstrated using a variety of metal carbonyls,<sup>12,13</sup> including  $\text{Fe}(\text{CO})_5$ .<sup>13</sup> The high photochemical activity exhibited by these compounds at easily accessible wavelengths is illustrated by attempts at multi-photon ionization<sup>14</sup> which succeed mostly in generating ionized metal atoms!

A potential problem for the stimulation of photochemical reactions at an interface is the ability of the solid to quench the photoexcited intermediate.

bulk solid of semiconductors and metals, in particular, possesses a variety of modes, active in the IR through the UV, for accommodating excess energy.<sup>15</sup> For instance, the excessively broadened electron-energy loss (EELS) lineshapes of excited electronic states of chemisorbed species are thought to be indicative of rapidly quenched excited states whose spectra are lifetime broadened by decay rates on the order of  $>10^{13} \text{ s}^{-1}$ .<sup>16</sup> Rates of chemical reactions may be orders of magnitude too slow to effectively compete with quenching mechanisms near surfaces which deplete excited state population on this timescale.

We have investigated the extent of the effect of molecule-solid energy transfer on a fast photochemical reaction, the ultraviolet photodissociation of  $\text{Fe}(\text{CO})_5$ . Three surfaces, sapphire ( $\text{Al}_2\text{O}_3$ ), silicon, and silver, were chosen for study, representing a wide range of energy transfer behavior: from very slow (an insulator, sapphire) to very fast (a nearly free electron metal, silver). There is extensive literature concerning the photochemistry of  $\text{Fe}(\text{CO})_5$  from which to draw, including reactions above other surfaces. The results we obtain are discussed in terms of the photochemistry observed in other systems as well as energy transfer considerations for the reaction.

## 2. Spectroscopy and Photochemistry of $\text{Fe}(\text{CO})_5$

The gas-phase absorption spectrum of  $\text{Fe}(\text{CO})_5$  and the relevant energetics are shown in Figure 1. The maximum at 280 nm ( $\epsilon_{abs} = 3900 \text{ M}^{-1}\text{cm}^{-1}$ ) is assigned to a metal-ligand charge transfer band (MLCT), while the weaker absorption to the red near 330 nm ( $\epsilon_{abs} \sim 500 \text{ M}^{-1}\text{cm}^{-1}$ ) is thought to be a ligand field transition.<sup>17,7</sup> The  $\text{N}_2$  laser excitation (337 nm) used in the reported experiments is thus expected

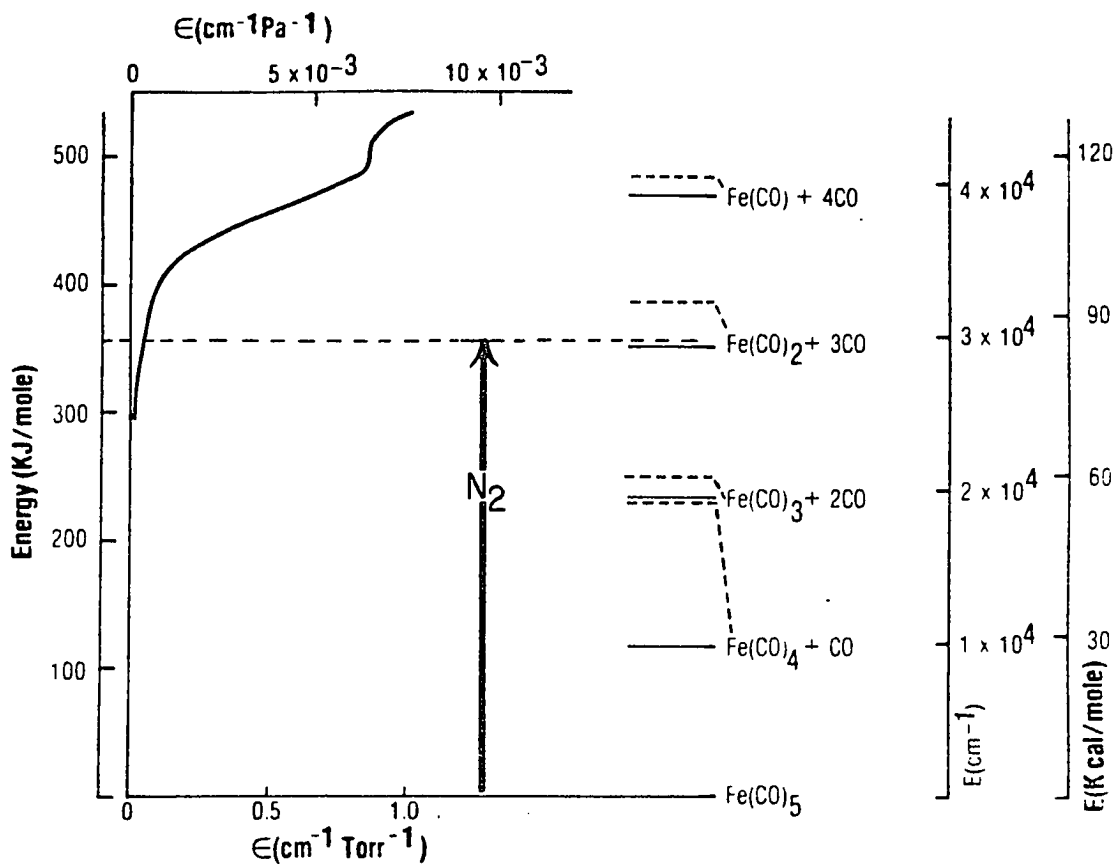


Figure 1. Absorption spectrum of  $\text{Fe}(\text{CO})_5$  with energetics of  $\text{Fe}(\text{CO})_x$  species (from Ref. [22a]).<sup>19</sup> Solid lines are for an average Fe-CO bond dissociation energy; the dashed lines are from Engleking and Lineberger.<sup>20</sup>

to excite the ligand field transition. These bands are broad and unresolved, indicating states are likely to be mixed in this region. Electron-impact spectra give some indication for triplet state character in analogous bands in  $\text{Cr}(\text{CO})_6$ ; preliminary spectra for  $\text{Fe}(\text{CO})_5$  were not conclusive about this point.<sup>18</sup> Not shown in Figure 1, an intense charge transfer band ( $\epsilon_{abs} = 15\,700\text{ M}^{-1}\text{cm}^{-1}$ ) is observed further in the UV with a maximum near 200 nm. The region of weak molecular absorption which is excited in our experiment serves to indicate the experimental sensitivity that is available.

Estimates for energy levels of the  $\text{Fe}(\text{CO})_x$  species are also included in Figure 1. Note that upon absorption of light at 337 nm, the  $\text{Fe}(\text{CO})_5$  molecule contains enough energy to lose at least 2 CO molecules.<sup>19</sup> Trapping experiments using  $\text{PF}_3$  have determined that excitation with light in the 352-192 nm range produces all possible fragments –  $\text{Fe}(\text{CO})_x$ ,  $x = 2, 3, 4$  – with branching ratios that suggest non-statistical distribution of internal energy in the  $\text{Fe}(\text{CO})_4$  fragment following initial prompt loss of CO.<sup>22</sup> The extent of decomposition has been verified by a gas-phase study in which  $\text{Fe}(\text{CO})_x$ ,  $x = 2, 3, 4$  species have been identified by IR absorption.<sup>23</sup> However, the presence of  $\text{PF}_3$  in the trapping experiments may influence the branching ratios since  $\text{PF}_3$  and CO have similar bond strengths to Fe, and the hot  $\text{Fe}(\text{CO})_4$  species might readily exchange the two ligands.

Of central importance in this study is the timescale of the initial photochemical decarbonylation step. The rate of energy transfer from an excited adsorbate to a substrate, especially with metals, is expected to be fast so photodissociation at the surface must be competitive. This criterion is fulfilled for  $\text{Fe}(\text{CO})_5$ , in which

the initial decarbonylation step is indeed rapid: from a multi-photon ionization study of the  $\text{Fe}(\text{CO})_5$  molecule, Whetten *et al.*<sup>24</sup> determined upper limits for the excited state lifetime and estimated that loss of CO occurs within 2.0 psec following excitation in the 300-310 nm region, and in less than 0.6 psec after irradiation in the 275-280 nm region. These values are derived from estimates of the up-pumping rate for second (ionization) photon absorption using the laser fluence and absorption intensity, and established the extremely fast (picosecond) nature of the dissociation timescale.

Extensive study of the UV and IR photochemistry of metal carbonyls in inert matrices has been conducted.<sup>8,9,25,27,31</sup> Unlike the gas phase behavior,  $\text{Fe}(\text{CO})_5$  irradiated in a matrix loses one CO molecule per UV photon, yielding either  $\text{Fe}(\text{CO})_4$  or a stable  $\text{Fe}(\text{CO})_4\text{-X}$  coordination complex with a matrix atom or molecule, **X** (e.g., **X** = Ar,  $\text{N}_2$  or  $\text{CH}_4$ <sup>8,9,25a,25b</sup>) filling the coordination sphere. Further irradiation in matrices with high  $\text{Fe}(\text{CO})_5$  concentration (1000:1) yields the  $\text{Fe}_2(\text{CO})_9$  and  $\text{Fe}_3(\text{CO})_{12}$  condensation species,<sup>25a</sup> as identified by separate IR characterization of the stable dimeric and trimeric species.<sup>25c,e</sup> In separate experiments,  $\text{Fe}_2(\text{CO})_9$  was also observed to photodissociate to yield  $\text{Fe}_2(\text{CO})_8$ .<sup>25d</sup> Additional photochemistry on the  $\text{Fe}_3(\text{CO})_{12}$  species has not been reported, as it seems the compound is not very photoactive,<sup>12</sup> in spite of intense bands which are present in the visible and UV.<sup>26</sup> Similar photochemical behavior has been exhibited by  $\text{Cr}(\text{CO})_6$  in the gas phase;<sup>9,27</sup> a fast initial decarbonylation step (< 100 nsec) is followed by production of  $\text{Cr}(\text{CO})_4$  from hot  $\text{Cr}(\text{CO})_5$ .<sup>28</sup> Formation of complexes of the highly-reactive  $\text{Cr}(\text{CO})_5$  species with inert ligands in the gas,<sup>29</sup> liquid<sup>30</sup> and

matrix-isolated phase<sup>31</sup> have been identified using detection of transients in the visible region. Similar characterization of visible and UV absorption of  $\text{Fe}(\text{CO})_4$  and its adducts has not been reported.

### 3. Experimental

#### 3.1 UHV chamber

An ultra-high vacuum (UHV) chamber was constructed for this study and is depicted in Figure 2. The chamber consists of two sections, a main chamber mounted on a pumping stack, both constructed by MDC of Mountain View, CA. The primary system pump was an Edwards E04 4" diffusion pump backed by a 2-stage direct-drive rotary pump (Alcatel Z-2008-A). The diffusion pump system is extensively interlocked to prevent pump fluids from reaching the main chamber, especially the rotary pump which can be automatically isolated by a pneumatic valve with position indicator (MDC AV-103-P). Above the diffusion pump is a right-angle Vacuum Generators liquid nitrogen cold trap (CCT-100V), which also includes an integral gate valve to isolate the pump and trap, or throttle the pumping speed for sputtering or dosing applications. The trap has a 16 hour hold time and, more importantly, all surfaces exposed to the vacuum chamber remain cold until the trap becomes completely empty. The pump-trap combination has a quoted pumping speed of  $200 \text{ l}\cdot\text{s}^{-1}$ . Rough pumping is accomplished using a pair of cryosorption pumps isolated by a bakeable metal seal valve (Granville-Phillips Mdl. 204). The cryopumps evacuate the chamber to  $\sim 10^{-4}$  Torr at which point the diffusion pump can be used to bring the pressure into the  $10^{-7}$ - $10^{-8}$  Torr range. After bakeout to  $200^\circ \text{ C}$  the pressure drops into the  $10^{-9}$  Torr range at which point a titanium

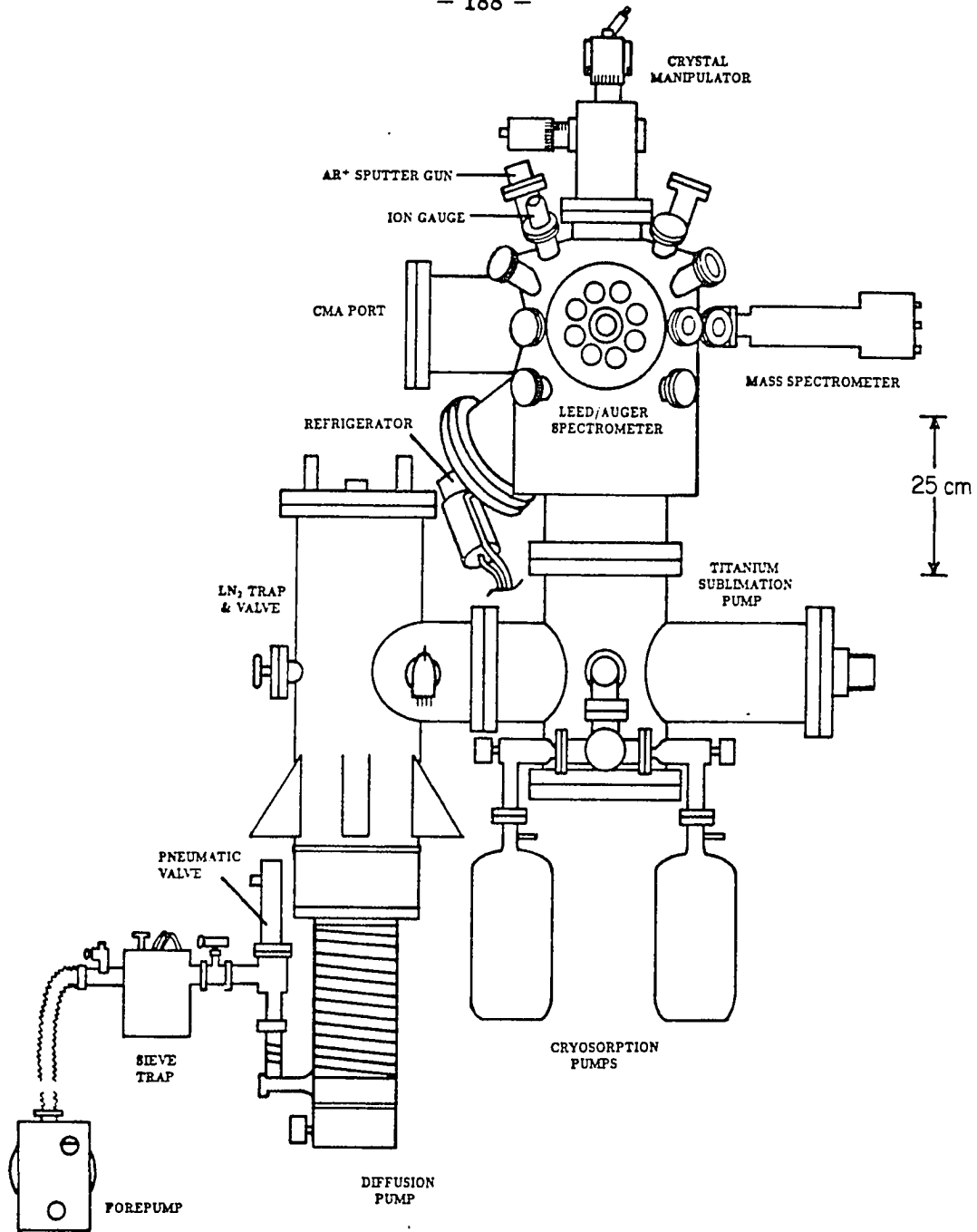


Figure 2. Diagram of the UHV apparatus.

sublimation getter pump works very effectively to achieve the base pressure of  $1-2 \times 10^{-10}$  Torr. At this pressure  $H_2O$ ,  $CO$ ,  $H_2$  and  $CO_2$  are the main species present. In addition, the helium closed-cycle refrigerator (see below) acts as a cryopump for condensibles during operation.

The main chamber is a variation of the standard Varian-type design (12" diameter), to which were added optical access ports, plus a second level to accommodate the helium refrigerator. The analytical tools in the chamber are: LEED/Auger screens (Varian), residual gas analyzer (VG SX-200 mass spectrometer),  $Ar^+$ -ion sputter gun (Perkin Elmer), and nude ionization gauge (Granville Phillips Mdl. 271). Two gas inlets are available, one for dosing from background, the other for directed doses through a multichannel array. For laser-surface interaction, entrance and exit ports at optimal angles for both metal ( $\theta = 88^\circ$  in the IR,  $65^\circ$  in the UV) and semiconductor ( $\theta = 75^\circ$ ) surfaces are provided. Differentially-pumped uncoated  $BaF_2$  flats (6 mm thickness) mounted on the  $75^\circ$  ports were used as laser entrance and exit windows throughout the course of the work reported here.

The low-energy electron diffraction (LEED) screens and electron gun are used for observation of surface order. The same apparatus is employed for Auger electron spectroscopy (AES) to monitor surface cleanliness. Home-built electronics for the electron pass energy ramp, amplifier and screen modulation voltage, plus a high-voltage supply (Kepco OPS-2000B) augment the Varian LEED screen and electron gun control modules. The mass spectrometer acts as a residual gas analyzer (to monitor chamber cleanliness), thermal desorption spectrometer, and product

detector for both the IR photodesorption experiments (see Chapter 4) and the UV photochemistry experiments summarized here. A channeltron electron multiplier provides high gain to amplify the ion current generated by an electron-impact ionization source. A Faraday cup is also available for gain calibration. A glass integrating nosecone<sup>32</sup> was fit around the ionization region to restrict the pumping speed, increase the dwell time of product molecules, and thus increase the sensitivity of the mass spectrometer at the expense of time resolution. The mass range of the quadrupole (0-200 amu) is sufficient to resolve the parent and fragment peaks of  $\text{Fe}(\text{CO})_5$  (196 amu), but not great enough to observe larger  $\text{Fe}_x(\text{CO})_y$  ( $x \geq 2, y \geq 4$ ) cluster products that may be formed.

For cryogenic cooling of the crystal sample, a helium closed-cycle refrigerator was employed. The refrigerator provides two cold stations of  $\sim 15^\circ \text{K}$  (2 W of power for sample cooling) and  $\sim 77^\circ \text{K}$  (25 W for heat shrouds and crystal support pre-cooling). The refrigerator was retro-fitted onto a Conflat flange by Cryosystems, Inc., for UHV compatibility. A bakeout control system was constructed to allow unattended baking of the UHV chamber to  $200^\circ \text{C}$  without adverse effects to the refrigerator cold head. The controller is described in detail in thesis appendix 2.

The manipulator assembly for crystal samples is shown in Figure 3a. The mount was appended to a standard manipulator (Huntington PM-600-XYZ-RC), and configured for a 2.5'' sample offset from the rotation axis. The coaxial motion provided by the manufacturer is levered to allow tilt of the sample, in addition to the  $x, y, z$  and rotary motions. The “high temperature” mount depicted in Figure 3(a) was designed to afford adequate cooling within the demands of heating the sapphire

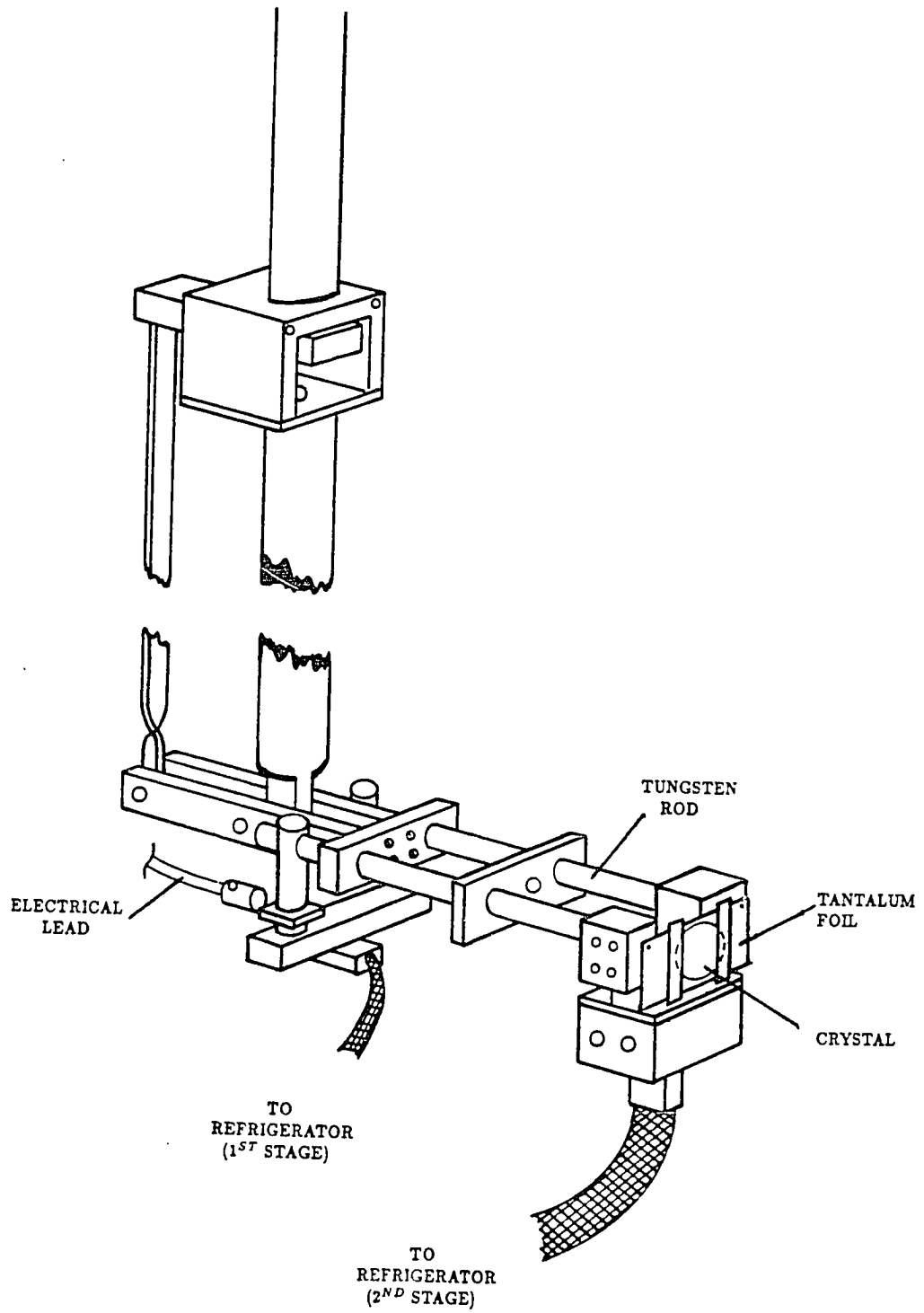
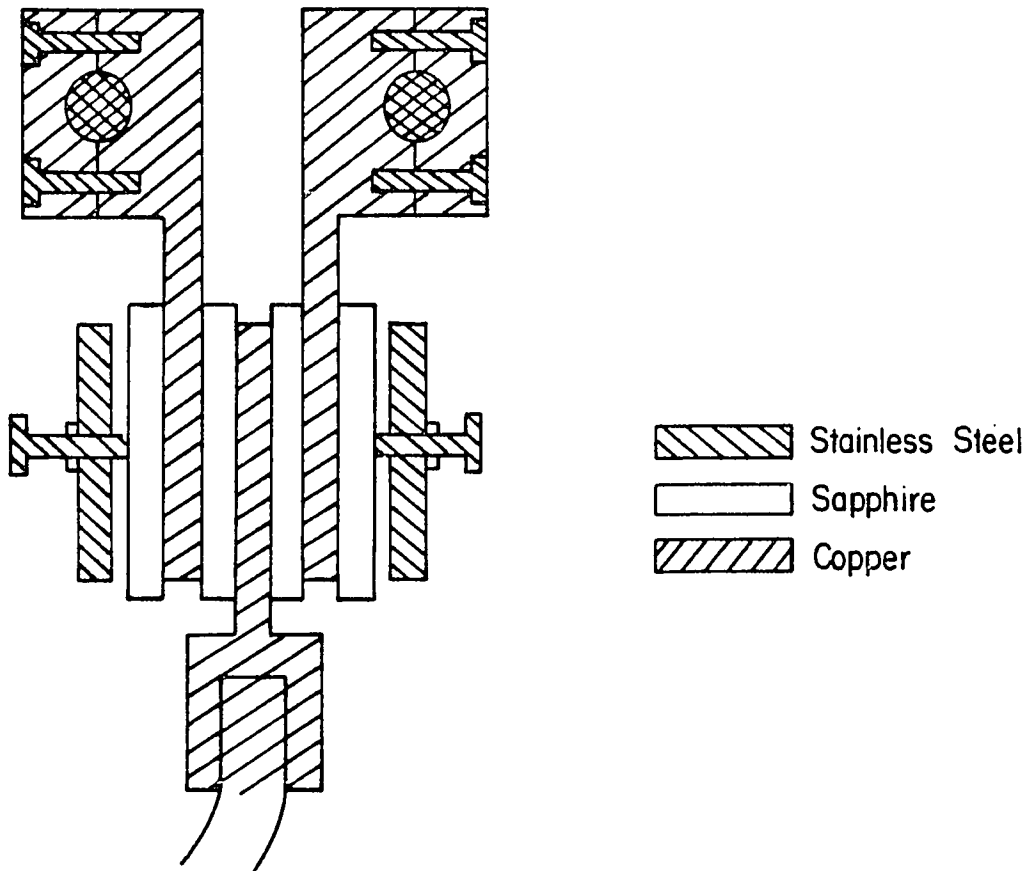


Figure 3a. Diagram of the crystal holder and manipulator.



**Figure 3b.** Detail of the coupling between the helium closed-cycle refrigerator and the crystal support rods. Polished sapphire flats provide both electrical isolation and good thermal contact at low temperature.

and silicon crystals to  $\geq 1000^\circ \text{C}$ ; since this is above the melting point of copper, direct thermal contact with the copper braid assembly to the refrigerator (as was the case with a “low temperature” mount used for IR photodesorption experiments) was not possible. Sapphire spacers are employed in the cooling path to both provide electrical isolation and act as a thermal switch- good thermal conductivity at low temperature for sample cooling, poor thermal conductivity above room temperature to isolate the copper braid during sample heating. Figure 3(b) shows the refrigerator connection in detail. All copper is OFHC, except the flexible braids to the two refrigerator stages which are 99.999% (5N) pure.<sup>33</sup> The tungsten support rods and large diameter copper electrical leads are pre-cooled to  $\sim 200 \text{ K}$  using the first stage of the refrigerator.

The crystal is mounted using a sheet of 0.001" Ta foil which provides resistive heating of the samples for cleaning and thermal desorption measurements. The foil is sandwiched between the crystal sample and a sapphire flat, and this assembly is banded together using Ta foil strips spot-welded to the main heater foil. Thermocouple pairs (Ch-Al) for temperature measurement are spot-welded under the Ta strips. Temperatures of 120-140 K were obtained with this configuration. The time for the crystal to cool to this temperature was 1-1/2 hours from the start of the refrigerator and 10-20 minutes after a flash to high temperature.

Two sample inlets were used throughout the course of this study. During initial experiments, vapor was dosed from background through a leak valve (VG MD-7R) and 1/8-inch stainless tube; however, this method admitted a large load of gases such as  $\text{Fe}(\text{CO})_5$  into the chamber. Later studies utilized a calibrated dosing line

which was equipped with a multichannel array doser to direct a significant fraction (0.1 - 0.3) of the gas sample onto the crystal face.<sup>34</sup> An 80  $\mu\text{m}$  diameter capillary tube limited the flow from a calibrated volume, so the flux of molecules emitting from the multichannel array could be determined by monitoring the pressure drop in the volume. With a pressure of 1.0 Torr in the calibrated volume,  $1.1 \times 10^{14}$  molecules/sec are emitted from the doser.

### *3.2 Sample Preparation*

A silver single crystal boule was obtained courtesy of the W.H. Weinberg group.<sup>35</sup> Since enhanced photochemistry can be effected by a roughened metal surface, effort was expended to polish, clean and characterize the silver crystal to eliminate the effects of surface roughness. A 2 mm thick disk of 1/2" diameter was spark cut and mechanically polished down to 0.25  $\mu\text{m}$  using a series of abrasive papers and diamond paste. The orientation was within  $1/2^\circ$  as determined by Laue X-ray backscattering. The surface that resulted was visibly scratched, presumably on the 1.0 - 0.25  $\mu\text{m}$  scale. Chemical polishing (100 ml saturated  $\text{K}_2\text{Cr}_2\text{O}_7$ , 2 ml saturated  $\text{NaCl}$ , 10 ml  $\text{H}_2\text{SO}_4$  diluted to twice the volume<sup>36</sup>) gave a highly reflective surface and removed some of the mechanical damage, as could be seen by eye and in the clarity of the Laue spots. Electrochemical polishing as implemented here (12 g  $\text{KCN}$ , 12 g  $\text{Na}_2\text{CO}_3$  in 200 ml  $\text{H}_2\text{O}$ <sup>36</sup>) tended to give a matted, milky appearance to the surface and was not used in the final polish sequence. The crystal was rinsed with ethanol after mounting and just prior to admission into the chamber. Cleaning in vacuum was accomplished using standard procedures.<sup>37-39</sup> Combinations of mild heating ( $220^\circ \text{C}$ ) in  $10^{-6}$  Torr  $\text{O}_2$  to remove surface carbon,<sup>38</sup> room temperature

dosing with CO to “clean off” atomic oxygen,<sup>39</sup> and cycles of Ar<sup>+</sup>-ion sputtering followed by annealing at 300° C, resulted in a clean silver surface as determined by Auger spectroscopy (Figure 4). The resolution was high enough to differentiate between the silver Auger transition at 262 eV and the carbon peak at 272 eV. The ratio of the three Ag peaks was ~7:2:1. The LEED pattern obtained from the clean and annealed crystal (Figure 5) indicates the presence of (110) ordering on the 50-100 Å dimension.<sup>40</sup> No evidence of faceting was detected.<sup>41</sup> However, the HeNe alignment laser reflected from the surface was not sharp, indicating roughness on the 0.6 μm scale.

The sapphire and silicon crystal samples were obtained as polished wafers and were not polished further. They were cleaned by heating in vacuum: Al<sub>2</sub>O<sub>3</sub> (obtained from Union Carbide cut ~30° to the *c* axis) to ~1050° C;<sup>42</sup> Si(100) (p-doped, from California Technical Services) to 900° C.<sup>43</sup> The cleanliness of the Si surface was verified by AES, but only faint LEED spots were observed. Charging effects caused difficulties in obtaining LEED and Auger spectra of Al<sub>2</sub>O<sub>3</sub>.

Fe(CO)<sub>5</sub>, obtained from Alfa Chemical (99.5 %), was used without further purification except for freeze-pump-thaw cycles to remove excess CO before each filling of the dosing volume. The observed cracking pattern of Fe(CO)<sub>5</sub> during a dose is shown in Figure 6, and is in reasonable agreement with published mass spectra.<sup>44</sup> The purity of the Fe(CO)<sub>5</sub> delivered to the chamber was constantly monitored by observing the intensity ratio between *m/e* 28 (CO<sup>+</sup>) and *m/e* 56 (Fe<sup>+</sup>) peaks and experiments were conducted with doses that exhibited approximately a 5:1 ratio of CO<sup>+</sup> : Fe<sup>+</sup> ratio which was the lowest value observed. Doses were

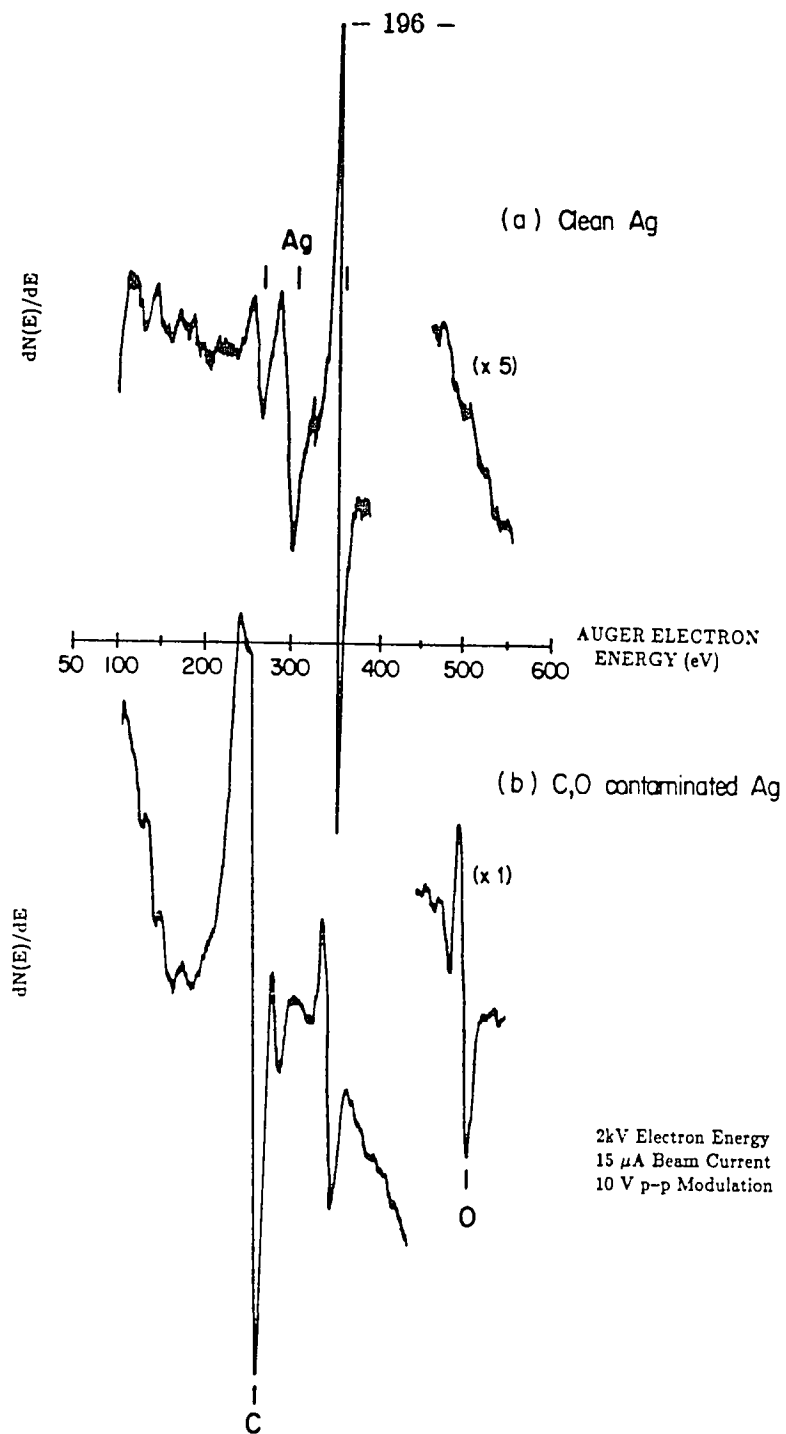
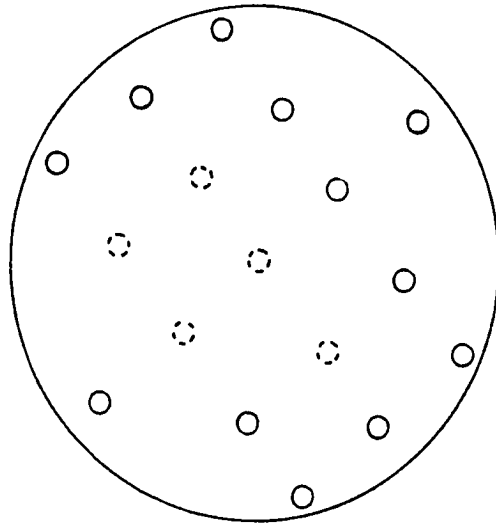
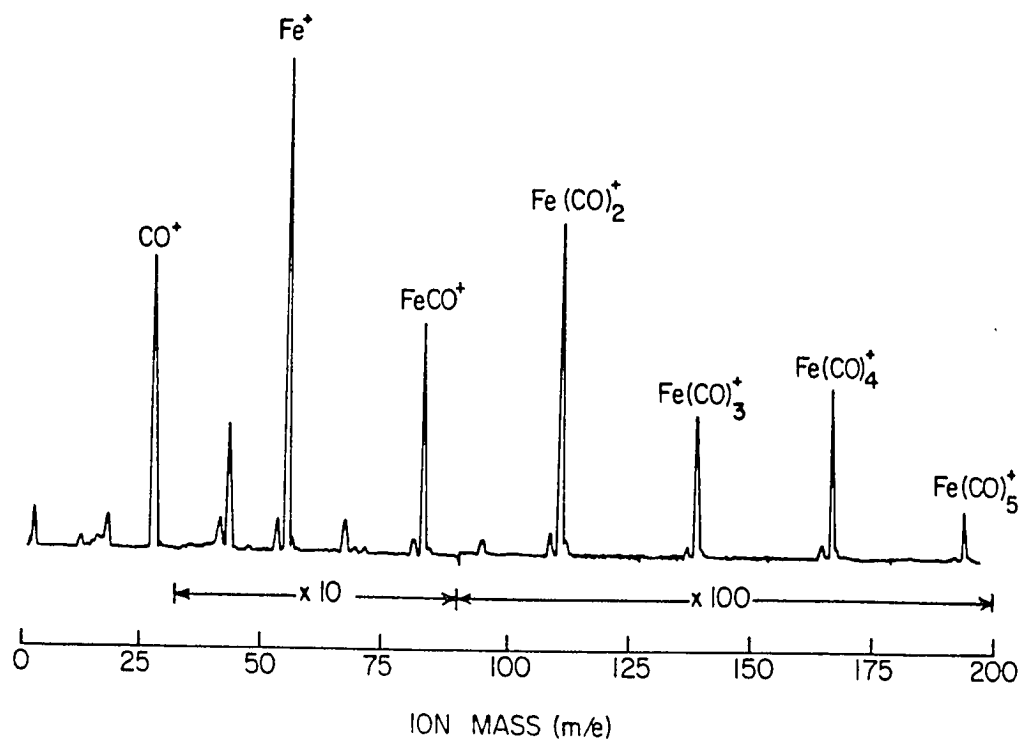


Figure 4. Auger electron spectrum of the (a) clean and (b) dirty Ag(110) surface. The C,O-contaminated surface was observed initially after chamber bakeout, the clean surface after extensive cleaning (see text). The three Ag features occur at 365, 302 and 263 eV, carbon and oxygen at 273 and 510 eV, respectively.



**Figure 5.** Sketch of LEED pattern obtained with Ag(110). The square array of spots is indicative of the (110) orientation. The interior (dashed) spots are extrapolations, being occluded by the crystal holder.



**Figure 6.** Mass spectrum of  $Fe(CO)_5$  during gas dose.  $^{54}Fe(CO)_x$  features can be seen to lower mass from the main  $^{56}Fe(CO)_x$  peaks.

administered to the crystal face with no line-of-sight between the crystal face and hot filaments. The filaments were switched off during longer ( $> 1$  min) doses.

### *3.3 Thermal Desorption Experimental*

Thermal desorption spectra of  $\text{Fe}(\text{CO})_5$  were obtained on the  $\text{Al}_2\text{O}_3$  and silicon crystal samples. A particular ion mass signal detected at the mass spectrometer is monitored as the temperature of the crystal is ramped. Because the entire crystal mount in the vicinity of the crystal and heater are at the same low temperature during a dose, adsorption by other surfaces may interfere with the thermal desorption spectrum. However, desorption from the crystal sample can be isolated by using a glass integrating nosecone<sup>17</sup> to monitor desorption. The sample was moved directly in front of the nosecone aperture, within 1 mm. Because of the lower local pumping speed due to the nosecone, a slow heating rate (2 K/sec) is employed, compared to a more common rate of 10 K/sec without nosecone. The crystal temperature ramp was manually controlled.

### *3.4 Photochemistry Experimental*

A schematic of the photochemistry experiment is depicted in Figure 7. A Molelectron UV-400  $\text{N}_2$  laser outputs 400 kW of 337.1 nm light in a 10 nsec pulse, but the output spot size is too large for irradiation of the crystal samples. Care was taken to reduce and shape the spot size with iris diaphragms and apertures so that only the crystal surface was irradiated. The resultant spot is approximately  $1 \times 3$  mm entering the chamber and spreads to  $4 \times 3$  mm across the crystal face due to the angle of incidence ( $75^\circ$ ), and provides  $70 \mu\text{J}\cdot\text{cm}^{-2}$  of energy density at the crystal face. The use of a 30 cm f.l. lens (the crystal was *not* at the focal point)

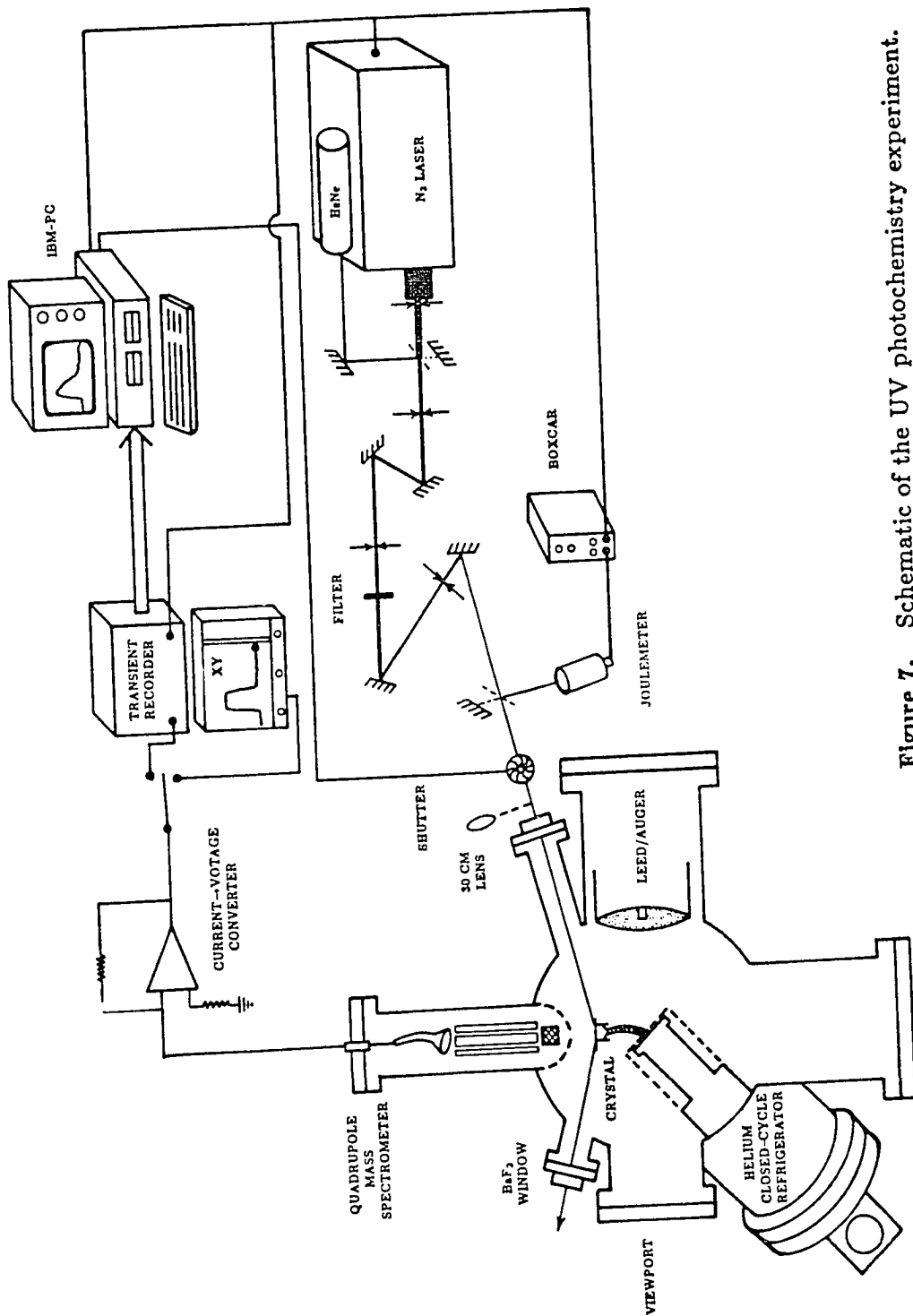


Figure 7. Schematic of the UV photochemistry experiment.

was estimated to increase the energy density by a factor between 10 and 100, the uncertainty arising from inability to accurately measure the spot size. Background laser-induced signals of  $m/e$  28 ( $\text{CO}^+$ ) and  $m/e$  44 ( $\text{CO}_2^+$ ) were observed upon laser irradiation, probably from stray UV which induces photodesorption from metal surfaces in the chamber.<sup>45</sup> The background  $\text{CO}^+$  intensity was never more than 5% of the photolysis signal. A He/Ne laser is used for initial alignment of the laser, then for reproducible placement of the crystal sample back to the irradiation position in front of the mass spectrometer. A calibrated pyroelectric joulemeter (Cooper Lasersonics J3) with quartz condenser lens and in combination with a boxcar integrator (Stanford Research Systems SR250) monitors the laser pulse energy. A set of quartz neutral density filters is used to variably attenuate the laser power.

The pulse of mass intensity generated by the laser was observed as a current pulse from the channeltron multiplier which was in most cases amplified by a current→voltage converter (Keithley Mdl. 427,  $10^4$ - $10^{10}$  volts/amp, 0.01-300 msec risetime). The output of the amplifier was fed into a chart recorder for yield measurements, or a transient digitizer (Biomation Mdl. 805) for waveform recording. The digitizer was interfaced to an IBM-PC through a TecMar Industries Labmaster board and a home-built interface. A fast amplifier (100 MHz, LeCroy TTB1000) was obtained for time-of-flight curve measurements.

## 4. Results

### 4.1 *Thermal Desorption*

An example of thermal desorption traces obtained during this study are shown

in Figure 8, for the case of  $\text{Fe}(\text{CO})_5$  on sapphire. The  $m/e$  56 signal is displayed as a function of the crystal temperature which is monitored by an attached  $\text{Ch-Al}$  thermocouple. The slow heating rate necessary for use with the glass nosecone configuration was controlled manually and causes some variation in the peak shapes and position (e.g., Figure 8, between 1.1 and 2.3 L, and the slightly odd multilayer peak shape of the 140 L profile). Thermal desorption was thus employed as a qualitative gauge of dosages and for observing the onset of multilayer adsorption. Doses are reported in units of Langmuirs ( $1 \text{ L} = 10^{-6} \text{ Torr-sec}$ ), as determined using the uncorrected ion gauge pressure for background doses and extrapolation of these values using the area of the thermal desorption curves for coverages from the multichannel array doser.

The desorption profiles of Figure 8 indicate the presence of two binding states for  $\text{Fe}(\text{CO})_5$  over sapphire, a low coverage state which is seen to desorb at about 260-280 K, and a second state which exists at higher coverage and desorbs at lower temperature,  $\sim 225 \text{ K}$ . From the photochemical behavior (*vide infra*) we designate the two states as being due to species bound directly to the surface layer (first monolayer) and subsequent  $\text{Fe}(\text{CO})_5$  layers condensed on top of the initial layer. The two states yield equal thermal desorption intensity at a dose of 21 L, indicating 10 L is roughly equivalent to a monolayer (which matches estimates of coverage from the laser experiments). This correlates to dosing the crystal face with  $\sim 30\%$  of the flux from the array doser and assuming unit sticking probability. At crystal temperatures near 140 K large multilayers were not stable to desorption on the time scale of the laser experiment causing a varying background in some cases.

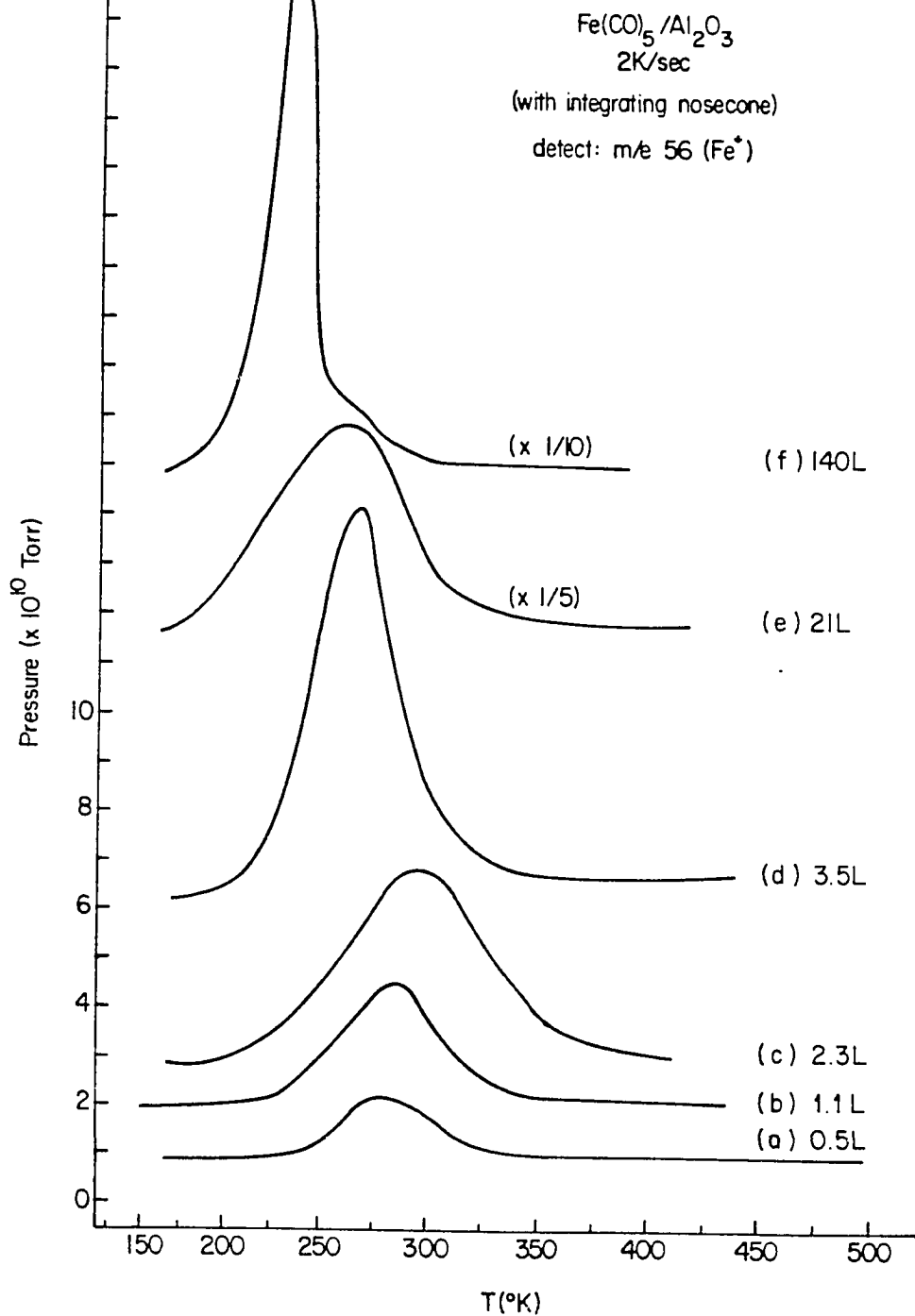


**Figure 8.** Thermal desorption spectra of  $\text{Fe}(\text{CO})_5$  on  $\text{Al}_2\text{O}_3$ . The different binding energies of surface adsorbates and multilayer species can be distinguished from the shift in the temperature of maximum desorption rate.

The energy of desorption can be estimated using the first-order Redhead analysis which yields,<sup>46</sup>

$$E/RT_p = \ln \frac{\nu_1 T_p}{\beta} - 3.64, \quad (1)$$

where  $E$  is the energy of desorption,  $T_p$  is the peak of the thermal desorption profile,  $\beta$  is the heating rate in K/sec, and  $\nu_1$  is the frequency factor, usually assumed to be  $10^{13} \text{ s}^{-1}$ . A first-order desorption rate is assumed for the surface and adsorbates used in these experiments. For a temperature of maximum desorption of 250 K, heating rate of 2 K/sec and frequency factor of  $10^{13}$ , the energy of desorption is 16 kcal/mole. This estimate gives a value that appears to be too large, considering that  $\text{Al}_2\text{O}_3$  is expected to exhibit only weak chemisorption to non-ionic species.<sup>47,48</sup> The heat of vaporization of  $\text{Fe}(\text{CO})_5$  (8.7 kcal/mole) and  $\text{CH}_3\text{OH}$  (8.4 kcal/mole) are quite similar,<sup>49</sup> and multilayers of  $\text{CH}_3\text{OH}$  are observed to desorb at  $\sim 140$  K. This value is more consistent for the temperature of maximum desorption than what we observe as the peak value of the thermal desorption profiles given our observation that the multilayers slowly desorb when the crystal temperature is near 130 K. The temperature of maximum desorption for  $\text{Fe}(\text{CO})_5$  on silicon has been determined by other workers to be 170 K,<sup>51</sup> and multilayers will certainly desorb at lower temperature. Finally, the other analytical techniques available, LEED and Auger, did not detect the presence of adsorbed  $\text{Fe}(\text{CO})_5$ . This is consistent with a previous study<sup>52</sup> which found  $\text{Fe}(\text{CO})_5$  to be molecularly desorbed by the flux from the electron gun.

#### 4.2 *UV photochemistry on surfaces*

The results of a typical photochemistry experiment, obtained for  $\text{Fe}(\text{CO})_5$  on

Si(100), are depicted in Figure 9. Figure 9(a) shows an XY-recorder trace of the  $m/e$  28 pressure as the laser shutter is toggled open and closed. The  $N_2$  laser pulses at 10 Hz, and the current pulses are averaged by the 300 msec time constant of the current-voltage converter (see Figure 3), giving the signal that appears continuous in time. When focussing lens is not used, the fraction of adsorbates that is photolyzed per pulse is small and the CO flux into the mass spectrometer remains constant. With this configuration, fluence dependences (*vide infra*) could be obtained using a single dose of  $Fe(CO)_5$ .

The bottom two traces (Figure 9, (b) and (c)) are typical of the response to a single laser pulse as observed using the transient recorder. The time constant of the current-voltage converter is lowered ( $\sim 15\mu\text{sec}$ ) and the waveform is averaged with the computer (1000 shots for those displayed in Figure 9). With the nosecone in place (Figure 9(b)), the time response of the signal is dominated by the pumping time constant within the nosecone volume,  $\sim 10$  msec. In the absence of the nosecone, the desorption signal becomes a measure of the flight time of product species between the crystal and mass spectrometer. It was determined, however, that even under our conditions a significant fraction of the time-of-flight curve was due to molecules which reach the mass spectrometer indirectly. Thus, translational energy distributions could not be obtained for the product CO molecules.

#### 4.2.1 *Si(100)*

Our initial results, summarized in Figure 10, were obtained for  $Fe(CO)_5$  dissociation on the Si(100) surface. Experiments were employed with the lens in place. Under these irradiation conditions, the observed  $m/e$  28 signal

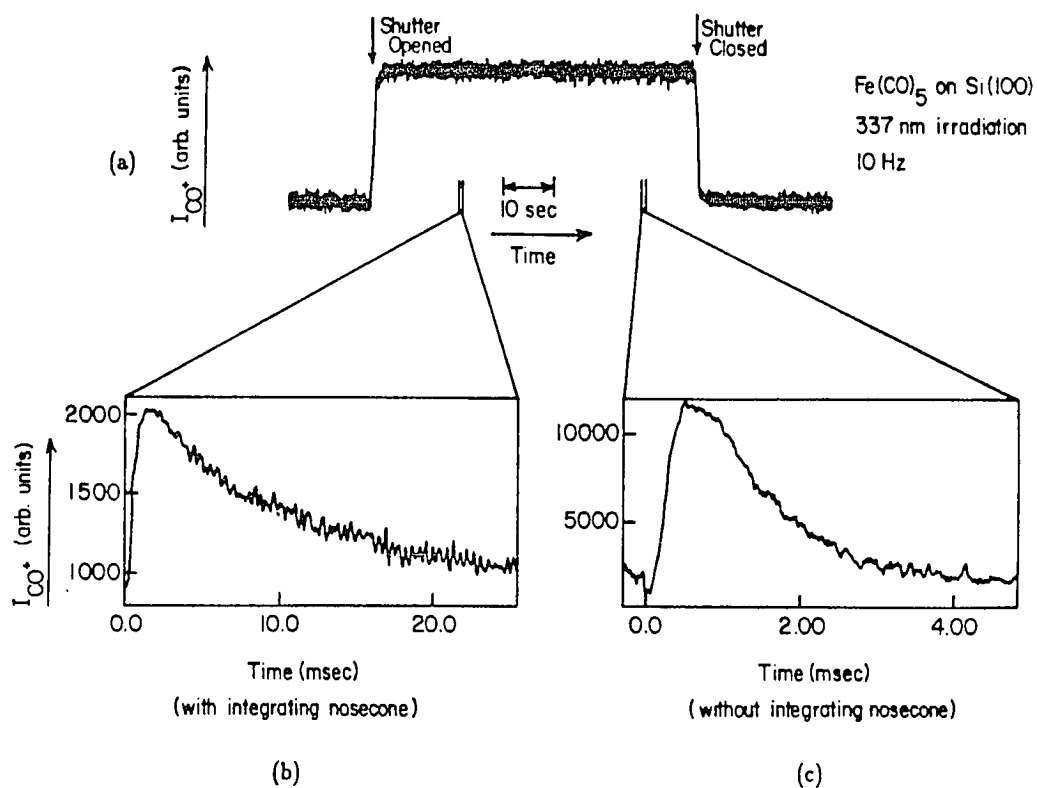


**Figure 9.** UV photochemistry signals,  $Fe(CO)_5$  on Si(100). (a) The top trace is an XY recorder trace of the CO pressure (300 msec time constant). The bottom waveforms are pressure bursts from individual laser shots, (b) with and (c) without the glass nosecone enclosing the mass spectrometer.

ANNEALING PHENOMENON:  $\text{Fe}(\text{CO})_5/\text{Si}(100)$

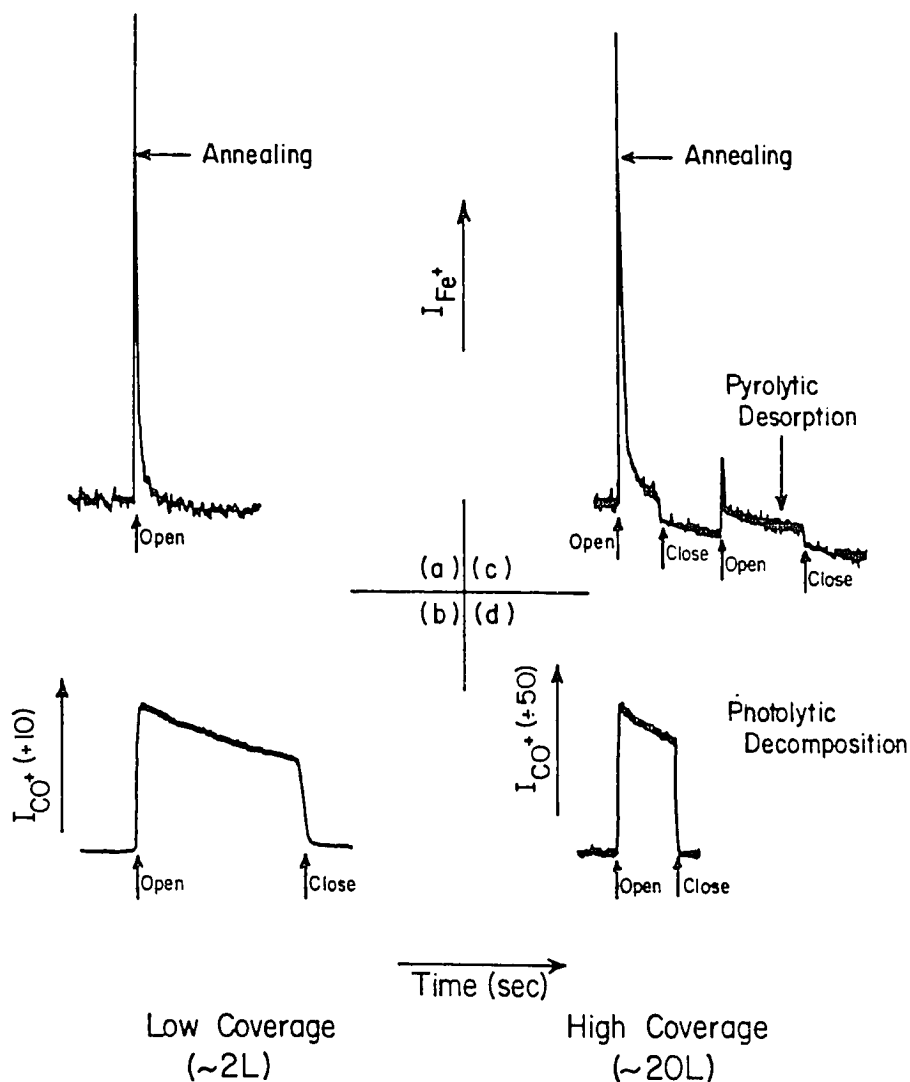


**Figure 10.** Observation of an annealing phenomenon  $\text{Fe}(\text{CO})_5$  on  $\text{Si}(100)$ . At low coverage (a) a burst of Fe-containing molecules occurs upon the first few laser shots, while (b) the CO flux is fairly constant in time. With coverage greater than one monolayer (c) a steady  $\text{Fe}^+$  signal is observed in addition to the initial pulse while (d) the CO flux is greater due to the higher coverage.

(Figure 10(b),(d)) decreases exponentially with time as the surface adlayer is depleted with the high laser fluence ( $\geq 700 \mu\text{J}\cdot\text{cm}^{-2}$ ). The observed signal does not return to the baseline, however, indicating a secondary process which exhibits an effective cross-section at least 10 times smaller than the primary dissociation process. Estimation of the dissociation cross section can be made using:

$$I/I_0 = \exp(-\Phi \sigma t) \quad (2a)$$

where  $\sigma$  is the dissociation cross-section (which equals that of the absorber for unity quantum yield),  $t$  is the time and  $\Phi$  is the photon flux. A plot of the logarithm of the observed  $\text{CO}^+$  yield *vs.* time should give a straight line with slope  $-\Phi\sigma$  for a process characterized by a single cross section. What is observed for the dissociation yield of  $\text{CO}^+$  from  $\text{Fe}(\text{CO})_5$  on  $\text{Si}(100)$  is a curve whose slope decreases at longer times ( $t \geq 60$  sec). Fits to the yield of various experiments at short times yield slopes of  $-(0.02 - 0.04)$ . Since the photon flux of the focussed laser is not well determined, we assume the  $\text{Fe}(\text{CO})_5$  gas phase absorption cross section of  $(1 - 2 \times 10^{-18} \text{ cm}^{-221,54})$  and from the slope determine a range for the photon flux of  $\sim 1 - 4 \times 10^{15}$  photons  $\text{cm}^{-2} \text{ sec}^{-1}$ ; this is a factor of 10 - 40 greater than the non-focussed laser case, and is within our estimate of the photon flux for the focussed beam at the crystal face. Thus, the gas-phase absorption strength is consistent with the observed  $\text{CO}^+$  yield. Similar curves were also obtained in the case of  $\text{Fe}(\text{CO})_5$  dissociation on  $\text{Al}_2\text{O}_3$  with the focussed laser.

Figures 10(a) and 10(c) document the observation of iron-containing species which are desorbed by UV radiation. At low coverages (less than a monolayer; Figure 10(a)), an  $\text{Fe}^+$  signal is only observed during the initial few laser pulses. At

higher coverages (2 or more monolayers; Figure 10(c)) laser irradiation causes a constant flux of Fe-containing compounds to be desorbed in addition to the large initial burst. Attempts to observe condensation photoproducts – that is, compounds containing  $\text{Fe}_x$ ,  $x = 2, 3$  – were not successful. The mass coincidence between Fe (m/e 56) and  $2^*\text{CO}_2$  (m/e 28) precludes detection at the  $^{56}\text{Fe}_2^+$  ion mass and we did not observe mass intensity of desorbing products at isotopic  $\text{Fe}_2^+$  masses due in part to the low intensity of the secondary isotopes (e.g.,  $I(^{54}\text{Fe}^{56}\text{Fe}) \sim 0.06 I(^{56}\text{Fe}_2)$ ).

#### 4.2.2 $\text{Al}_2\text{O}_3$

Results obtained on the  $\text{Al}_2\text{O}_3$  surface using the unfocussed shaped output of the  $\text{N}_2$  laser are shown in Figures 11 and 12. The power dependence of the  $\text{CO}^+$  yield (Figure 11) obtained by inserting neutral density filters in the laser beam is normalized to the  $\text{CO}^+$  yield at  $70 \mu\text{J}\cdot\text{cm}^{-2}$  fluence. A straight line is obtained at all coverages, some of which are plotted in Figure 11. This indicates that the dissociation is a one-photon process, and that the  $\text{Fe}(\text{CO})_5$  layer is optically thin: for negligible fraction dissociated, the observed  $\text{CO}^+$  signal is the limit of the exponential of Eq. 3:

$$I_{obs} \sim -\Phi \sigma t \quad (2b)$$

The evaluation of Eq. 4 for the unfocussed laser fluence and the molecular absorption of gas-phase  $\text{Fe}(\text{CO})_5$  gives a value of  $2.3 \times 10^{-4}$  as the fraction of the initial coverage that is dissociated per pulse. This value is consistent with estimates for a monolayer surface coverage ( $1.2 \times 10^{14}$  molecules/ $\text{cm}^2$ ), the flux of CO molecules into the nosecone ( $2 \times 10^{10}$  molecules/sec) and the efficiency of the collection

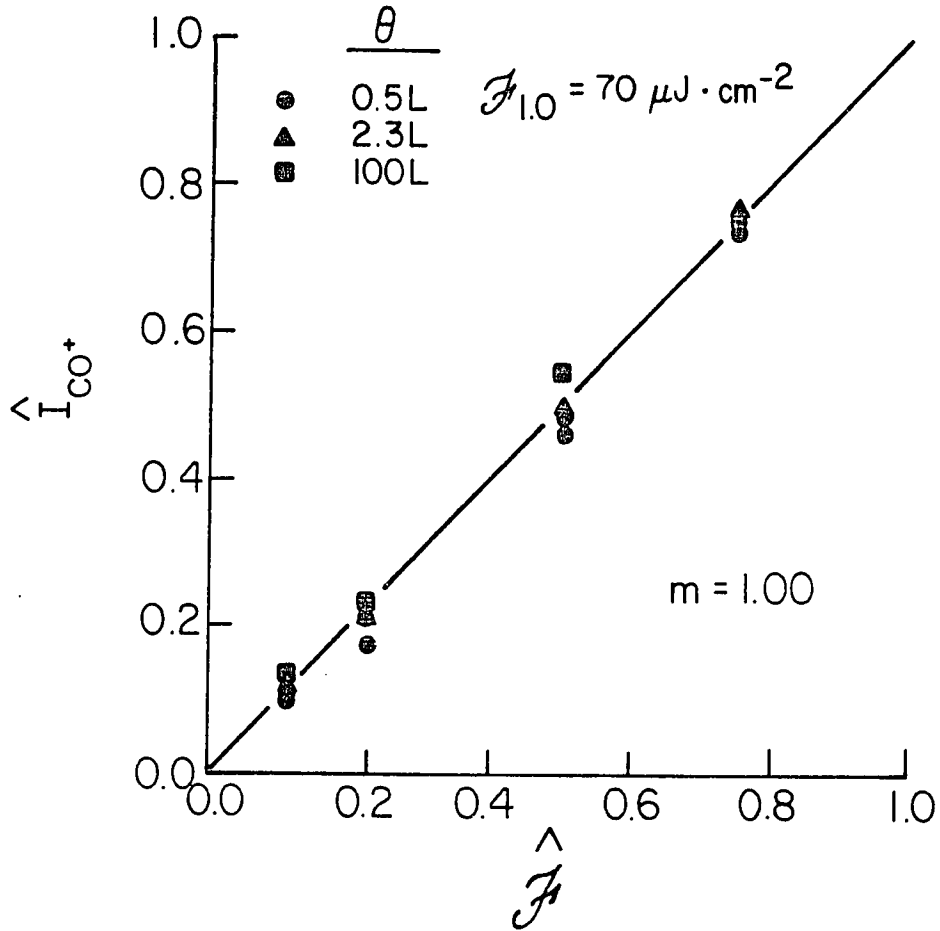


**Figure 11.** The dependence of the  $\text{CO}^+$  yield on laser fluence. The fluence is normalized to  $70 \mu\text{J} \cdot \text{cm}^{-2}$  and the  $\text{CO}^+$  yield is normalized to the signal produced by  $70 \mu\text{J} \cdot \text{cm}^{-2}$  at the various coverages. Neutral density filters are used to attenuate the laser power. The straight line (slope = 1.00) is a fit to data from all coverages shown in Figure 12, only some of which are indicated in this plot. The linear dependence indicates the dissociation is a one-photon process and that the  $\text{Fe}(\text{CO})_5$  layer is optically thin.

geometry ( $\sim 15\%$ ), but predicts depletion of the surface overlayer to  $1/2$  of the initial coverage in  $\sim 200$  sec, whereas the yield is constant over this time span. This estimate is based on the production of 1 CO molecule per  $\text{Fe}(\text{CO})_5$ . After removal from the vacuum chamber no metallic deposits on the  $\text{Al}_2\text{O}_3$  crystal could be detected by eye.

The dissociation and thermal desorption yields as a function of dosing coverage are shown in Figure 12. The laser-induced signal shows a saturation effect while the integral of the thermal desorption peaks continues to increase indicating that the number of adsorbates is increasing with increasing dosage, albeit at a reduced uptake rate. Both the dissociation and thermal desorption yield curves exhibit a knee in the 5 - 10 L dose region. The onset of  $\text{Fe}^+$  laser-induced desorption is observed in the same region, which we interpret as indicative of second layer coverage. Saturation of the laser-induced  $\text{CO}^+$  dissociation yield occurs in the 2 - 3 layer regime.

#### 4.2.3 *Ag(110)*

Preliminary positive results have been obtained for the UV-induced  $\text{Fe}(\text{CO})_5$  photoreaction on  $\text{Ag}(110)$ . This is the first observation of a photochemical reaction occurring above a clean, smooth metal surface in the ultra-high vacuum environment. The observed  $\text{CO}^+$  signal from  $\text{Fe}(\text{CO})_5$  dissociation on silver surface is similar (within a factor of 2) to the  $\text{Fe}(\text{CO})_5$  dissociation on  $\text{Al}_2\text{O}_3$  at low (3 L) and high (20 L) coverages. If one can extrapolate these two data points, they indicate a saturation of the  $\text{CO}^+$  yield similar to that observed in the  $\text{Fe}(\text{CO})_5/\text{Al}_2\text{O}_3$  system (Figure 12). Comparison of the yield for the reaction on the  $\text{Ag}(110)$  and  $\text{Al}_2\text{O}_3$

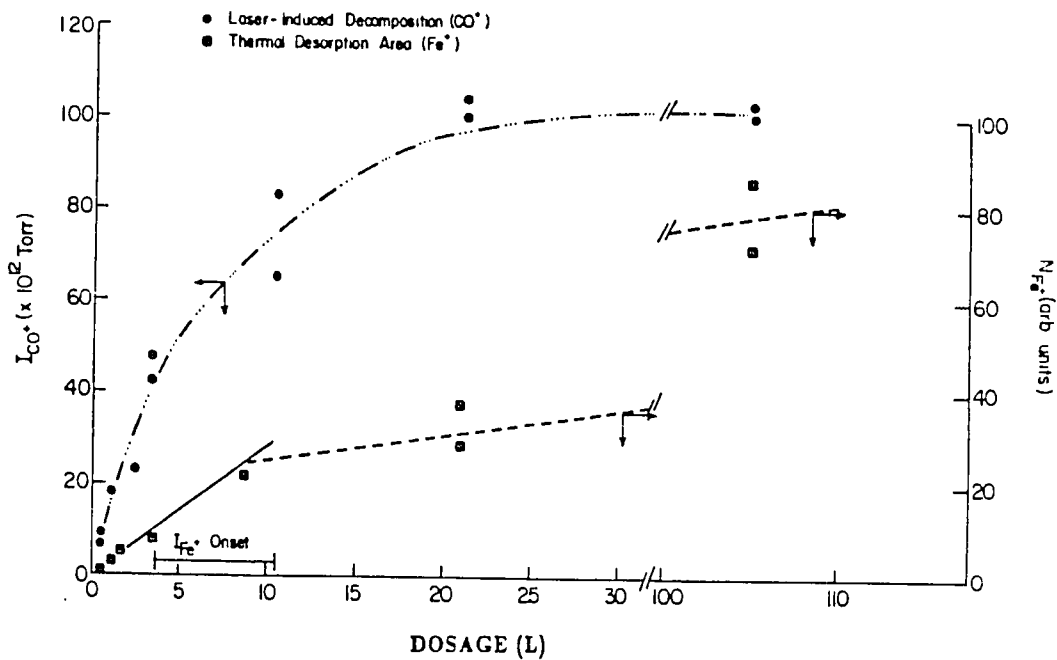


Figure 12. Comparison of the dosage dependence of the laser-induced CO<sup>+</sup> yield and the Fe(CO)<sub>5</sub> coverage, as determined by the area under the Fe<sup>+</sup> thermal desorption peaks for the Al<sub>2</sub>O<sub>3</sub> surface. The knee in the thermal desorption coverage curve plus the onset of laser-induced desorption of Fe-containing species (I<sub>Fe<sup>+</sup></sub>) suggest population of the second overlayer. The dissociation yield levels off for coverages of  $\geq 2 - 3$  monolayers, while the thermal desorption areas indicate that the coverage continues to increase for longer gas doses.

surfaces with that of silicon may not be consistent due to the replacement of the channeltron after the silicon experiments.

#### 4.2.4 Summary

Our observations of the photodissociation of  $\text{Fe}(\text{CO})_5$  on the single crystal surfaces of  $\text{Al}_2\text{O}_3$ ,  $\text{Si}(100)$  and  $\text{Ag}(110)$  are summarized as follows:

- (1) UV irradiation of  $\text{Fe}(\text{CO})_5$  on all the studied surfaces yields an increase in the  $\text{CO}^+$  mass signal which is attributed to the dissociation of  $\text{Fe}(\text{CO})_5$  by the 337 nm radiation. At low  $\text{Fe}(\text{CO})_5$  coverages, no Fe-containing species (e.g.,  $\text{Fe}(\text{CO})_5$ ,  $\text{Fe}_3(\text{CO})_{12}$ ) are observed with a sensitivity at least a factor of 10 greater than would yield  $\text{Fe}^+$  from cracking of  $\text{Fe}(\text{CO})_5$ . This indicates the observed  $\text{CO}^+$  signal is not due to pyrolytic desorption of  $\text{Fe}(\text{CO})_5$  from the surfaces. Calculations suggest that thermal heating of the substrate is not important with the unfocussed  $\text{N}_2$  laser (*vide infra*).
- (2) Irradiation of either the  $\text{Si}(100)$  or  $\text{Al}_2\text{O}_3$  surface with mildly focussed 337 nm light produces an exponentially decreasing  $\text{CO}^+$  flux at short times ( $\sim 200$ -500 shots), while a nearly constant flux is observed at long times. This “constant” dissociation may be due to either diffusion of  $\text{Fe}(\text{CO})_5$  into the irradiated area or evidence of dissociation products on the surface, either from dissociative adsorption or the photochemical reaction, which have lower dissociation cross sections. No other evidence for non-volatile reaction products were observed.
- (3) A pulse of Fe-containing molecules is observed upon initial irradiation of a freshly dosed sample. This effect was observed on both silicon and sapphire surfaces, with either focussed or unfocussed light, suggesting the energy

absorption is through the  $\text{Fe}(\text{CO})_5$  molecules. Similar effects were noted in IR photodesorption experiments of various organics (see Chapter 4). The initial pulse of  $\text{Fe}(\text{CO})_5$  is believed to be due to either an annealing effect, in which the annealing energy causes desorption, or the result of molecules in thermodynamically unstable sites desorbed by energy deposited in the layer. In addition, at higher (>monolayer) coverages, a constant flux of Fe-containing species is observed. These are most likely  $\text{Fe}(\text{CO})_5$  molecules desorbed thermally by dissipation of energy in the  $\text{Fe}(\text{CO})_5$  layer (although *not* surface heating). Other possibilities are: (a) the formation of condensation products ( $\text{Fe}_2(\text{CO})_9$  or  $\text{Fe}_3(\text{CO})_{12}$ ); these should also be observed at lower coverage but are not; (b) other photofragments ( $\text{Fe}(\text{CO})_x$ ); the formation of surface-bonded species which is possible at low coverage may be blocked at higher coverage, enabling  $\text{Fe}(\text{CO})_x$  species to be desorbed.

- (4.) Observation of  $\text{Fe}(\text{CO})_5$  dissociation on  $\text{Ag}(110)$  indicates the energy transfer rate, which will be faster on silver than silicon or  $\text{Al}_2\text{O}_3$ , occurs on a timescale slower than the  $\text{Fe}(\text{CO})_5$  dissociation. Estimates for the energy transfer rate are given in section 5.

### 4.3 Surface heating

The temperature rise at a solid surface due to incident pulsed radiation is considered. We are interested in the predicted heating effect for the laser conditions we have employed, particularly on the absorbing Si and Ag substrates. The solution to this problem is given by Bechtel:<sup>53</sup>

$$\Delta T = \frac{I_m(1-R)\tau^{1/2}}{(\pi K \rho c)^{1/2}} \cdot \Theta_s(\theta, \mu, \zeta, \lambda) = F \cdot \Theta_s \quad (3)$$

where the temperature rise at the surface,  $\Delta T$ , is a function of the laser and bulk solid parameters (grouped together as  $F$ ), and a function  $\Theta_s$ , which gives the time response of the surface as a function of various reduced parameters. The function  $\Theta_s$ , plotted in Ref. [53], has a maximum value of 2 which we use to calculate the maximum temperature rise. The appropriate constants for the substrates silicon and silver ( $R$ , the reflectivity,  $K$ , the thermal conductivity,  $\rho$ , the density and  $c$ , the heat capacity) are summarized in Table 1. The laser parameters are the pulse width,  $\tau = 10$  nsec, and the irradiance,  $I_m$ , which is approximated as  $50 \mu\text{J}\cdot\text{cm}^{-2}$  for the unfocussed laser (temperature rise =  $\Delta T_u$ ) and a factor of 100 higher for the focussed laser to give an upper bound on the temperature rise ( $\Delta T_f$ ). The values calculated (Table 1) show that similar temperature rises can be expected on both Si and Ag in the region of  $\text{N}_2$  laser excitation. Surface heating is not important for the unfocussed laser case, but may cause a significant rise if the irradiance is increased by a factor of 100. Thermal effects due to surface heating have not been observed in the reported experiments with either focussed or unfocussed light.

## 5. Discussion

### 5.1 Surface Photochemistry

The question of the identity and whereabouts of Fe-containing photoproducts which are the non-volatile by-products of the UV-initiated reaction needs to be resolved. As summarized previously, photolysis of  $\text{Fe}(\text{CO})_5$  under low temperature conditions results in the generation of  $\text{Fe}(\text{CO})_4$ . Further decarbonylation, which has been inferred to yield  $\text{Fe}(\text{CO})_2$  species in the gas phase, is halted by quenching of the hot  $\text{Fe}(\text{CO})_4$  intermediate in the matrix. However, this reactive species can

**Table 1**  
*Parameters<sup>†</sup> and Results for Surface Heating Calculation*

	Si	Ag
$K$ (W/cm·K)	14.	4.8
$c$ (cal/mole · K)	2.3	5.1
$\rho$ (g/cm <sup>3</sup> )	2.40	10.5
$R$	0.5	0.3
$F$ (K)	0.044	0.063
$\Delta T_u$ (K)	0.09	0.13
$\Delta T_f$ (K)	8.8	13.

† Optical constants for R from Refs. [54,55]; all others from Ref. [49].

proceed to form  $\text{Fe}_2(\text{CO})_9$  and  $\text{Fe}_3(\text{CO})_{12}$  even in the low-temperature environment. Irradiation of silica-adsorbed  $\text{Fe}(\text{CO})_5$  likewise results in formation of  $\text{Fe}_3(\text{CO})_{12}$  (without  $\text{Fe}_2(\text{CO})_9$ , due to the instability of this species on the silica). Although  $\text{Fe}_3(\text{CO})_{12}$  has a large absorption cross-section in the near UV, the compound does not appear to be photoactive. It is thus plausible that  $\text{Fe}_3(\text{CO})_{12}$  would be the final product of UV irradiation, and may exhibit a reduced CO yield. The role of subcarbonyl species ( $\text{Fe}(\text{CO})_x$ ) bonded to the surface also needs to be addressed. No evidence for the identity of the photoproduct has been obtained in this study.

Deposition of iron films through the use of UV irradiation and pyrolytic decomposition of  $\text{Fe}(\text{CO})_5$  have been previously reported.<sup>6,53,56,58</sup> Iron films on a single crystal Si(100) sample were induced using both UV irradiation of adsorbed  $\text{Fe}(\text{CO})_5$  and dosing of a heated surface ( $\sim 300^\circ \text{C}$ ).<sup>52</sup> Irradiation of adsorbed layers with a *high* energy electron beam mainly stimulated desorption of molecular  $\text{Fe}(\text{CO})_5$ , with the deposited film which was produced being more highly contaminated with carbon and oxygen than from the other two techniques. No mechanistic information was obtained in this study. Decomposition of  $\text{Fe}(\text{CO})_5$  over soda-lime glass and silver foil was attributed to initiation by low-energy electrons which are generated in the near-surface region by the UV light.<sup>6,58</sup>

The possible reaction mechanisms to be considered for the UV photodissociation of  $\text{Fe}(\text{CO})_5$  on surfaces are shown schematically in Figure 13. Gas-phase absorption and decomposition is negligible at these pressures ( $10^{-10}$  Torr total pressure, with a much lower partial pressure of  $\text{Fe}(\text{CO})_5$ ). The photoelectric mechanisms can be discounted as the primary mechanism for  $\text{Fe}(\text{CO})_5$  decomposition in the

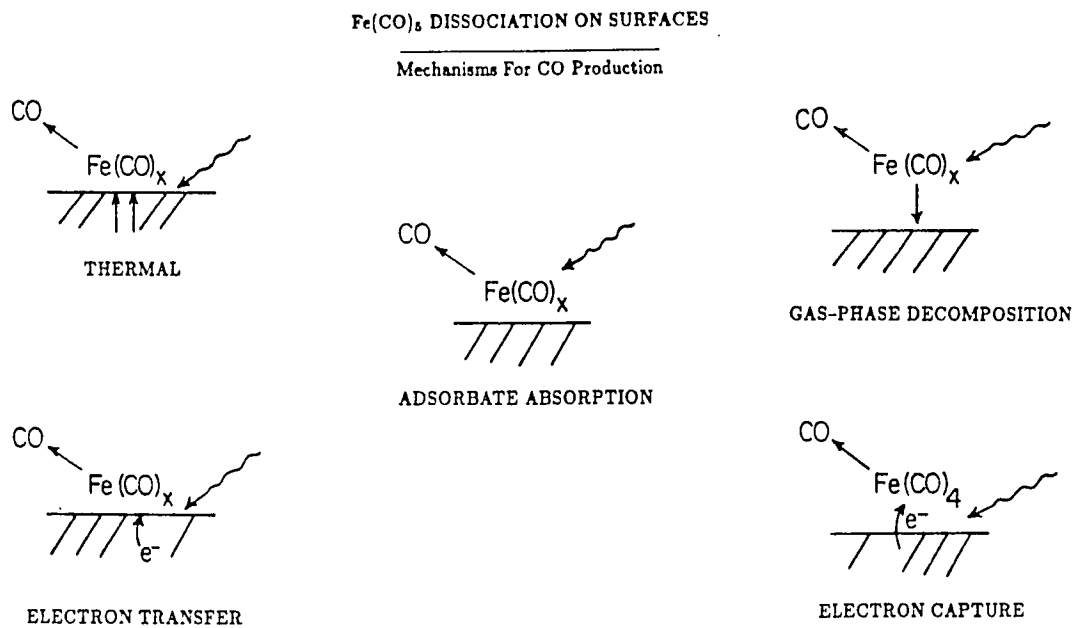


**Figure 13.** Mechanisms considered in the UV dissociation of  $\text{Fe}(\text{CO})_5$  over solid surfaces (after George<sup>58</sup>). The dominant mechanism in our experiment is the direct excitation of adsorbed  $\text{Fe}(\text{CO})_5$ .

reported experiments: the photon energy is below any interband transitions in sapphire and silver. Irradiation of semiconductors with energy above the bandgap energy can induce photodesorption and stimulate reactions at surfaces, and might be expected to be important in the  $\text{Fe}(\text{CO})_5$  reaction on Si(100). However, the similarity in reaction yield between the Si,  $\text{Al}_2\text{O}_3$  and silver indicates the electron-induced decomposition mechanism is not of major importance under these conditions. Heating of the substrate is calculated to be negligible for the unfocussed laser conditions. Laser-induced thermal desorption is not observed even with the laser mildly focussed, so thermal decomposition, which would require much higher temperatures (400 - 600 K<sup>52</sup>), is not a plausible mechanism. We conclude that absorption of the UV light by adsorbed  $\text{Fe}(\text{CO})_5$  followed by fast dissociation is the only mechanism consistent with our observations.

The results of a dynamical study of UV photodissociation of an adsorbed molecule were recently reported by Bourdon *et al.*<sup>60</sup> Submonolayer coverages of  $\text{CH}_3\text{Br}$  on an insulator, LiF(001), were irradiated with 222 and 308 nm light, and the time-of-flight of the desorbed species was recorded. Two effects are stimulated by the radiation: a direct photodissociation of the adsorbed  $\text{CH}_3\text{Br}$ , analogous to the dissociation of  $\text{Fe}(\text{CO})_5$  reported here, and photodesorption of molecular  $\text{CH}_3\text{Br}$  due to absorption of radiation by the crystal. The photolysis of the  $\text{CH}_3\text{I}$  in the gas phase occurs through excitation to a repulsive state and is ultra-fast ( $0.6 \times 10^{-13}$  s), and the same mechanism is postulated for  $\text{CH}_3\text{Br}$  dissociated in the gas phase and on the LiF surface.<sup>60</sup> Excitation of adsorbed  $\text{CH}_3\text{Br}$  at 222 nm produces  $\text{CH}_3$  fragments with 2.2 eV of translational energy, out of 2.6 eV available to products

(from the photon energy minus the energy of the CH<sub>3</sub>-Br bond) – the CH<sub>3</sub> group appears to simply recoil from the surface. The photolytic yield resulting from the estimated coverage agrees with the gas-phase absorption cross section of CH<sub>3</sub>Br. The failure to observe products upon 308 nm radiation is also consistent with the low gas-phase absorption in this region. The eventual buildup of a carbon film did not affect the results.

## 5.2 Energy Transfer Theory

Interest in the phenomenon of energy transfer to surfaces was initially stimulated by observations that the lifetime of fluorescing molecules was modulated by a reflecting metal surface.<sup>61,62</sup> A layer of rhodamine 6G dye molecules was located at varying distances from a silver metal film, using fatty acid layers, and excited in the visible region. The fluorescence lifetime oscillates with frequency of the order of the wavelength of the emitted light. The interference effects due to the reflection of the field of the oscillating dipole from a mirror accounts well for the data at long distances ( $d > 1000 \text{ \AA}$ ), but additional and drastic quenching not reproduced by this treatment occurs if the molecule is located close to the surface. More recent experiments that preferentially probe the behavior of the emitter lifetime in the near-surface region quantify this result.<sup>63-67</sup> An approach that quantitatively treated the early results and that remains fairly successful even in light of recent experiments is the classical approach of Chance, Prock and Silbey.<sup>68</sup> Considering a point dipole at a given distance above an infinite and smooth surface, the lifetime of the dipole can be predicted using only the measured dielectric constant of the solid,  $\epsilon(\omega)$ . The reflection of the surface modifies the radiative lifetime at long distances

while non-radiative energy transfer to the solid dominates the short distance regime, and both can be deduced from this treatment.

Of particular interest here is the nonradiative decay rate and mechanism at short molecule-surface separation,  $d$ . The classical theory<sup>68</sup> predicts a short-distance energy transfer rate that varies as  $1/d^3$ , which can be understood on very physical grounds.<sup>66,67</sup> The well-known Förster dipole-dipole energy transfer rate between two molecules exhibits an  $1/d^6$  dependence, from the same considerations that derive the van der Waals induced dipole interaction  $\frac{1}{r^6}$  distance dependence. A point dipole above a surface interacts with a three dimensional array of dipoles; integration over this volume leads to a  $1/d^3$  dependence of the lifetime. Similarly, a  $1/d^4$  dependence might be expected in the case of quenching of the emitter by a two-dimensional (surface) dipole phenomenon.<sup>66</sup> The results of the Chance, Prock and Silbey model<sup>68</sup> are summarized here. Consider the classical harmonic, damped oscillator (point dipole) driven by its own electromagnetic field reflected from the surface:

$$\ddot{\mu} + \omega^2 \mu = \frac{e^2}{m} E_R - b_0 \dot{\mu}, \quad (4)$$

where  $\omega$  is the free molecule oscillation frequency,  $E_R$  is the reflected field at the dipole position and the damping constant,  $b_0$ , is the inverse lifetime in the absence of the mirror – just the emission lifetime. The decay rate in the presence of the mirror,  $b$ , normalized to the free molecule rate is (Eq. 2.7 of Ref. [68]):

$$\hat{b} = b/b_0 = 1 + \frac{3q n_1^2}{2\mu_0 k_1^3} \text{Im}(E_0), \quad (5)$$

where  $n_1$  and  $k_1$  are the index of refraction and propagation constant, respectively,

of the medium containing the dipole,  $\mu_0$  is the transition dipole moment of the transition and  $E_0$  is the radiated electric field. Determination of the electric field is accomplished using Fourier analysis of the dipole field. The result of this treatment for the normalized decay rate is:<sup>67,68</sup>

$$\hat{b} = 1 + A \cdot q \times \text{Im} \int_0^{+\infty} [B \cdot R^p + C \cdot R^s] e^{-2l_1 \hat{d}_1} \frac{u^3}{l_1} du, \quad (6)$$

where  $u$  is the wavevector normalized to the photon wavevector,  $R^{p,s}$  are the complex Fresnel reflection coefficients for incident light p- or s-polarized (parallel or perpendicular) to the plane of incidence,  $\hat{d}_1$  is the normalized dipole-surface distance,  $l_1 = -i(1 - u^2)^{1/2}$ , and A, B and C are factors that depend on the orientation of the dipole (also functions of  $u$ ). The second term expresses the modification of the fluorescence yield as an integral over all wavevectors which are the Fourier components of the dipole field. The important point here is that the integration can be broken down into regions associated with physical mechanisms: for  $0 < u < 1$ , or wavelengths longer than the radiating field, the decay process is radiative due to emission of a photon; for  $1 < u < \infty$ , non-radiative processes account for the decay. Near  $u = 1$  resonant decay pathways exist in which the light wavevector nearly matches that of the surface mode – e.g., in the visible region, surface plasmons on silver or polaritons in semiconductors can quench the field of the dipole. The rest of the high wavevector contributions to the decay rate represent all other possibilities for energy loss to the solid, which within the classical model are electron scattering mechanisms. These contributions become more important to the integral at smaller distances to the surface, where the high wavevector components dominate.

Figure 14 depicts the  $\text{Fe}(\text{CO})_5$  dissociation experiment described within the

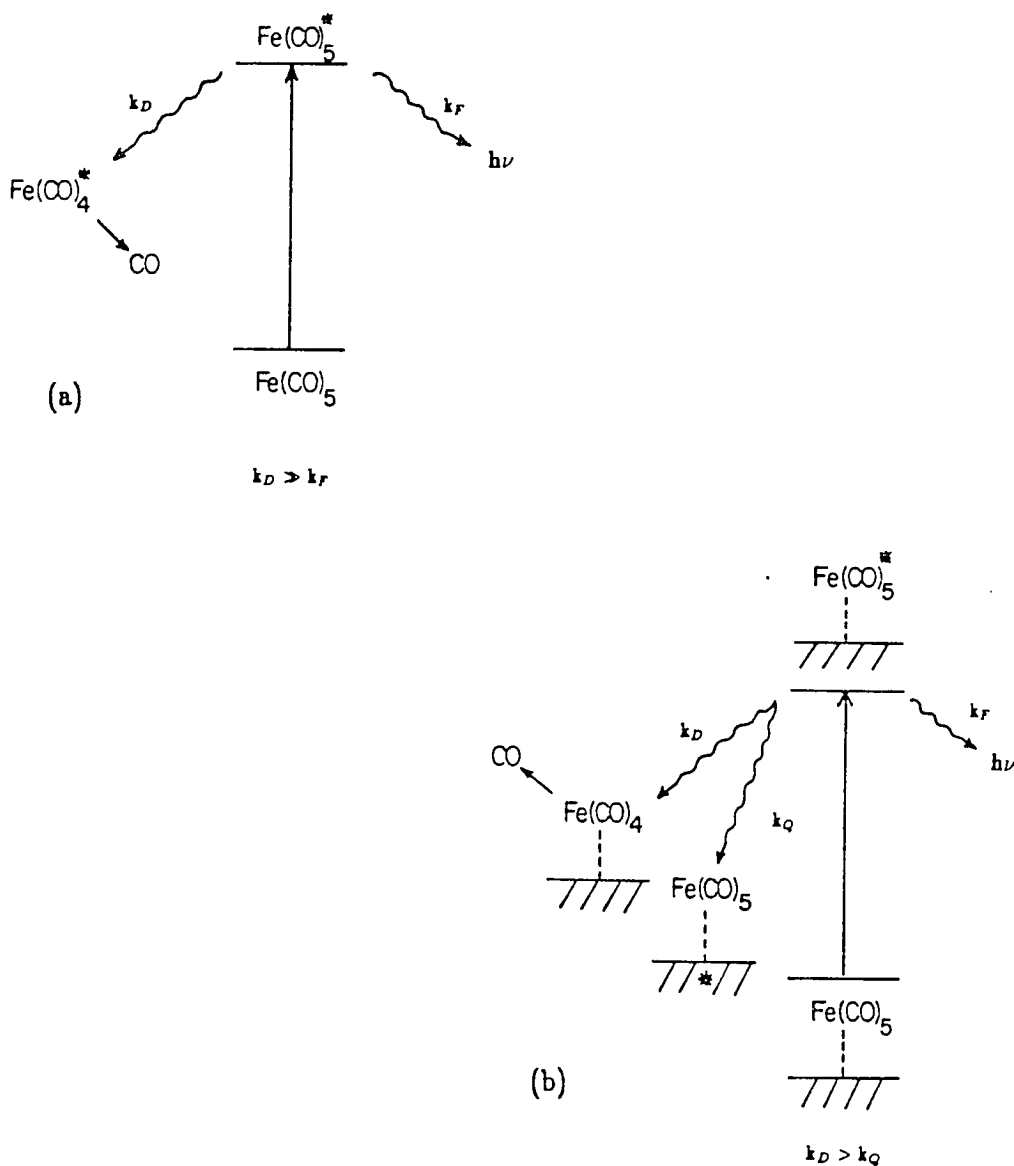


**Figure 14.** Schematic of (a) excited gas-phase  $\text{Fe}(\text{CO})_5$  which relaxes by fluorescence (with rate  $k_F$ ) and dissociation ( $k_D$ ). For  $\text{Fe}(\text{CO})_5$ ,  $k_D \gg k_F$  - that is, no fluorescence is observed from any excited state of  $\text{Fe}(\text{CO})_5$ . The fluorescence rate of  $\text{Fe}(\text{CO})_5$  is an important quantity only for calculation of the quenching rate constant (see text). (b) The addition of a quenching mechanism ( $k_Q$ ) representative of energy transfer into the solid. With excitation at 337 nm, we find  $k_D > k_Q$  for  $\text{Fe}(\text{CO})_5$  on the  $\text{Ag}(110)$ ,  $\text{Si}(100)$  and  $\text{Al}_2\text{O}_3$  surfaces.

classical model. The free molecule case is shown in Figure 14(a), with the dissociation rate dominating the relaxation. In Figure 14(b) the energy transfer rate from the excited state to the solid competes with the decarbonylation rate. This modelling also assumes an intermediate state with a finite lifetime, consistent with a recent theoretical study of the  $\text{Fe}(\text{CO})_5$  decomposition<sup>69</sup> which suggests absorption occurs into the first singlet state and crosses into the triplet manifold. The initial excitation should be better classified as occurring into a state of mixed singlet-triplet character (see Section 2), so it appears reasonable to assume an intermediate state.

To calculate the rate of non-radiative energy transfer to the surface we need the free molecule relaxation rate – that is, the radiative decay rate predicted for  $\text{Fe}(\text{CO})_5$  in the absence of dissociation – which can be derived from the oscillator strength of the transition and the Einstein relations. The oscillator strength is<sup>70</sup>

$$f = 4.32 \times 10^{-9} \int \epsilon_{abs}(\omega) d\omega \quad (7)$$

where the integral over the absorption strength can be approximated by the maximum  $\epsilon_{abs}$  times the halfwidth. For the  $\text{Fe}(\text{CO})_5$  absorption at 337 nm we estimate  $\epsilon_{abs} \sim 400 \text{M}^{-1} \text{cm}^{-1}$  and an upper limit for  $\delta\omega_{1/2}$  is 60 nm. This yields an emission lifetime of 2  $\mu\text{sec}$ . The energy transfer rate in the limit of short distance becomes:<sup>68</sup>

$$b_{ET} = b_0 \frac{3(\lambda/2\pi)^3 n_2 k_2}{2d^3 n_1 |\epsilon_1 + \epsilon_2|^2} = b_0 \frac{\beta}{d^3}, \quad (8)$$

where the dielectric constants for silver (337 nm)<sup>55</sup> and silicon (350 nm)<sup>54</sup> are  $-0.907 + 0.081 i$  and  $14.7 + 29.3 i$ , respectively. The calculated excited state lifetimes at various distances are collected in Table 2. We have assumed a 337 nm emission

**Table 2**  
*Results of Energy Transfer Calculations*

$\beta(\text{cm}^{-3})$	$d(\text{\AA})$	$\beta/d^3$	$\tau(\tau_0 = 2\mu\text{sec})$	$\tau(\tau_0 = 10\mu\text{sec})$
$6.16 \times 10^{-16}$	1.0	$6.2 \times 10^8$	$3.2 \times 10^{-15}$	$1.6 \times 10^{-14}$
	2.0	$7.7 \times 10^7$	$2.6 \times 10^{-14}$	$1.3 \times 10^{-13}$
	Ag	4.5	$6.8 \times 10^6$	$2.9 \times 10^{-13}$
	10.	$6.2 \times 10^5$	$3.2 \times 10^{-12}$	$1.6 \times 10^{-11}$
$3.10 \times 10^{-18}$	1.0	$3.1 \times 10^6$	$6.5 \times 10^{-13}$	$3.2 \times 10^{-12}$
	2.0	$3.9 \times 10^5$	$5.1 \times 10^{-12}$	$2.6 \times 10^{-11}$
	Si	4.5	$3.4 \times 10^4$	$5.9 \times 10^{-11}$
	10.	$3.1 \times 10^3$	$6.5 \times 10^{-10}$	$3.2 \times 10^{-9}$

wavelength, since we have no estimate for the energy of the triplet state. For an excited  $\text{Fe}(\text{CO})_5$  molecule described as a dipole with  $\tau_0 = 2 \mu\text{sec}$  at the van der Waals radii of  $\text{Fe}(\text{CO})_5$  ( $\sim 4.5\text{\AA}$ ) from the silver surface, the calculated energy transfer rate is  $\sim 10^7$  faster than the emission lifetime, and an order of magnitude faster than the 2 psec dissociation rate estimate. The dissociation and quenching rates are equal for  $\tau_0 = 10 \mu\text{sec}$  (from using a smaller estimate of the width of the absorption feature<sup>17</sup>). Because of the  $d^3$  dependence, the quenching rate drops by an order of magnitude if the dipole is spaced an additional 5  $\text{\AA}$  from the surface. The quenching rate on silicon is smaller by a factor of 200. These calculations show the qualitative behavior one would expect for the quenching rate of the two surfaces as a function of distance, but quantitatively predict severe attenuation of the  $\text{Fe}(\text{CO})_5$  dissociation should be observed on the silver surface. Since no significant quenching of the decarbonylation yield is observed over silver, the quenching rate must in fact be at least two orders of magnitude slower than the dissociation rate. Refinements to the simple classical theory (*vide infra*) will *increase* the calculated rate. The possible enhancement of the photochemical rate by surface roughness is discussed in Section 5.3, but we note here that roughness is also expected to enhance the quenching rate<sup>84</sup>. Thus, the dissociation rate of  $\text{Fe}(\text{CO})_5$  appears to be an order of magnitude faster than the present upper limit of 2 psec.<sup>24</sup>

The assumptions in the theory of Chance *et al.* need to be modified as the dipole-surface distance become small. In the classical model, the decay mechanisms are only those which are probed by the optically-measured dielectric constant,  $\epsilon(\omega)$ , i.e., only local effects that do not depend on electron correlation. Non-local effects

have been theoretically taken into account<sup>71,72</sup> with the use of a modified form of the dielectric constant,  $\epsilon(\omega, k)$ . The result is the inclusion of the electron-hole generation mechanism which, because of its contribution at high wavevector, will be an important damping mechanism for dipoles at short distance from the solid. In addition, due to momentum constraints, the unphysical singularity in the classical result at high wavevector (i.e., the energy transfer rate goes to infinity at  $d = 0$ ) is removed. A  $d^{-4}$  distance dependence, important at short distances –  $d < 30$  Å in the visible and longer distances,  $d < 100$  Å, in the infrared – is predicted in the Persson theory,<sup>72</sup> and has been observed in the visible region on silver.<sup>66</sup> The use of non-local optical theory has accounted for the ultra-fast ( $> 10^{14} \text{ s}^{-1}$ ) decay rates implied by linewidth measurements on Al<sup>16a</sup> and Ag.<sup>73</sup>

Another difficulty with the classical model is the sharp boundary at the interface. Metiu<sup>74</sup> first used a jellium model of the surface and obtained a smoothly varying dielectric function across the solid surface. The results of his calculations predict that the classical theory will successfully model the energy transfer rate down to  $\sim 6$  Å! The improved modelling of the surface potential has also been employed in recent work by Persson.<sup>75</sup> Specific cases of the energy transfer rate in chemisorbed states which involves electron overlap at these short distances have also been modelled,<sup>76</sup> but these are not expected to be of importance in the case of weakly bound Fe(CO)<sub>5</sub>.

### *5.3 Surface-enhanced effects*

The observation of the surface-enhanced Raman (SERS) effect generated considerable excitement.<sup>77</sup> It is now known that the primary component of the

enhancement is due to plasma resonances in surface structures present on a rough surface.<sup>78–80</sup> Particularly noteworthy are the experiments of Campion, *et al.*,<sup>79</sup> in which no Raman enhancement on smooth single-crystal silver surfaces was observed, and that of Chen and Osgood,<sup>80</sup> which demonstrated the enhanced fields surrounding elliptical silver particles irradiated near the plasma resonance. Theoretical treatments<sup>78</sup> have come to similar conclusions about the source of the Raman enhancement, and predictions of enhanced photochemistry have been advanced,<sup>81</sup> and since then been demonstrated.<sup>80,82,83</sup> The yield of two-photon generated surface carbon production from irradiation of aromatics over a roughened silver surface was seen to maximize at  $\sim 20 \text{ \AA}$ ,<sup>83</sup> perhaps indicative of a competition between the enhanced photochemistry effect and the shorter-range energy transfer process.<sup>81</sup> Surface roughness is also theoretically expected to *increase* the energy transfer rate beyond the classical model, even for long distances ( $d \sim 50 \text{ \AA}$ ).<sup>84</sup>

Since silver is an excellent substrate on which to obtain enhancement effects, the characterization of the surface morphology is an important consideration. As recounted in the experimental section, care was taken to polish and anneal the crystal, but imperfections and corrugation were still present. Although at the present time we believe these effects to be minimal, enhancement effects due to rough surfaces are known to diminish or disappear as the crystal surface smooths over the period of days to weeks (unfortunately for those trying to generate such effects!),<sup>36</sup> so the long-time reproducibility of the photochemical behavior will indicate the importance of roughness features. Short-term tests which will provide an assessment of the magnitude of this possible effect given the available equipment

include: the intentional roughening of the surface; the spacing the reactant  $\text{Fe}(\text{CO})_5$  molecule off of the surface to search for a maxima in the yield a short distance away from the surface – the yield near the smooth surface should maximize at long distances, if indeed there is some change in the yield of dissociation.

## 6. Conclusions

We report the observation of laser-induced dissociation of  $\text{Fe}(\text{CO})_5$  on three surfaces,  $\text{Al}_2\text{O}_3$ ,  $\text{Si}(100)$  and  $\text{Ag}(110)$ , demonstrating the fast dissociation successfully competes with mechanisms of energy transfer into the solid. Photolytic effects are observed without competing processes such as pyrolytic or electron-induced dissociation. The dissociation yield, as monitored by CO production, is similar on the three surfaces, suggesting the reaction mechanism does not directly involve the substrate. Dissociation via direct absorption of 337 nm light by the metal carbonyl has been postulated. The inferred Fe-containing photoproducts of the dissociation have not been identified.

## 7. Future Work

The present report is a preliminary study, and there are many continuations that would both better characterize the studied system and provide extensions to other systems. Of primary importance is identification of photoproducts and characterization of the surface species. The use of tunable UV radiation would provide clues to the nature of the absorbing species. Other organometallics with large absorption cross-sections in this wavelength region such as  $\text{Cr}(\text{CO})_6$  or  $\text{Mn}_2(\text{CO})_{10}$  have parent ions that are too massive to observe with the present mass spectrometer, but would also be interesting to study. More importantly, surface

spectroscopies such as EELS would be quite valuable to identify surface species.

It would be interesting to observe whether the ultra-fast  $\text{Fe}(\text{CO})_5$  reaction would occur on a free-electron metal, such as Al, where quenching of electronic energy appears to be extremely efficient.<sup>16</sup> The use of other small molecular systems with slower dissociation rates would be advantageous for many reasons. The smaller molecule would enable the “classical dipole” to approach closer to the surface and assuming attenuation of the dissociation rate can be observed, information would be gained from a distance dependence of the reaction rate. Simplification of the reaction possibilities and the capability to observed reaction products in the mass spectrometer would be quite advantageous. A possible systems for study would be  $\text{H}_2\text{CO}$ , which exhibits a much slower dissociation rate ( $\sim 10^7 \text{ s}^{-1}$ ) and has been well-studied on a number of surfaces.

Differential pumping of the mass spectrometer in the present system is needed to obtain the important TOF measurements to differentiate between surface mechanisms. The distribution of translational energy would indicate whether the photolytically generated CO is equilibrated at the surface temperature or a direct product of the dissociation event. The availability of state-specific detection techniques will provide further characterization of the photoproducts.

### **Acknowledgements**

I would like to thank Prof. A. Kuppermann for the generous loan of the  $\text{N}_2$  laser, Roya Maboudian for the sapphire crystal and Malina Hills for assistance and guidance in polishing the silver crystal. I also appreciate the critical reading of this chapter by Malina Hills and Paul Whitmore. This work was supported by the Office of Naval Research, contract no. N00014-82-K-0506.

## References

1. T.F. Deutsch, in *Laser Processing and Diagnostics*, ed. D. Bäuerle (Springer-Verlag, Berlin, 1984).
2. R.M. Osgood, Jr., *Ann. Rev. Phys. Chem.* **34** (1983) 77.
3. D. Bäuerle, in *Laser Processing and Diagnostics*, ed. D. Bäuerle (Springer-Verlag, Berlin, 1984).
4. D.J. Ehrlich, R.M. Osgood, Jr. and T.F. Deutsch, *J. Vac. Sci. Tech.* **20** (1982) 738.
5. R. Solanki, P.K. Boyer, J.E. Mahan and G.J. Collins, *Appl. Phys. Lett.* **38** (1981) 572.
6. P.M. George and J.L. Beauchamp, *Thin Solid Films* **67** (1980) L25.
7. G.L. Geoffroy and M. Wrighton, *Organometallic Photochemistry* (Academic, New York, 1979);  
M. Wrighton, *Chem. Rev.* **74** (1974) 401.
8. J.K. Burdett, *Coord. Chem. Rev.* **27** (1978) 1.
9. M. Poliakoff, *Chem. Soc. Rev.* (1978) 527.
10. M.A. Duncan, T.G. Dietz and R.E. Smalley, *J. Am. Chem. Soc.* **103** (1981) 5245.
11. M.A. Hanratty, C.A. Wight and J.L. Beauchamp, to be published;  
M.A. Hanratty, Ph.D. Thesis, California Institute of Technology, 1985.
12. J.L. Graff, R.D. Sanner and M.S. Wrighton, *J. Am. Chem. Soc.* **101** (1979) 273;

- D.J. Perettie, M.S. Paguette, R.L. Yates and H.D. Gafney, in *Laser Applications in Chemistry*, eds., K.L. Kompa and J. Wanner (Springer-Verlag, Berlin, 1982).
13. R.L. Whetten, K.-J. Fu and E.R. Grant, *J. Am. Chem. Soc.* **104** (1982) 4270; P.A. Teng, F.D. Lewis and E. Weitz, *J. Phys. Chem.* **88** (1984) 4895.
  14. M.A. Duncan, T.G. Dietz and R.E. Smalley, *Chem. Phys. Lett.* **44** (1979) 415; D.P. Gerrity, L.J. Rothberg and V. Vaida, *Chem. Phys. Lett.* **74** (1980) 1; G.J. Fisanick, A. Gedanken, T.S. Eichelberger IV, N.A. Kuebler and M.R. Robin, *J. Chem. Phys.* **75** (1981) 5215.
  15. O. Madelung, *Introduction to Solid State Theory*, (Springer-Verlag, Berlin, 1978).  
C. Kittel, *Introduction to Solid State Physics*, (Wiley, New York, 1976).
  16. (a) Ph. Avouris, D. Schmeisser and J.E. Demuth, *J. Chem. Phys.* **79** (1983) 488;  
(b) J.E. Demuth and Ph. Avouris, *Phys. Rev. Lett.* **47** (1981) 61.
  17. M. Dartiguenave, Y. Dartiguenave and H.B. Gray, *Bull. Soc. Chim. Fr.* **12** (1969) 4223.
  18. C.F. Koerting, K.N. Walzl and A. Kuppermann, to be published;  
C.F. Koerting, Ph.D. Thesis, California Institute of Technology, 1985.
  19. The levels with solid lines are derived from assuming identical Fe–CO bond dissociation energy (28 kcal/mole). The dashed lines from are an experimental determination which indicates the initial Fe(CO)<sub>4</sub>–CO dissociation is much higher in energy than subsequent ones;<sup>20</sup> Another more recent experiment<sup>21</sup> has found the first dissociation energy to be close to the average Fe–CO bond value.

20. P.C. Engleking and W.C. Lineberger, *J. Am. Chem. Soc.* **101** (1979) 5569.
21. K.E. Lewis, D.M. Golden and G.P. Smith, *J. Am. Chem. Soc.* **106** (1984) 3905.
22. (a) G. Nathanson, B. Gitlin, A.M. Rosan and J.T. Yardley, *J. Chem. Phys.* **74** (1981) 361;  
(b) J.T. Yardley, B. Gitlin, G. Nathanson, and A.M. Rosan *J. Chem. Phys.* **74** (1981) 370.
23. A.J. Oudekirk and E. Weitz, *J. Chem. Phys.* **79** (1983) 1089.  
A.J. Oudekirk, P. Wermer, N.L. Schultz and E. Weitz, *J. Am. Chem. Soc.* **105** (1983) 3354.
24. R.L. Whetten, K.-J. Fu and E.R. Grant, *J. Chem. Phys.* **79** (1983) 4899.
25. (a) M. Poliakoff and J.J. Turner, *J. Chem. Soc. Dalton* (1974) 210.  
(b) M. Poliakoff and J.J. Turner, *J. Chem. Soc. Dalton* (1974) 2276.  
(c) M. Poliakoff and J.J. Turner, *J. Chem. Soc. Dalton* (1973) 1351.  
(d) M. Poliakoff and J.J. Turner, *J. Chem. Soc. A.* (1971) 2403.  
(e) M. Poliakoff and J.J. Turner, *J. Chem. Soc. A.* (1971) 654.
26. D.R. Tyler, R.A. Levenson and H.B. Gray, *J. Am. Chem. Soc.* **100** (1978) 7888.
27. J.J. Turner, J.K. Burdett and M. Poliakoff, *Pure and Appl. Chem.* **49** (1977) 491.
28. T.R. Fletcher and R.N. Rosenfeld, *J. Am. Chem. Soc.* **105** (1983) 6358.
29. W.H. Breckenridge and N. Sinai, *J. Phys. Chem.* **85** (1981) 3557.
30. R. Bonneau and J.M. Kelly, *J. Am. Chem. Soc.* **102** (1980) 1220;  
J.A. Welch, K.S. Peters and V. Vaida, *J. Phys. Chem.* **86** (1982) 1941;  
J.D. Simon and K.S. Peters, *Chem. Phys. Lett.* **98** (1983) 53.

31. R.N. Pruetz and J.J. Turner, *J. Am. Chem. Soc.* **97** (1975) 4791.
32. P. Feulner and D. Menzel, *J. Vac. Sci. Tech.* **17** (1980) 662.
33. S. Samson, E. Goldish and C.J. Dick, *J. Appl. Cryst.* **13** (1980) 425.
34. C.T. Campbell and S.M. Valone, *J. Vac. Sci. Tech.* **A3** (1985) 408.
35. T.E. Felter, W.H. Weinberg, P.A. Zhdan and G.K. Boreskov, *Surf. Sci.* **97** (1980) L313.
36. P.M. Whitmore, personal communication.
37. C.T. Campbell and M.T. Paffett, *Surf. Sci.* **143** (1984) 517.  
H.A. Engelhardt and D. Menzel, *Surf. Sci.* **57** (1976) 591.  
A.M. Bradshaw, A. Engelhardt and D. Menzel, *Ber. Bunsenges. Physik. Chem.* **76** (1972) 500.
38. J.C. Hemminger, personal communication.
39. M. Bowker, M.A. Barteau and R.J. Madix, *Surf. Sci.* **92** (1980) 528.  
H. Albers, W.J.J. van der Wal, O.L.J. Gijzeman and G.A. Bootsma, *Surf. Sci.* **77** (1978) 1.
40. G. Ertl and J. Küppers, *Low Energy Electrons and Surface Chemistry*, (Verlag Chemie, Weinheim, 1974).
41. R.F. Steiger, J.M. Morabito, Jr., G.A. Somorjai and R. H. Muller, *Surf. Sci.* **14** (1969) 279.
42. W.J. Gignac, R.S. Williams and S.P. Kovalczyk, preprint;  
R.S. Williams, personal communication;  
P.S.P. Wei and A.W. Smith, *J. Vac. Sci. Tech.* **9** (1972) 1209.
43. Y.W. Chung, W. Siekhaus and G.A. Somorjai, *Surf. Sci.* **58** (1976) 341;

- F. Meyer and G.A. Bootsma, *Surf. Sci.* **16** (1969) 221.
44. R.E. Winters and R.W. Kiser, *Inorg. Chem.* **3** (1964) 699;  
M.S. Foster and J.L. Beauchamp, *J. Am. Chem. Soc.* **97** (1975) 4808.
45. J.W. McAllister and J. M. White, *J. Chem. Phys.* **58** (1973) 1496.  
D. Lichtman and Y. Shapira, *CRC Critical Rev. Solid State Mater. Sci.* **8**  
(1978) 93.
46. P.A. Redhead, *Vacuum* (1962) 203.
47. J. King, Jr. and S.W. Benson, *J. Chem. Phys.* **44** (1966) 1007;  
W.H. Wade and N. Hackerman, *J. Phys. Chem.* **64** (1960) 1196.
48. Very little study of adsorption on  $\text{Al}_2\text{O}_3$  surfaces has been reported; see: V.F. Kiselev and O.V. Krylov, *Adsorption Processes on Semiconductors and Dielectric Surfaces I* (Springer-Verlag, Berlin, 1978).
49. AIP Handbook of Physics, ed., D.E. Gray (Addison-Wesley, New York, 1970).
50. B. Sexton, *Surf. Sci.* **102** (1981) 271;  
M. Bowker and R.J. Madix, *Surf. Sci.* **95** (1980) 190.
51. W. Ho, AVS Symposium abstract, 1984.
52. J.S. Foord and R.B. Jackman, *Chem. Phys. Lett.* **112** (1984) 190.
53. J.H. Bechtel, *J. Appl. Phys.* **46** (1975) 1585.
54. D.E. Aspnes and A.A. Studna, *Phys. Rev. B* **27** (1983) 985;  
H.R. Philipp and H. Ehrenreich, *Phys. Rev.* **129** (1963) 1550.
55. P.M. Whitmore, unpublished data.
56. N. Bottka, P.J. Walsh and R.Z. Dalbey, *J. Appl. Phys.* **54** (1983) 1104.

57. R.L. Jackson and M.R. Trusheim, *J. Am. Chem. Soc.* **104** (1982) 6590.
58. P.M. George, Ph.D. Thesis, California Institute of Technology, 1980.
59. J.C. Hemminger, R. Carr and G.A. Somorjai, *Chem. Phys. Lett.* **57** (1978) 100.
60. E.B.D. Bourdon, J.P. Cowin, I. Harrison, J.C. Polanyi, J. Segner, C.D. Stanners and P.A. Young, *J. Phys. Chem.* **88** (1984) 6100.
61. H. Kuhn, *J. Chem. Phys.* **53** (1970) 101.
62. K.H. Drexhage, *J. Luminescence* **1/2** (1970) 693.
63. R. Rossetti and L.E. Brus, *J. Chem. Phys.* **76** (1982) 1146;  
R. Rossetti and L.E. Brus, *J. Chem. Phys.* **73** (1980) 572.
64. P.M. Whitmore, H.J. Robota and C.B. Harris, *J. Chem. Phys.* **77** (1982) 1560;  
P.M. Whitmore, H.J. Robota and C.B. Harris, *J. Chem. Phys.* **76** (1982) 740;  
A. Campion, A.R. Gallo, C.B. Harris, H.J. Robota and P.M. Whitmore, *Chem. Phys. Lett.* **73** (1980) 447.
65. P.M. Whitmore, A.P. Alivisatos and C.B. Harris, *Phys. Rev. Lett.* **50** (1983) 1092.
66. A.P. Alivisatos, D.H. Waldeck and C.B. Harris, *J. Chem. Phys.* **82** (1985) 541.
67. P.M. Whitmore, Ph.D. Thesis, U.C. Berkeley, 1982.
68. R.R. Chance, A. Prock and R. Silbey, *Adv. Chem. Phys.* **47** (1978) 1.
69. C. Daniel, M. Bénard, A. Dedieu, R. Wiest and A. Veillard, *J. Phys. Chem.* **88** (1984) 4805.
70. W. Guillory, *Molecular Spectroscopy*, (Academic, New York, 1900).

71. G.W. Ford and W.H. Weber, *Surf. Sci.* **109** (1981) 451.  
W.H. Weber and G.W. Ford, *Phys. Rev. Lett.* **44** (1980) 1774.
72. B.N.J. Persson, *J. Phys. C* **11** (1978) 4251.
73. Ph. Avouris and J.E. Demuth, *J. Chem. Phys.* **75** (1981) 4783.
74. G.E. Korzeniewski, T. Maniv and H. Metiu, *J. Chem. Phys.* **76** (1982) 1564.
75. B.N.J. Persson and N.D. Lang, *Phys. Rev. B* **26** (1982) 5409;  
Ph. Avouris and B.N.J. Persson, *J. Phys. Chem.* **88** (1984) 837.
76. B.N.J. Persson and Ph. Avouris, *J. Chem. Phys.* **79** (1983) 5156.
77. R.P. van Duyne, in *Chemical and Biochemical Applications of Lasers*, vol. 4,  
ed. C.B. Moore (Academic, New York, 1979).
78. J. Gersten and A. Nitzan, *J. Chem. Phys.* **75** (1981) 1139, and references  
therein.
79. C.J. Chen and R.M. Osgood, *Phys. Rev. Lett.* **50** (1983) 1705.
80. A. Campion and D.R. Mullins, *Chem. Phys. Lett.* **94** (1983) 576.
81. A. Nitzan and L.E. Brus, *J. Chem. Phys.* **74** (1981) 5321;  
A. Nitzan and L.E. Brus, *J. Chem. Phys.* **75** (1981) 2205.
82. S. Garoff, D.A. Weitz and M.S. Alvarez, *Chem. Phys. Lett.* **93** (1982) 283.
83. G.M. Goncher, C.A. Parsons and C.B. Harris, *J. Phys. Chem.* **88** (1984) 4200.
84. J. Arias, P.K. Aravind and H. Metiu, *Chem. Phys. Lett.* **85** (1982) 404.

*APPENDIX 1*

**VIBRATIONAL PREDISSOCIATION SPECTRUM  
OF METHYL FLUORIDE DIMER**

In work prior to the study described in Chapter 3, we attempted to obtain the vibrational predissociation spectrum of isolated van der Waals complexes of  $\text{CH}_3\text{F}$ . The dimers proved to be quite difficult to isolate, due to the large dipole of  $\text{CH}_3\text{F}$ . Recently, we managed to obtain the dissociation spectrum of methyl fluoride dimer,  $(\text{CH}_3\text{F})_2$ , presented in Figure 1. The lowest profile most clearly presents the structure that is obvious in the spectra obtained over a variety of conditions. There is no additional narrowing of the profile down to 660 Torr backing pressure but a loss of peak intensity which is observed; this could be due to either a higher rotational temperature at the lower pressure or loss of  $\text{He}\cdot(\text{CH}_3\text{F})_2$  complexes, if they contribute to the observed spectrum. The profile is very broad ( $\sim 20 \text{ cm}^{-1}$ ) and exhibits structure which is partially resolved by the  $\text{CO}_2$  laser. The extreme broadness suggests a substantially lifetime broadened spectrum, on the order of that observed for  $(\text{C}_2\text{H}_4)_2$ . The structured contour should make it possible to model the dimer structure.

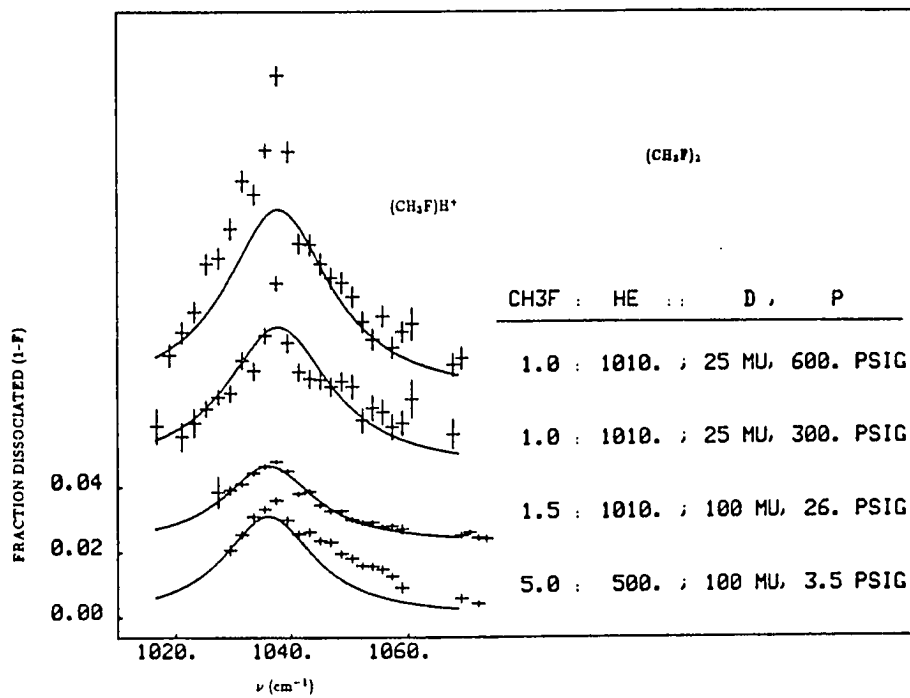


Figure 1. Vibrational predissociation spectrum of  $(\text{CH}_3\text{F})_2$ .

*APPENDIX 2*

**BAKEOUT CONTROLLER SYSTEM**

**BAKEOUT CONTROLLER FOR THE USE OF HELIUM CLOSED-CYCLE  
REFRIGERATORS IN UHV APPLICATIONS\***

Francis G. Celi,† Paul M. Whitmore and Kenneth C. Janda‡

*Arthur Amos Noyes Laboratory of Chemical Physics,  
California Institute of Technology, Pasadena, California 91125, USA*

**ABSTRACT**

Simple control electronics are described which provide automated bakeout of an UHV chamber equipped with a helium closed-cycle refrigerator. By preventing the refrigerator from reaching elevated temperatures ( $T \leq 50^\circ \text{C}$ ) during bakeout, these devices can be utilized in the ultra-high vacuum environment.

---

\* Contribution No. 7236

† Atlantic Richfield Foundation Fellow

‡ Camille and Henry Dreyfus Foundation Fellow

## 1. Introduction

The helium closed-cycle refrigerator provides a convenient way to achieve ultra-low temperature without the daily consumption of cryogenic liquids. Matrix isolation spectroscopists today utilize these as cryostats almost exclusively,<sup>1</sup> and they are widely used as the heart of cryopumps.<sup>2</sup> There have been a number of recent crystal manipulator designs based on the use of flowing cryogenes.<sup>3–7</sup> Devices such as the CTI Model 350 refrigerator,<sup>8</sup> would be useful as an alternative to cooling crystal samples for surface science applications – the 350 provides 2 W of cooling power at 15 K (second stage) with 20 W of heat load at 77 K (first stage) – but they are not UHV compatible. Joints that are normally soft-soldered can be replaced with silver-soldered joints,<sup>9</sup> but lead shot in the displacer as well as the piston assembly in the head which is not rated above 150° F preclude the necessary practice of a 150-200° C bakeout. We have found, however, that with careful control of the refrigerator temperature during bakeout, these devices can be utilized in the UHV environment. This note describes the temperature sensing and control electronics we have employed for this purpose.

## 2. Bakeout Control System

As implemented in our system, the bakeout control system is configured in 3 sub-units, as illustrated in Figure 1:

- a.) The *bakeout controller* houses the thermocouple amplifier, which senses the temperature of the refrigerator's second cold stage. An additional amplifier stage provides a convenient monitor voltage, and comparators establish under- and over-temperature set points.

BAKEOUT CONTROL SYSTEM

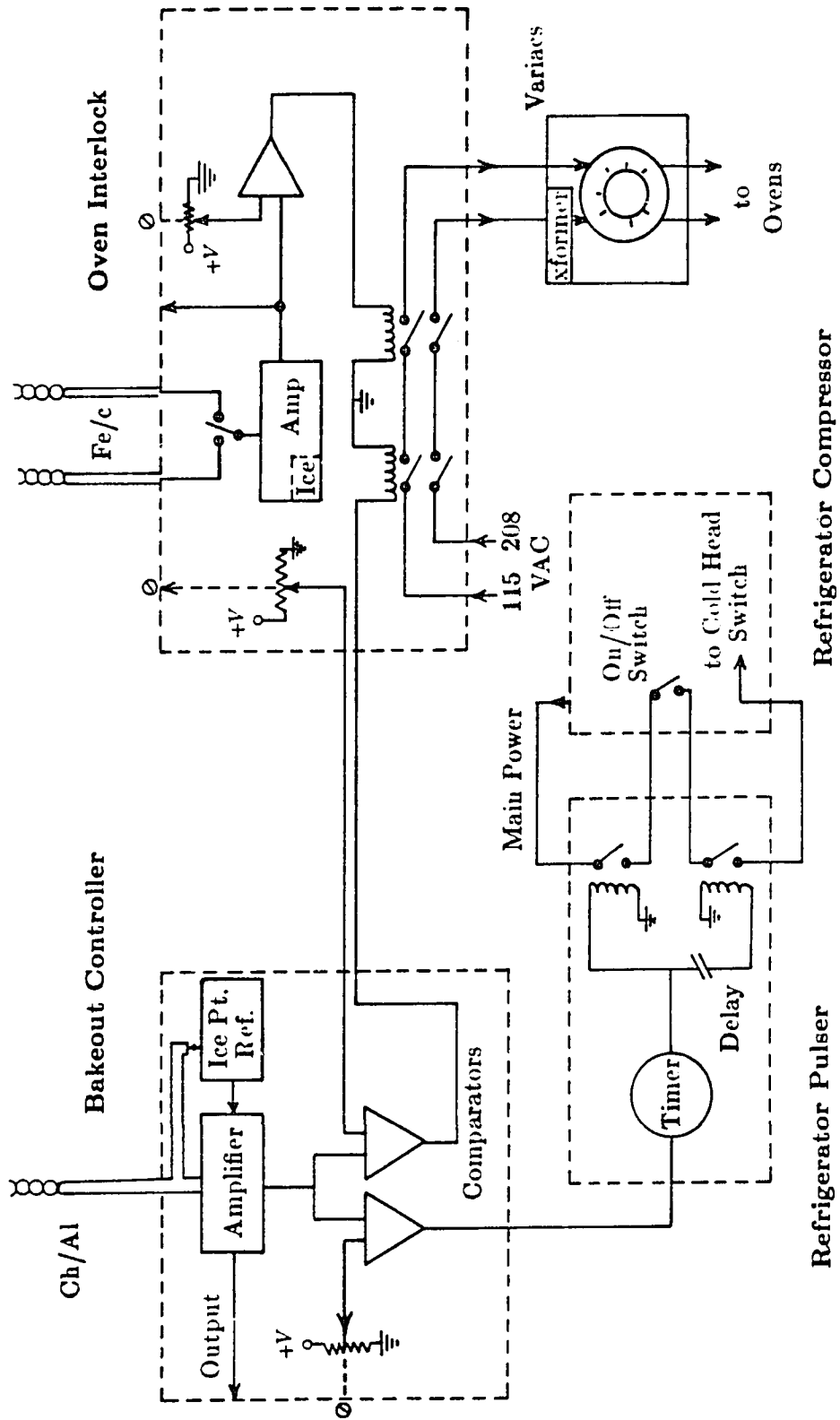


Figure 1. Schematic of the bakeout controller system.

- b.) The *refrigerator pulser* responds at the first (lower) set point of the bakeout controller to activate a cooling cycle of the refrigerator.
- c.) The *oven interlock* severs power to the bakeout ovens in the event of an over-temperature condition (second set point).

The heart of the bakeout controller (Figure 2) is the AD595, a thermocouple amplifier with internal ice-point reference.<sup>10</sup> A particularly convenient feature of this amplifier is that the sensing thermocouple junction can be grounded – in the case of a differential amplifier, one would need to electrically isolate the junction while maintaining good thermal contact. The standard 10 mV/° C output of the AD595 is additionally amplified by a second stage ( $\times 10$ ), providing a monitor output as well as input to the comparators. The comparators (LM321) provide the levels to open or close relays in the refrigerator pulser and oven interlock.

The refrigerator pulser (Figure 3) provides automated control of both the refrigerator compressor unit and the cold head piston. A pair of 3-conductor 14-gauge cables are interposed behind the two switches on the front panel of the compressor unit. This is the only modification made to the original compressor unit and is accomplished so that the cover can still be conveniently removed. The signal from the bakeout controller, through a low-current relay, initiates a Cycl-Flex 0→10 minute timer<sup>11</sup> which in turn activates the compressor. A time-delay relay allows the compressor to stabilize ( $\sim 10$  sec) before providing power to the cold head piston. A manual override provides constant operation for crystal cooling purposes.

The oven interlock (Figure 4) provides power to the bakeout ovens through a

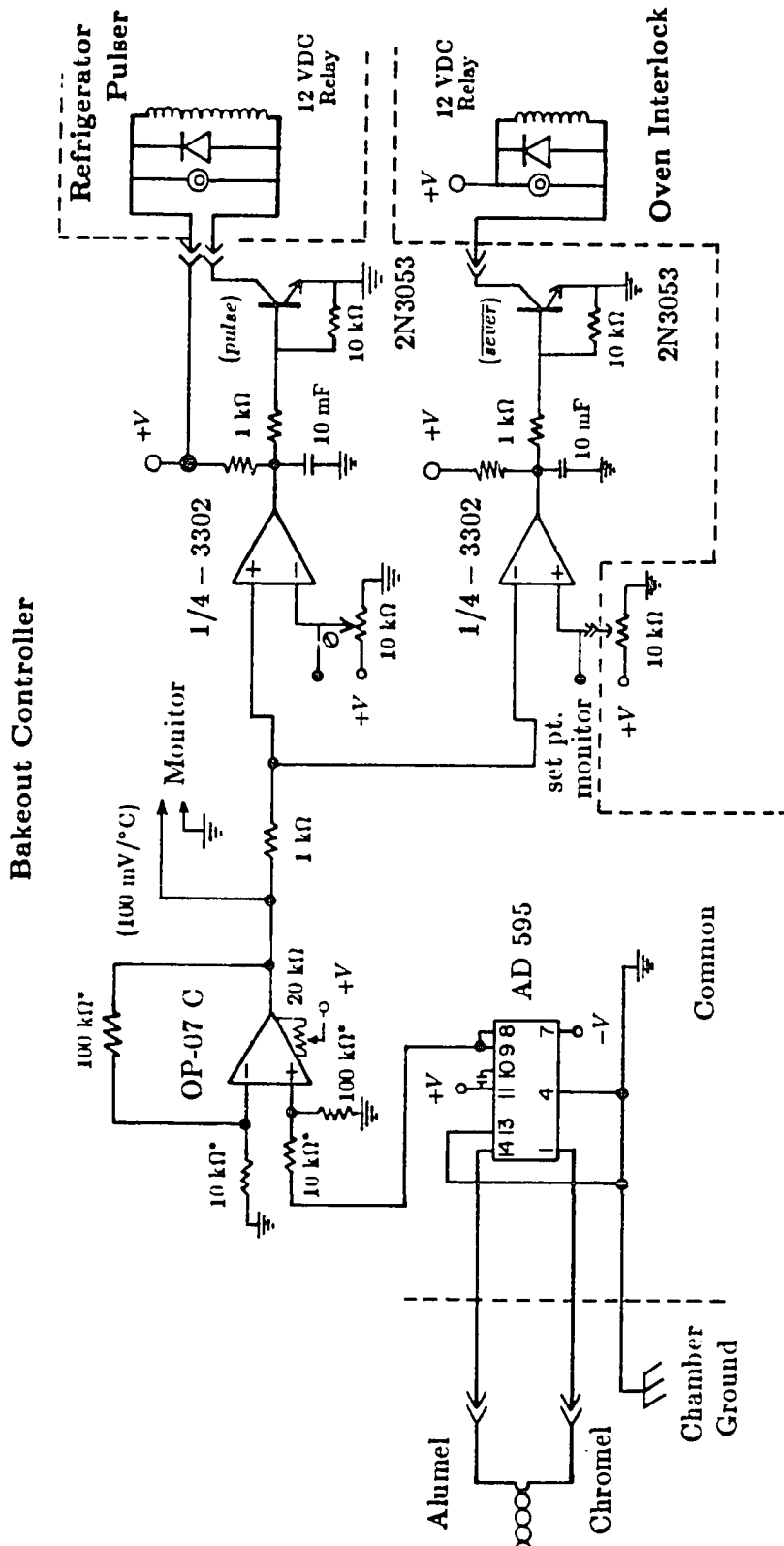


Figure 2. Diagram of the bakeout controller.

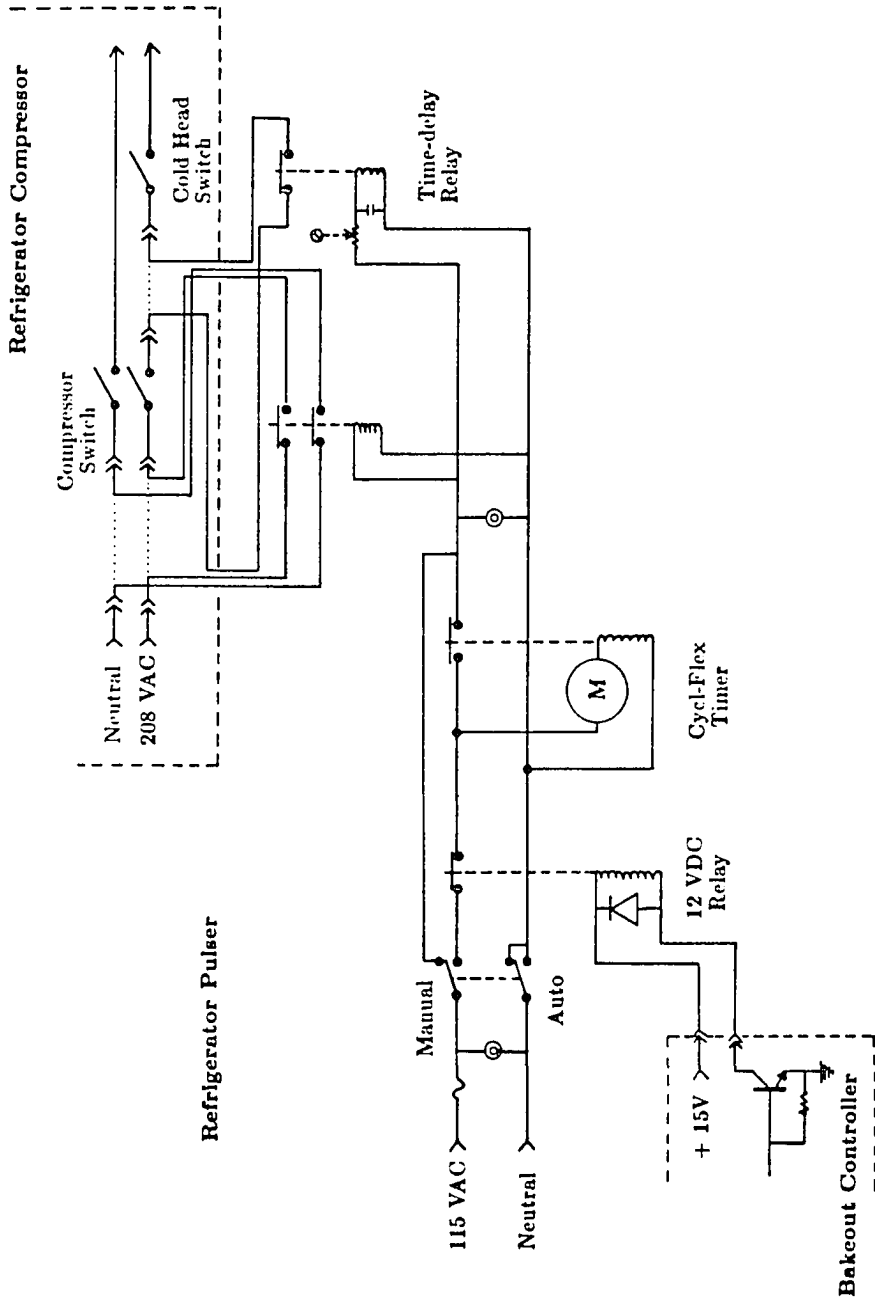


Figure 3. Diagram of the refrigerator pulser.

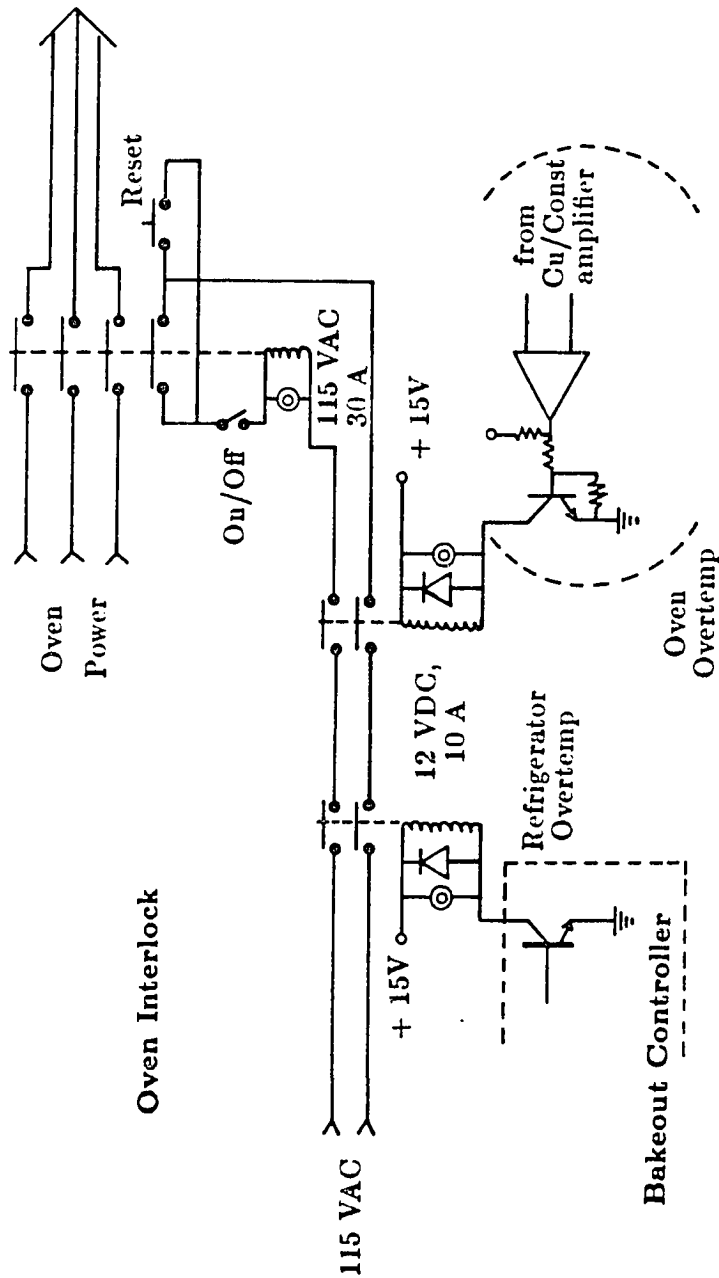


Figure 4. Diagram of the oven interlock. The segment in parentheses can be implemented if the oven temperature can reach over 200°C.

latched relay. Should the refrigerator not remain sufficiently cool, the bakeout would be stopped. Provision could be made here for maintaining the bakeout temperature below a maximum value, but this is not a problem in our system.

### 3. Operation

A sample ion-gauge trace during a bakeout using this controller system is shown in Figure 5. The gradual decrease in chamber pressure is modulated by the refrigerator cooling cycles. Gases desorb as the refrigerator surface warms to 35 ° C, the first set point. Chamber pressures in the low  $10^{-7}$  Torr range are achieved during bakeout, and titanium pumping after cooldown routinely results in pressures of  $1 - 2 \times 10^{-10}$  Torr. Refrigerator pulses of 5 - 7 minutes are required every 20 - 30 minutes during the 200° C bakeouts. The piston assembly in the cold head is located outside the ovens, and remains relatively cool with the use of a fan.

Using the 2-stage cooling provided by the CTI 350, we have achieved crystal temperatures as low as ~35 K (using a calibrated chromel vs. gold-5% iron thermocouple pair) with heat conduction through a high-grade (99.999%, or 5N grade) flexible Cu braid,<sup>12</sup> to allow crystal rotation on a manipulator with 2½-inch offset, and without extensive crystal shielding. Presumably the design of this low-temperature sample mount could be improved. We have also used a high-temperature mount, which is equipped to heat samples to 1500 K, and with this configuration the crystal cools to 120 K. In addition to providing the two cold stations, the refrigerator acts as an integral cryopump during operation. A multichannel array gas doser is therefore desirable so that samples may be preferentially adsorbed on the crystal sample rather than the refrigerator. The

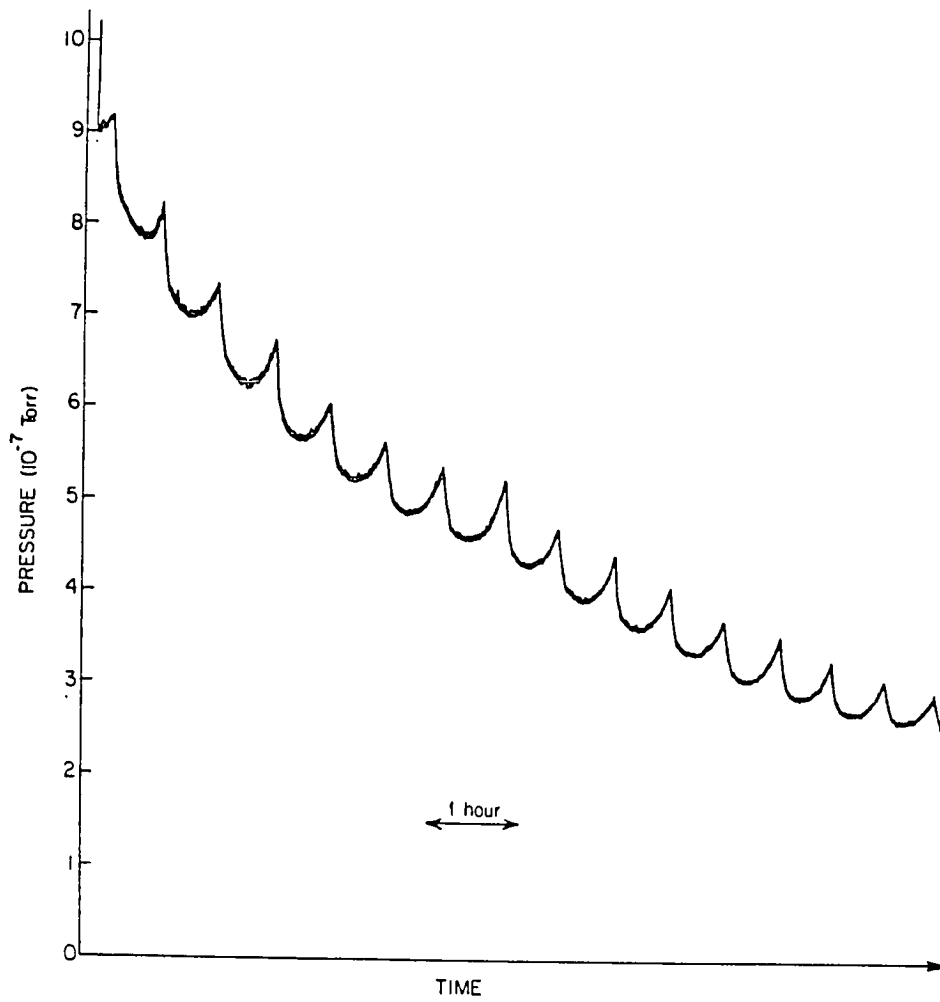


**Figure 5.** Ion gauge trace obtained during bakeout of UHV chamber. The chamber pressure is modulated by on-off cycles of the refrigerator.

refrigerator being pulsed on-off during bakeout prevents H<sub>2</sub>O and other condensibles from freezing onto the cold refrigerator surfaces and remaining in the chamber.

### **Acknowledgement**

We are grateful to Professor Sten Samson for advice on low-temperature techniques, as well as for the thermocouple wire and the loan of a Si diode system, for temperature calibration.

## References

1. A.J. Barnes and H.E. Hallam, in *Vibrational Spectroscopy – Modern Trends*, A.J. Barnes and W.J. Orville-Thomas, eds. (Elsevier, New York, 1977).
2. M. Michaud and L. Sanche, *J. Vac. Sci. Tech.* **17** (1980) 274;  
R.A.A. Kubiak, W.Y. Leong, R.M. King and E.H.C. Parker, *J. Vac. Sci. Tech.* **A1** (1983) 1872.
3. J.A. Stroschio and W. Ho, *Rev. Sci. Instrum.* **55** (1984) 1672.
4. P.A. Thiel and J.W. Anderegg, *Rev. Sci. Instrum.* **55** (1984) 1669.
5. N.J. DiNardo, J.E. Demuth, W.A. Thompson and P.G. Ledermann, *Rev. Sci. Instrum.* **55** (1984) 1492.
6. E.E. Chaban and Y.J. Chabal, *Rev. Sci. Instrum.* **54** (1983) 1031.
7. I. Arakawa and Y. Tuzi, *Rev. Sci. Instrum.* **55** (1984) 617.
8. CTI Cryogenics, Kelvin Park, Waltham, MA 02154; the same model refrigerator can be purchased mounted on a conflat flange from: Cryosystems, Inc., 190 Heatherdown Dr., Westerville, OH 43081.
9. G.L. Fowler and J.A. Panitz, *Rev. Sci. Instrum.* **51** (1980) 1730.
10. Analog Devices AD595 (pre-trimmed for chromel-alumel) or AD594 (iron-constantan).
11. Cycl-Flex HP54, Eagle Signal, 736 Federal St., Davenport, IA 52803.
12. S. Samson, E. Goldish and C.J. Dick, *J. Appl. Cryst.* **13** (1980) 425.